ROTORCRAFT WAKE ANALYSIS FOR THE PREDICTION OF INDUCED VELOCITIES

Anton J. Landgrebe, et al

United Technologies Research Center

Prepared for:

Army Air Mobility Research and Development Laboratory

January 1976

DISCLAIMER NOTICE

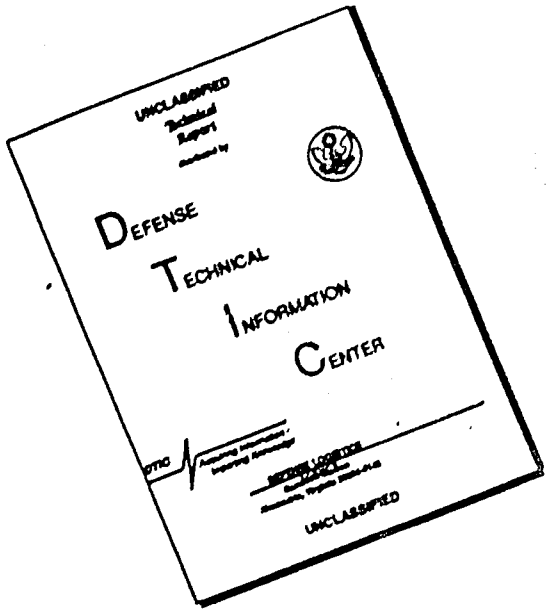

THIS DOCUMENT IS BEST QUALITY AVAILABLE. THE COPY FURNISHED TO DTIC CONTAINED A SIGNIFICANT NUMBER OF PAGES WHICH DO NOT REPRODUCE LEGIBLY.

USAAMRDL-TR-75-45

ROTORCRAFT WAKE ANALYSIS FOR THE PREDICTION OF INDUCED VELOCITIES

United Technologies Research Center
East Hartford, Conn. 06108

January 1976

Final Report for Period February 1974 - October 1975

Approved for public release;
distribution unlimited.

Prepared for

EUSTIS DIRECTORATE
U. S. ARMY AIR MOBILITY RESEARCH AND DEVELOPMENT LABORATORY
Fort Eustis, Va. 23604

EUSTIS DIRECTORATE POSITION STATEMENT

This report has been reviewed by the Eustis Directorate, U. S. Army Air Mobility Research and Development Laboratory and is considered to be technically sound. The analysis for predicting induced velocities at the rotor disk and at other field points due to rotor(s) and a wing is shown to be in generally good agreement with test data. The method is limited by the assumptions of lifting line elements and prescribed wake geometry. The computer program used for this study is in the public domain and is available through the Administrative Support Division of the Eustis Directorate.

The technical monitors for this contract were Mr. Edward E. Austin and ILT Lane F. Ellington, Aeromechanics Technical Area, Technology Applications Division.

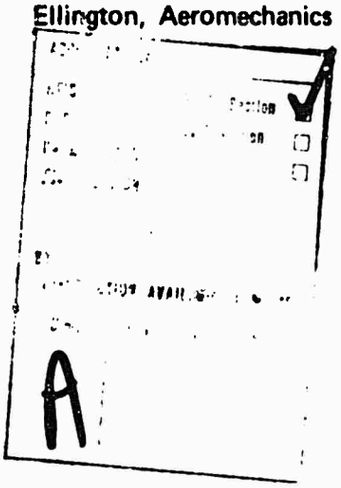

DISCLAIMERS

The findings in this report are not to be construed as an official Department of the Army position unless so designated by other authorized documents.

When Government drawings, specifications, or other data are used for any purpose other than in connection with a definitely related Government procurement operation, the United States Government thereby incurs no responsibility nor any obligation whatsoever; and the fact that the Government may have formulated, furnished, or in any way supplied the said drawings, specifications, or other data is not to be regarded by implication or otherwise as in any manner licensing the holder or any other person or corporation, or conveying any rights or permission, to manufacture, use, or sell any patented invention that may in any way be related thereto.

Trade names cited in this report do not constitute an official endorsement or approval of the use of such commercial hardware or software.

DISPOSITION INSTRUCTIONS

Destroy this report when no longer needed. Do not return it to the originator.

Unclassified

SECURITY CLASSIFICATION OF THIS PAGE (When Data Entered)

REPORT DOCUMENTATION PAGE		READ INSTRUCTIONS BEFORE COMPLETING FORM
1 REPORT NUMBER USAAMRDL-TR-[illegible]	2. GOVT ACCESSION NO.	3. RECIPIENT'S CATALOG NUMBER
4. TITLE (and Subtitle) ROTORCRAFT WAKE ANALYSIS FOR THE PREDICTION OF INDUCED VELOCITIES		5 TYPE OF REPORT & PERIOD COVERED Final Feb. 1974 - Oct. 1975 6 PERFORMING ORG. REPORT NUMBER UTRC Report R75-911852-18
7. AUTHOR(s) Anton J. Landgrebe T. Alan Egolf		8. CONTRACT OR GRANT NUMBER(s) DAAJ02-74-C-0027
9. PERFORMING ORGANIZATION NAME AND ADDRESS United Technologies Research Center East Hartford, Connecticut 06108		10 PROGRAM ELEMENT, PROJECT, TASK AREA & WORK UNIT NUMBERS 62209A 1F262209AH76 00 026 EK
11 CONTROLLING OFFICE NAME AND ADDRESS Eustis Directorate U. S. Army Air Mobility R&D Laboratory Fort Eustis, Virginia 23604		12. REPORT DATE January 1976 13. NUMBER OF PAGES 173
14 MONITORING AGENCY NAME & ADDRESS(if different from Controlling Office)		15. SECURITY CLASS. (of this report) UNCLASSIFIED 15a. DECLASSIFICATION/DOWNGRADING SCHEDULE

16 DISTRIBUTION STATEMENT (of this Report)

Approved for public release; distribution unlimited.

17 DISTRIBUTION STATEMENT (of the abstract entered in Block 20, if different from Report)

18. SUPPLEMENTARY NOTES

19. KEY WORDS (Continue on reverse side if necessary and identify by block number)

Helicopter
Helicopter Aerodynamics
Wake Geometry
Induced Velocities
Rotorcraft Wake Analysis
Rotor Wake
Rotor Performance

20. ABSTRACT (Continue on reverse side if necessary and identify by block number)

A Rotorcraft Wake Analysis for computing flow velocities induced by the rotors and wing of a helicopter is described, and predicted induced velocities are compared with experimental data from many sources. Combined in a single computerized analysis are the capabilities for calculating three components of time-averaged and instantaneous induced velocities on or off the rotor(s) of single-rotor, dual-rotor, and winged helicopter configurations

DD FORM 1 JAN 73 1473 EDITION OF 1 NOV 65 IS OBSOLETE

Unclassified

SECURITY CLASSIFICATION OF THIS PAGE (When Data Entered)

in hovering and forward flight. Generality of the wake representation is provided in the analysis by the use of wake modeling options and prescribed undistorted and distorted wake geometries. The analysis is intended for use in conjunction with a rotor performance and blade response analysis such as the Rotorcraft Flight Simulation Analysis available to the Government. The accuracy of the Rotorcraft Wake Analysis is demonstrated through comparison of the predicted induced velocities with available experimental data. The generally successful prediction of primary characteristic features of both time-averaged and instantaneous induced velocity distributions in and out of the rotor wake, and local velocity variations with rotor design and test condition parameters, is demonstrated within the scope of the available test data. Although the predicted velocities are generally in good agreement with the test data, the degree of accuracy at specific field points is shown to be sensitive to the accuracy of the prescribed wake representation and the proximity of the field points to a wake boundary or blade, in addition to the flight condition, rotor control, and blade motion information provided as input to the analysis.

PREFACE

This investigation was sponsored by the Eustis Directorate of the U. S. Army Air Mobility Research and Development Laboratory under Contract DAAJ02-74-C-0027, Project 1F262209AH76. The development of the components of the Rotorcraft Wake Analysis was conducted at the United Technologies Research Center (UTRC) over a period of more than 10 years. The Rotorcraft Wake Analysis was furnished as a result of the on-going UTRC research program. In accordance with the immediate objective of the contract, the analysis was furnished for use with the Rotorcraft Flight Simulation Analysis (C-81 Program) available to the Government. The correlation, demonstration, and documentation of the Rotorcraft Wake Analysis, as reported herein, were conducted under the contract.

The technical representatives of the Contracting Officer were Mr. Edward Austin and Lt. Lane Ellington of the Technology Applications Division, Eustis Directorate. Their assistance in the demonstration of the computer program for the Rotorcraft Wake Analysis on the Eustis Directorate computer is gratefully acknowledged. Contract management at the United Technologies Research Center was conducted by Mr. Anton J. Landgrebe (Supervisor, Rotary Wing Technology) and Mr. Marvin C. Cheney, Jr. (Chief, Aerodynamics).

TABLE OF CONTENTS

TABLE OF CONTENTS (CONT'D)

LIST OF ILLUSTRATIONS

LIST OF TABLES

INTRODUCTION

The task of predicting the flow field induced by a helicopter rotor continues to be of primary importance for providing and evaluating improved rotor designs. The continuing development of more accurate aerodynamic methods for predicting the temporal and spatial variation of velocities at the rotor blades and in the rotor flow field is resulting in significant advances in rotor aerodynamic methodology important to nearly every area of rotary-wing design. These areas include performance, vibrations, structural reliability, and acoustics. For example, in addition to performance improvement, improved capability to predict the detailed flow characteristics results in the prediction of more accurate blade loads and thus a more rational design of the blade structure. This, in turn, can lead to reduced aircraft development and maintenance costs and improved performance because of the resulting more optimized design. Also, the capability to predict rotor-induced flow velocities away from the rotor is important for the calculation of aerodynamic interference effects at aircraft components such as the fuselage, wing, and tail surfaces.

In order to design and evaluate new rotor systems, it is recognized that a reasonably accurate method for predicting rotor-induced velocities is required. It should be capable of predicting velocities for all existing and contemplated helicopters operating over the entire speed range. It should be cost-effective and efficient to operate. It should represent the current state of the art, be reasonably accurate, but not be overly complex. In addition, it should have the growth potential to incorporate new technology advances as they are developed or become cost-effective.

The major technological advance in recent years to rotor-induced velocity methodology has been the improvement in the mathematical modeling of the rotor wake. This has become possible with the advent of high-speed digital computers. Many efforts have been directed toward providing this methodology as shown in the survey presented in Reference 1. As a major part of a long-term effort to advance the technology associated with the aerodynamic and aeroelastic behavior of helicopter rotor blades, the United Technologies Research Center, UTRC (formerly, United Aircraft Research Laboratories), has for the last decade, been conducting studies on the influence of the rotor and wing wakes on rotor inflow and dependent rotorcraft characteristics. Some of the research programs conducted in this area are discussed in References 1 through 13. The scope of this effort has included both analytical and experimental programs, distorted and undistorted wake analyses, single- and multi-rotor configurations, conventional and compound helicopters, and hover and forward flight conditions. Methods developed are currently in use at several organizations within the Government and industry.

With the above requirements and capabilities in mind, an effort was undertaken to consolidate and expand several of the available UTRC analyses to form a single comprehensive helicopter rotor and wing wake analysis to predict induced velocities for use with rotor performance and airloads analyses, such as the Government's Rotorcraft Flight Simulation Program (Computer Program C-81). The resulting analysis is entitled the UTRC Rotorcraft Prescribed Wake Induced Velocity Analysis, and will hereafter be referred to briefly as the Rotorcraft Wake Analysis. It will be shown that the Rotorcraft Wake Analysis is applicable to single and dual (tandem, side-by-side, and coaxial) rotor systems, and both conventional and compound (winged) helicopter configurations. It incorporates a cost-effective prescribed wake option which allows for a selection between undistorted, experimental and analytical wake representations. A flow chart of the Rotorcraft Wake Analysis, which will be described in detail in the body of the report, is presented in Figure 1.

The accuracy of the component methods of the Rotorcraft Wake Analysis has previously been evaluated in conjunction with rotor performance and airloads analyses by comparing the resulting analytical performance, airloads, blade response and bending moments with test data. Many of these comparisons are included in the aforementioned references. In order to provide a more direct assessment of the Rotorcraft Wake Analysis by comparing the output induced velocities with measured test data from many sources, an induced velocity correlation study was performed, and the results are presented herein. The use of the Rotorcraft Wake Analysis in conjunction with the Government's Rotorcraft Flight Simulation Program has been demonstrated.

Thus, the objective of the research program reported herein was to develop, evaluate, and demonstrate the Rotorcraft Wake Analysis. More specifically, it was to provide an analysis for computing induced velocities both at and away from the rotor, based on prescribed undistorted and distorted wake representations for hover and steady forward flight conditions, and for a wide range of rotor configurations including dual rotors and a wing. In accordance with this objective, the following sections consist of (1) a description of the Rotorcraft Wake Analysis, (2) results of the induced velocity correlation study, and (3) conclusions and recommendations.

DESCRIPTION OF THE ROTORCRAFT WAKE ANALYSIS

COMPONENT ANALYSES

The Rotorcraft Wake Analysis was developed by incorporating and extending the following three UTRC prescribed wake analyses and a rotor-wing interference analysis in a self-consistent, single computer program:

1. UTRC Prescribed Wake Rotor Inflow Analysis (UTRC Deck F389)
2. UTRC Prescribed Wake Hover Performance Analysis (UTRC Deck F456)
3. UTRC Coaxial Rotor Prescribed Wake Hover Analysis (UTRC Deck G413)
4. UTRC Rotor/Wing Interference Analysis (UTRC Deck F109)

In general, these methods are not redundant in that they are directed toward a specific flight mode or type of configuration. They have been combined and expanded to provide flexibility with regard to flight mode and configuration in one computer program. Although the capability of the composite Rotorcraft Wake Analysis has been extended beyond the scope of the individual analyses listed above, these analyses form the foundation of the new computer program. Thus, a brief description of each is presented below prior to a description of the interrelationship of the analyses and the refinements included in the composite analysis. More detailed descriptions, applications, and correlations of the individual methods can be found in References 1 through 12.

UTRC Prescribed Wake Rotor Inflow Analysis

The function of the UTRC Prescribed Wake Rotor Inflow Analysis (UTRC Deck F389) is to compute the time-varying circulation and inflow distributions along the blades that are compatible with a prescribed set of blade section operating conditions and a prescribed wake geometry. This analysis is primarily used for single-rotor forward-flight conditions, although it is also applicable, but not cost-effective, to time independent hover conditions. The fundamentals of this analysis generally represent an extension of the classical lifting line approach used successfully for fixed-wing aircraft, which was initially applied to the rotary-wing problem by Piziali and DuWaldt in Reference 14. That is, although the rotary-wing problem is much more complex than the fixed-wing problem, due to multiple blades and the complex wake geometry and unsteady flows due to blade rotation, the fundamental aerodynamic relations of blade circulation to lift coefficient, angle of attack, blade motions, control settings, induced velocity, and wake geometry remain valid for this analysis.

The blade section operating conditions (nonaerodynamic) are generally prescribed from blade motion and control information obtained from a separate rotor performance and blade response analysis. The wake geometry representation is either generated internally in the computer program (undistorted wake for forward flight) or prescribed by input or a separate wake geometry program. A flow chart showing the relation of the inflow analysis to the rotor performance/blade response analysis and the wake geometry analysis is presented in Figure 2. Descriptions and results pertaining to the development and application of the rotor inflow program are presented in References 1 through 7.

Briefly, the mathematical model in the rotor inflow program consists of the representation of each blade by a segmented lifting line, and the helical wake of the rotor by discrete segmented vortex filaments consisting of trailing vorticity, which result from the spanwise variation of bound circulation. The circulation of the wake for each blade changes with azimuth position and is periodic for each rotor revolution. The blades are divided into a finite number of radial segments, and the induced velocity at the center of each selected blade segment is computed by summing the contributions of each bound and trailing wake segment. The contribution of each vortex segment is obtained through use of the Biot-Savart law, which expresses the induced velocity in terms of the circulation strength of the vortex segment and its geometrical position relative to the blade segment at which the induced velocity is desired. The bound circulation distribution is determined by relating the wake circulations to the bound circulations, expressing the wake induced velocities in terms of the unknown bound vortex strengths by means of the Biot-Savart law, and developing a set of simultaneous equations relating the bound circulation and local blade angle of attack at each blade segment. These equations thus involve the known flight condition, wake geometry, lift-curve slope, blade motion and control parameters, and the unknown bound circulation values. The circulation equations represent a matrix of terms, the number of which (number of equations and terms in each) equals the square of the number of points on the rotor disk (number of azimuth positions times number of radial stations). Solution of these equations yields the desired bound circulation values, which, when combined with the appropriate geometrical relations in the Biot-Savart law, produce the required induced velocities at or away from the rotor blades.

A simplified flow diagram showing the sequence of operations of the program is presented in Figure 3. The known section parameters (airfoil noninduced velocity components, lift-curve slope, and geometric angle of attack) are computed. The blade-wake geometry is formulated. The wake

influence coefficients (geometric coefficients) at the blades are calculated using the Biot-Savart law. Numerical techniques are used to solve the circulation matrix. Finally, the blade inflow and induced velocities off the blades are computed.

More specifically, the rotor inflow program is based on the following formulation and assumptions:

1. Each blade is represented by a lifting line (bound vortex) divided into a finite number of segments (blade segments), each having a different circulation strength (see Figure 4). The aerodynamic characteristics at the centers of each segment are assumed to be representative of the entire segment over a finite azimuth interval.

2. The wake is represented by a finite number of vortex filaments trailing from the blade segment boundaries. Each filament is divided into straight segments, the lengths of which are determined by a specified wake azimuth interval which is equivalent to the azimuth interval of each blade (see Figure 4). The circulation strength of each trailing vortex segment is constant along its length, and is equivalent to the difference between the circulation values of its adjacent bound vortex segments when shed in accordance with the Helmholtz laws of conservation of vorticity. The circulation strengths of different vortex segments along a vortex filament vary in accordance with the variation of the bound circulations with azimuth position.

3. Viscous dissipation effects on the wake circulation strengths are neglected, in that the circulation of a given wake segment is constant with time. However, the number of wake revolutions retained in the analysis can be limited to evaluate an abrupt dissipation of the wake. Also, the viscous roll-up of the tip vortex can be approximated by combining tip filaments beyond a prescribed roll-up azimuth interval. In addition, a vortex core size is assigned to each vortex filament. Potential theory is assumed to apply outside the vortex core. Inside the vortex core an option for rotational or zero flow is provided.

4. It is assumed that the rotor is operating in steady-state flight. The inflow and wake from each blade is assumed to be periodic with blade spacing. That is, the inflow and wake geometry are the same for each blade when at a specific azimuth position.

5. Shed wake segments (segments normal to the trailing wake segments mentioned above) arising from time, rather than radial variations of bound vorticity, are not included in the wake model. Although this omission

technically violates a Helmholtz law, it is believed that a more accurate representation of the shed wake effects is obtained through the use of experimental unsteady airfoil characteristics in the analysis. This implies that the primary effects of the shed vorticity are those associated with the shed wake immediately behind the blade, and thus can be approximated by those of a fixed-wing type of wake. Miller (Reference 15) shows that this is reasonable at least for moderate rotor advance ratios. This approach not only permits a reduction factor of two in computer time and prevents unrealistic results associated with a finite filament wake model but, more importantly, permits nonlinear unsteady stall effects to be included in a rational manner in a blade response program through the use of unsteady airfoil data.

6. The wake geometry is prescribed from analytical or experimental results. Various options to be discussed are available for selecting the representation of the wake model.

7. The airfoil at the blade is assumed to be two-dimensional (radial velocity components are neglected). For the linearized circulation solutions and associated calculations, lift-curve slopes, stall angles of attack, and angles of zero lift are provided which vary with Mach number. These values may be based on unsteady aerodynamic data, if available, and provided directly from a blade response program. Below stall, the lift-curve slope is assumed to be constant. The blade section circulation is limited to a constant value for each Mach number for angles of attack above stall.

8. In the blade-wake geometry calculations the blades are assumed to be straight (rigid blades). However, flexibility effects may be included in the circulation solution by providing the necessary noninduced velocity at each segment associated with flexible blade motions and controls from a blade response program.

9. Tangential and radial induced velocity components are neglected in the circulation solution.

10. Small-angle assumptions are included in the circulation solution.

11. The aerodynamic interference effects of the rotor hub, fuselage, and tail rotor are neglected. The rotor is assumed to be operating out of ground effect.

Forward-Flight Wake Geometry

The rotor inflow analysis requires that the rotor wake geometry be specified in order for circulations and induced velocities to be determined. Since the wake geometry is prescribed, the wake may vary from an undistorted

wake model to a complex experimental or distorted analytical wake model with tip vortex roll-up and vortex core effects mathematically modeled. Thus, there are several alternatives for rotor wake geometry. The least complex is a classical undistorted wake which is simply a function of the flight condition and momentum inflow velocity. The coordinates of this helical wake, which is skewed in forward flight, are easily generated in this prescribed wake type of analysis given the governing parameters which can be iterated on if desired. The generation of analytical distorted wake geometries require more complex and operationally expensive computer analyses. Appropriate experimental wake data are certainly most desirable but, except for hover, are not currently available for most rotor configurations and forward flight conditions. It has been established that the requirement for distortions from the classical type wake geometry is dependent on the rotorcraft configuration, flight condition, parameter of interest, and accuracy required. For example, an undistorted wake geometry is often sufficiently accurate for integrated performance calculations (thrust, torque, etc.) for conventional rotorcraft operating in high-speed flight. However, for hover and low-speed conditions, wake distortions are very significant. Either an undistorted or a distorted wake geometry may be used in the analysis. Distorted wake geometry may be from analytical or experimental sources.

In its simplest form, the wake from each blade can be assumed to be a classical undistorted skewed helical sheet of vorticity defined from momentum considerations. An option is provided in the computer program for representing the roll-up of the outer portion of the blade's wake into a concentrated tip vortex. To distinguish between the two optional wake representations without wake distortions, the following nomenclature will be used herein:

Classical Wake Representation -- The analytical wake representation in which wake distortions are neglected, and all vortex filaments are retained for the same number of wake revolutions (classical vortex sheet representation of the wake).

Undistorted Wake Representation -- The analytical wake representation in which wake distortions are neglected, but the roll-up of the outer vortex filaments into a concentrated tip vortex is modeled by combining the outer filaments into a single tip vortex filament at a prescribed azimuthal distance from the blade. A vortex core size is prescribed for the tip vortex filament.

The same undistorted inboard wake representation as in the classical wake representation is retained.

Sample forward flight wake representations are shown in Figures 5 through 7. In Figure 5, a sample computer plot of the classical wake representation for a two-bladed rotor at a 30-kt flight condition is presented. All vortex filaments are shown. For the "undistorted" wake representation, as defined above, the five outboard filaments for this condition would be combined at 15 deg behind each blade to simulate each rolled-up tip vortex. In Figure 6, the tip vortex filaments are presented. (The filaments representing the inboard vortex sheets have been omitted in this figure for clarity. However, they are identical to the inner filaments of the classical wake representation shown in Figure 5.) The coordinates of the undistorted wake representation are obtained from the rotor advance ratio, μ, thrust coefficient, C_T, and angle of attack relative to the tip path plane, α. For example, the top view of the tip vortex filaments in Figure 6 is obtained directly from the helicoidal path of the blade tip as it translates at the velocity $V\cos\alpha$ and rotates at the velocity ΩR. The side view is dependent on the wake skew angle, χ (angle between normal to the rotor disk and wake boundary), which is defined in the following manner:

$$\tan \chi = \frac{\text{ROTOR FORWARD VELOCITY COMPONENT IN PLANE OF ROTOR DISK}}{\text{MEAN ROTOR INFLOW VELOCITY NORMAL TO ROTOR DISK}}$$

or

$$\chi = \tan^{-1} \left\{ -\frac{V\cos\alpha}{V\sin\alpha - v_o} \right\} .$$

To eliminate the necessity for prescribing a classical or undistorted wake geometry, input provisions are made to obtain more realistic distorted wake geometries from experiment or a wake geometry analysis. For example, a distorted wake analysis developed at UTRC, entitled the Rotor Wake Geometry Analysis (UTRC Deck F506), involves the following. First, an undistorted wake model is defined along with the distribution of circulation strengths of the various vortex elements comprising the wake. The classical Biot-Savart law is then applied to determine the velocities induced by each vortex wake element at numerous points in the wake. These distorting velocities are then numerically integrated over a small time increment to obtain new wake element positions. The process of alternately computing new velocities and positions is continued until a converged, periodic distorted wake geometry is attained. Further details of the procedures used to compute wake geometries and results are given in References 1 through 9.

Sample computer plots of the distorted tip vortex geometry are presented in Figures 7 and 8. In Figure 7, the distorted tip vortex geometry is shown for the same 30-kt flight condition (μ = 0.068) as that of Figure 6. In Figure 8, the side view of the distorted tip filament of one blade is compared with the undistorted tip filament for a higher speed condition (μ = 0.14). In Figure 9 through 11, sample comparisons from References 2 and 3 of predicted wake geometries with experiment are presented for low and moderate speed conditions.

If available, experimental tip vortex coordinates may be prescribed in the analysis. A sample flow visualization photograph comparing the forward wake boundary of a UTRC model rotor indicated by tip vortex cross sections with the classical wake boundary is presented in Figure 12.

Circulation and Induced Velocity Solution

Following the formulation of the wake geometry representation in the program, the geometric relations between the wake and the blades are calculated, and the equations for the blade circulations and induced velocities are applied. The Kutta-Joukowski law and the Biot-Savart law are the basic relations used to obtain a closed-form solution for these parameters. The Kutta-Joukowski law relates the blade circulation and induced velocity distributions. The Biot-Savart law relates the blade induced velocity distribution to the wake circulations and wake geometry. The term "geometric coefficient" is used to describe the influence coefficients in the latter relation, which are functions only of the wake geometry. That is, once the circulations are computed, the velocities induced by the bound and trailing vorticity of the rotor can be determined through application of the Biot-Savart law, which can be expressed simply in the following form:

$$v = f\ (\Gamma, \text{Wake Geometry})$$

$$= \frac{1}{4\pi R} \Sigma(\Gamma)\ (GC)$$

Here the induced velocity at a point on the blade, v, is a function of the circulations and wake geometry, and is proportional to the summation of the products of the circulation strength, Γ, and the geometric influence coefficient, GC, of each element of vorticity in the rotor-wake system. The geometric coefficient is related only to the geometry between a wake element and the point at which the induced velocity is computed. Equations for the induced velocity components are presented in Appendix A. Several assumptions, mentioned above, for the airfoil lift characteristics, velocity components, and inflow angles were included in the establishment of the circulation

matrix in order to linearize the solution. The solution procedure consists mainly of 1) determination of the geometric coefficients, 2) establishment of the circulation matrix, 3) solution of the circulation matrix by a modified Gauss-Seidel iteration technique, 4) solution of the induced velocity distribution. Inflow with the results of the circulation solution, and 5) harmonic analysis of the inflow solution and calculation of aerodynamic parameters. In order to present the technical approach in greater detail and to indicate where assumptions are made, the primary equations contained in the circulation and inflow solution and a brief derivation thereof are presented in Appendix A.

As shown in Figure 4, the predicted induced velocity distribution can be used as input to a blade response program such as the Sikorsky "UTX" Blade Response Program (Reference 10) or the Boeing-Vertol Flight Simulation Computer Program (Ref. 11). An iteration is normally performed between the program to insure compatibility of the induced velocities and the blade section aerodynamic and dynamic boundary conditions. However, convergence in the past is usually obtained. Induced velocity, airloads, performance, and blade stress results predicted by the analysis with various wake models are presented in References 1 through 4. Sample induced velocity and airload distributions based on a undistorted wake are presented in Figures 13 and 14. As shown in Figure 14, the analysis, based on an undistorted wake, generally results in poor correlation for airloads except in regions where wake distortion or lifting surface effects are significant (0.9 R, 1.0 leg).

"UTX" Prescribed Wake Rotor Performance Analysis

The "UTX" Prescribed Wake Rotor Performance Analysis (UTX Deck #36) is used to compute the blade circulation, inflow distribution, and the corresponding performance of a hovering rotor based on a prescribed wake geometry. The technical formulation, wake representations, and applications of this analysis are presented in References 1, 2, 3 and through 11.

The formulation for this rotor analysis is similar to that of the Prescribed Wake Rotor Inflow Analysis described previously except that the time integration has been eliminated. The rotor is assumed to be hovering out of ground effect, and the wakes from the blades are assumed to be steady and identical to each other and displaced symmetrically. Thus, the blade and wake characteristics at a specific radial position are assumed to be independent of azimuth position. Since the circulation strength of each trailing vortex filament is equivalent to the difference between the circulation values of the adjacent bound vortex segments which are time independent, the circulation strength of each trailing vortex filament is constant along its length.

A flow diagram from Reference 8 showing the primary input items, sequence of major operations, and output of the computer program is presented in Figure 15. As indicated in this figure, the program is divided into three independent parts. The first transforms the wake geometry input to wake coordinates. The second contains the computation of the wake influence coefficients (geometric coefficients) at the blade as defined by the Biot-Savart law and the numerical procedures for solving the circulation matrix and associated induced velocity distribution. In the third part, performance characteristics are computed. A brief description of the techniques used in each of the three parts is presented below.

Hovering Wake Geometry

Generality regarding the specification of the wake geometry was provided in the computer program to permit the evaluation of a wide variety of wake geometry models. This was accomplished by requiring only general cylindrical wake coordinates for the wake segment end points in the main portion of the program. The specific wake model can then be selected from a series of separate wake geometry subroutines representing various methods for prescribing the wake shape. This facilitates the adaptation of improved wake models to the program as they become available. It also permits the assessment of classical wake models such as the Goldstein-type uncontracted wake. Sample computer plots of a typical distorted wake representation (far wake instability neglected) and a classical wake representation for a hovering rotor are presented in Figure 16.

For the classical wake representation, the radial coordinates of the wake segment end points comprising each trailing wake filament are everywhere equivalent to the blade radial coordinate from which they originated. The surface boundary of the resulting wake model is therefore cylindrical in shape. The axial velocity of all wake segment end points is equal to a constant which is an input item. The momentum induced velocity is normally used for this value. Each wake filament thus forms a helix, and wake points at an equivalent azimuthal distance from the rotor are also at an equivalent axial distance. A sample computer plot of a classical wake geometry is included in Figure 16.*

---

*Consistent with the forward flight wake discussed previously, a distinction in nomenclature will be made herein between undistorted wake representations with and without tip vortex roll-up. That is, the wake representation without tip vortex roll-up will be called the "classical wake representation," and the wake representation with tip vortex roll-up will be called the "undistorted wake representation."

The requirement for a method employing an accurate distorted wake model for hovering conditions is established in References 8 and 10. It was found that the rapid contraction of the slipstream under a hovering rotor places the vortex system sufficiently close to the rotor blades that it can cause significant changes in the radial distributions of induced velocities and a loss in hover performance relative to that predicted by the classical wake theories.

For hovering conditions, systematic model rotor wake geometry data have been acquired experimentally at UTRC. Sample flow visualization photographs are presented in Figure 17. The data have been generalized in Reference 8 to facilitate the rapid estimation of wake geometry for a range of rotor designs and operating conditions. The generalized wake equations for the hovering rotor are presented in Appendix C. A special computer subroutine has been prepared to model the hovering rotor wake in accordance with the generalized wake representation.

Rather than input coordinates for each vortex element in the wake, the wake equations presented in Appendix C are used to define the wake, and the individual coordinates are computed in the program. Use of the wake equations greatly simplifies the input requirements while retaining sufficient accuracy for the computation of induced velocities at the rotor blades.

Figure 16 illustrates how the computer transforms the input wake constants to coordinate form and plots the resulting wake pattern. On the left side of this figure are the top and side views of the computer representation of a typical distorted wake. For clarity, only the wake from 1 blade and 12 vortex filaments are shown. For this wake model, 5 of the 16 available vortex filaments were used over the outer 8 percent of the blade to represent the tip vortex.

The following is a description of the major features and assumptions of the generalized wake representation.

1. A smoothly contracting, stable wake is assumed. The axial velocity of a wake filament is assumed to be constant within specified azimuth regions; for example, the first being between the originating blade and the following blade.

2. The wake filaments are divided into tip vortex filaments and vortex sheet filaments for which the geometry is defined independently by separate sets of wake constants.

3. The spanwise division between the vortex sheet and tip vortex region is determined by the requirement that the tip vortex filaments have the same circulation sense, and one which is consistent with a negative spanwise derivative of the final computed bound circulation distribution over the tip region of the blade. This results in the radial location of the peak bound circulation as the dividing point at the blade between the inboard vortex sheet and the tip vortex filaments.

4. A provision is incorporated in the program for approximating the roll-up of the tip vortex filament into a single filament. This is accomplished by truncating the inner tip vortex filaments at an input azimuth and assigning the prescribed tip vortex geometry and combined circulation strength to the remaining filament (Figure 16).

5. Each cross section of the vortex sheet at a specific wake azimuth is assumed to be linear with radial position. The radial positions of the filaments representing the vortex sheet, at a given azimuth, are assumed to be linearly proportional to the radial coordinate of the vortex sheet boundary. Beyond an azimuth position corresponding to the azimuth spacing between blades, the vortex sheet is assumed to extend to the tip vortex boundary.

Circulation, Induced Velocity, and Performance Solutions

Following the transformation of the analytical wake geometry representation from input wake constants to wake coordinates, the equations for the blade circulations and induced velocities are applied in a manner similar to that described previously for the Prescribed Wake Rotor Inflow Analysis used for forward-flight conditions. The primary equations for the Prescribed Wake Hover Performance Analysis are presented in Appendix D. Comparison with the forward-flight equations of Appendix B reveals that the equations are similar but simplified due to the absence of azimuth dependency.

Following the solution for the blade-induced velocity distribution, the rotor hovering performance is determined based on conventional strip theory and two-dimensional airfoil data.

In addition to improving the hover performance predictions of a wide range of full-scale helicopter rotors (Reference 16), this analysis has been modified and successfully applied to predict propeller performance based on generalized propeller wake data (Reference 17).

UTRC Coaxial Rotor Prescribed Wake Hover Analysis

The UTRC Coaxial Rotor Prescribed Wake Hover Analysis (UTRC Deck G413) was developed to compute the blade inflow, airloading and rotor performance of a coaxial type rotor such as that of the Sikorsky/Army Advancing Blade Concept (ABC) Demonstrator Aircraft. Considering the success of the prescribed wake method for single rotors based on model rotor wake geometry, the prescribed wake approach was expanded to accommodate dual rotors. The program is a direct expansion of Deck F456, described previously, except that provisions have been made for an azimuthal variation of blade loading and prescribed wake geometry. A comparison of the blade-induced velocity and airload distributions for a model rotor at one phase angle is presented in Figure 18. Significant differences are shown between the results for upper and lower blades which were set at the same collective pitch values. A sample UTRC flow visualization photograph used to establish the prescribed wake geometry is presented in Figure 19.

UTRC Rotor/Wing Interference Analysis

The UTRC Rotor/Wing Interference Analysis (UTRC Deck F109) is a method of calculating the wing-induced flow through a rotor for use in conjunction with rotor performance and dynamic response computer programs. The analysis calculates the rotor inflow resulting from an assumed wing vortex geometry consisting of a classical lifting line and a series of semi-infinite trailing vortex filaments. With this method, it is possible to account for any desired spanwise wing circulation distribution by varying the vortex geometry and strength.

The mathematical relation used to relate the parameters indicated in Figure 20 as influencing the rotor inflow distribution induced by the wing is the classical Biot-Savart law, which was used to express the induced contribution of each vortex element in terms of the wing circulation and rotor/wing geometry. The total wing-induced velocity at each point in the rotor disk is calculated by superposition of the individual contribution of all the wing bound and trailing vortex elements.

The rotor/wing geometry is shown in Figure 21. This analysis is described in Reference 12, where results are presented for a model compound helicopter. Contours of the derivative of induced velocity at the rotor with wing lift coefficient are shown in Figure 22. A sample comparison of the predicted rate of change of rotor lift coefficient with wing lift coefficient from Reference 12 is shown in Figure 23.

CONSOLIDATION AND EXPANSION OF THE ANALYSES

An mentioned earlier, the Rotorcraft Wake Analysis was developed by consolidating and expanding the previously described computer analyses in a self-consistent single computer program. A flow chart of the resulting Rotorcraft Wake Analysis is presented in Figure 1. As shown, it is mainly comprised of a rotor analysis (the primary subprogram), a wing analysis, and a dual rotor program control. Descriptions of the components of the Rotorcraft Wake Analysis and its input-output are presented below. Descriptions of the refinements and additional capabilities provided in this combined analysis are included in the following sections.

Rotor Analysis

Basic Rotor Input

The basic rotor input to the Rotorcraft Wake Analysis, shown in Figure 1, consists of the flight condition, blade geometry, airfoil data, blade controls, and response input. The flight condition input consists of the flight velocity, rotor tip speed, and shaft angle. Since the blades and wake representations are based on a finite-element approach with numbers of elements limited only by the size of the computer, distributions of blade design properties can be adequately represented. For example, airfoil variations, twist distributions, and chord distributions can be modeled. It includes the capability to accept blade geometry inputs at arbitrary radial spacing. Airfoil data are input and an unsteady airfoil data input option is available. From one to eight blades can be accommodated with articulated, teetering, or hingeless root conditions. Blade controls and response inputs (collective and cyclic pitch, blade flapping and, if desired, bending) must be provided from a rotor performance/blade response program (e.g., the Government's Rotorcraft Flight Simulation Program, C-81) or test data.

Wake Geometry

Generality regarding the specification of the rotor wake geometry was retained in the computer program. This was accomplished by requiring that the wake coordinates for the wake segment end points be stored for computational purposes in a prescribed format; thus no requirement was made as to how these coordinates are obtained. This facilitates the adaptation of improved wake models to the program as they become available. For this program, at the present time, the following options are available for wake geometry:

1. A classical wake model option is available for hover and forward flight, in which the classical wake coordinates are computed internally.

2. An undistorted wake model option (with tip vortex roll-up) is available internally for hover and forward flight, in which the undistorted wake coordinates are computed internally.

3. A generalized wake model is available for hover conditions, which is based on the generalized experimental wake equations of Reference 8 as presented in Appendix C.

4. Distorted wake geometries (experimental or analytical) may be prescribed in coordinate form via tape. Tip vortex coordinates may be input directly.

Options for the number of wake revolutions, vortex filament spacing, wake roll-up and vortex core representation and size are included.

Rotor Wake Influence Coefficients and Circulation Solution

Following the establishment of the rotor wake geometry (see Figure 1), the Rotorcraft Wake Analysis calculates rotor wake influence coefficients at the rotor and, if applicable, the wing and other arbitrary input points based on the Biot-Savart law and a mathematical representation for a finite viscous vortex core. Circulation strengths at the blade and in the wake are then calculated based on the input flight condition, airfoil data, blade geometry, controls, and response (with or without the effects of blade flexibility) as previously described.

Induced Velocity Solution

As shown in the flow chart (Figure 1), the final output of the Rotorcraft Wake Analysis is the temporal and spatial variation of induced velocities at the rotor, wing, and other arbitrary points. These induced velocities are calculated from the blade and wake circulations and geometric influence coefficients.

One of the major refinements incorporated in the Rotorcraft Wake Analysis is the added provision for calculating velocities induced by the rotor at points removed from the blades. Three components of velocity are calculated at selected input points at or away from the rotor disk in the tip path plane and free-stream coordinate systems. Instantaneous velocities are calculated for the selected points at times corresponding to rotor azimuth intervals. For each point, an average of the instantaneous velocities over

one rotor revolution is computed to represent the time-averaged induced velocity. Since steady conditions are assumed, the instantaneous velocities at each point are periodic and the time-averaged velocity is representative of all time. The availability of the above induced velocity provisions extends the capability of the analysis to the determination of rotor flow interference effects and permits comparison with experimental velocity data measured in the rotor flow field.

Rotor Performance

Although the primary objective of the Rotorcraft Wake Analysis is to compute induced velocities for incorporation in a separate rotor performance analysis, provisions for estimating rotor performance have been included. The performance equations are based on blade-element theory for rigid blades and use of tabulated two-dimensional airfoil data. The performance calculations are based on input blade motions and controls (blade response is not calculated). Thus, for applications requiring rotor trim, iteration with a more sophisticated rotor performance/blade response program is necessary to result in consistent predictions of rotor performance, blade motions, controls, and inflow distribution.

Special Provisions for Hover Conditions

For hover conditions, it is cost effective in a computer analysis to take advantage of the symmetrical wake structure and the lack of azimuth variation of the blade controls, airloading, and response. When the UTRC Prescribed Wake Hover Performance Analysis (Deck F456) was incorporated in the Rotorcraft Wake Analysis, this feature was retained. Also, the wake generalization equations and experimental wake constants for hover presented in Reference 8 have been retained in the computer program to facilitate the input preparation for hover conditions.

DUAL ROTOR AND CONTROLLABLE-TWIST ROTOR PROVISIONS

The Rotorcraft Wake Analysis has the capability of computing induced velocities for the following dual-rotor helicopter configurations: coaxial rotor, tandem rotor, and side-by-side rotor. The dual-rotor provision resulted from an extension of the Coaxial Rotor Prescribed Wake Hover Analysis (UTRC Deck G413) and the Prescribed Wake Rotor Inflow Analysis (UTRC Deck F389) for forward flight and noncoaxial counterrotating rotors. Provisions are included for blade phasing, interrotor and wing interference, different wake geometries for each rotor, and two sets of input and induced velocity output. No restrictions are placed on the relative positioning or inclination of the two rotors. An option is provided for calculating

induced velocities at the blades of each rotor and/or at arbitrarily selected points in a selected reference axis system. As indicated in Figure 1, a dual-rotor program control is incorporated to control the flow of the program for each rotor.

The Rotorcraft Wake Analysis is also capable of calculating induced velocities of controllable-twist type rotors (CTR). The time-varying flap control is provided for through proper input of chord and the unsteady airfoil lift coefficient characteristics for the control flap blade section. The controlled torsional deflections due to the prescribed flap controls are accounted for in Figure 1 in the blade controls and response input.

Wing Analysis

A modified version of the UTRC Rotor Wing Interference Analysis (UTRC Deck F109) was incorporated in the Rotorcraft Wake Analysis. As described previously, this computer program calculates the inflow distribution at the rotor due to a wing as represented by a series of semi-infinite horseshoe vortices. Following the wing circulation solution, the Biot-Savart law is used to determine the influence of the horseshoe vortices on the rotor inflow at each blade station and azimuth angle.

As shown in the Rotorcraft Wake Analysis flow chart in Figure 1, the components of the wing analysis subprogram are essentially those of the Deck F109 flow chart previously presented in Figure 20. The analysis has been modified and expanded to include the following features:

1. The capability to iterate between the rotor inflow distribution and wing inflow distribution to account for the mutual rotor/wing wake interference.

2. The capability to calculate the wing circulation and induced velocity distribution and associated wing lift coefficient in a self-consistent iterative manner. This provides an alternate to the use of Shrenk's rule (as used in Reference 12) and also a means for including the induced velocity due to the rotor in a more accurate wing inflow iteration.

3. The capability for arbitrary relative positioning between the rotor and wing.

4. The capability to include inclination of the wing wake to provide a first approximation for wing wake deflection as influenced by the rotor wake.

The provision to iterate between the rotor and wing inflow distributions was incorporated by making use of the expanded rotor analysis capability of computing off-rotor induced velocities. Time-averaged velocities induced by the rotor at the wing stations are added to the wing's self-induced velocity distribution to determine the wing circulation distribution. Iteration between the rotor characteristics, including wing interference effects, and wing characteristics, including rotor interference effects, results in a self-consistent solution for rotor and wing.

Options for prescribing or calculating the wing circulation distributions have been provided. If calculated, one approach is to use the experimental wing downwash factor (Reference 12) to obtain the wing lift/rotor lift derivative and then to appropriately scale Shrenk's wing circulation distribution. This does not account for the spanwise and timewise variation of rotor interference at the wing. The second approach is the lifting line solution in which spanwise variations are accounted for.

Computer Program Cost Efficiency, Operational Simplicity, and Growth Potential

In addition to accuracy, a primary concern in the development of the several UTRC wake analyses has been cost efficiency. Avoidance of redundant and insignificant calculations and inclusion of a fast iterative technique for solving large matrices have resulted in significant reductions in computer time requirements. Although the Rotorcraft Wake Analysis is a large computer program, careful control of program call sequences and overlay techniques has resulted in the maintenance of program storage and computer time efficiency and the allowance for the advantages of a single, composite, self-consistent program.

Attention has been given to operational simplicity for the computer analysis. Commonality between the input-output of the various subprograms has been provided. Provisions for self-consistent iterations within the program have been included along with a multiple case option.

Through the division of the Rotorcraft Wake Analysis into component subprograms, growth potential has been provided, in that any subprogram can be updated or replaced as the state of the art advances or the need arises. Also, the use of a prescribed wake in the analysis retains flexibility on the type and source of the wake geometry. As additional accurate and generalized wake geometry data becomes available, it may be readily incorporated in the analysis.

INDUCED VELOCITY CORRELATION STUDY

In order to demonstrate the accuracy of the Rotorcraft Wake Analysis, a correlation study was conducted in which the analysis was applied to compare with induced velocity test data from many sources. The selection of the test data, the limitations of the test data, the procedures used to apply the analysis to the test conditions, and the results of the correlation study for both hover and forward-flight conditions are presented below.

SELECTION OF INDUCED VELOCITY TEST DATA

In the selection of the induced velocity test data, it was recognized that, in addition to being accurate, the data selected should cover a wide range of rotorcraft configurations, sizes, flight conditions and test point locations relative to the rotor(s). That is, it was desired to compare predicted velocities with measured values for points near the rotor disk, and points within and outside of the rotor wake for various combinations of flight speed and thrust level. Test data that include hover and low- and high-speed flight conditions for the various types of configurations that the analysis is applicable to, i.e. single, tandem, coaxial, side-by-side, compound (winged), and CTR type rotorcraft, were desired.

To establish what induced velocity data existed for selection in this correlation study, a search of the available literature on this subject was conducted. Ten sources of data were selected (References 18 to 27). Pertinent information on each are listed in Table 1. The sources include data accumulated over a time span of two decades (1954 to 1974) by Army, NASA, and industry organizations.

The Rotorcraft Wake Analysis was applied to 25 rotor conditions (combinations of rotor configuration and test condition) selected from the available test data. Although the data do have significant limitations (to be described), the overall range of the data selected from the references is quite comprehensive in that the following are included:

1. Hover and forward-flight conditions (μ = 0 to 0.23)
2. Single and tandem-rotor configurations
3. Model and full-scale rotors (R = 1 to 17.6 ft)

TABLE 1. SELECTED SOURCES OF INDUCED VELOCITY TEST DATA FOR CORRELATION STUDY

Ref. No.	Author(s) & Reference	Rotor Configuration	No. of Blades	Flight Condition	Type of Test	Scale	Radius (ft)	Type of Velocity Data	Location of Velocity Data	Velocity Instrumentation
18	Boatwright (USAAMRDL TR 72-33)	Single	2	Hover	Whirl Stand	Full	17.6	Time Avg and Instantaneous	Under Rotor	Hot-Film
19	Heyson (NACA TN D-393)	Single	2	Hover	Whirl Stand	Model	5	Time Avg & Instantaneous	Under Rotor	Pitot Tubes & Hot-Wire
20	McKee & Naeseth (NACA TN 4239)	Single	2	Hover	Hover Stand	Model	3	Time Avg	Under Rotor	Pitot Tubes & Dynamic Pressure Disks
21	Fradenburgh (AHS, 1958)	Single	2	Hover	Hover Stand	Model	1	Time Avg	Under Rotor	Pitot Tubes
22	Flemming (SA, Unpub.)	Single	7	Hover	Hover Stand	Model	2	Time Avg	Under Rotor	Hot-Film
23	Miller, Tang, & Permutter (USAAVLABS TR 67-68)	Single	3	Hover & Forward Flight	Flight Test	Full	12.7	Time Avg & Instantaneous	Under Rotor	Pitot Tubes & Hot-Film
24	Heyson & Katzoff (NACA TR 1319)	Single	2	Forward Flight	Wind Tunnel	Model	7.5	Time Avg	Above, Under & Downstream of Rotor	Pitot Tubes
25	Landgrebe & Johnson (AHS J1 July 1974)	Single	2	Forward Flight	Wind Tunnel	Model	2.2	Instantaneous	Near Rotor @ $\psi = 180^{\circ}$	Laser Velocimeter
26	Biggers & Orloff (AHS J1, Jan. 1975)	Single	2	Forward Flight	Wind Tunnel	Model	3.5	Time Avg & Instantaneous	Near Rotor @ $\psi = 90, 270^{\circ}$	Laser Velocimeter
27	Heyson (NACA TN 3242)	Single & Tandem	2	Forward Flight	Wind Tunnel	Model	7.5	Time Avg	Under Rotors	Pitot Tubes

4. Model hover test stand, outdoor whirl tower, wind tunnel (4 x 6 ft to 40 x 80 ft) and flight test data

5. Rotors with 2, 3, and 7 blades

6. Thrust coefficients (C_T) from 0.002 to 0.010

7. Tip speeds (ΩR) from 110 fps to 700 fps

8. Varying blade designs (twist, taper, airfoil section, and root constraint)

9. Local time-averaged (mean) and local time-dependent (instantaneous) velocities

10. Three velocity components (some sources)

11. Velocities measured by pressure (Pitot-static tubes and dynamic pressure disks), anemometers (hot-wire and hot-film), and laser velocimeter techniques

12. Velocities at points near and far from the rotor, and inside and outside of the rotor wake

LIMITATIONS OF THE INDUCED VELOCITY TEST DATA

The general limitations of the available induced velocity test data are:

1. No one test contained data which were sufficiently extensive to provide a single set of accurate, self-consistent data for absolute correlation of time-averaged and instantaneous velocities for all desired locations over a wide range of conditions.

2. Most of the data sources did not measure or properly document all of the associated information required for the Rotorcraft Wake Analysis. That is, in most cases, the complete combination of rotor design parameters, pitch control angles, blade response (coning and flapping), and rotor performance (forces and moments) was not known or noted in the reference. Although sufficient information was generally provided to estimate the missing information or to determine it from a rotor performance analysis, this detracted from the absolute correlation of the Rotorcraft Wake Analysis.

3. In most cases, wake geometry was not measured along with the induced velocities. In no case were blade airloads measured. If measured, these items and more complete rotor performance data would have been of significant value for checking the analytical wake representations and circulation solutions used to compute induced velocities.

4. Only one of the sources of hover data included quantitative instantaneous induced velocities. The others were limited to time-averaged (mean) velocities. The sources of forward-flight data with meaningful instantaneous velocities reported on initial demonstration tests using recently developed laser velocimeter techniques, and they were limited to selected points at one or two blade azimuth positions.

5. Except for the laser velocimeter data, all available velocity data were measured away from the rotor blades. The measurement of the instantaneous induced velocities at the blades over a complete revolution, which is of extreme interest to the rotor designer, has yet to be attempted.

6. Flow velocity data remain to be acquired for many types of rotor configurations and test conditions. In particular, information is almost completely lacking for dual rotors (tandem, coaxial, and side-by-side rotors), compound (winged), and controllable twist (CTR) configurations. Also, available velocity data for forward-flight conditions and varying combinations of blade designs are very limited.

7. The accuracy of the available velocity data is limited to the recognized degree of accuracy obtainable with the respective type of equipment used, and by the size of the rotor and the procedures and facilities used by the test conductor. For example, Pitot-static tubes, dynamic pressure disks, and hot-wire equipment have known limitations regarding flow angularity and magnitude. In most sources of data, the accuracy of the measured velocities was not noted. This makes questionable the extent to which the velocities predicted with the Rotorcraft Wake Analysis can be confidently compared with the test data on an absolute basis.

8. The test data were not always acquired under the ideal environmental conditions and rotor response behavior assumed by the analysis. The analysis is based on the assumption of steady-state conditions in forward flight and the absence of wind in hover. In

practice, particularly under realistic outdoor conditions, ideal conditions are seldom present, as was attested to in several data sources. Also, the blades were assumed to be manufactured identically and to respond accordingly. The sensitivity of local induced velocities to wind and blade-to-blade imperfections is recognized, especially at hover and low-speed conditions, and for some cases influence the degree of velocity correlation on a local point basis.

Although the above list of test data limitations appears formidable, it is not intended to imply that the forthcoming correlation results are not useful for determining the accuracy of the Rotorcraft Wake Analysis. The intent will be to show that, although in single cases questions may arise regarding the absolute comparison of the predicted and test results, in total the accuracy of the analysis in its current form can be reasonably assessed on an initial basis. With the recent advances in velocity measurement techniques, it is expected that an extensive amount of accurate induced velocity data will become available to further evaluate the analysis and to provide direction for its refinement. Continued application of the Rotorcraft Wake Analysis in conjunction with rotor performance and blade response analyses to correlate airloads, blade motions, and bending moments will also demonstrate the accuracy of the analysis.

CORRELATION STUDY FOR HOVERING CONDITIONS

Six of the selected sources of data (References 18 to 23) contain information pertaining to hovering test conditions. Comparisons of results of the Rotorcraft Wake Analysis with test data from each are presented below.

Comparison With Test Data of Boatwright, USAAMRDL TR 72-33

Induced velocity data for a full-scale, two-bladed, OH-13E helicopter rotor tested outdoors on a 60-ft rotor test tower are presented in the following reference (Reference 18);

> Boatwright, D.W., Measurements of Velocity Components in the Wake of a Full-Scale Helicopter Rotor in Hover, Mississippi State University, USAAMRDL Technical Report 72-33, Eustis Directorate, U.S. Army Air Mobility Research and Development Laboratory, Fort Eustis, Va., August 1972, AD 754644.

This report presents three-component velocity measurements made below the rotor with a split-film total vector anemometer. Test data were acquired by traversing the total vector probe along an instrumentation boom which extended radially into the rotor wake.

The boom was positioned at preselected distances below the rotor, and instantaneous velocities were measured. The term instantaneous will be used herein in the broad but conventionally used sense (assuming periodicity) to indicate that the velocity is for a fixed blade azimuth position relative to a measurement point. This distinguishes it from the mean or time-averaged value obtained by time averaging the velocity at a point over a continuous time period.*

Information on the rotor design and test conditions are presented in Table 2. As noted in the table, data for three test conditions were presented which include independent variations of thrust coefficient (by varying collective pitch) and tip speed. The measured thrust coefficient values were accurately predicted by using the test collective pitch values in the Rotorcraft Wake Analysis. Predicted rotor torque levels for the generalized wake representation were in the vicinity of the high limit of the range of measured torque data presented in the reference. Predicted torque levels for the undistorted wake representation were generally higher than the measured values.

Predicted induced velocities were obtained from six computer cases of the Rotorcraft Wake Analysis comprising the combinations of the three test conditions with two types of prescribed wake representations. The two wake representations used were the undistorted wake and the generalized wake based on the model rotor wake data of Reference 8 (see Figure 17). The undistorted wake model, as defined earlier, is the same as the classical wake model except that it combines the tip filaments of the classical wake into a single undistorted tip filament. This wake model was used initially for this source of data instead of the classical wake because it was potentially a better representation for correlating with instantaneous velocities.

---

* In USAAMRDL Report 72-33, the term instantaneous is used in the exact sense to indicate a velocity measurement taken at a point at one instant of time. The "mean" values in that report are not the continuous time-averaged values at a point, but rather the instantaneous velocities for one rotor azimuth position averaged for 25 rotor revolutions, each of which would be equivalent if there were no unsteadiness of the hovering rotor and wake. Thus, they are actually a time-dependent mean of the local instantaneous velocities corresponding to one rotor position. Since wake unsteadiness is not incorporated in the Rotorcraft Wake Analysis, instantaneous velocities are calculated assuming periodicity, which, although labeled instantaneous herein, correspond to the "mean" values of the reference.

TABLE 2. ROTOR AND TEST INFORMATION -- BOATWRIGHT, USAAMRDL 72-33

Rotor Type

OH-13E, single, full-scale, teetering rotor

Rotor Design

Number of blades	2	Rotor solidity	0.03625
Rotor radius, ft	17.56	Blade taper ratio	1.38
Root chord, ft	1.167	Blade twist, deg	-4.25 (avg.)
Tip chord, ft	0.845	Airfoil section	NACA 0015

Test Conditions

Condition 1: $\mu = 0$, $\Omega R = 625$ fps, $\theta_{75} = 6.25$ deg, $C_T = 0.0020$, $v_o = 19.8$ fps

Condition 2: $\mu = 0$, $\Omega R = 450$ fps, $\theta_{75} = 10.75$ deg, $C_T = 0.0040$, $v_o = 20.1$ fps

Condition 3: $\mu = 0$, $\Omega R = 450$ fps, $\theta_{75} = 6.25$ deg, $C_T = 0.0020$, $v_o = 14.2$ fps

Two uncertainties were present when the wake representations were established. First, blade tip position due to coning and blade bending were not indicated in Reference 18 and thus had to be estimated. Second, the wake generalization of Reference 8 does not include provision for tapered blades, and thus the influence of taper on the generalized wake geometry was not included.

The positions of the tip vortices of the generalized wake model, as indicated by the cross-section locations of the tip filaments, are shown in Figure 24. The tip vortex positions are shown for the three test conditions and the following two instants of time: (1) when the reference blade is at ψ = 0 deg, which indicates that the blade is directly above the measurement point; and (2) when the reference blade is at ψ = 90 deg. As shown, the generalized wake positions are identical for test conditions 1 and 3 due to the independence of hovering rotor wake geometry to tip speed variations at constant thrust coefficient, as described in Reference 8. Also indicated in Figure 24 are the z/R elevations of the probe locations and the approximate mean of the measured radial excursions of the tip vortices at these elevations. Measured vertical and radial excursions of tip vortex points as large as 5 to 10 percent of the rotor radius are indicated in the reference, even for near-wake points. These excursions, due mainly to ambient wind effects, include the generalized wake positions in the near wake (at z/R = -0.1 and -0.3 in Figure 24). Figure 24 will be useful in describing the induced velocity results.

Comparisons of the measured and theoretical instantaneous induced velocities are presented in Figures 25 through 29. The induced velocities have been nondimensionalized by the momentum theory values of induced velocity at the rotor, which are 19.8, 20.1, and 14.2 fps for test conditions 1, 2, and 3, respectively. In Figure 25, a comparison of the radial distribution of the three velocity components is presented for test condition 1 at the vertical location nearest to the rotor: z/R = -0.1. The components are based on a right-handed coordinate system. Considering the plane of measurement points to be at ψ = 0 results in the normal component, v_z, positive up; the radial component, v_x, positive outward; and the tangential component, v_y, positive in the direction of rotation. The generalized wake results exhibit good correlation with the test data and a significant improvement over the undistorted wake results. The latter is most evident near the wake boundary, where the results are very sensitive to the accurate positioning of the tip vortices, both radially (wake contraction) and vertically. In Figure 26, the normal velocity component is compared at three elevations below the rotor for test condition 1. Good agreement is indicated

between the generalized wake results and the test data at z/R = -0.1 and -0.3. At z/R = -0.7, the correlation is poor near the wake boundary. This is due to the known shortcoming of the generalized wake of Reference 8, which was modeled therein, concentrating on near-wake accuracy for predicting induced velocities at the rotor. As demonstrated in both the model rotor flow visualization results and the results of the Wake Geometry Analysis in Reference 8, the far wake of a hovering rotor does not continue to contract smoothly as assumed in the generalized wake representation, but rather expands in an unsteady and unstable manner. This wake expansion was evident in Boatwright's full-scale rotor test data, as shown in Figure 24; its effect is shown in Figure 26 at z/R = -0.7 by the outward shift of the measured velocity distribution. An indication of the capability of the Rotorcraft Wake Analysis to more accurately account for this if the generalized wake were refined to include the wake expansion is shown by the outward shift of the undistorted wake velocities relative to the generalized wake velocities due to the complete lack of contraction.

In Figure 27, the results for test conditions 2 and 3 are added to the results for test condition 1 presented in Figure 26. As stated in Reference 18, when the measured velocity components are nondimensionalized by the momentum values of induced velocity, no large differences between the radial distribution of the velocity components are generally detected. The differences that do occur could not be directly attributed to variations of the test parameters, because variations due to ambient wind effects produced wake geometry deviations between test periods which masked any possible deviations due to test parameters. This was particularly true at the wake boundary, where unsteady variations of the paths and transport velocities of the tip vortices between repeat test conditions were found to be large even near the rotor. Also, a mismatch of blade twist rate between the two blades (-4.0 and -4.5 deg) resulted in wake geometry variations between the two blades.

The generally small variations with test conditions of the predicted velocity results from the Rotorcraft Wake Analysis, also shown in Figures 27 and 28, are in agreement with the test findings. The predicted results for test conditions 1 and 3 are identical (same generalized wake was used), indicating that nondimensionalized induced velocity is independent of tip speed. The predicted velocity variations due to thrust coefficient are generally small. However, the existence of exceptions is indicated in Figure 28 for the radial component at z/R = -0.1, where the theory predicts a large local radial inflow at the wake boundary for conditions 1 and 3 which is not predicted for test condition 2. The presence of large local velocity gradients such as this is

explained by the close proximity of a point to a tip vortex. In Figure 24, it is shown that when the reference blade is at ψ = 0 deg, a tip vortex is located just below the z/R = -0.1 elevation, which, considering the counterclockwise circulation sense of the tip vortex, produces the large radial inflow near the 0.85 radial station. For test condition 2, the tip vortex positions corresponding to ψ = 0 deg are not near the z/R = -0.1 elevation, and thus a large velocity gradient is not produced. The test data in Figure 28 indicate a large radial velocity near the wake boundary for test condition 1, which is consistent with the predicted results. However, unlike the predicted results, the magnitude is decreased for test condition 3. This is probably attributable to the movement of the tip vortex caused by ambient wind effects, and illustrates the sensitivity of local velocity magnitudes to tip vortex relocations due to environmental factors.

The sensitivity of the local instantaneous induced velocities to tip vortex position is further illustrated in Figure 29, in which the theoretical velocities are compared with the test data at z/R = -0.1 for test conditions 1 and 2 when the reference blade is 90 deg ahead of the measurement azimuth (ψ = 90 deg). In Figure 29, the measured normal velocities indicate the close proximity of a tip vortex near x/R = 0.83 for both test conditions. The theoretical results are consistent with those of the test for test condition 2, but not for test condition 1. This is explained by referring again to Figure 24 and noting that a tip vortex in the generalized wake representation is located just above the z/R = -0.1 elevation for test condition 2 when ψ = 90 deg, but not for test condition 1. The requirement for accurate tip vortex positioning is emphasized further in Figure 29, where the predicted radial velocity component for test condition 2 is similar to the test results in exhibiting a large peak magnitude at the wake boundary, but is opposite in direction radially (outward rather than inward). This is easily explained by the generalized wake position of the tip vortex for this test condition and azimuth as shown in Figure 24 to be 0.015R above the z/R = -0.1 elevation. If it were shifted by just 2.5 percent of the radius to 0.01R below the measurement line, good correlation with the radially inward velocity would result. It is thus concluded that the capability of the Rotorcraft Wake Analysis to predict local instantaneous velocity peaks at the wake boundary depends upon a very accurate positioning of the tip vortices in the wake representation.

Regarding the lack of correlation in Figure 29 for test condition 1, the test data indicating a strong peak downwash at the wake boundary may be questioned due to the lack of a similar peak for the radial component

for this condition, and thereby questioning the presence of a close tip vortex.

In summary, analysis of the comparisons of the predicted instantaneous induced velocities with the Boatwright test data revealed the following:

1. The correlation of the generalized wake results was generally good.

2. Where correlation was lacking, it could generally be attributed to known shortcomings of the generalized wake representation (e.g., the far wake) or to the sensitivity to wake excursions during testing due to ambient wind effects and the 0.5 deg difference in twist between the two blades. However, due to the large measured wake excursions and the uncertain test coning angle, the direct correlation between the wake representation generalized from model tests and the wake geometry of the full-scale OH-13E rotor could not be concluded.

3. The use of the generalized wake resulted in a considerable improvement in the correlation over that of the undistorted wake.

Comparison With Test Data of Heyson, NACA TN D-393

Induced velocity data for a two-bladed, 10-ft-diameter rotor model tested on a whirl stand mounted in the full-scale tunnel at the NASA-Langley Research Center are presented in the following reference (Reference 19);

> Heyson, H.H., Measurements of the Time-Averaged and Instantaneous Induced Velocities in the Wake of a Helicopter Rotor Hovering at High Tip Speeds, NACA Technical Note D-393, July 1960.

This report presents radial distributions of the time-averaged component of induced velocity normal to the rotor disk at two elevations below the rotor ($z/R = -0.145$ and -0.45). Measurements were taken in and out of the wake of the hovering rotor using rakes of total-head and static pressure tubes. In addition, a constant-temperature hot-wire anemometer was installed at one position ($z/R = -0.145$, $r/R = 0.67$) to record the time history of the instantaneous velocities essentially normal to the rotor disk.

Information on the rotor design and test conditions are presented in Table 3.

TABLE 3. ROTOR AND TEST INFORMATION -- HEYSON, NACA TN D-393

Rotor Type

Single, model, teetering rotor

Rotor Design

Number of blades	2	Rotor solidity	0.10
Rotor radius, ft	5.0	Blade twist, deg	-12.0
Tip chord, ft	0.63	Airfoil section	NACA 0012
Blade taper ratio	2.0		

Selected Test Conditions

Condition 1: $\mu = 0$, $\Omega R = 700$ fps, $\theta_{75} = 4$ deg, $C_T \cong 0.00225$*, $v_o = 23.5$ fps

Condition 2: $\mu = 0$, $\Omega R = 700$ fps, $\theta_{75} = 8$ deg, $C_T \cong 0.0064$*, $v_o = 39.5$ fps

Condition 3: $\mu = 0$, $\Omega R = 700$ fps, $\theta_{75} = 12$ deg, $C_T \cong 0.0106$*, $v_o = 51.0$ fps

Condition 4: $\mu = 0$, $\Omega R = 500$ fps, $\theta_{75} = 8$ deg, $C_T \cong 0.0058$*, $v_o = 27.0$ fps

* C_T not indicated in reference; calculated values listed.

Data for four test conditions were selected which include variations of collective pitch and tip speed. Measured values of thrust coefficient were not included in the reference. The calculated values using the test collective pitch with both the generalized and classical wake representations were similar (within approximately 3 percent), and are listed in Table 3 along with the corresponding momentum-induced velocity values.

Comparisons of the measured and theoretical time-averaged normal velocities at the two vertical distances ($z/R = -0.145$ and -0.45) are presented in nondimensional form in Figures 30 through 33. In Figures 30 and 31, comparisons of the classical and generalized wake results with the test data are presented for three values of collective pitch and a constant tip speed of 700 fps. Although the magnitude of the theoretical downwash distribution within the wake is generally less than measured, the general characteristics of the velocity distributions and the influence of collective pitch (thrust level) are predicted accurately. As expected, relative to the classical wake results in Figure 30, the results in Figure 31 based on the generalized wake are in much better agreement with the test data near the wake boundary.

The disagreement in magnitude of the downwash based on the generalized wake is at least partially attributable to the lack of experimental wake geometry data for tapered blades. Limited wake geometry data acquired in the test reported in Reference 11 for a model rotor with six tapered blades (2:1 taper ratio) indicate an effect of taper on wake geometry, but the data were not of sufficient extent to be generalized.

The capability of the Rotorcraft Wake Analysis to predict the insensitivity of nondimensionalized induced velocity to tip speed variations, evident in the test results, is shown in Figures 32 and 33. In these figures, results for test conditions 2 and 4 are compared, which correspond to tip speed variations between 700 and 500 fps, respectively, a collective pitch value of 8 deg, and similar thrust coefficients. Independence of tip speed at similar thrust coefficient levels is predicted by both the classical and generalized wake results. These results are consistent with the statement of Reference 19 and the experimental wake generalization of Reference 8 that tip speed (at least up to 700 fps) has essentially no independent effect on the wake of the hovering rotor.

In Figure 34, the time history of the instantaneous induced velocity component normal to the rotor disk measured at one point in the rotor wake with a hot wire is reproduced directly from the reference. Although

no scale is included, the shape of the 2/rev velocity pulses associated with the two-bladed rotor is clearly defined. For comparison of the shape of the velocity pulses, the velocity time history predicted using the generalized wake was normalized and phased to the test data. As shown in Figure 34, the shapes of the theoretical and experimental time histories are similar. Also presented in Reference 19 are the recorded root-mean-square values of the velocity pulses. For the test condition shown (Condition 3), the velocity fluctuations are recorded as 13 percent of the local mean induced velocity and 25 percent of the momentum induced velocity. The predicted fluctuations were found to be in favorable agreement with these measured values, in that the respective predicted fluctuations

$$\frac{1/2\ v_{z_{PTP}} - \bar{v}_z}{\bar{v}_z} \quad \text{and} \quad \frac{1/2\ v_{z_{PTP}} - \bar{v}_z}{v_o}$$

were calculated to be 15 percent and 26 percent.

Comparison With Test Data of McKee and Naeseth, NACA TN 4239

Induced velocity data in the form of local dynamic pressure measurements for a two-bladed, 6-foot-diameter rotor model with constant chord, untwisted blades are presented in the following reference (Reference 20);

> McKee, J.W. and R.L. Naeseth; Experimental Investigation of the Drag of Flat Plates and Cylinders in the Slipstream of a Hovering Rotor, NACA TN 4239, April 1958.

The model rotor was tested in a partially enclosed outdoor area. Dynamic pressure data were taken using both Pitot tubes and small disks at various radial and vertical locations on the slipstream side of the hovering rotor. Local dynamic pressures normal to the rotor disk were measured which are proportional to the time-averaged normal component of induced velocity squared.

Information on the rotor design and single test condition is presented in Table 4. The test was run at a tip speed of 367 fps and a collective pitch of 11 deg, and rotor performance was measured.

Sample dynamic pressure test data, reproduced directly from the reference, are presented in Figure 35. Differences in the data between the two measurement devices and data fluctuations excited by

recirculation from the surrounding walls and ambient wind are cited in the reference. Random variations of the time histories were especially large near the wake boundary, and it was consistently noted that the slipstream was not centered with respect to the rotor.

TABLE 4. ROTOR AND TEST INFORMATION -- McKEE & NAESETH, NACA TN 4239

Rotor Type

Single, model, teetering rotor

Rotor Design

Number of blades	2	Blade taper ratio	1.0
Rotor radius, ft	3.0	Blade aspect ratio	9.1
Blade chord, ft	0.33	Blade twist, deg	0.0
Rotor solidity	0.071	Airfoil section	NACA 0012

Test Condition

$\mu = 0$, $\Omega R = 367$ fps, $\theta_{75} = 11.0$ deg, $C_T = 0.00602$, $v_o = 20.13$ fps

Comparisons of the predicted and measured dynamic pressures are presented in Figures 35 and 36 for five elevations ranging from $z/R = -0.104$ to -0.993. Figure 36 includes the data variations from the two measurement devices and the unsymmetrical side-to-side variations due to wake unsteadiness. The predicted and test results are generally in good agreement near the rotor. The magnitudes of the predicted results are generally somewhat lower than the test results, although the dynamic pressure differences relative to differences in induced velocities are accentuated. For example, a 20 percent difference in dynamic pressure is representative of a 10 percent difference in induced velocity due to the square relation. Also, to achieve the measured thrust

coefficient in the Rotorcraft Wake Analysis, the collective pitch was lowered from the 11 deg stated in the reference to 10.4 deg. If the 11 deg had been used in the analysis, the predicted dynamic pressure level would have been increased and would have agreed more closely with the test data. However, assuming the test information to be accurate, the analytical inconsistency is recognized, and a preferred choice between the two approaches is not apparent. The generalized wake results, which properly account for near-wake contraction, are in better agreement with the classical wake results near the rotor. The unsteady behavior and vortex core dissipation in the real hovering far wake, not represented in the analytical wake models, are evident in the test data by the increased region of test data and lower and broadened pressure peaks at $z/R = -0.660$ and -0.993.

Comparison With Test Data of Fradenburgh

Experimental induced velocity contours for a two-bladed, 2-foot diameter rotor model tested on an indoor hover test stand are presented in the following reference (Reference 21);

> Fradenburgh, E. A., Flow Field Measurements for a Hovering Rotor Near the Ground. Proceedings of the 5th Annual Western Forum of the American Helicopter Society, Los Angeles, California, September 1958.

Although the data from this reference have some limitations for correlation purposes, they were selected recognizing that the model test was one of the first to provide a comprehensive set of downwash data beneath a hovering rotor and has remained over the years as one of the few published sources of such data. The limitations are associated with the small rotor size, low aspect ratio, and the use of Pitot tubes to measure the time-averaged velocity component normal to the rotor disk in a fluctuating flow field.

Rotor and test information are presented in Table 5. The rotor was tested out-of-ground-effect at one test condition for which the thrust coefficient was approximately 0.007. Collective pitch (θ_{75}) was not indicated in the reference. The θ_{75} values used in the analysis were the values required to produce the test thrust coefficients ($\theta_{75} = 9.2$ deg for classical wake; $\theta_{75} = 10.0$ deg for generalized wake).

The experimental downwash velocity contours measured at four locations below the rotor (indicated by the dotted lines), and nondimensionalized by the momentum induced velocity ($v_o = 35.5$ fps), are presented in Figure 37.

TABLE 5. ROTOR AND TEST INFORMATION -- FRADENBURGH

Rotor Type

Small, single, model, hingeless rotor

Rotor Design

Number of blades	2	Blade taper ratio	1.0
Rotor radius, ft	1.0	Blade aspect ratio	6.0
Blade chord, ft	0.167	Blade twist, deg	0.0
Rotor solidity	0.106	Airfoil section	NACA 0012

Test Condition

$\mu = 0$, $\Omega R = 600$ fps, θ_{75} not indicated, $C_T \cong 0.007$, $v_o = 35.5$ fps

Velocity contours calculated using the classical and generalized wake representations in the Rotorcraft Wake Analysis are presented in Figures 38 and 39. Direct comparisons of the analytical time-averaged velocities with the test velocities can be made by comparing the contours shown in Figures 38 and 39 with those of Figure 37.

Comparisons of the predicted velocities with the test data reveal the following:

1. The general character of the analytical and experimental velocity contour lines are similar.

2. As anticipated, the velocity contours based on the classical wake geometry are shifted outward from the experimental contours below the blade tip region due to the absence of wake contraction. It is noted that the experimental velocities do not show evidence of the expansion of the boundaries of the far-wake region evident in other sources of data. (A wake photograph in Reference 21 indicates expansion at $z/R = -1.2$.)

3. On a point-to-point basis, the analytical velocity contours based on the generalized wake geometry are consistently lower than the experimental values by an increment of approximately 0.5 v_o.

4. A larger region of upflow beneath the rotor hub is noted for the analytical results which is attributable to the establishment of the inboard wake boundary in the analysis below the root cutout location, and to the lack of a provision for mixing of the flow in this low-pressure region.

There are several reasons for the third observation, and they are primarily related to the accuracy of the analytical wake representation. A comparison of the generalized wake representation used for this rotor in the analysis with the wake geometry indicated in a photograph in the Fradenburgh reference revealed significant differences. This is believed to be attributable to the extrapolation of the generalized wake results of Reference 8 acquired for two-bladed rotors with relatively low solidities (0.035 and 0.047), resulting from high aspect ratios (18.2 and 13.6), to a rotor with a solidity of 0.1 and an aspect ratio of 6. Recent indications are that the generalized wake equations (Appendix C) do not apply to rotors with low-aspect-ratio, high-solidity blades. For example, indications are that the tip vortex axial coordinates (k_1 in Appendix C) should be generalized on a parameter such as C_T/b rather than C_T/σ, to apply to such rotors.

Comparison With Test Data of Flemming

The previously presented sources of hovering rotor data have all been for rotors with two blades. In order to compare the induced velocities from the Rotorcraft Wake Analysis with test data for a large number of blades, hot-film anemometer data for a seven-bladed rotor were selected from Reference 22.

Flemming, R. J., 1/20 Scale Model Rotor Wake Survey, Internal Sikorsky Documents, May 1969 and March 1972.

The Sikorsky-sponsored test program was conducted at the UTRC model rotor hover test facility. Hot film anemometer equipment was employed to measure the time-averaged downwash velocity at several collective pitch angles (thrust levels) and two tip speeds. Traverses of a hot-film probe were made at several elevations below the rotor to result in radial distributions of the induced velocity component normal to the rotor disk. Information on the rotor design and four selected test conditions is presented in Table 6.

TABLE 6. - ROTOR AND TEST INFORMATION -- FLEMMING

Rotor Type

Single, model, semiarticulated (flapping) rotor

Rotor Design

Number of blades	7	Blade taper ratio	1.0
Rotor radius, ft	1.975	Blade aspect ratio	18.2
Blade chord, ft	0.108	Blade twist, deg	-4.0
Rotor Solidity	0.122	Airfoil section	NACA 0012

Test Conditions

Condition 1: $\mu = 0$, $\Omega R = 620$ fps, $\theta_{75} = 9$ deg, $C_T = 0.0069$, $v_o = 36.3$ fps

Condition 2: $\mu = 0$, $\Omega R = 620$ fps, $\theta_{75} = 10$ deg, $C_T = 0.0079$, $v_o = 39.0$ fps

Condition 3: $\mu = 0$, $\Omega R = 620$ fps, $\theta_{75} = 12$ deg, $C_T = 0.0103$, $v_o = 44.5$ fps

Condition 4: $\mu = 0$, $\Omega R = 465$ fps, $\theta_{75} = 9$ deg, $C_T = 0.0067$, $v_o = 27.0$ fps

The Rotorcraft Wake Analysis was run with classical and generalized wake models for the four test conditions. When necessary, collective pitch was adjusted in the analysis from the test values to produce the measured thrust coefficients. Comparisons of the theoretical and measured time-averaged induced velocities for each test condition at two distances below the rotor hub center ($z/R = -0.158$ and -0.316) are presented in Figures 40 to 43. Similar to previous comparisons with other data sources, both wake models in the analysis correctly predict the character of the radial distributions of velocity. The analytical results in the outboard region reflect the lack of contraction of the classical wake and the smooth contraction to 0.78R of the generalized wake. The general increase in inboard flow velocity, at fixed radial coordinates, with increased distance from the rotor is consistently predicted for this rotor. Figure 44 is included to show that this applies over the full range of z/R elevations ($z/R = -0.085$ to -0.99) for which measurements were made. For clarity, results for three intermediate positions ($z/R = -0.158$ and -0.316 presented in Figure 41 and -0.478) have

been omitted, but the analytical velocities in the slipstream progressively increased in magnitude with increasing distance from the rotor consistent with the test results.

Use of the generalized wake representation overpredicts the absolute magnitude of the induced velocity, and the classical wake results generally indicate better correlation inboard than the generalized wake results for this rotor. However, due to the large number of wakes for seven blades, and the close passage of the tip vortices to the blades, the results were found to be very sensitive to wake representation (tip vortex geometry, analytical modeling of tip vortex roll-up, and selection of radial points of origination of tip vortex filaments from the blades). Also, the time-averaging of induced velocities calculated at discrete time increments is sensitive to the selection of blade azimuth increment for the closely spaced seven blades. In addition, the close proximity of successive tip vortices for a seven-bladed rotor results in tip vortex mixing, wake unsteadiness, and tip vortex core dissipation closer to the rotor than for rotors with lower numbers of blades. This trend with increasing number of blades is evident in the flow visualization results shown in Reference 7, in which the wakes of two-, four-, six- and eight-bladed rotors are presented. For example, the tip vortices of the eight-bladed rotor were found to become unsteady at about 0.2R from the rotor compared to 0.4 to 0.5R for the two-bladed rotor. In general, the results indicate the importance of accurately modeling the complex wake of hovering rotors with large numbers of blades.

Comparison With Rotor Test Data of Miller, Gray and Perlmutter, USAAVLABS TR 67-74

In order to compare theoretical induced velocities with data from the flight tests of a full-scale helicopter, the following reference (Reference 74) was selected:

> Miller, R. H., C. G. Gray and A. A. Perlmutter. Theoretical and Experimental Investigation of the Instantaneous Induced Velocity Field in the Wake of a Lifting Rotor. Dynasciences Corp., USAAVLABS Technical Report 67-74, Eustis Directorate, U.S. Army Air Mobility Research and Development Laboratory, Fort Eustis, Va., January 1968, AD 672-4.

Velocity test data were measured in flight on an Army UH-55A helicopter using both pressure (Pitot probes) and hot-film instrumentation mounted on a radially extending boom located in the rotor at various azimuth

positions and axial distances from the rotor disk. Both time-averaged and instantaneous velocity data were acquired. In the course of conducting this correlation study, it was found that the data in this reference was not very useful due to the imprecise manner of data presentation, the limited extent of the data, and the degree of scatter in some of the data. In particular, it was found that the instantaneous velocity data were presented in unusable form.

Rotor and hover flight test information is presented in Table 7. Collective pitch was not documented in the reference, and was thus established in the analysis as 6.8 deg to produce a thrust coefficient consistent with the nominal gross weight of the aircraft.

TABLE 7. ROTOR AND TEST INFORMATION --
MILLER, TANG & PERLMUTTER, USAAVLABS TR 67-68

Rotor Type

TH-55A, full-scale, articulated rotor

Rotor Design

Number of blades	3	Blade taper ratio	1.0
Rotor radius, ft	12.645	Blade aspect ratio	15.9
Blade chord, ft	0.80	Blade twist, deg	-8.0
Rotor solidity	0.060	Airfoil section	NACA 0015

Hover Test Condition (Flight Test)

$\mu = 0$, $\Omega R = 596$ fps, θ_{75} not indicated, $C_T = 0.00377$*, $v_o = 25.9$ fps

* Based on nominal gross weight.

The three components of predicted time-averaged induced velocity are compared with both the hot-film and pressure data for the hover condition in Figures 45 and 46. The velocities, nondimensionalized by the momentum value, are presented for the measurement radial stations between 0.55R and 0.80R at two distances below the rotor (z/R = -0.26 and -0.45). The theoretical results are shown to correlate well within the scatter and limited extent of the test data. The limited radial extent of the test data precludes the opportunity to comparatively assess the results based on the classical and generalized wake representations at and outboard of the wake boundary.

CORRELATION STUDY FOR FORWARD-FLIGHT CONDITIONS

Five of the selected sources of data (References 23 to 27) listed in Table 1 contain information pertaining to forward-flight test conditions. Comparisons of results of the Rotorcraft Wake Analysis with test data from each are presented below.

Comparison With Test Data of Heyson and Katzoff, NACA TR 1319

Induced velocity data for a 15-foot diameter, two-bladed model rotor tested in the NASA Langley full-scale wind tunnel are presented in the following reference (Reference 24):

> Heyson, H. H. and S. Katzoff, Induced Velocities Near a Lifting Rotor With Nonuniform Disk Loading, NACA Technical Report 1319, 1957.

Presented in this reference are time-averaged values of the component of induced velocity normal to the rotor disk. These measurements were acquired by surveying a large number of points above, below, and aft of the rotor with a rake of pressure tubes.

Information on the rotor design and test conditions is presented in Table 8. As noted in the table, data for three test conditions with advance ratios of 0.095, 0.140 and 0.232 were selected for this correlation study. An undistorted wake model with a rolled-up tip vortex was used in the calculations. Sample results of the correlation study are presented in Figures 47 through 53. These figures contain comparisons of measured and theoretical values of the time-averaged induced velocity ratio (normal to the rotor disk) at selected field points.*

---

*The comparison is made with test data exactly as presented in the reference, in which downflow is positive. To be consistent with the sign convention used herein for v_z/v_o (downflow negative), the notation $-v_z/v_o$ is used in the figures.

TABLE 8. ROTOR AND TEST INFORMATION -- HEYSON & KATZOFF, NACA TR 1319

Rotor Type

Single, model, teetering rotor

Rotor Design

Number of blades	2	Blade taper ratio	1
Rotor radius, ft	7.5	Blade aspect ratio	11.7
Blade chord, ft	0.64	Blade Twist, deg	0
Rotor solidity	0.0543	Airfoil section	NACA 0012

Test Conditions

Condition 1: $\mu = 0.095$, $\Omega R = 500$ fps, $C_T = 0.00320$, $\alpha = -9.2^\circ$, $v_o = 8.0$ fps

Condition 2: $\mu = 0.140$, $\Omega R = 500$ fps, $C_T = 0.00371$, $\alpha = -5.3^\circ$, $v_o = 6.50$ fps

Condition 3: $\mu = 0.232$, $\Omega R = 450$ fps, $C_T = 0.00321$, $\alpha = -9.5^\circ$, $v_o = 3.04$ fps

Blade control angles not indicated in reference.

For Figures 47 through 49 the advance ratio is 0.140, the thrust coefficient is 0.0037, and the wake skew angle is 82.3 degrees based on a momentum induced velocity of 6.5 fps. In Figure 47, the induced velocity ratios are compared at several distances above and below the rotor disk in the lateral plane of symmetry of the rotor. In Figure 48, comparisons are made at several distances fore and aft of the rotor center and in a plane parallel to and 0.07R beneath the rotor. This plane was selected for comparison on the basis that it contains the measured points that are closest to the rotor and within the rotor wake. The trends of the velocity distributions are predicted accurately, and good correlation is noted except at some points beneath the advancing side of the rotor. In Figure 49, the predicted values are compared with the data as interpolated in NACA TR 1319 along the longitudinal and lateral centerlines of the rotor disk. Good correlation is noted along the longitudinal centerline except at $x/R = 3.14$, for which the number of wake revolutions used in the Rotorcraft Wake Analysis was insufficient (four wake revs were used which truncated the wake in the vicinity of $x/R = 3.14$). However, lack of correlation in this downstream region is also expected due to the down-

stream distortions of the wake. Reasonable correlation is noted on the retreating side of the lateral centerline. However, on the advancing side, the induced velocity is overpredicted as is consistent with the previous figures.

In Figure 50, the induced velocity ratio is compared for the test condition defined by an advance ratio of 0.095 and a thrust coefficient of 0.0032. The undistorted wake skew angle for this condition is 75 deg, based on a momentum induced velocity of 8.0 fps. The degree of correlation is generally similar to that at the 0.140 advance ratio. Comparisons of measured and predicted velocities for the 0.232 advance ratio condition are presented in Figures 51 to 53. The undistorted wake skew angle for this condition is 84 degrees and the momentum induced velocity is 3.0 fps. Since at high rotor advance ratios the wake is swept back rapidly, leaving the forward half of the rotor in relatively clean flow (few blade-vortex interactions), comparisons were made at points in the aft region of the rotor. Comparisons are presented at the lateral plane of symmetry, $x/R = 0$, and at the $x/R = 0.5$ and 1.07 planes. It is noted that the experimental accuracy for this condition was recorded in the reference as a ± 25 percent compared to the ± 10 percent for the other conditions.

Generally, the degree of correlation appears to be reasonable, considering the undistorted wake representation used in the analysis. Significant distortions and mixing of the wake on the lateral portions of the rotor (roll-up into a pair of vortices similar to a fixed wing) are evident from the velocity contours presented in the reference and more recent flow visualization results. Whether the discrepancies that do exist (particularly on the advancing side at $x/R = 0$, $z/R = 0$ and -0.07) are due to wake distortions, the finite filament wake representation, inaccuracies in the input analytically determined controls and flapping that affect lateral trim, or sensitivity to other assumptions or limitations of the analysis, remains to be determined.

Comparison With Forward Flight Test Data of Miller, Tang, and Perlmutter, USAAVLABS TR 67-68

In addition to the comparison with the hover test data, presented previously, induced velocities from the Rotorcraft Wake Analysis were compared with the forward flight test data from the following reference (Reference 23).

Miller, N., J. C. Tang and A. A. Perlmutter, Theoretical and Experimental Investigation of the Instantaneous Induced Velocity Field in the Wake of a Lifting Rotor, USAAVLABS Technical Report 67-68, January 1968.

Rotor and forward flight test information are presented in Table 9. As noted in this table, the two flight conditions have low advance ratios, 0.049 and 0.11, corresponding to flight speeds of approximately 17 and 40 knots, respectively.

Radial distributions of induced velocity were predicted for the following test azimuth and axial positions:

Hot-Film Boom Azimuth Positions, ψ, deg	30, 90, 150, 210, 270, 330
Axial Position (from hub), z/R	-0.22, -0.26, -0.49

The momentum skew angles of the classical wake representation were χ = 58 and 80 deg, corresponding to the momentum induced velocity values of 18.6 and 9.3 fps for the 17- and 40-kt conditions. Results for the two flight

TABLE 9. ROTOR AND TEST INFORMATION -- MILLER, TANG & PERLMUTTER, USAAVLABS TR 67-68, FORWARD FLIGHT

Rotor Type

TH-55A, full-scale, articulated rotor

Rotor Design

Number of blades	3	Blade taper ratio	1.0
Rotor radius, ft	12.645	Blade aspect ratio	15.8
Blade chord, ft	0.80	Blade twist, deg	-8.0
Rotor solidity	0.060	Airfoil section	NACA 0015

Forward Flight Test Conditions (Flight Test)

Condition 1: μ = 0.049, ΩR = 596 fps, C_T = 0.00377*, α = -0.2°, v_o = 18.6 fps

Condition 2: μ = 0.11, ΩR = 596 fps, C_T = 0.00377*, α = -2.3°, v_o = 9.3 fps

Blade control angles not indicated in reference.

* C_T based on nominal gross weight.

conditions are compared with the time-averaged test data (normal component) in Figures 54 and 55. (Instantaneous velocity data in the reference was presented in unusable form.) As revealed in these figures, the degree of correlation varies from good to poor. This is believed to be partially attributable to the increased sensitivity of local velocities to wake distortions for low-speed conditions. To illustrate this, two plots were selected from Figures 54 and 55 and are presented in Figure 56, they are representative of the range of correlation. The test results at the selected 90-degree azimuth are fairly similar at the two flight speeds. Although the theoretical results correlate well at the 40-kt condition, a significant difference is noted at the two near positions to the rotor for the 17.4-kt condition. The change from large downflow values to upflow in the predicted radial distributions for these two positions is indicative of the close proximity to and crossing of the wake boundary. The high inboard downwash velocities predicted for these two axial positions are indicative of placement within the wake. The velocity gradient indicates the wake boundary, and the upflow predicted outboard indicates placement outside the wake. For the furthest axial position ($z/R = -0.49$), the velocity distribution changes character since the points beyond approximately 0.6R lie outside the wake. The discrepancy is thus believed to be mainly attributable to the classical wake representation used in the analysis, for flow visualization studies have indicated that distortions of the wake boundary are most severe at low-speed conditions. Although some differences are expected due to uncertainties in the rotor test condition parameters and other accumptions in the analysis, results for points at other azimuth positions appear to support the conclusion that the degree of correlation depends on the degree of wake distortion. In general, points with low theoretical induced velocity magnitudes are outside the classical wake, and points with the higher magnitudes are within the wake.

Comparison With Test Data of Landgrebe and Johnson

The flow velocity data of primary interest to the rotor aerodynamicist are the instantaneous velocities in the vicinity of the rotor blades. The accurate measurement of these velocities has until recently presented the rotor experimentalist with a dilemma -- how to measure the flow at the rotor disk without influencing the flow and without requiring concern for the physical impact of the blades with the measurement device. In the last 3 years, it has been demonstrated that the dilemma can be solved by using a laser velocimeter (LV). The experimental velocities of the correlation study presented below, and the one following, were acquired from LV measurements.

In 1973, LV techniques were applied at UTRC to a model rotor in a wind tunnel, and velocity time-histories were measured at several fixed points in close proximity to passing blades. This demonstration test is described in the following reference (Reference 25).

> Landgrede, A. J., and B. V. Johnson, Measurement of Model Helicopter Rotor Flow Velocities with a Laser Doppler Velocimeter, Jl. American Helicopter Society, Vol. 19, No. 3, July 1974.

A photograph of the rotor and LV system in the UTRC 4- x 6-foot wind tunnel is shown in Figure 57. The velocity measurement point is the focal point (intersection) of the two laser beams shown. Rotor design and test information are presented in Table 10. A schematic showing the side view of the two-bladed rotor with the blades in the fore and aft positions (ψ= 0 and 180 deg) for the 0.15 advance ratio condition is presented in Figure 58. The test was conducted as a demonstration to show the feasibility of applying LV techniques in a wind tunnel to measure rotor instantaneous flow velocities, and thus only a limited number of velocity measurements were taken. Velocity data were measured at

TABLE 10. ROTOR AND TEST INFORMATION -- LANDGREBE & JOHNSON

Rotor Type

Single, model, articulated rotor

Rotor Design

Number of blades	2	Blade taper ratio	1
Rotor radius, ft	2.15	Blade aspect ratio	17.6
Blade chord, ft	0.122	Blade twist, deg	0
Rotor solidity	0.0363	Airfoil section	NACA 0012

Test Condition

$\mu = 0.15$, $\Omega R = 300$ fps, $C_T = 0.0026$, $\theta_{75} = 9^\circ$, $v_o = 2.5$ fps,

$A_{1_s} = 0^\circ$, $B_{1_s} = 0^\circ$, $a_o = 3^\circ$, $a_{1_s} = 3.2^\circ$, $\alpha = -12.8^\circ$

points in the rotor vertical plane of symmetry forward of the rotor hub for several vertical distances from the rotor disk. These vertical distances ranged from 0.08R above the disk to 0.16R below the disk (measured from the flapped blade at ψ = 180 deg), as shown in Figure 58. Vertical, $v_{z'}$, and streamwise, $v_{x'}$, velocity components were measured.

To assist in the interpretation of data, flow visualization photographs (similar to Figure 12) were taken during the test to measure the time-varying positions of the tip vortices relative to the focal points. Specifically, they were used to determine the rotor wake boundary in the plane of measurements, and to establish where the tip vortices crossed the plane for specific blade azimuth positions. The vortex positions and their circulation sense for two rotor positions are shown in Figure 59. Coincidentally, for the 0.15 advance ratio tested, when a blade was at ψ = 180 deg, the focal points at 0.75R were midway between the blade's own tip vortex and the tip vortex at r/R = 0.5 from the preceding blade. When the blades were at ψ = 90 and 270 deg, the tip vortex from the blade at 90 deg crossed the measurement plane at the measurement station, 0.75R. The experimental wake boundary, as defined by the centers of the tip vortices at their intersections with the measurement plane, is shown in Figure 58. Also, shown are the undistorted and analytical distorted wake boundaries. Although slightly more contracted, the distorted wake boundary, which was calculated using the UTRC Wake Geometry Analysis described previously, agrees closely with the mean experimental wake boundary (within the accuracy and excursions of the test data). Predicted and experimental tip vortex distortions in the streamwise direction near the measurement points were found to be small (within 0.01R) for the selected test conditions.

In the selection of the focal points for use in the correlation study, the experimental accuracy of the test data was considered. Since the LV test was primarily for demonstration purposes, sophisticated instrumentation to statistically process the LV data was not used. Taking advantage of the periodicity associated with the steady test condition, the experimental results were obtained by fairing the data from many rotor revolutions. In this manner, time histories representing the mean of the instantaneous velocities were acquired. Although this procedure is reasonably accurate when the fluctuations of the data are small, accuracy was lost at some focal points due to large fluctuations. As expected, these fluctuations were generally the largest at focal points close to the wake boundary. The focal points were thus selected from those having the least data scatter. It is noted, however, that the data fairings presented are believed to be reasonable but could include some inaccuracy, especially for those points within the wake. For example, high harmonic content could possibly have been faired out.

Time histories of the instantaneous vertical velocity component at three focal points, 0.75R forward of the hub, are presented in Figure 60. The selected focal points are 0.08R and 0.02R above the blade and 0.02R below the blade, and they represent points away from the blade, near the blade, and in and out of the wake. The velocities are presented for varying time as related to the azimuth position of a blade, and are shown to be periodic with blade passage interval (two cycles per rotor revolution). The instants of time corresponding to blade passages directly above or beneath a focal point are at Ψ = 0 and 180 deg. As described in the reference, considering the circulation sense and position of the bound and tip vortex of each blade relative to each focal point, the flow directions and locations of the peak velocities are found to be as expected. For the points under consideration at r/R = 0.75R, at a blade passage time, a selected focal point is midway between the adjacent tip vortices as shown in Figure 59. The distance of the tip vortices and their cancelling effect allow the bound vorticity to predominate. The rapid change of the velocity direction from upflow to downflow, as indicated near ψ = 0 and 180 deg, substantiates this. When the blades are at 90 and 270 deg, a tip vortex passes directly beneath the focal points. The distance of the blades and their cancelling bound vorticity now allows this tip vortex to predominate, as noted by the rapid change from downflow to upflow before and after the vortex passage (ψ = 90 and 270 deg in the figures). The combination of the above two effects to form a fairly smooth time history is illustrated in Figure 61. Of course, the relative degree of influence of the separate effects is dependent on the relative distances from the tip vortex and blade to the particular focal point. For example the more predominant influence of the blade (bound vortex) at the z'/R = 0.08 focal point is indicated in Figure 60(a) by the steeper gradients at ψ = 0 and 180 deg. Similarly, the influence of the tip vortex passage is somewhat more predominant for the z'/R = -0.02 point between the rotor and the wake boundary, as indicated in Figure 60(c) by the steeper gradients at ψ = 90 and 270 deg. As expected, the peak-to-peak velocity amplitudes increase with increasing proximity to the rotor and wake.

In Figure 60, the time histories predicted using the Rotorcraft Wake Analysis are generally in good agreement with the time histories measured with the laser velocimeter. The character and phasing of the experimental time histories are predicted as well as the relative local gradients and the growth in peak-to-peak amplitude with decreasing distance to the rotor and wake. It is not known whether the small differences in peak-to-peak amplitude and mean velocity are attributable to the analysis or the experimental data, since the differences are within the accuracy of the demonstration test. The increased peak-to-peak amplitudes of the distorted wake results relative to those of the undistorted wake are due to the upward tip vortex distortions which place the tip vortex passage closer to focal points above it.

Time histories of vertical and streamwise instantaneous velocities for two focal points along the vertical traverse at the r/R = 0.5 location are presented in Figures 62 and 63. The two selected points consist of a point above the rotor (at $\Delta z'/R = 0.04$) and a point below the rotor and in the wake (at $\Delta z'/R = -0.04$). These points are shown in Figure 58. The character and phasing of the vertical velocities differ from those at the r/R = 0.75 location, mainly due to the change in phasing of the tip vortex passage. As shown in Figure 59, the tip vortex passes these points when the blades are at $\psi = 0$ and 180 deg. When the blades are at $\psi = 90$ and 270 deg, the blades and vortices are at their furthest distances from these focal points and are in essentially self-cancelling positions. Although the bound and tip vortex effects on the vertical velocity are opposing before and after their passage, they produce maximum velocity gradients near their passage at $\psi = 0$ and 180 deg. The magnitude of the streamwise velocity agrees closely with the free-stream velocity (V = 46 fps) at 90 and 270 deg, where, as mentioned above, the blades and tip vortices have the least influence. Since the bound vorticity does not contribute to the streamwise velocity component when a blade is above or below the focal points under consideration, the increased streamwise velocities noted in Figures 62 and 63 near $\psi = 0$ and 180 deg are produced by the tip vortex passages. The character and phasing of the predicted time histories at the 0.5R location are generally similar to the test data; however, some differences do exist. In the wake at $\Delta z'/R = -0.04$ (Figure 3), the effect of the tip vortex appears to predominate and produces downflow prior to its passage and upflow following its passage by the points at r/R = 0.5. The closer passage of the distorted tip vortex produces a higher predicted peak velocity. The high harmonic content in the predicted time histories are believed to be artificially produced by the finite filament representation of the inboard wake. In Figure 62, the velocities for the point 0.04R above the rotor are shown to be reduced relative to those at the point 0.04R below (Figure 63), which is consistent with the increased distance from the tip vortices.

Generally, it has been shown that the time histories of induced velocities predicted using the Rotorcraft Wake Analysis are in favorable agreement with the limited amount of useful, time-history test data. Similar data for further evaluation of the analysis at other test conditions and azimuth positions are required.

Comparison With Test Data of Biggers and Orloff

The use of a laser velocimeter to measure the flow velocities in the wake of a two-bladed model helicopter rotor is also reported in the following reference (Reference 26):

Biggers, J. C., and K. L. Orloff, Laser Velocimeter Measurements of the Helicopter Rotor-Induced Flow Field, Journal of the American Helicopter Society, Vol. 20, No. 1, January 1975.

Laser velocimetry techniques were used to measure two components of induced velocity in the outboard vicinity of blades at two azimuth positions. Time-averaged and instantaneous velocity components in the vertical and streamwise directions (v_z' and v_x') were measured in the NASA-Ames 7- by 10-foot wind tunnel at a rotor advance ratio ($V/\Omega R$) of 0.18. Measurements were made at a series of stationary points in a vertical plane through the center of the hub (the x-y plane) at the advancing and retreating blades (ψ = 90 and 270 deg). Results were obtained primarily for the advancing blade. Time-averaged velocities were measured by continuously averaging the velocities of seeded particles passing through the fixed focal points. To measure instantaneous velocities, a strobe technique was used which relies upon the periodicity of the rotor flow for steady-state conditions. Data were accepted only once per revolution during a short "data window", which was open only when the blade was at a prescribed azimuth. Information on the rotor design and single test condition is presented in Table 11. Thrust was not measured.

TABLE 11. ROTOR AND TEST INFORMATION -- BIGGERS & ORLOFF

Rotor Type

Single, model, hingeless rotor

Rotor Design

Number of blades	2	Blade taper ratio	1.0
Rotor radius, ft	3.5	Blade aspect ratio	9.9
Blade chord, ft	0.354	Blade twist, deg	0
Rotor solidity	0.0644	Airfoil section	NACA 0012

Test Condition

μ = 0.18, ΩR = 110 fps, θ_{75} = 8.5°, α = -6.6°, v_o = 1.83 fps

A_{1_s} = 0°, B_{1_s} = 0°, C_T not measured (calculated C_T = 0.0048)

In order to show the sensitivity of the predicted velocities to tip vortex distortions, the Rotorcraft Wake Analysis was run with both undistorted and distorted wake representations. The test control angles and rotor tilt angles were used in the analysis. Top, side, and rear views of the analytical undistorted and distorted tip vortex geometries relative to the tip-path coordinate axes are presented in Figures 64 and 65, respectively. The undistorted wake skew angle, χ, is 78.2 deg. The tip vortices from both blades are shown for the rotor position at which instantaneous velocities were measured at the advancing and retreating blades. By comparing the tip vortex positions between these two figures, it is evident that the tip vortex distortions predicted by the UTRC Wake Geometry Analysis (Deck F506) are relatively small near the blades for this rotor position and test condition. Greater tip vortex distortions occur downstream, but they are of minor consequence to the induced velocities near the advancing and retreating blades.

The location of the tip vortex from the preceding blade was determined during the test when it crossed the advancing blade at ψ = 90 deg. A comparison of the test tip vortex location with the analytical undistorted and distorted tip vortex locations is presented below:

	x'/R	y'/R	z'/R	Δz'/R
Measured tip vortex location	0.0	0.85	-0.05	-0.048
Undistorted tip vortex location	0.0	0.87	-0.104	-0.102
Distorted tip vortex location	0.0	0.86	-0.045	-0.043

The z'/R values are relative to the rotor hub center in the wind tunnel coordinate system. Considering the preconing and lateral tilt of the rotor, the vertical distances between the tip vortex and the blade are listed as $\Delta z'/R$. As indicated above, the predicted and measured tip vortex positions are in good agreement.

The velocities calculated using the Rotorcraft Wake Analysis with undistorted and distorted wake representations are compared with the laser velocimeter test data in Figures 66 through 71. In most cases, the plot format of the reference has been retained to maintain a direct relationship with the test data as presented therein. Velocities are nondimensionalized by tip speed, and the wind tunnel axis system is used.

Time-Averaged Velocities

In Figure 66, the predicted and experimental radial distributions of the time-averaged vertical velocities are presented for several vertical positions near the rotor. The $v_{z'}$ axis for each plot is placed at the z'/R location for that set of data (the z'/R scale is expanded to ten times the y'/R scale for clarity of presentation). The radial distributions are characterized by downflow inside the wake, changing to upflow outside the wake due to the passage of the tip vortices. The gradients diminish with increasing distance from the rotor. The analytical velocity distributions are in agreement with these features. The variations of time-averaged vertical velocities (predominantly downwash) with vertical position are plotted in Figure 67 for several radial locations. The $v_{z'}$ axis for each traverse is placed at the y'/R location for that data set. Again, the predicted velocity distributions exhibit the same character as the measured values, although absolute differences exist. Moving down each vertical traverse, the predicted and measured downwash increases to a peak, decreases rapidly to the vicinity of the time-averaged wake boundary, and then gradually diminishes to zero. Differences in location of the primary velocity gradients in Figures 66 and 67 indicate the extent of the difference between the predicted and measured time-averaged wake boundaries. In Figure 68, the predicted and measured radial distributions of the time-averaged streamwise velocity are compared at the $z'/R = -0.05$ location (the free-stream $V/\Omega R = 0.18$ is included).

Instantaneous Velocities

Radial distributions of instantaneous vertical velocities are presented in Figure 69 for the same vertical positions as Figure 66. As mentioned above, the measured tip vortex location was at $x'/R = 0.85$, $z'/R = -0.05$. This tip vortex location is evident in the measured instantaneous velocity profile, which shows a sharp downward peak at $y'/R = 0.845$ and a less pronounced upward peak at $y'/R = 0.860$. The predicted instantaneous velocities based on the distorted wake representation are much improved over the undistorted wake results due to the more accurate positioning of the tip vortex. At the $z'/R = -0.05$ elevation, the presence of the distorted tip vortex is also evident (exact location is $z'/R = -0.045$), whereas the undistorted tip vortex is most evident at $z'/R = -0.09$ (exact location is $z'/R = -0.104$). Consistent with the experimental results, the influence of the predicted distorted tip vortex from the preceding blade is less pronounced as the distance away from the core increases. However, its influence is still significant as far as $z'/R = -0.09$.

A comparison of the radial distributions of instantaneous streamwise velocity for the $z'/R = -0.05$ elevation is included in Figure 68. The limitations of the Rotorcraft Wake Analysis for predicting the local instantaneous velocities in the immediate vicinity of blades with a high degree of accuracy are illustrated in Figures 70 and 71.* It will be shown that the limitations are primarily due to the lifting line representation of the blades in the analysis. However, before describing the results, it is noted that when the analysis is used to compute induced velocities at the blades for blade airloads and performance purposes, the influence of the blade bound vortex (lifting line) at blade segment points along itself is eliminated. Although it is recognized that finite chord and thickness effects on the local flow at the blade are neglected, the oversensitivity of the local flow predictions to small distances from a concentrated bound vortex, such as will be shown, does not exist in such applications.

In Figure 70, the predicted and measured instantaneous vertical velocities at $r/R = 0.95$ are presented for the advancing and retreating blades, respectively. In the reference, the velocity profile of the experimental data in Figure 70 (a), showing upward flow above the blade and downward flow below it, is attributed primarily to the influence of the airfoil and its attitude; that is, (1) streamline divergence effects due to airfoil profile (maximum thickness is at the 30-percent chord, and the measurements were made at the 25-percent chord), and (2) the upward component of blade circulation at the upper surface, and the downward component at the lower surface associated with the 1.5-deg nosedown attitudes of the airfoil section relative to the measurement axes. These effects are neglected in the analysis. In fact, the bound vortex in the analysis does not affect the vertical velocities at all for these results because the vertical axes in Figure 70 pass directly through the quarter-chord where the bound vortex is located. The analytical velocity profile in Figure 70(a) is attributed to the influence of the tip vortices. That is, as the traverse is made starting above the blade, increasing downflow is due to the advancing blade's own tip vortex and then the upflow is due to the tip vortex of the preceding blade which is at a lower position. For a similar traverse for the retreating blade shown in Figure 70(b), the velocity profile is different. The peak downflow at the blade may be attributed to the retreating blade's own tip vortex, and the lack of a similar upflow peak may be attributed to the position of the previous blade's tip vortex at a much larger distance from 0.95R on the retreating side (see Figure 65). However, the absence of experimental upflow below

*Vertical distances in Figures 70 and 71 are relative to the blade ($\Delta z'/R$) rather than the hub (z/R) as in previous figures.

the blade due to the above two real airfoil influences, cited in the reference, is somewhat contradictory, particularly since the airfoil is at a higher noseup attitude (18 deg) relative to the x' axis.

Vertical traverses of the instantaneous streamwise velocities near the advancing and retreating blades at r/R = 0.95 are presented in Figure 71. Since the blades' own tip vortices are essentially aligned with the x' axis near the measurement plane when the blades are at the azimuth positions investigated, their contribution to the streamwise velocities is small. Thus, the bound vorticity is the major contribution to the streamwise velocities in these figures. In both figures the predicted velocities result mainly from the bound vortex induced flow toward the trailing edge above the blade, and toward the leading edge below the blade. This induced flow is superposed on the free-stream flow. For the retreating blade (Figure 71(b)), the experimental flow reversal is evident. However, for the advancing blade (Figure 71(a)), it is not. In the latter figure, the analytical induced velocities are accurate above the blade. Just below the blade, the reason for the absence of upstream induced velocities (relative to the free-stream velocity) in the test data, expected from bound vorticity, is not known. The magnitudes of the predicted velocity peaks in Figure 71(b) are dependent on the lifting line representation, and they were found to be very sensitive to small changes in chordwise variations of the traverse line. The peak values and their location are also sensitive to the artificial vortex core size (diameter = 0.15 chord) assigned to the bound vortex to preclude velocities approaching infinite magnitude very close to the lifting line. In addition, the accuracy of the velocity values at a point near the blade is dependent on the accuracy of the calculated circulation strengths of the bound vortex segments near the point.

It is noted in Figures 70 and 71 that the distorted wake results are similar to the undistorted wake results. This is explained by the relatively small distortions and the small effect of the tip vortices of the preceding blades on the vertical and streamwise instantaneous velocities at the 0.95R locations for these figures. Greater wake distortions and associated induced effects occur at other blade azimuths than those tested.

Generally, the results presented above indicate that the Rotorcraft Wake Analysis predicts the features of the velocity distributions in the wake, but the degree of accuracy varies depending on the accuracy of the wake representation. Also, as expected, for points removed from, but in the immediate vicinity of, a passing blade, a lifting line representation of the blade is insufficient. Laser velocimetry is shown to be an excellent means of providing data for correlation purposes. LV data for other test conditions and at other blade azimuths where wake distortions are more significant are required.

Comparison With Test Data of Heyson, NACA TN 3242

Following the incorporation in the Rotorcraft Wake Analysis of a provision for the computation of off-rotor velocities for dual rotors, the computer analysis was applied to calculate the induced velocity field of the tandem- and single-rotor configurations described in the following reference (Reference 27):

> Heyson, H. H., Preliminary Results from Flow-Field Measurements Around Single and Tandem Rotors in the Langley Full-Scale Tunnel, NACA TN 3242, November 1954.

The rotor and test information from this reference are presented in Table 12. The 15-foot diameter rotors were tested in the NASA-Langley Full-Scale Wind Tunnel at an advance ratio of 0.15. One of these rotors was used in the previously described experimental program of Reference 24. A five-tube pressure survey rake was used to measure local downwash angles in the survey planes indicated in Figure 7. The local downwash angles were averaged spanwise (i.e., laterally) at each elevation and

TABLE 12. - ROTOR AND TEST INFORMATION -- HEYSON, NACA TN 3242

Rotor Types

Single and tandem, model, teetering rotors

Rotor Design

Number of blades	2	Blade taper ratio	1
Rotor radius, ft	7.5	Blade aspect ratio	11.7
Blade chord, ft	.64	Blade twist, deg	0
Rotor solidity	0.0543	Airfoil section	NACA 0012

Test Condition for Single and Tandem Rotors

μ = 0.15, ΩR = 500 fps, C_T = 0.0034, v_o = 5.6 fps

Blade control angles and flapping not indicated in reference.

nondimensionalized by the downwash angle at the center of a single-rotor based on momentum theory. Single-rotor data were acquired by simply removing the rear rotor from the tandem configuration. The tandem rotor was set to operate at the same lift coefficient as the single rotor by maintaining the single-rotor controls for the forward rotor and adjusting the rear rotor controls. These controls were not provided in the reference, but were estimated to correspond to the specified lift coefficient and wake momentum skew angle (82.7°).

Comparisons of the predicted results from the Rotorcraft Wake Analysis with the experimental data are presented in Figure 72. As noted, the trends with vertical and longitudinal position and the trends from single to tandem rotors are accurately predicted. Good agreement with test data is shown for both the single and tandem rotors in the forward survey plane. However, the accuracy deteriorates in the rearward survey planes. This inaccuracy is believed to be inherent for the undistorted wake model used in the analysis. The wake downstream from a rotor exhibits significant distortions which, as shown in the reference, are characterized by the downstream transformation of the wake into a single pair of vortices for both single and tandem rotors. Thus, significant distortions of the wake from the forward rotor mixed with the wake from the rear rotor occur near the rear rotor. These are not represented in the wake model. Also, some inaccuracy may be associated with the uncertainties in the controls and dependency of the spanwise average on the selection of points, particularly near the wake boundaries. Local velocity data would have been more desirable for comparison purposes. Nonetheless, these initial results indicate that improvements in the tandem-rotor downwash predictions may be anticipated through the use of the dual rotor provision in the Rotorcraft Wake Analysis, which accounts for the influence of the wakes of both rotors.

CONCLUDING REMARKS

The development of the UTRC Rotorcraft Prescribed Wake Induced Velocity Analysis ("Rotorcraft Wake Analysis") provides, in a single computer analysis, the capability for calculating flow velocities induced by the rotor(s) for the following field points, configurations, conditions, and wake representations:

a. Time-averaged and instantaneous induced velocities (three components) on and off the rotor.

b. Single and dual rotor configurations (coaxial, tandem, side-by-side, etc.).

c. Steady hover and forward flight conditions.

d. Undistorted and distorted, analytical and experimental, prescribed wake geometries.

For rotor configurations and conditions for which test data were available, the induced velocities calculated in the rotorcraft wake analysis are generally in good agreement with measured velocities. The successful prediction of primary characteristic features of both time-averaged and instantaneous induced velocity distributions in and out of the rotor wake, and local velocity variations with several rotor design and test condition parameters, has been demonstrated within the scope of the available test data. However, the degree of accuracy at a specific field point is sensitive to the accuracy of the prescribed wake representation, proximity of the field point to a wake boundary or blade, and the input flight condition, rotor control, and blade motion information.

RECOMMENDATIONS

The Rotorcraft Wake Analysis represents the combination and extension of component computer programs which have been developed and in use at the United Technologies Research Center for many years. During this time, the component analyses have been applied to many and varied problems, and the results have generally been favorable. However, like any analysis, the Rotorcraft Wake Analysis should continue to be refined and checked to remove limitations and to incorporate advances in applicable technology as they become available. The following recommendations for acquiring additional experimental data, performing a sensitivity study, continuing application and evaluation, and providing refinements to the analysis are thus offered:

1. Additional Experimental Data - Additional experimental data are required to further evaluate the Rotorcraft Wake Analysis, and to provide wake geometry data for improving the analytical representation. Systematic data should be acquired over an increased range of rotor designs, flight conditions, and field points for single-rotor, dual-rotor, and winged configurations of interest. In addition to flow velocity data, wake geometry and airloads data should be acquired concurrently to provide a consistent set of correlative information. Laser velocimeter techniques should continue to be used to provide velocity data at the rotor blades as well as in the wake, and to provide blade airload distributions (bound vorticity). The analysis should be used for guidance in a systematic selection of test conditions and field points to acquire the most useful data cost-effectively.

2. Sensitivity Study - The sensitivity of the induced velocities predicted by the Rotorcraft Wake Analysis to small variations in input flight condition, rotor controls, blade motions, and wake representation should be investigated for selected sources of correlative data to determine the degree of accuracy required of the input parameters and test information used to establish the input. The sensitivity of the correlation results to the assumed wake representation should be investigated by systematically varying the wake parameters (wake azimuth increment, number of wake revolutions, vortex core size, vortex filament distribution, etc.) in the analysis. This has been accomplished to some extent in the past with the component programs of the Rotorcraft Wake Analysis by comparing rotor performance and blade bending moments. With the availability of additional test data at and away from the rotor and the provision

of the off-rotor velocity capability in the analysis, a more accurate sensitivity study should be performed to assist with future applications and evaluations of the analysis.

3. Continued Application and Evaluation - Application of the Rotorcraft Wake Analysis in conjunction with rotor performance and blade response analyses, and comparison of the results with test data, should be continued to further evaluate the induced velocities, airloads, rotor performance, blade response, and bending moments predicted with the combined analysis. As correlative test data become available, the range of configurations and test conditions for which induced velocities are compared should be extended. In particular, further comparison is required for low-speed test conditions and dual-rotor and winged helicopter configurations.

4. Refinements - The Rotorcraft Wake Analysis has been organized to allow components applicable to specific technical areas, configurations, or flight modes, to be updated or replaced as the state of the art advances or the need arises. Also, the use of a prescribed wake in the analysis retains flexibility in the type and source of wake geometry representation. As additional accurate and generalized wake geometry information becomes available from experimental programs and/or wake geometry analyses, it can be incorporated in the analysis. Wake modeling refinements to account for wake mixing, vortex core dissipation, and inboard wake distortions should eventually be incorporated. The inclusion of an optional replacement of the lifting line representation of the blade by a lifting surface representation, at least in local areas of significance, should be considered. Also, the analysis should be extended to include a fuselage and tail rotor, operation near the ground (in ground effect), and operation in transient (maneuvers and unsteady wind) conditions.

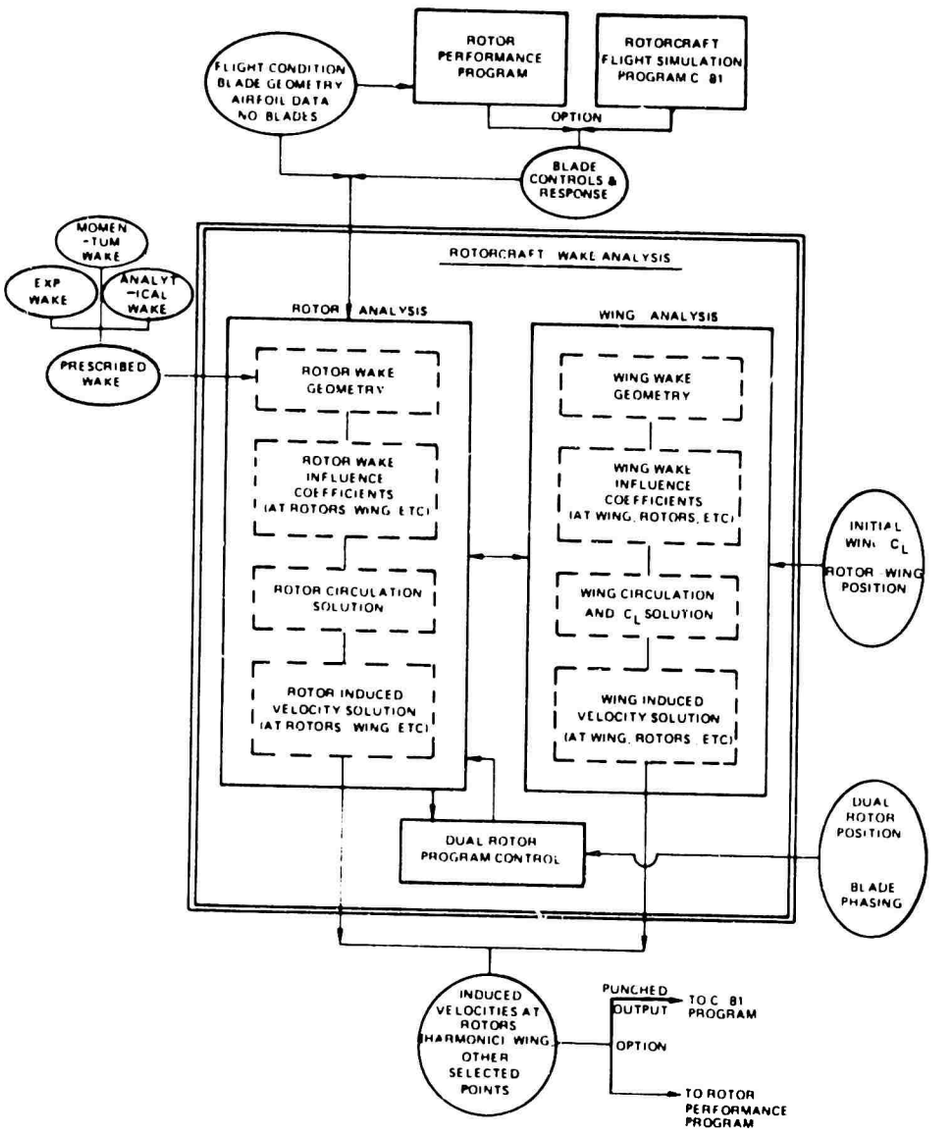

Figure 1. Flow Chart of the Rotorcraft Wake Analysis.

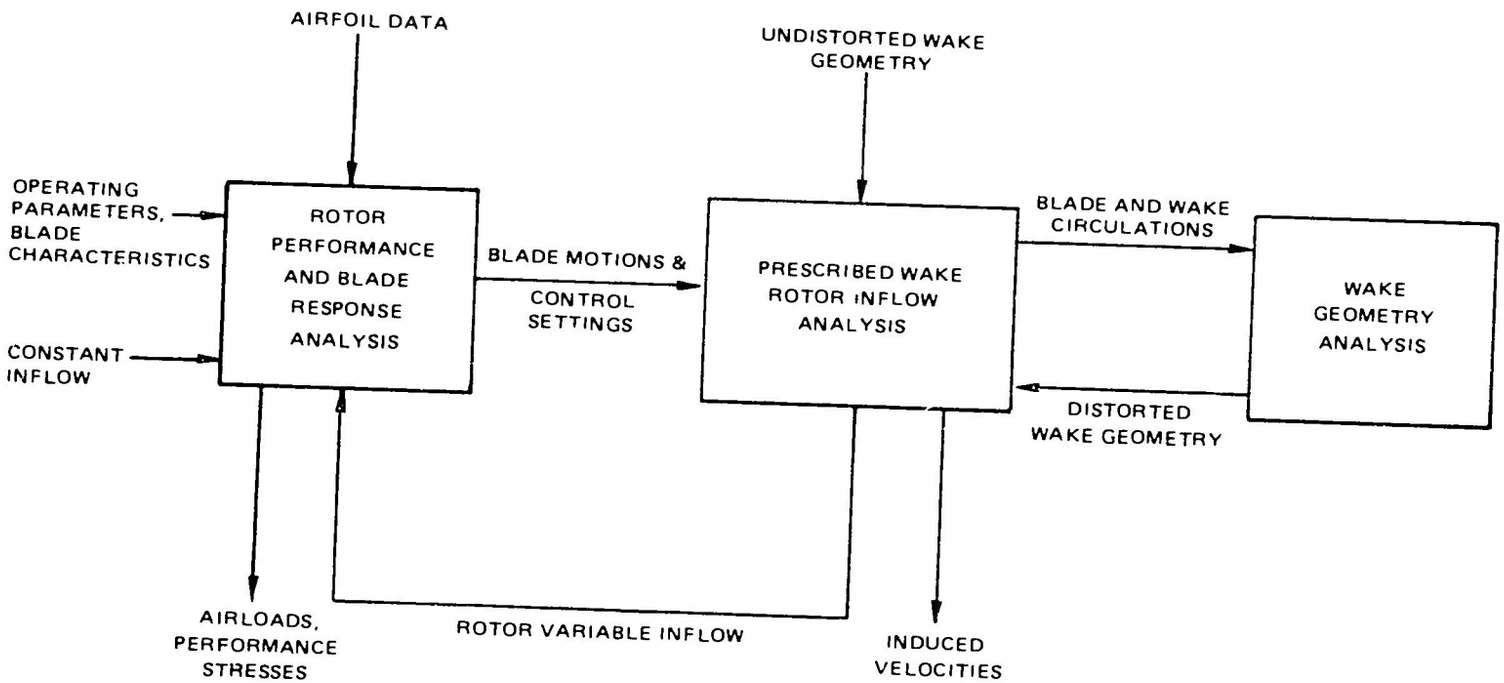

Figure 2. Flow Chart of the UTRC Prescribed Wake Rotor Inflow Analysis as Used in Combination with a Rotor Performance and Blade Response Analysis and a Wake Geometry Analysis.

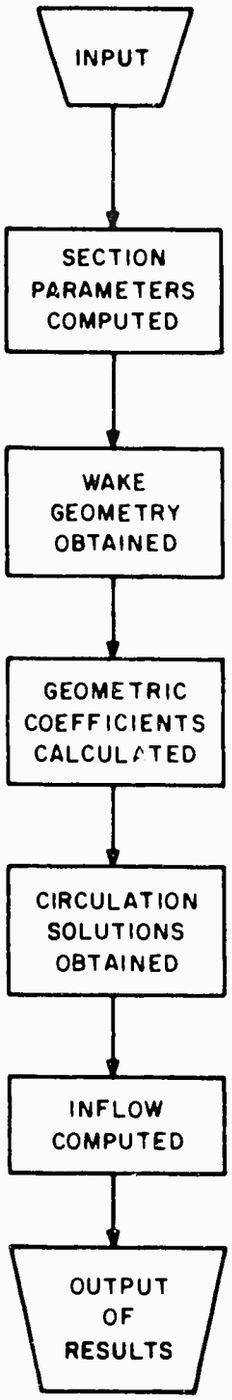

Figure 3. Sequence of Operations for the Prescribed Wake Rotor Inflow Analysis.

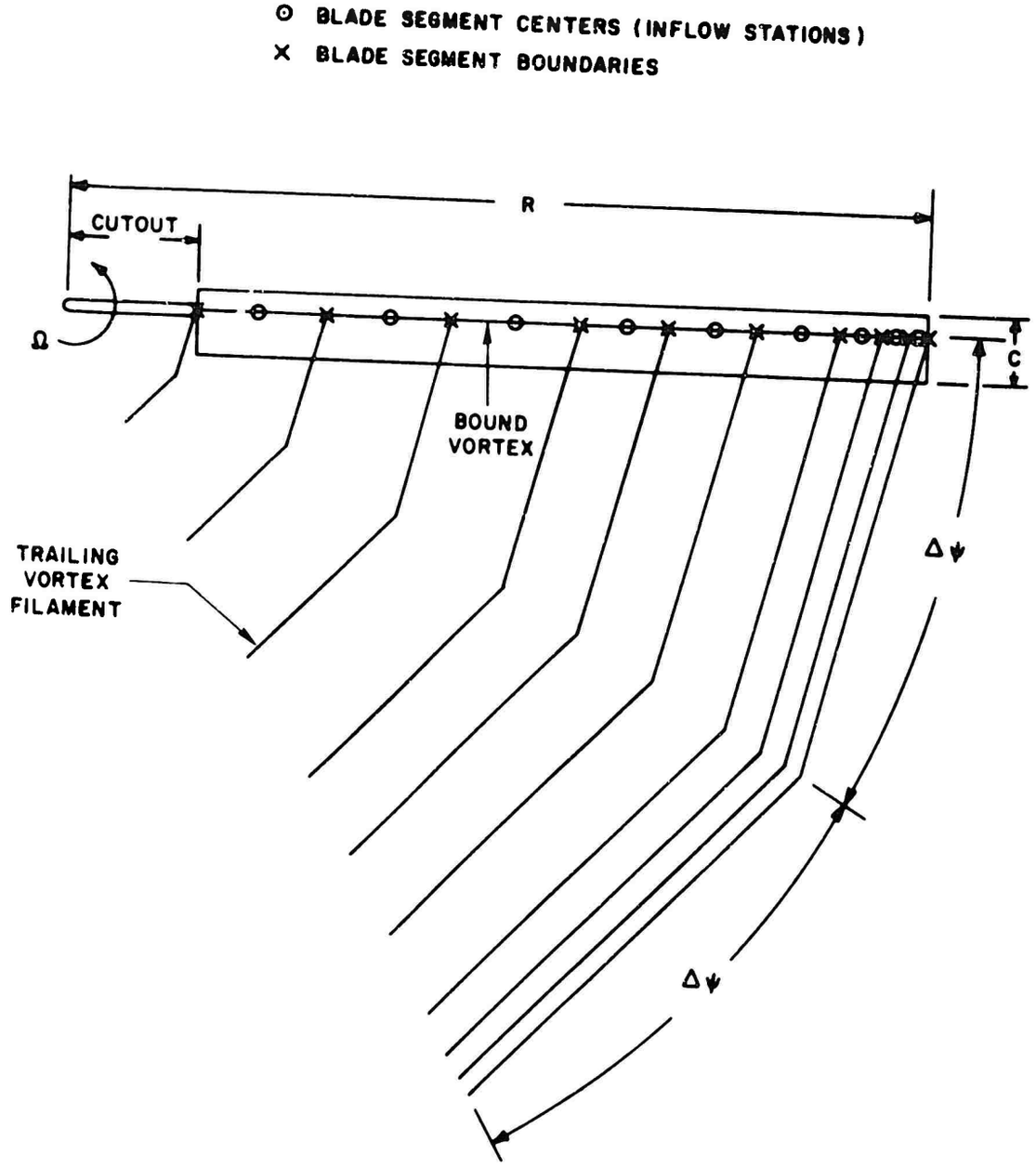

Figure 4. Representation of Blade and Wake by Bound and Trailing Vortex Segments.

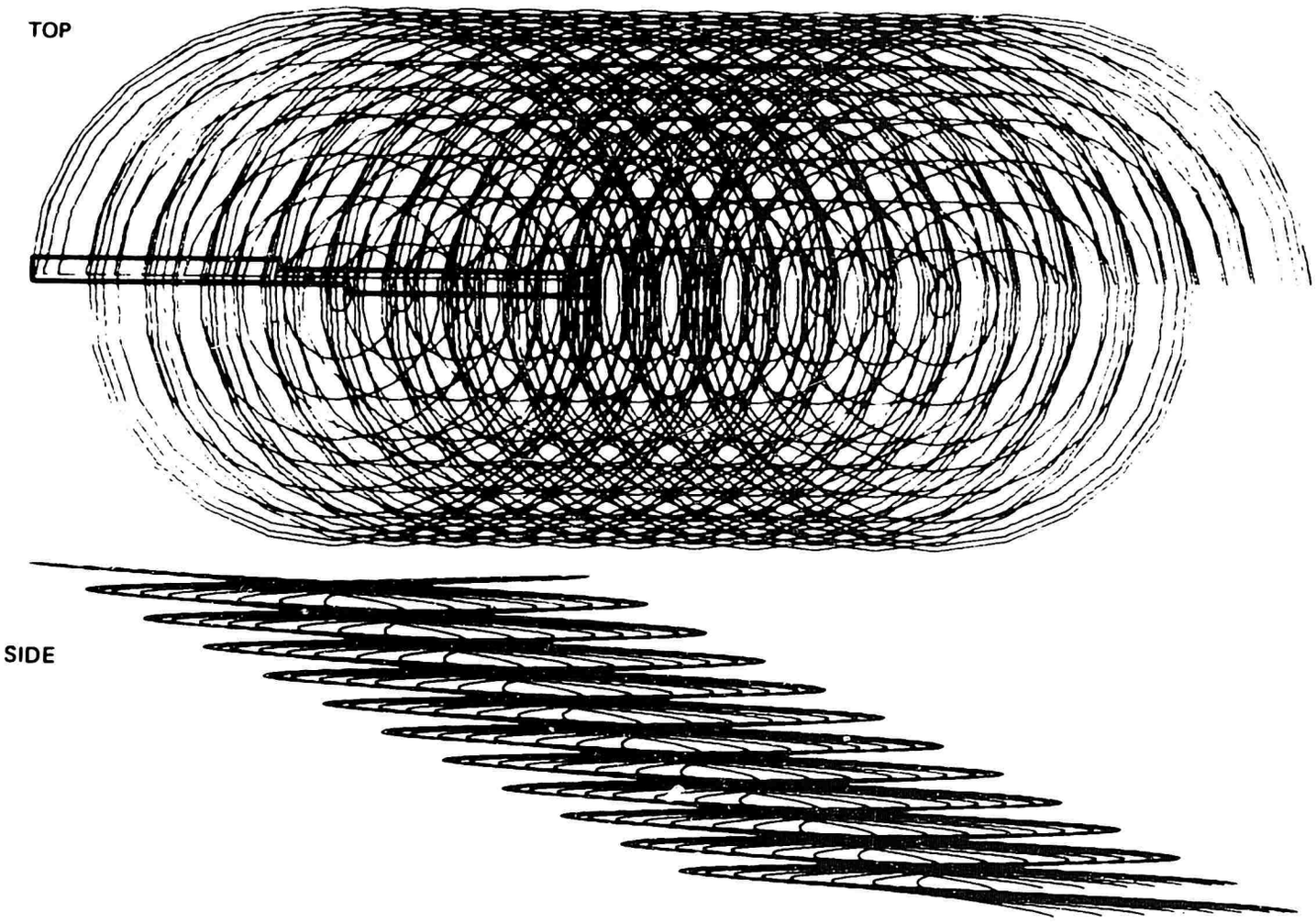

Figure 5. Computer Wake Representation for a Forward Flight Condition -- Classical Wake Model.

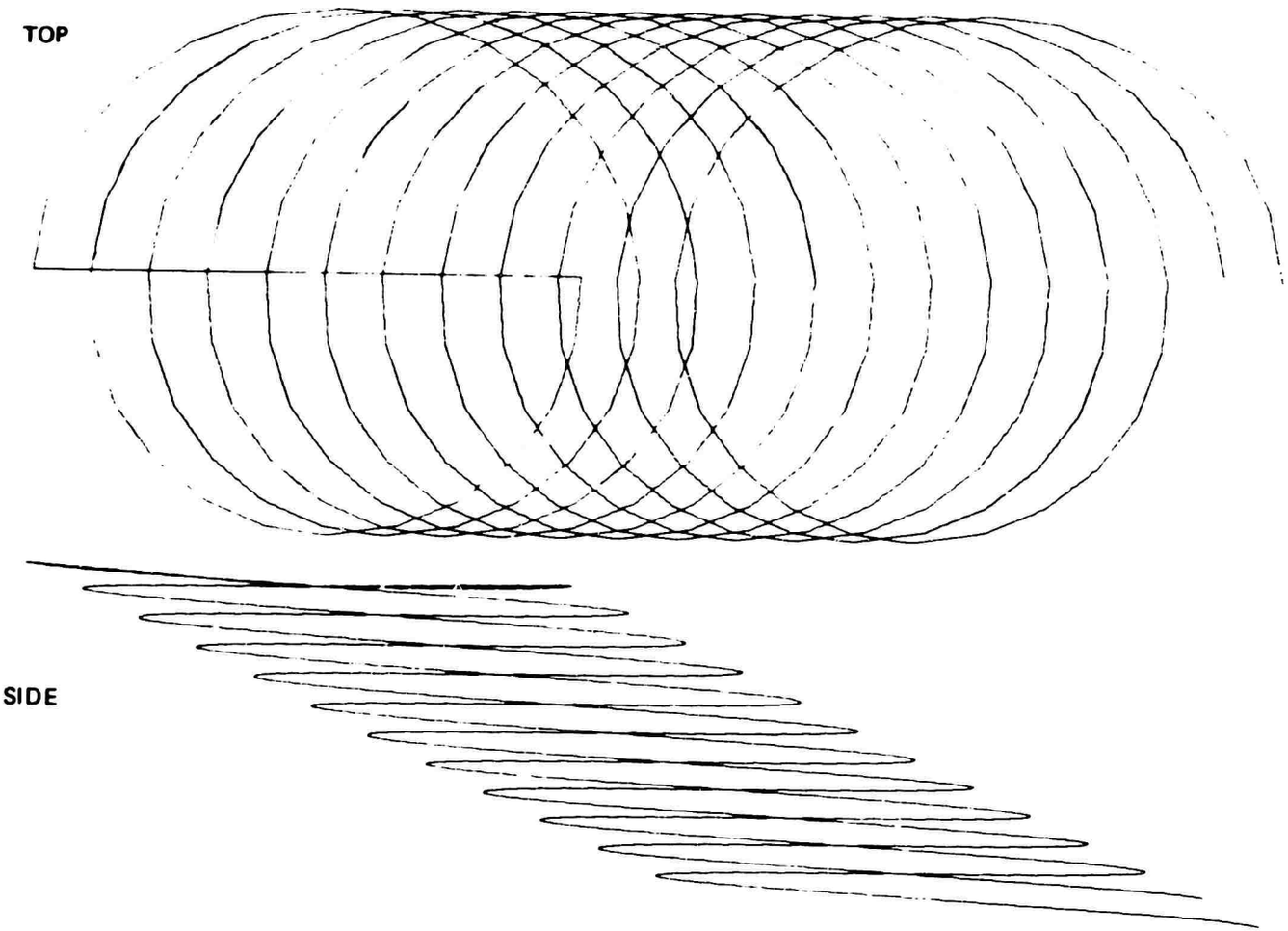

Figure 6. Computer Wake Representation for a Forward Flight Condition -- Undistorted Wake Model, Tip Filaments Only, V = 30 kt.

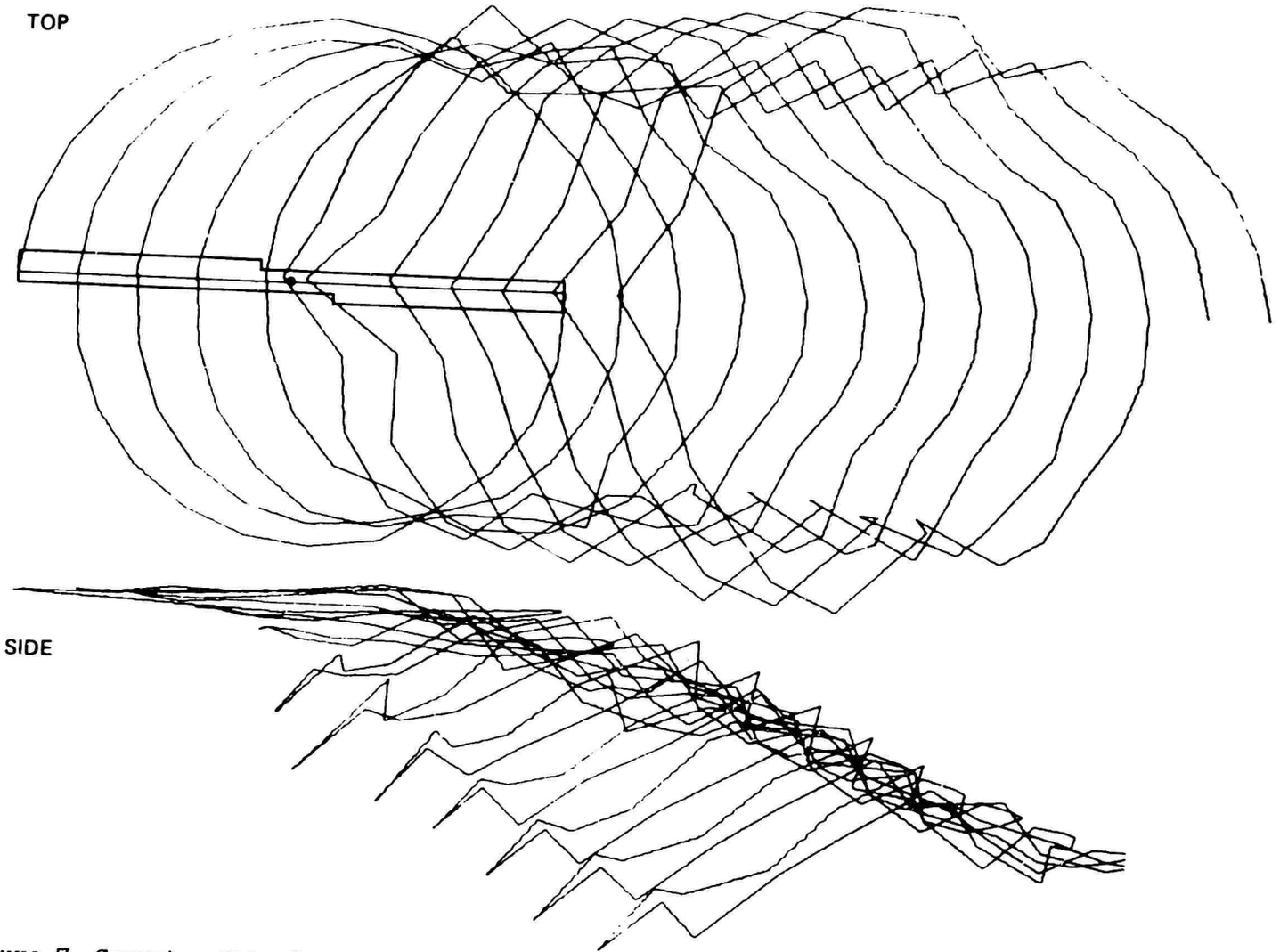

Figure 7. Computer Wake Representation for a Forward Flight Condition -- Distorted Wake Model, Tip Filaments Only, V = 30 kt.

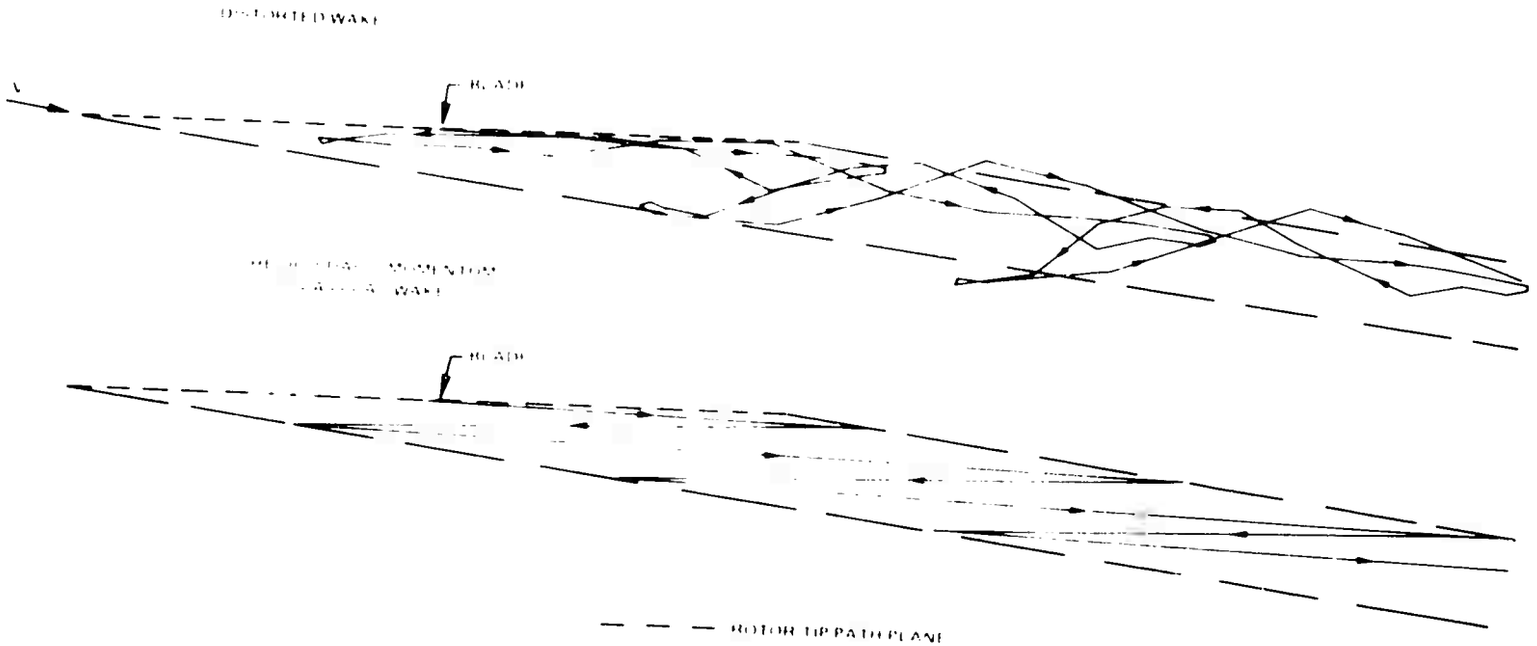

Figure 8. Comparison of Analytical Distorted and Undistorted Wake--
Side View of Tip Filament of One Blade, $\mu = 0.14$.

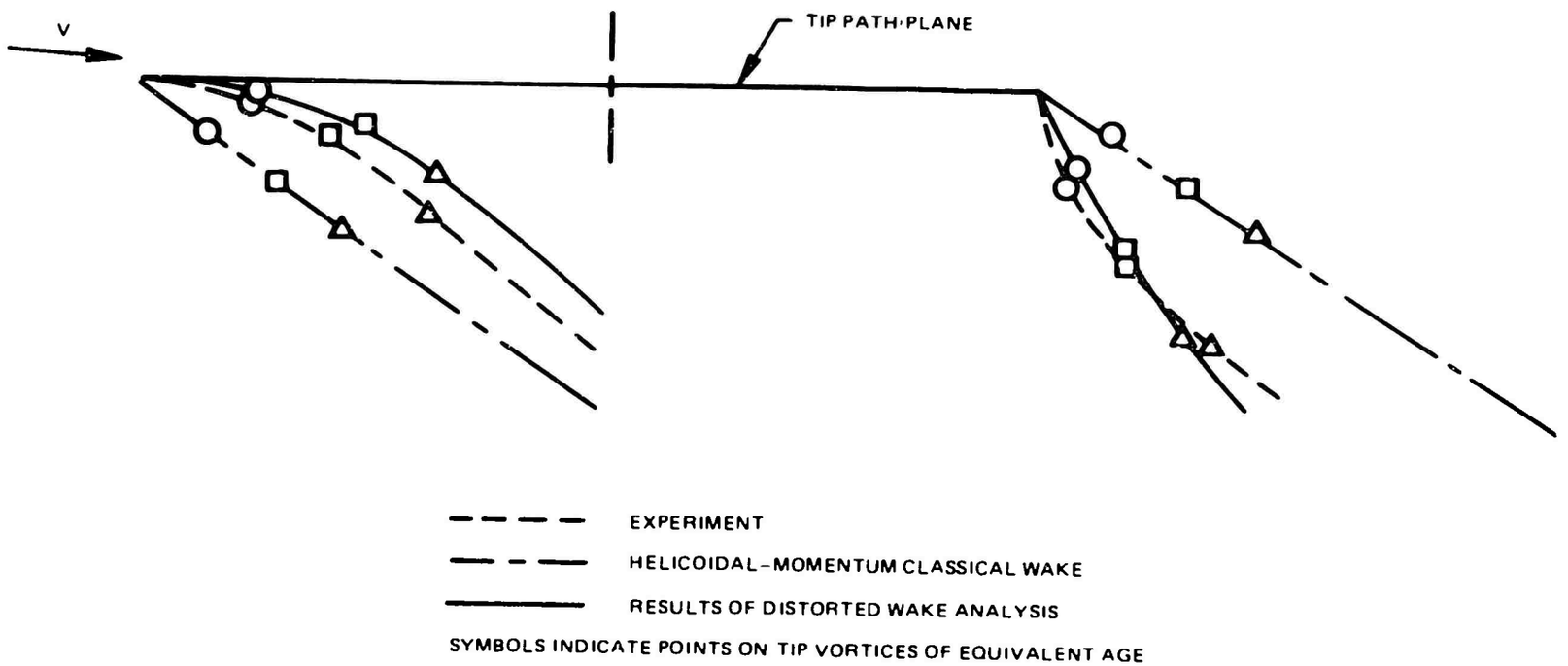

Figure 9. Comparison of Analytical and Experimental Rotor Wake Boundaries -- $\mu = 0.05$.

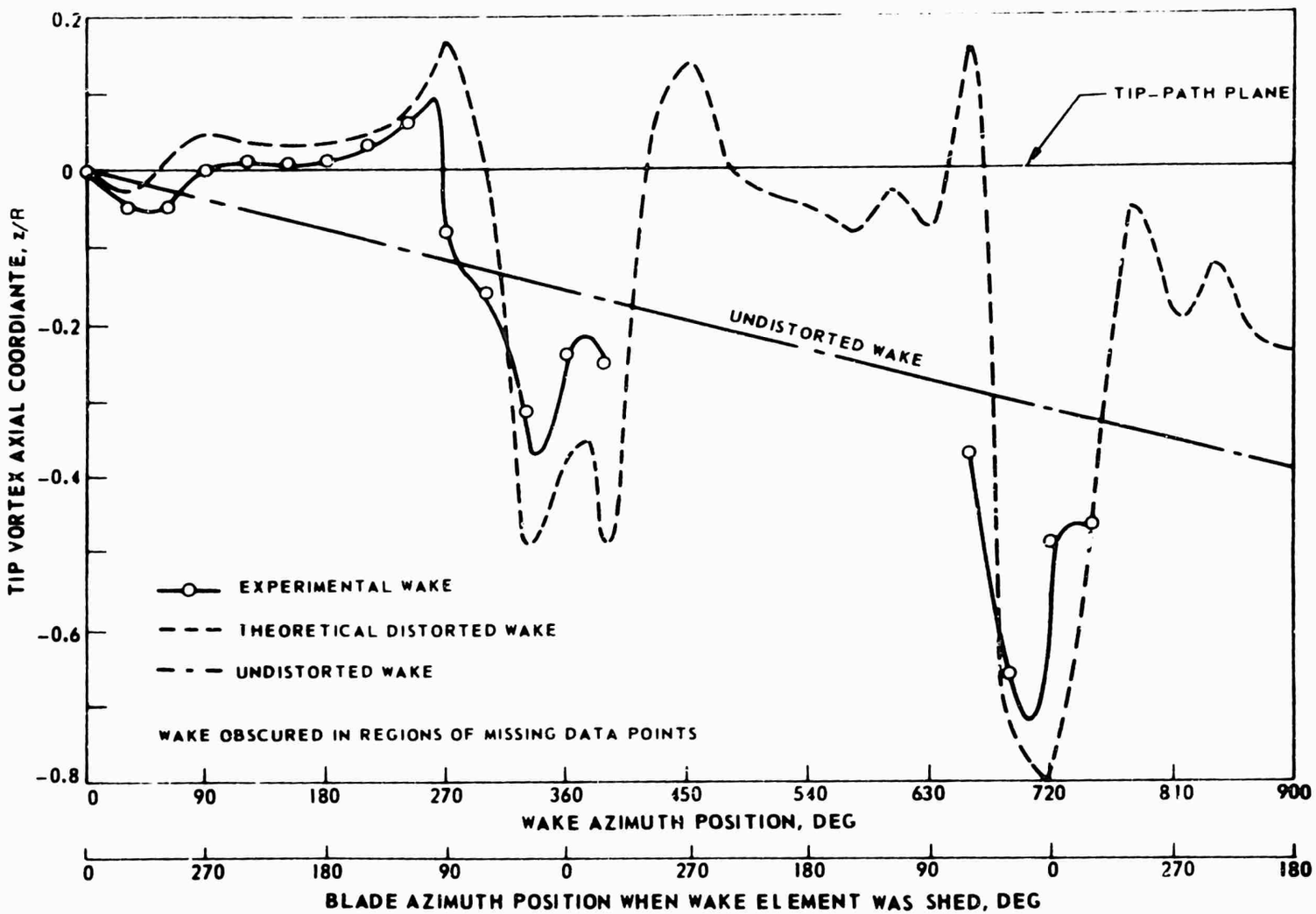

Figure 10. Comparison of Analytical and Experimental Tip Vortex Axial Coordinates -- Model Rotor, Simulated 35 kt and 10,000-lb lift.

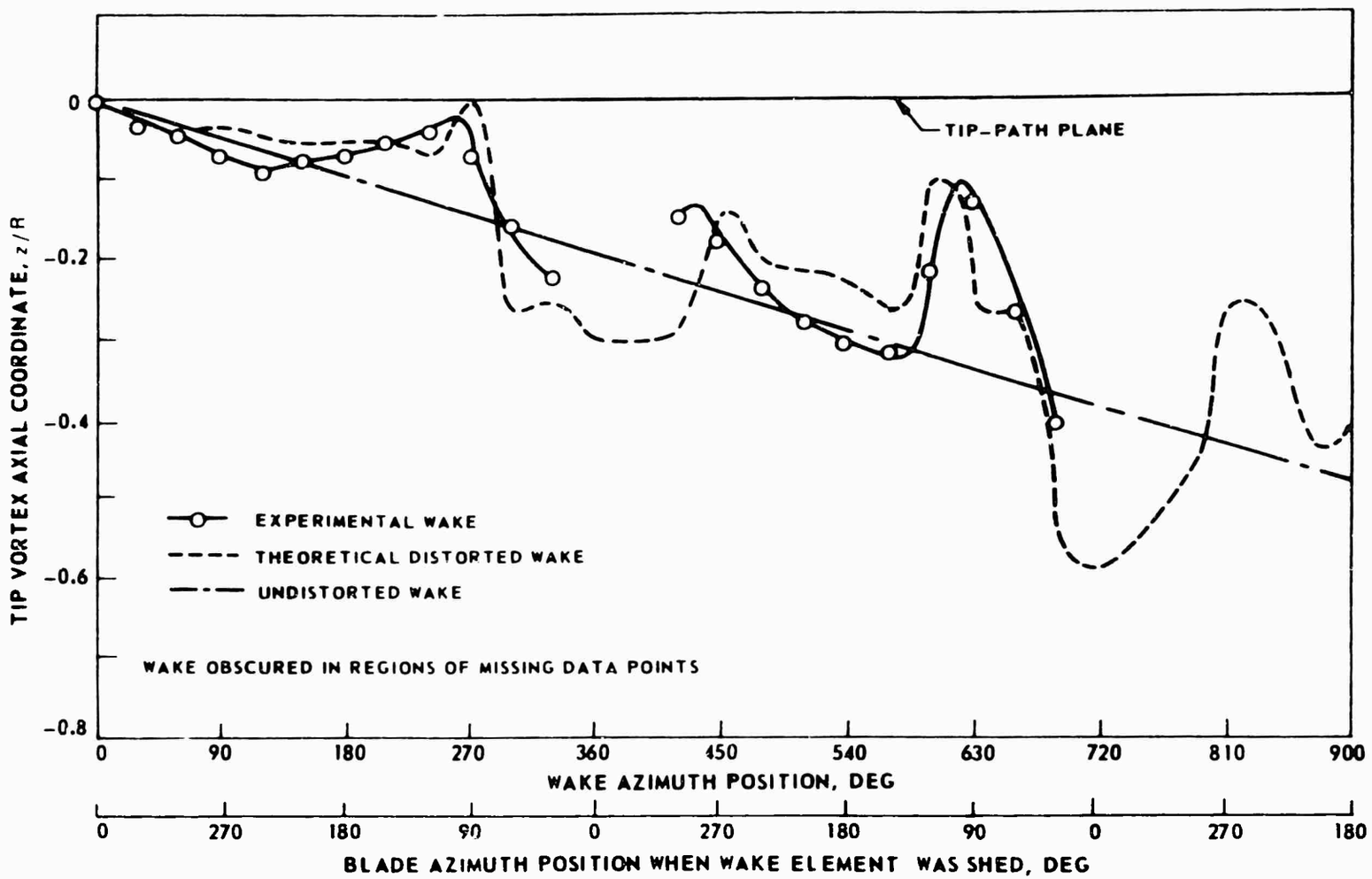

Figure 11. Comparison of Analytical and Experimental Tip Vortex Axial Coordinates -- Model Rotor, Simulated 90 kt and 10,000 lb lift.

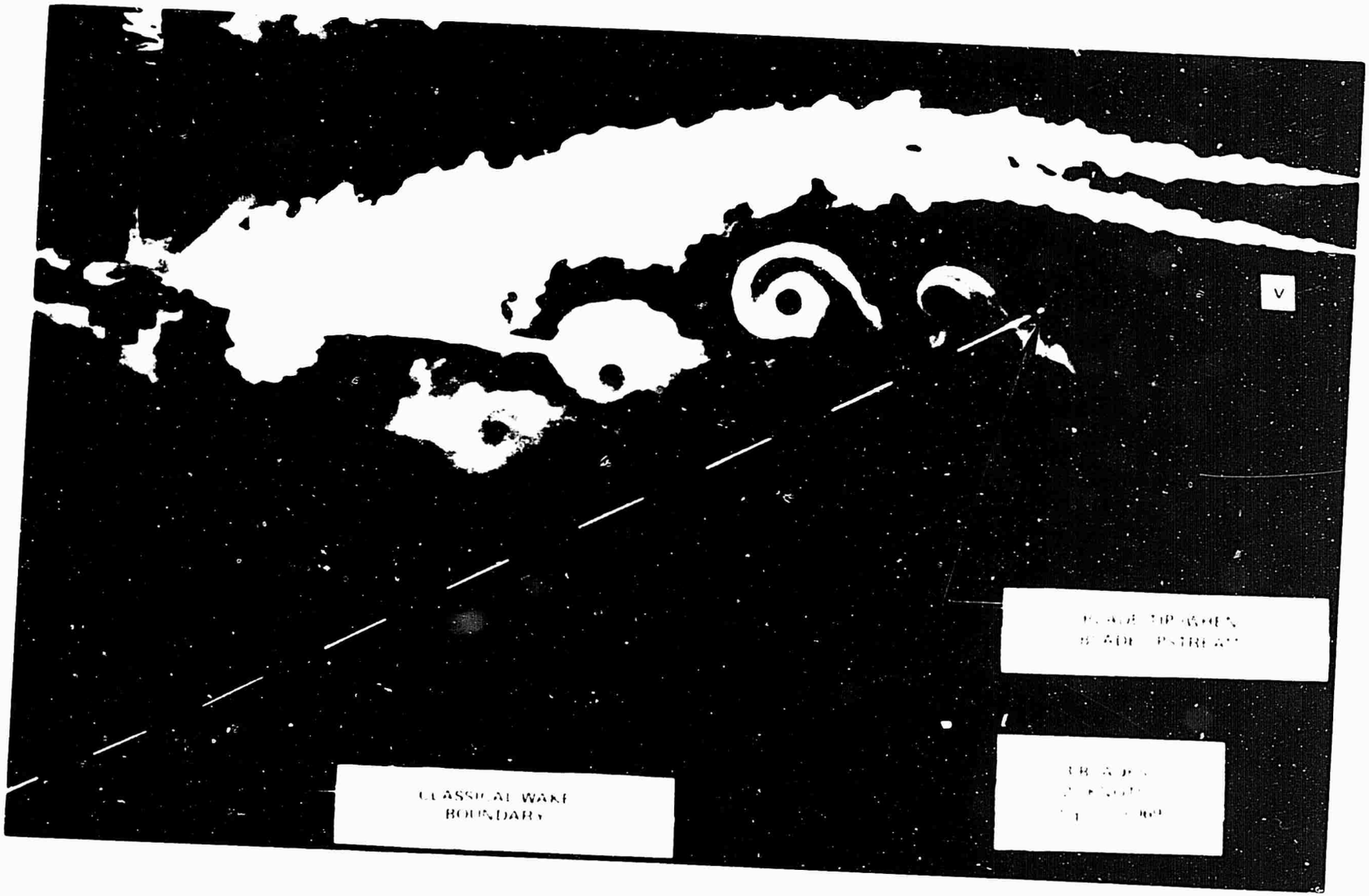

Figure 12. Flow Visualization Photograph of Forward Wake Boundary of Model Rotor .

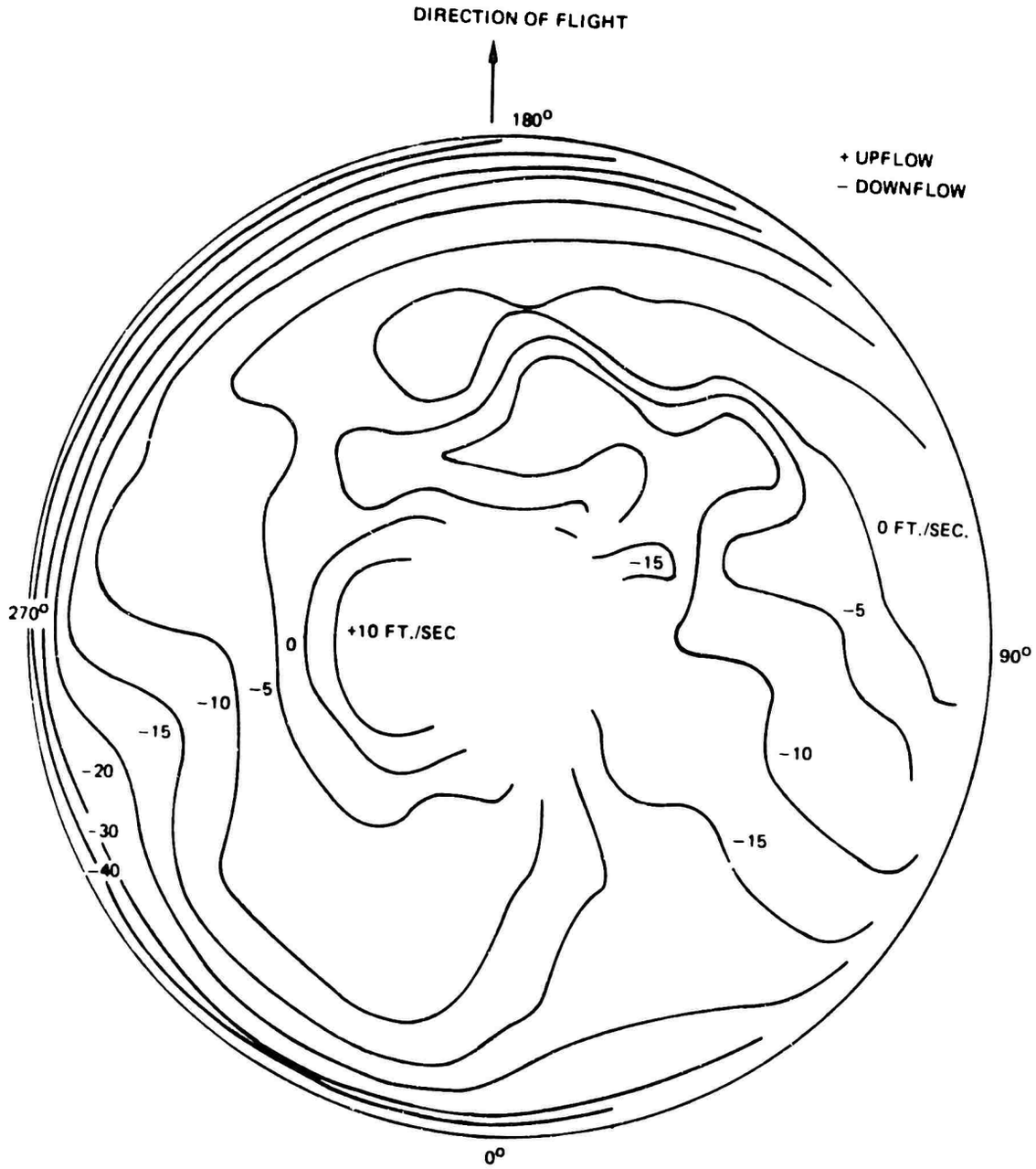

Figure 13. Calculated Induced Velocity Distribution Based on a Classical Wake Representation--H-34, 112 kt.

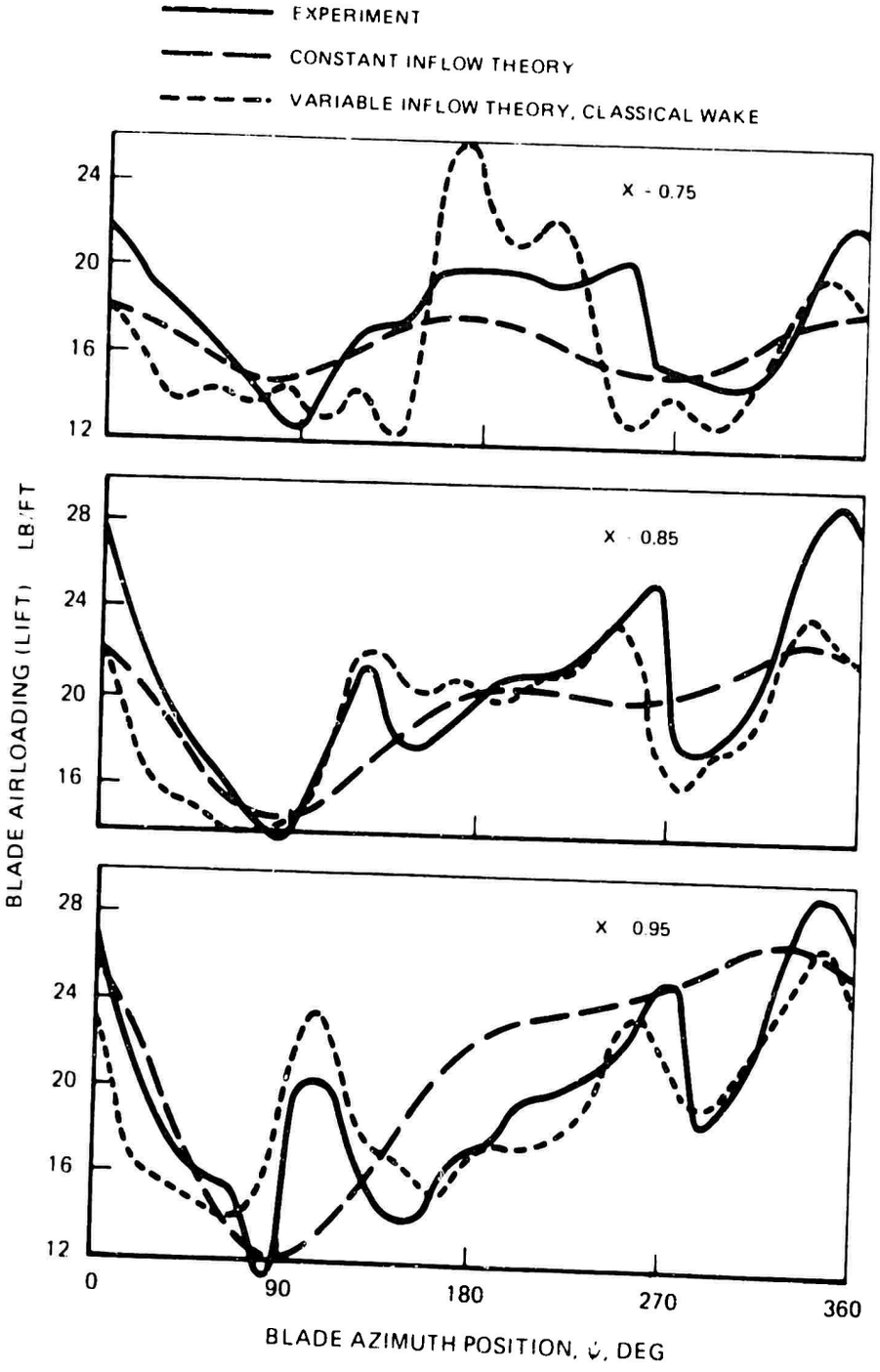

Figure 14. Comparison of Analytical and Experimental Blade Airloads--H-34, 70 kt.

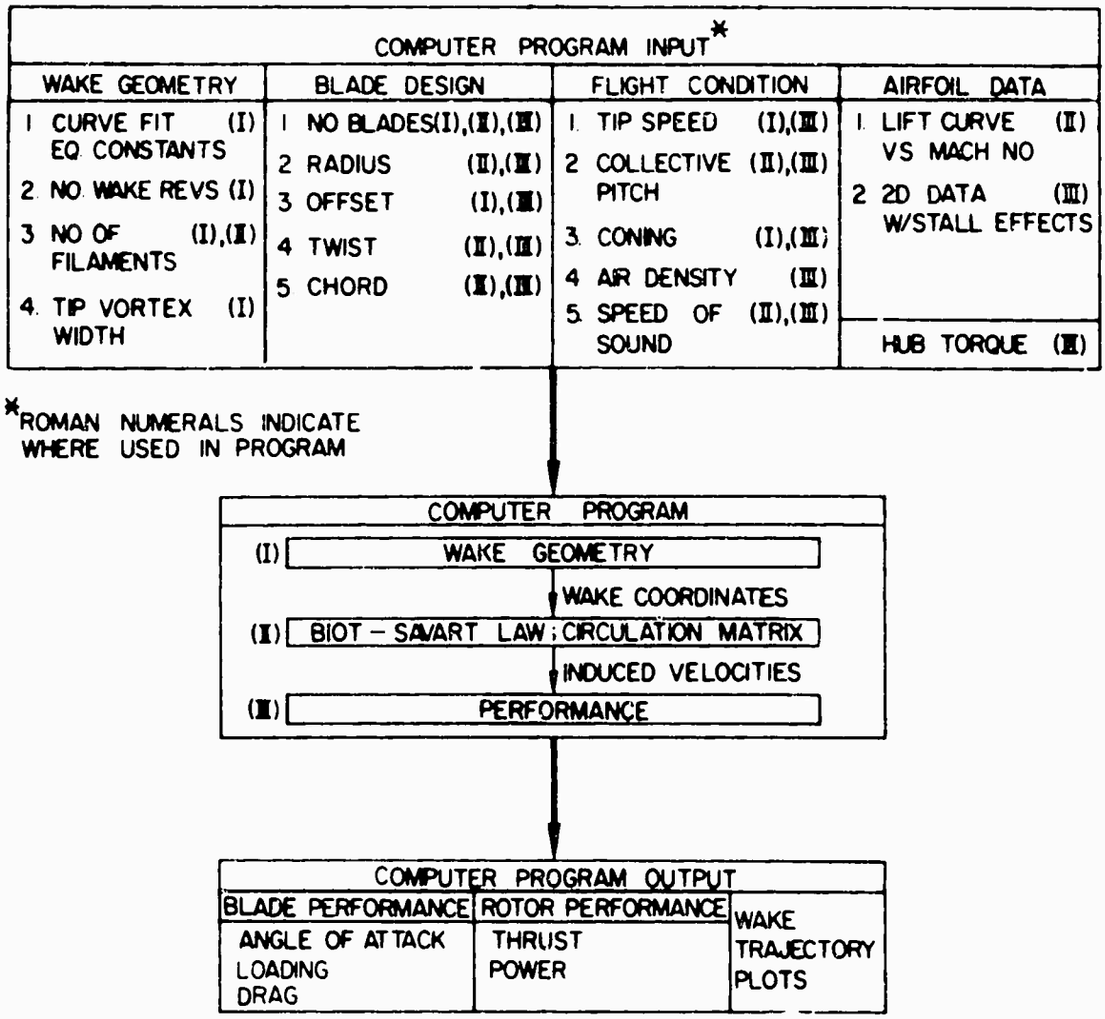

Figure 15. Flow Chart of the UTRC Prescribed Wake Hover Performance Analysis.

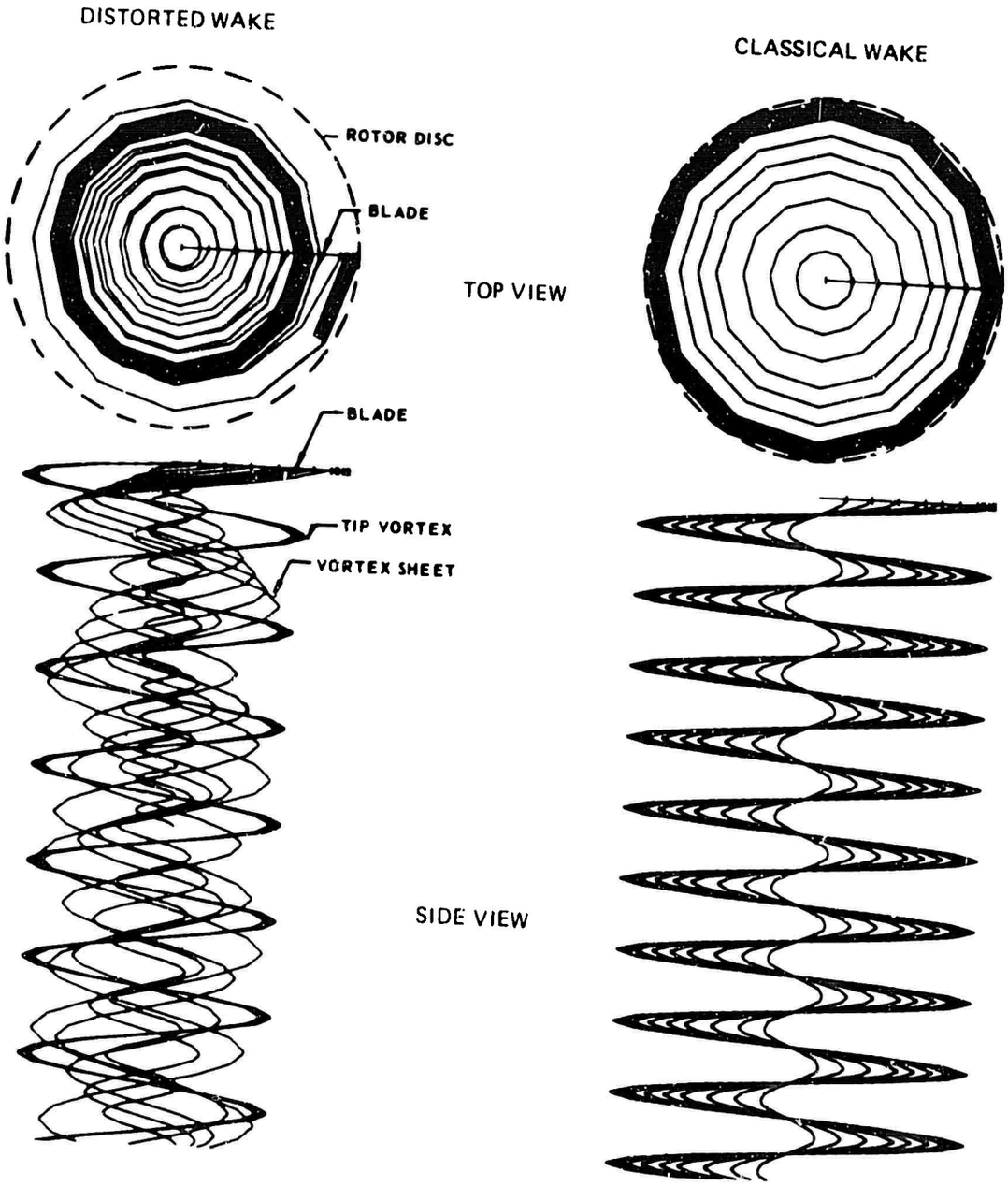

Figure 16. Computer Wake Representations for One Blade of a Hovering Rotor--Classical and Distorted Wake Models.

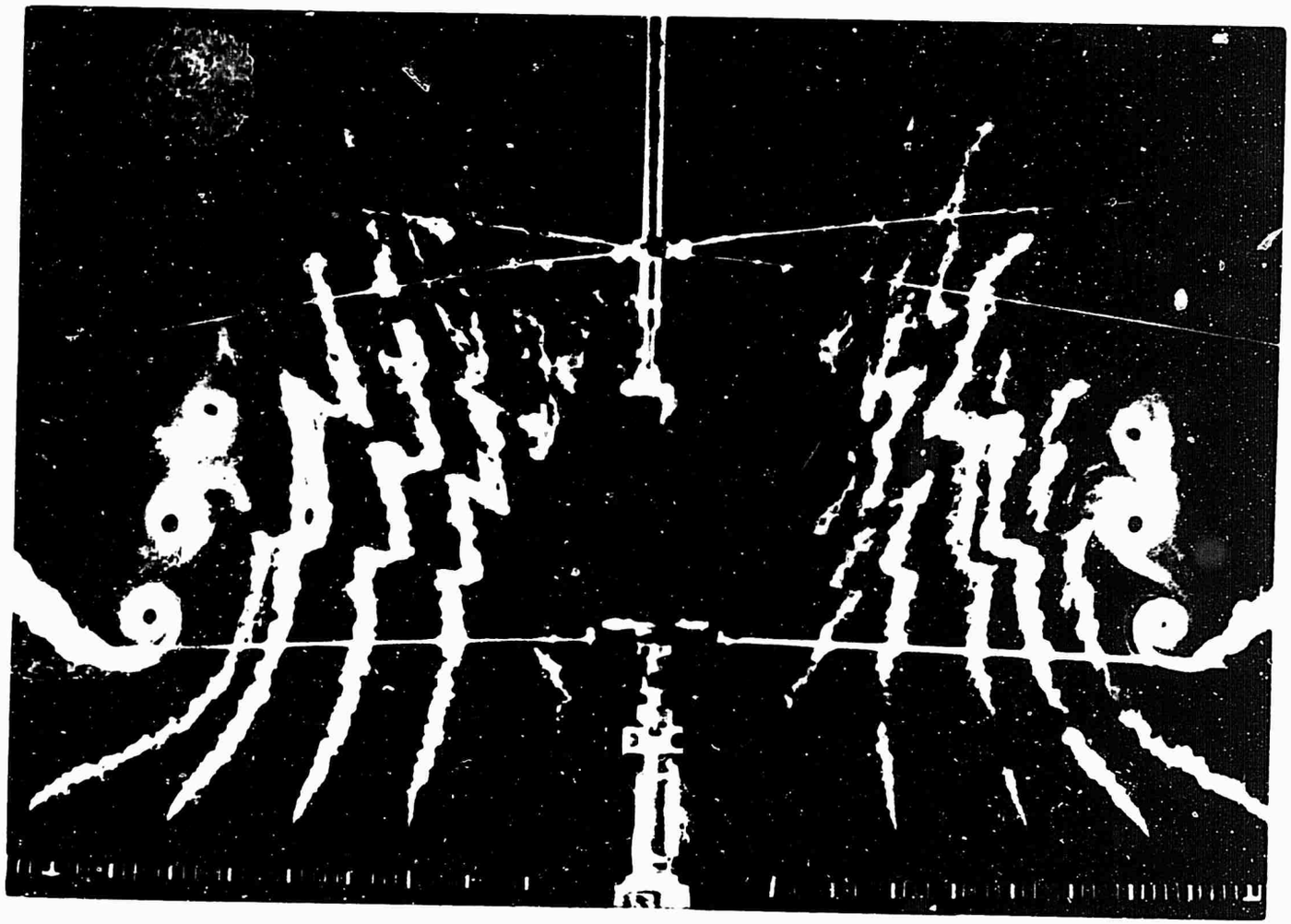

(a) Smoke Flow Visualization

Figure 17. Sample Flow Visualization Photographs for a Hovering Model Rotor .

(b) Schlieren Tip Vortex Visualization

Figure 17. Concluded

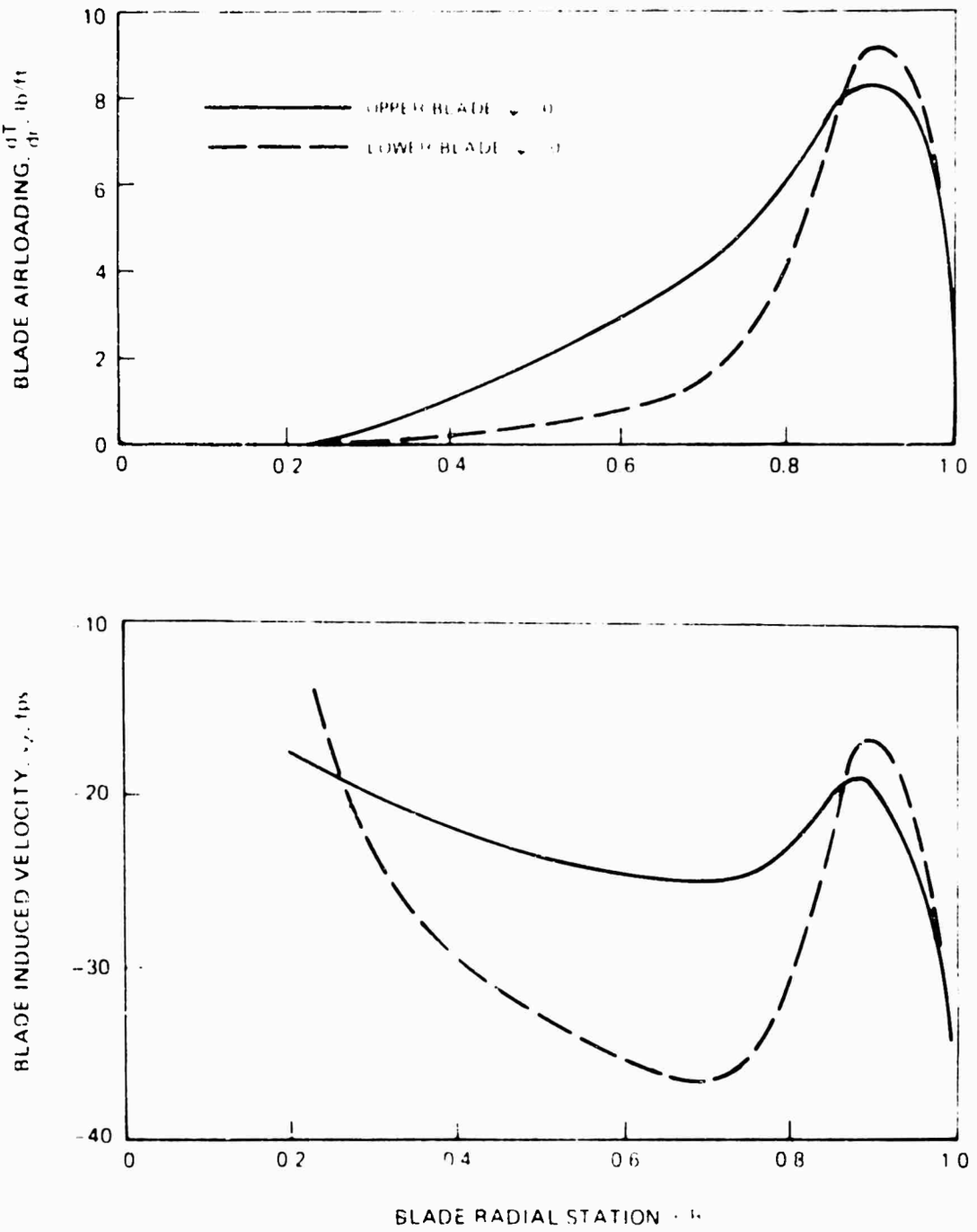
BLADE AIRLOADING, $\frac{dT}{dr}$, lb/ft
10
8
6
4
2
0
0
0.2
0.4
0.6
0.8
1.0
BLADE INDUCED VELOCITY, v, fps
-10
-20
-30
-40
0
0.2
0.4
0.6
0.8
1.0
BLADE RADIAL STATION, r

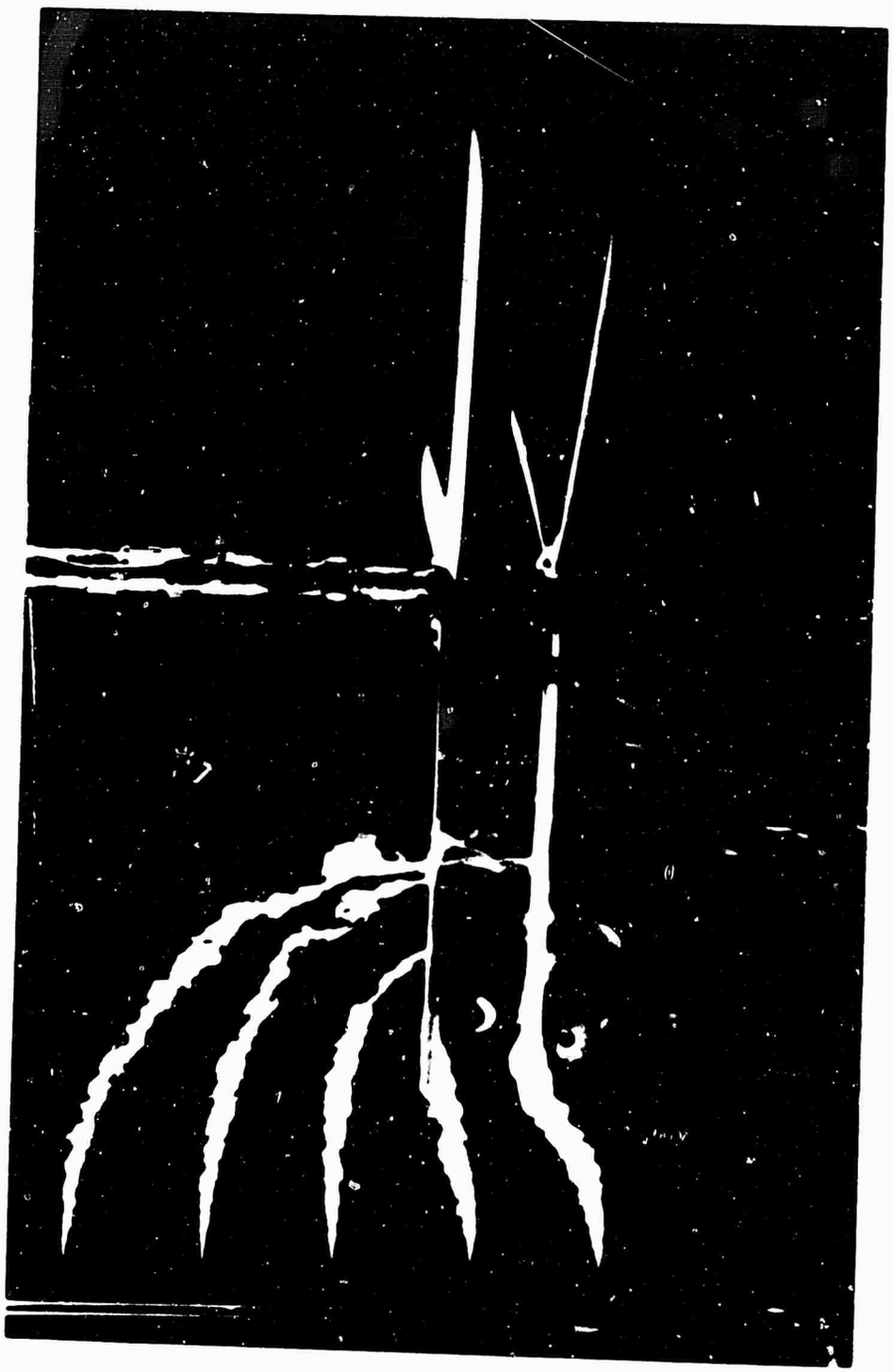

Figure 19. Flow Visualization Photograph -- Model Coaxial Counter - Rotating Rotor .

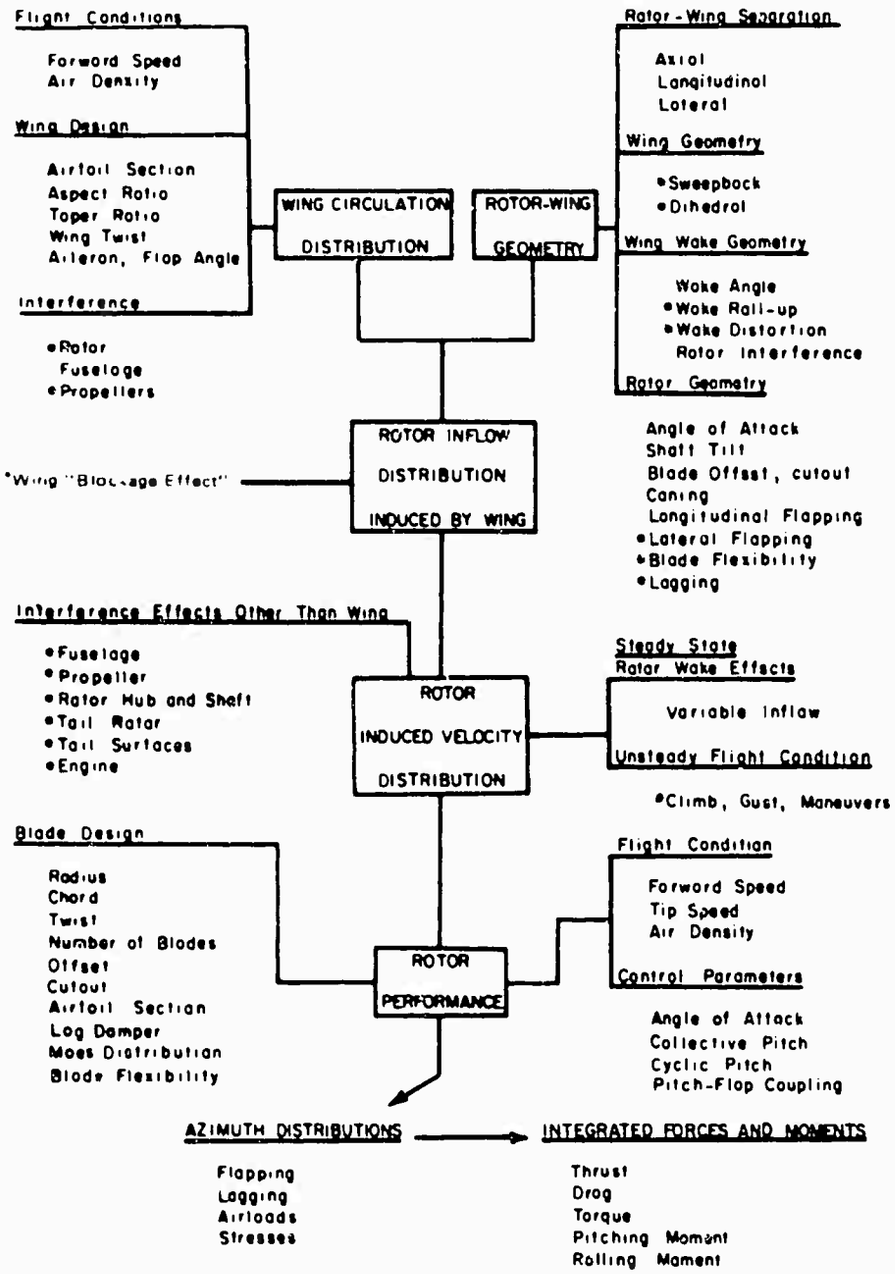

Figure 20. Parameters for Wing Induced Aerodynamic Interference at a Rotor .

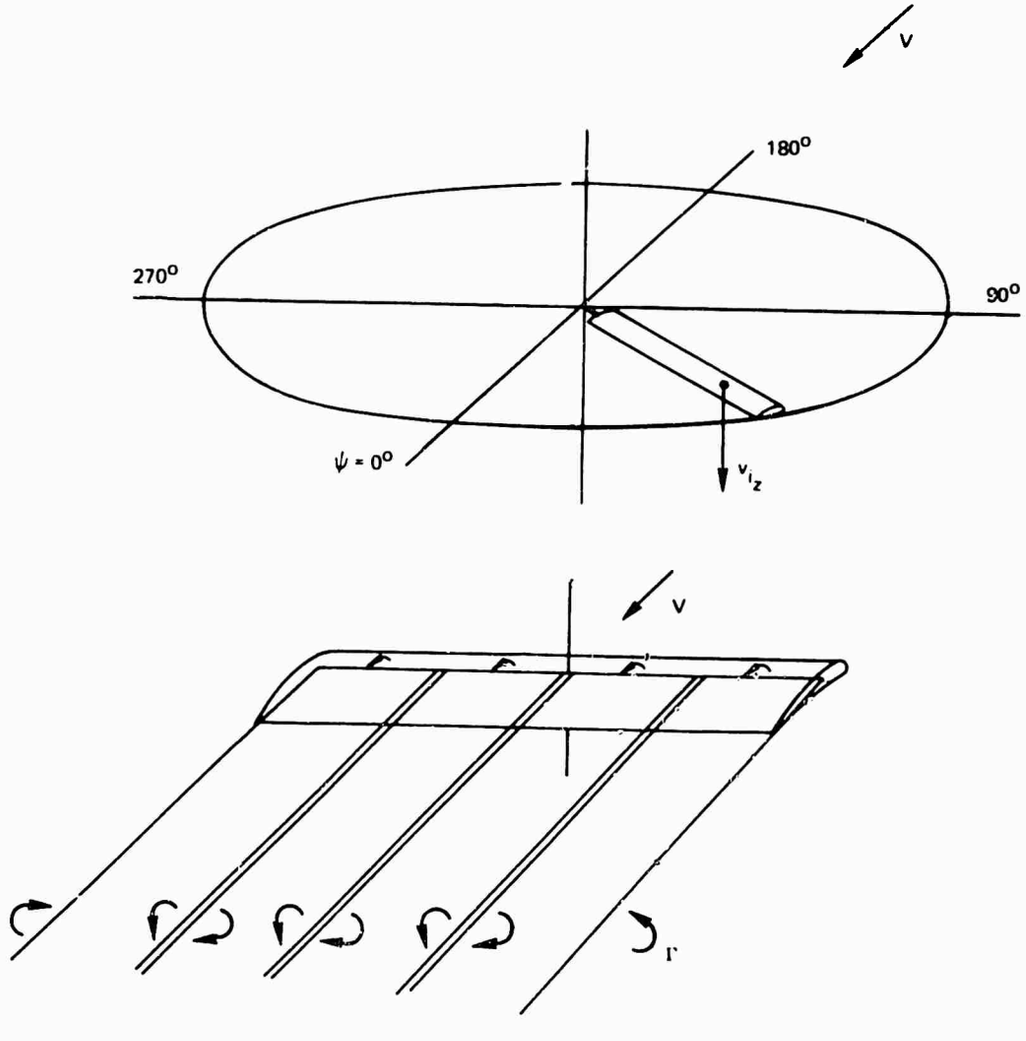

Figure 21. Wing Wake Representation for Wing/Rotor Interference.

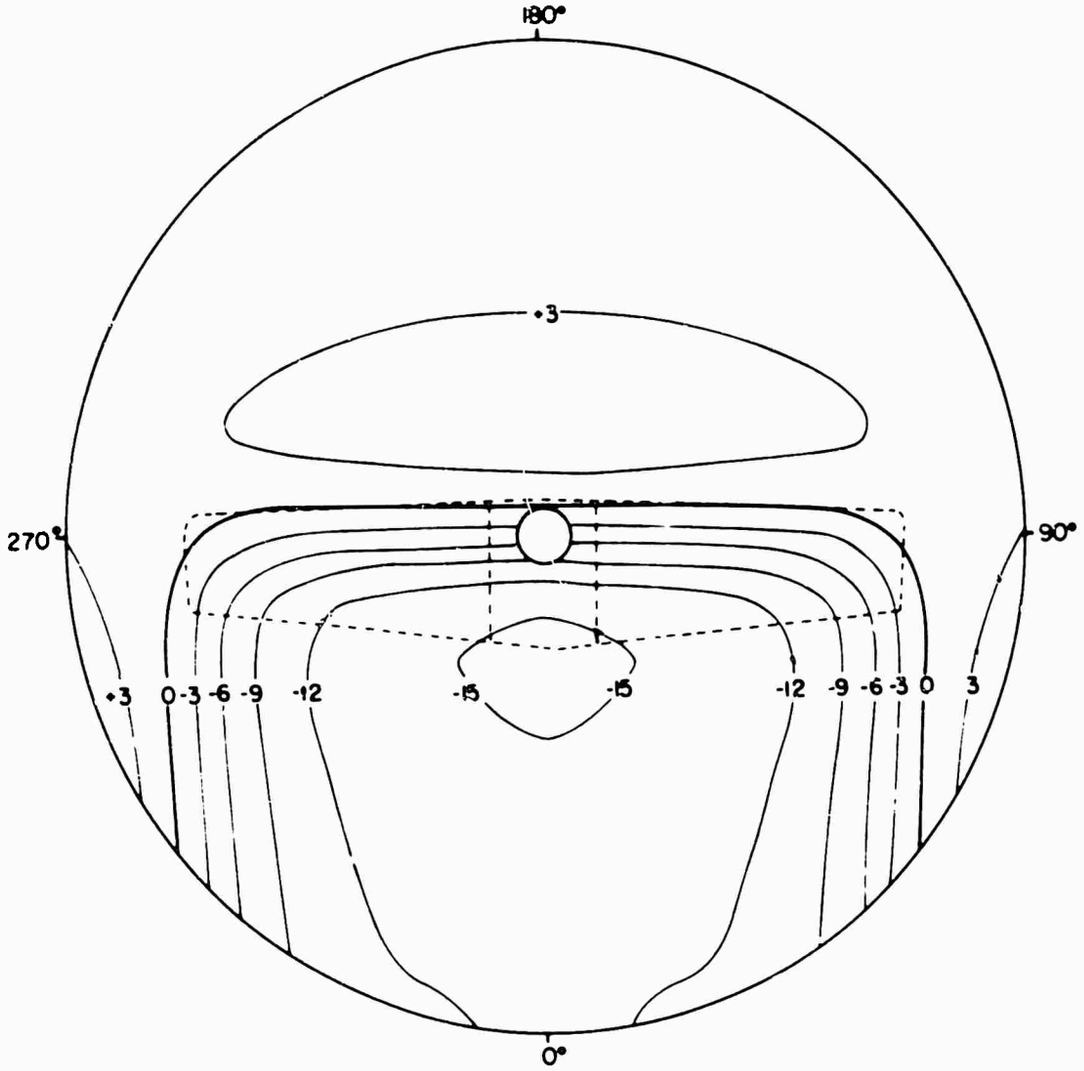

Figure 22. Analytical Normal Velocity Component Induced by Wing at Rotor.

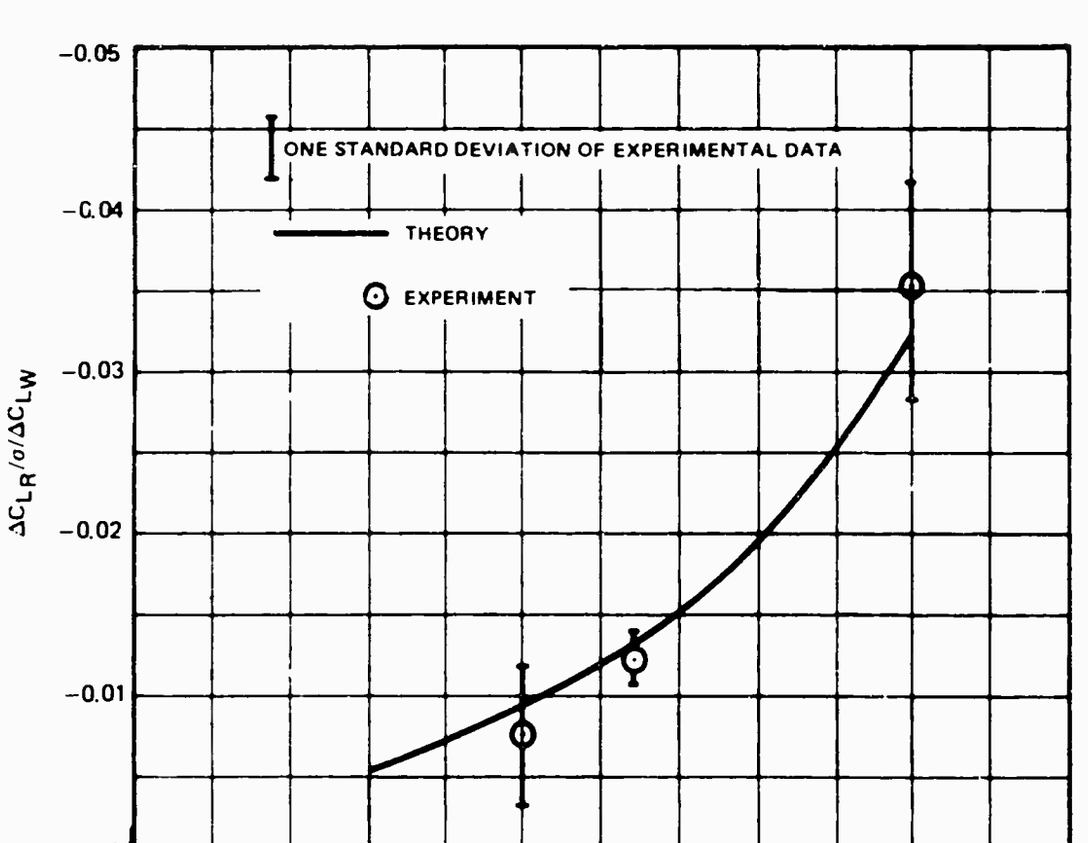

Figure 23. Comparison of Predicted and Measured Effect of Wing Interference on Rotor Lift.

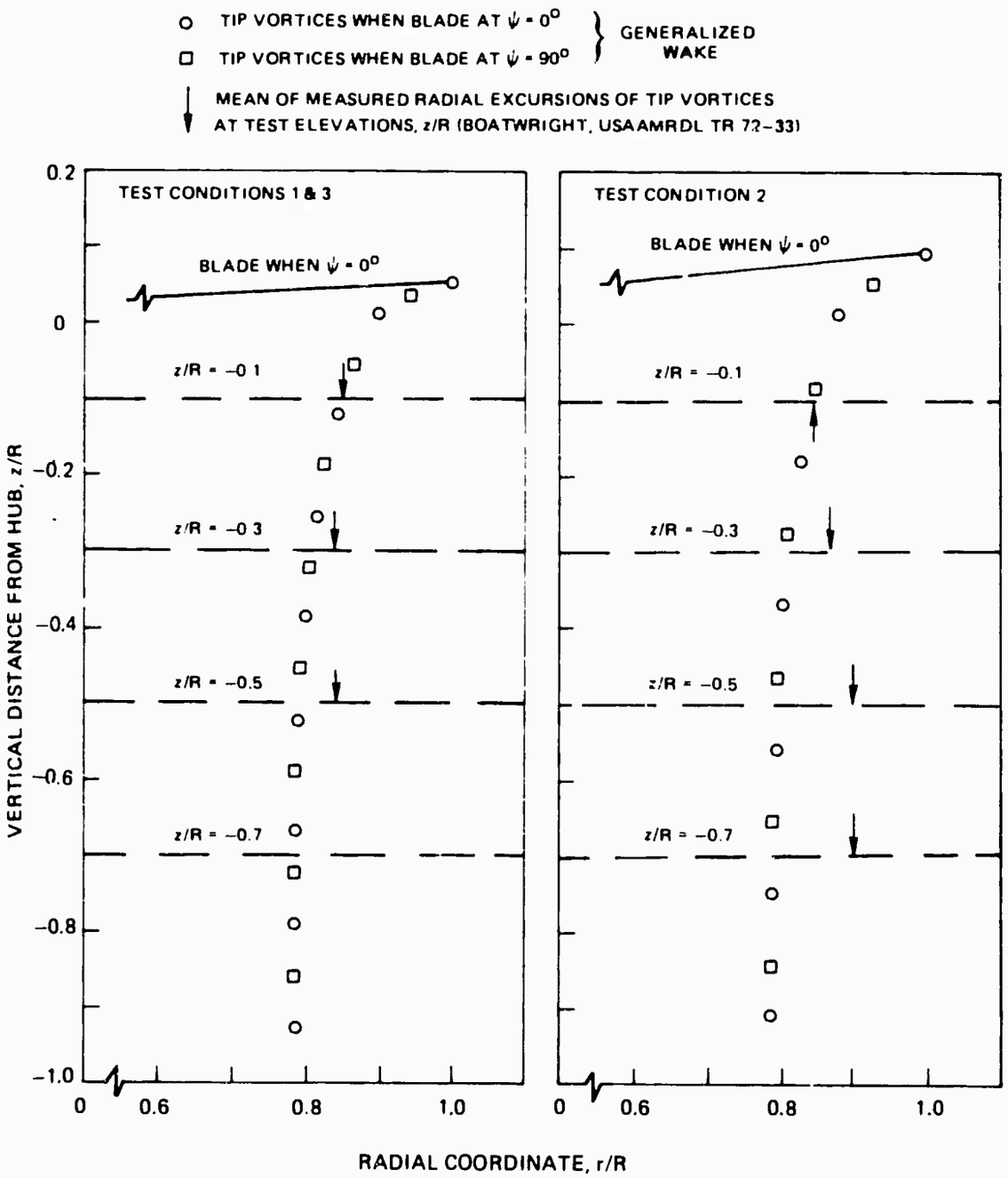

Figure 24. Tip Vortex Positions for the Three Test Conditions of Boatwright, USAAMRDL TR 72-33, $\mu = 0$.

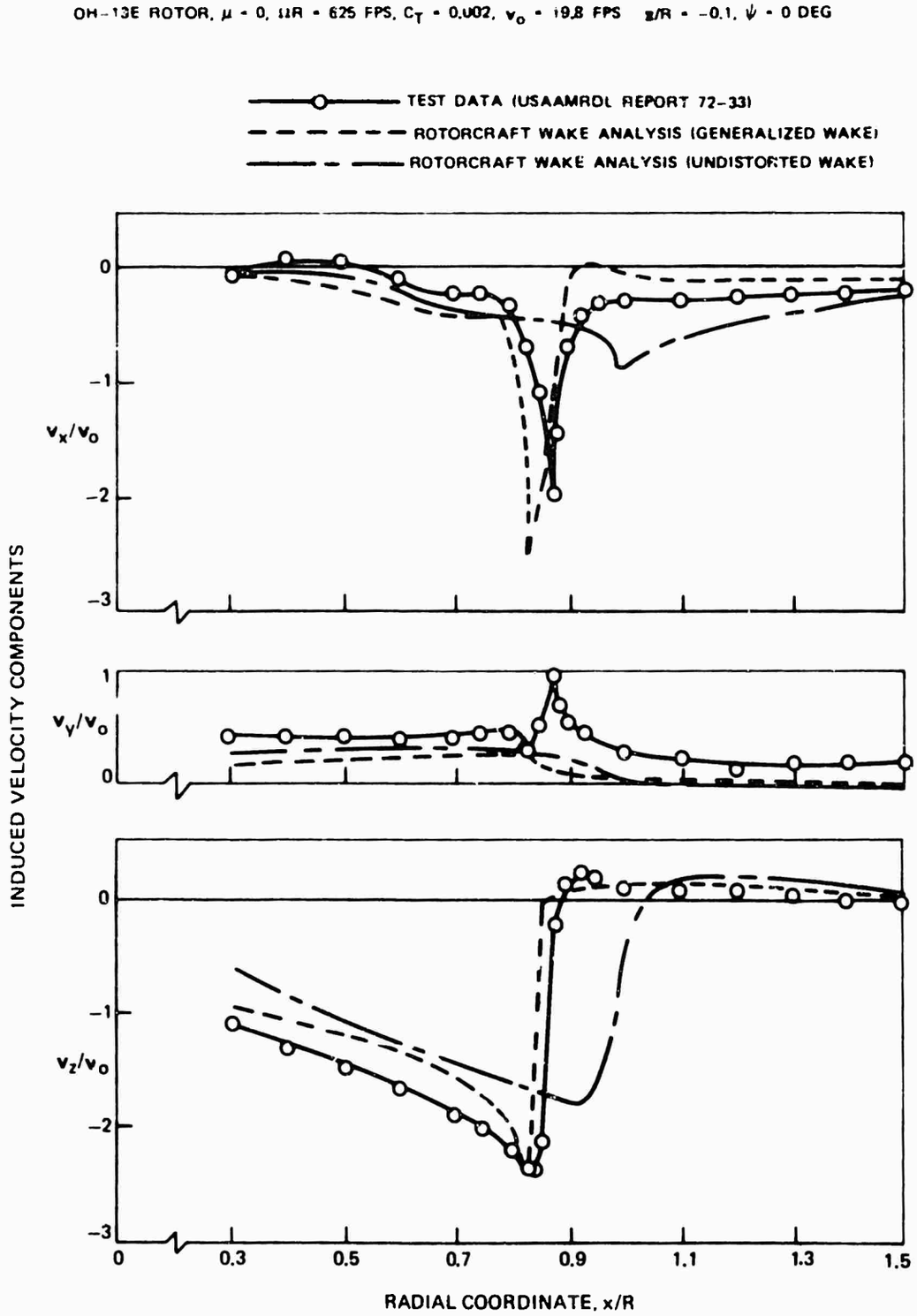

Figure 25. Comparison of Instantaneous Induced Velocity Components--Boatwright, USAAMRDL TR 72-33, $\mu = 0$, Test Condition 1, $z/R = -0.1$, $\psi = 90$ deg.

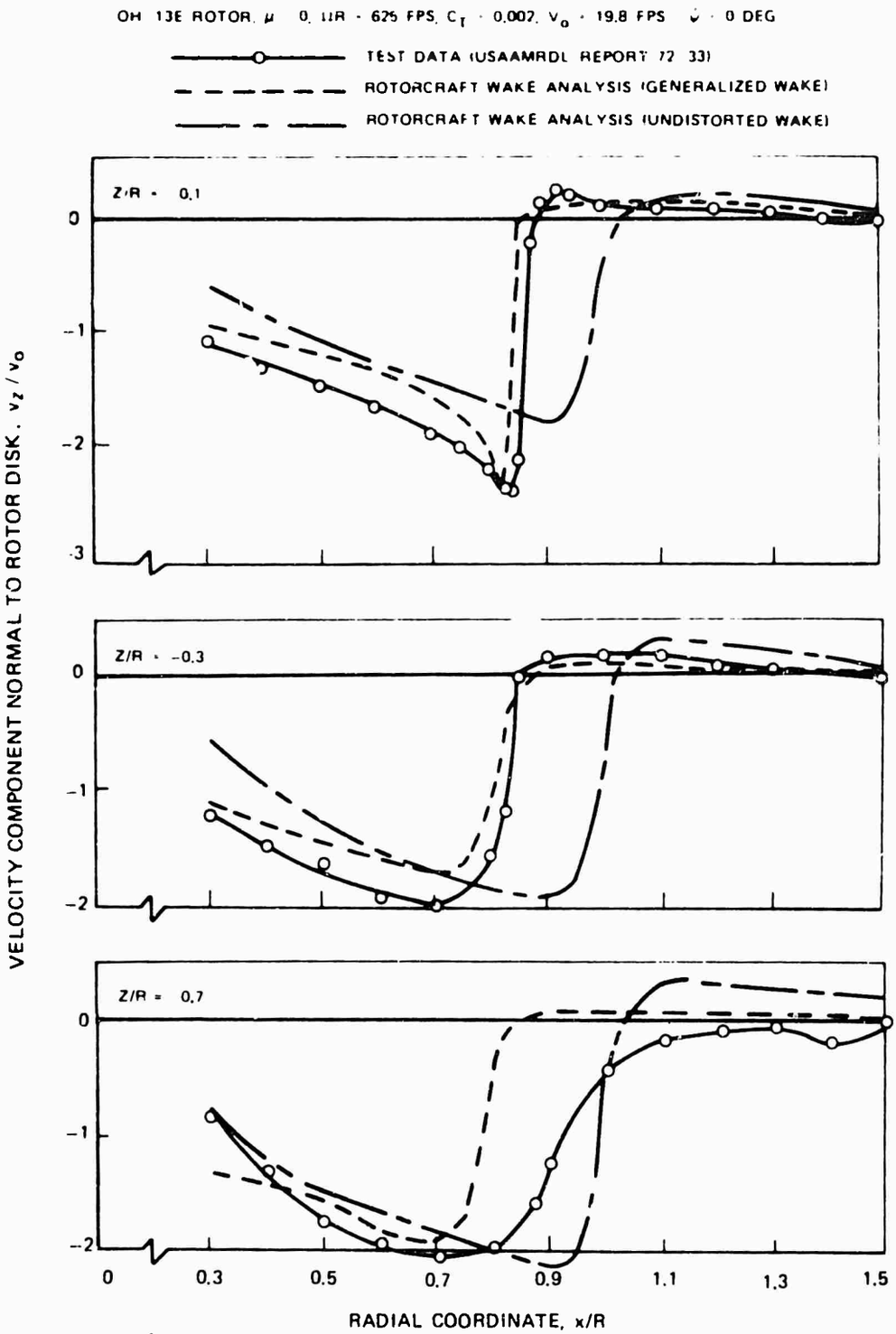

Figure 26. Comparison of Instantaneous Normal Component of Induced Velocity at Several Distances from Rotor--Boatwright, USAAMRDL 72-33; $\mu = 0$, Test Condition 1, $\psi = 0$ deg.

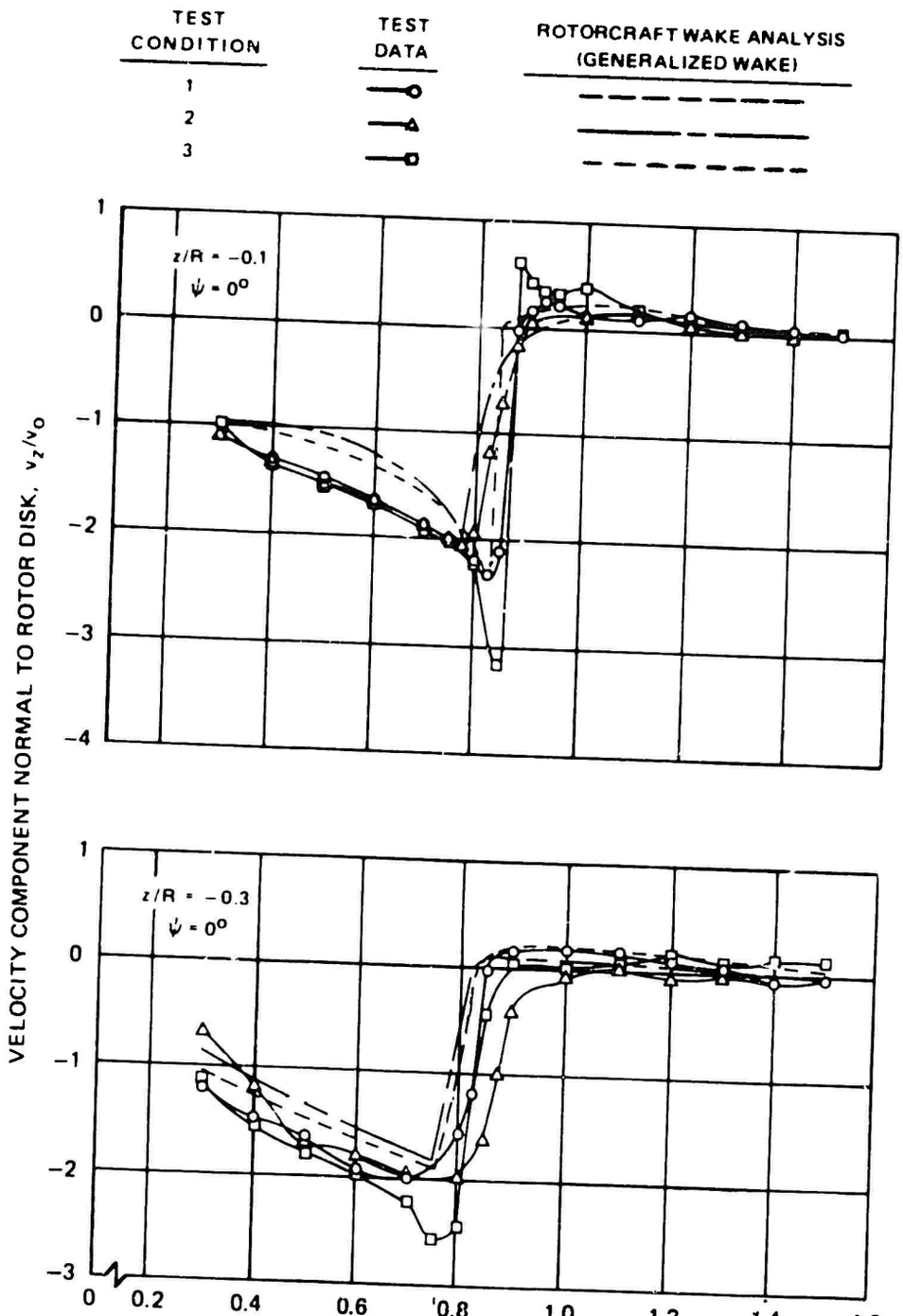

Figure 27. Comparison of Radial Distributions of Instantaneous Normal Velocity Component for Three Rotor Test Conditions-- Boatwright, USAAMRDL TR 72-33, $\mu = 0, \psi = 0$ deg.

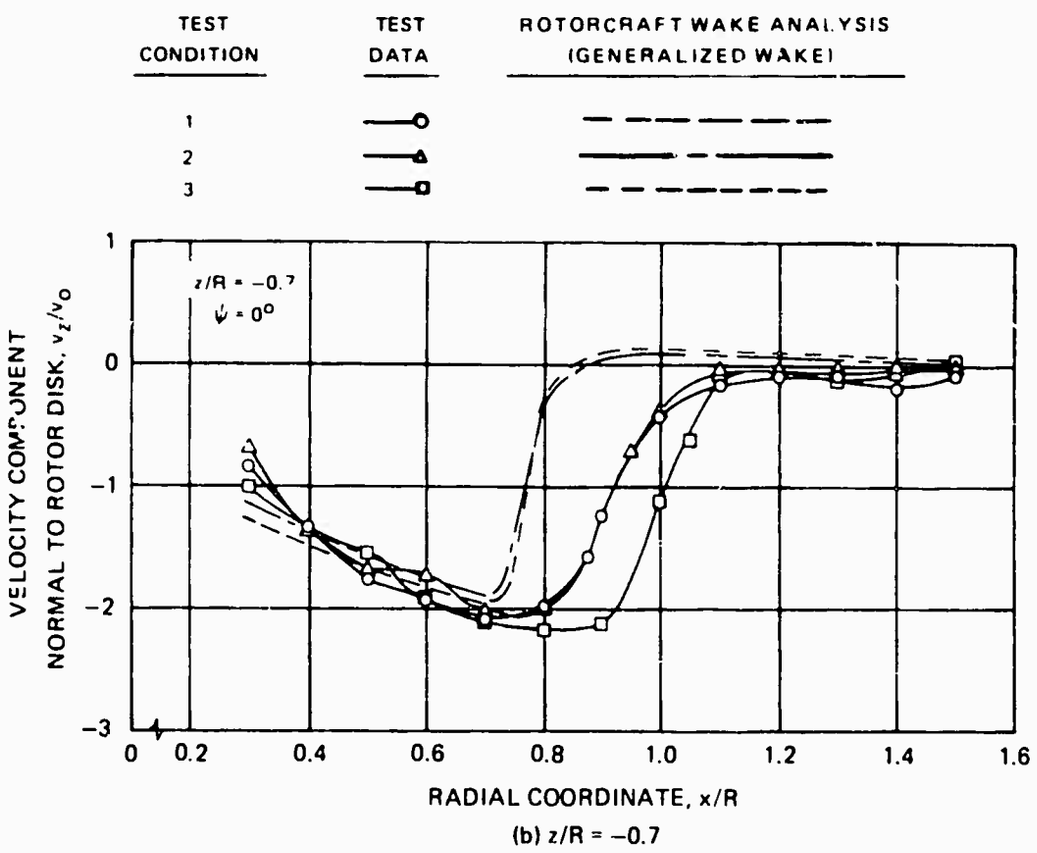

(b) z/R = −0.7

Figure 27. Concluded

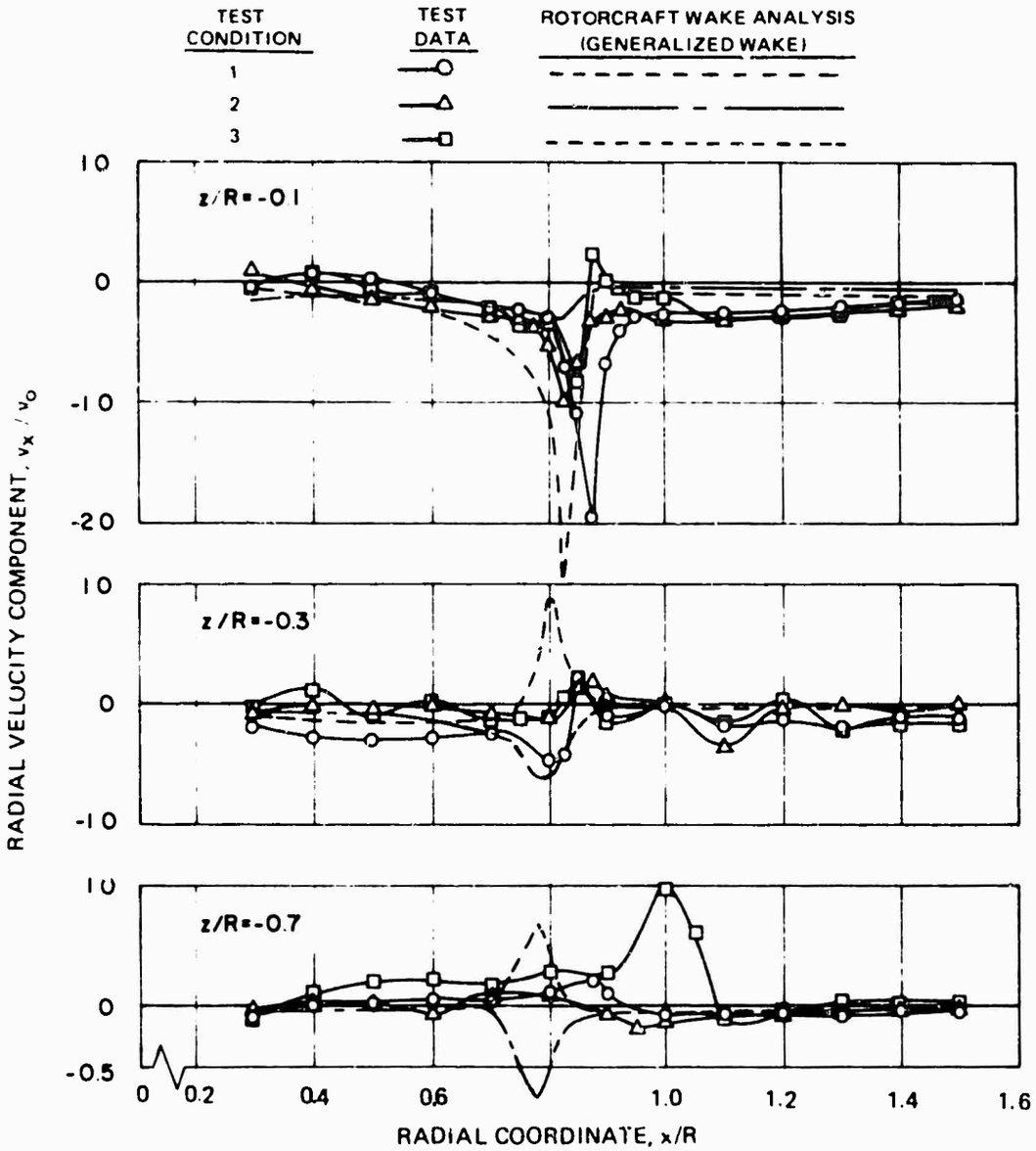

Figure 28. Comparison of Radial Distributions of Instantaneous Radial Velocity Component for Three Rotor Test Conditions and Several Distances Under Rotor--Boatwright, USAAMRDL TR 72-33, $\mu = 0$, $\psi = 0$ deg.

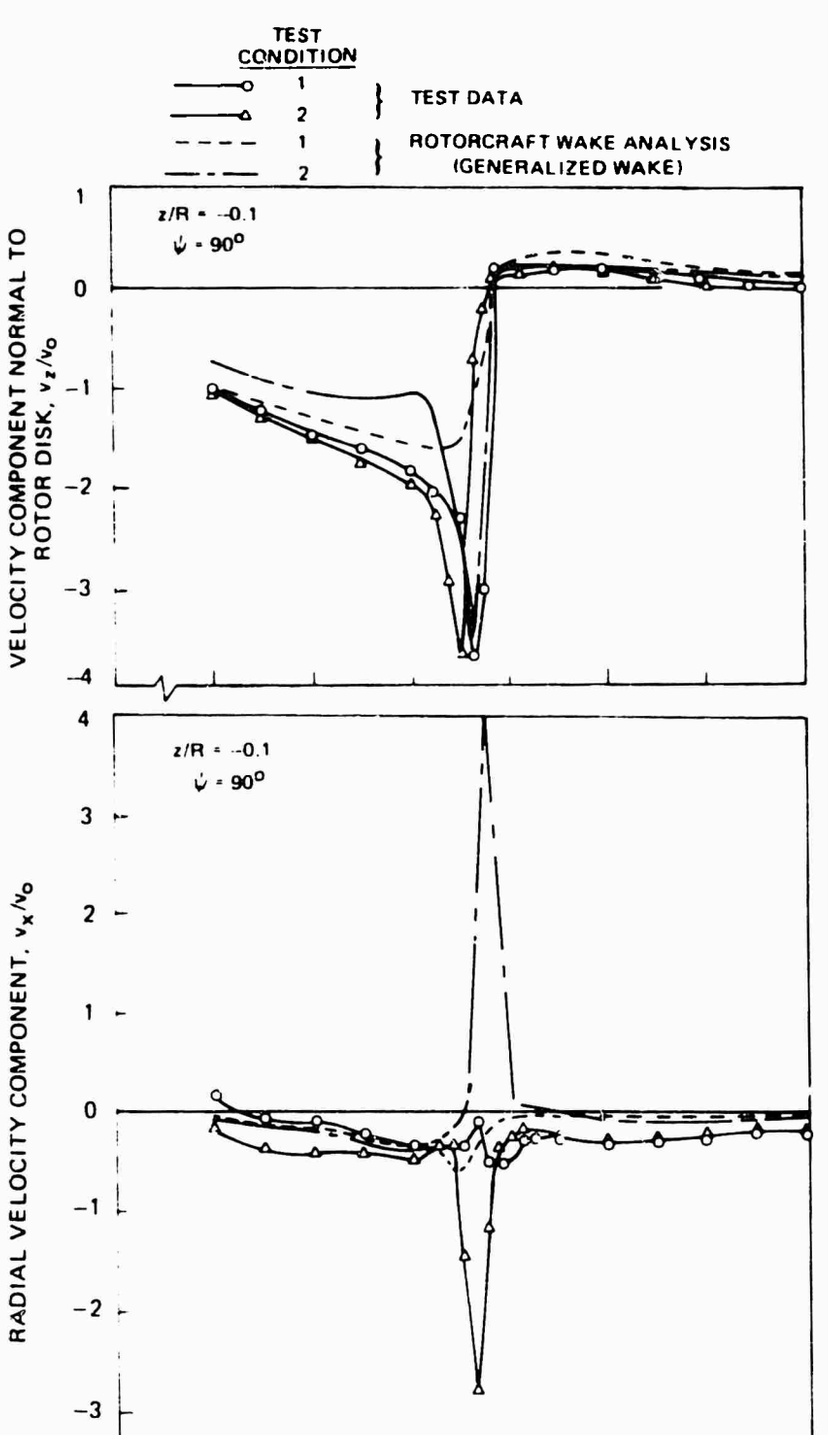

Figure 29. Comparison of Instantaneous Induced Velocity Components for Two Test Conditions--Boatwright, USAAMRDL TR 72-33, z/R = -0.1, ψ = 90 deg.

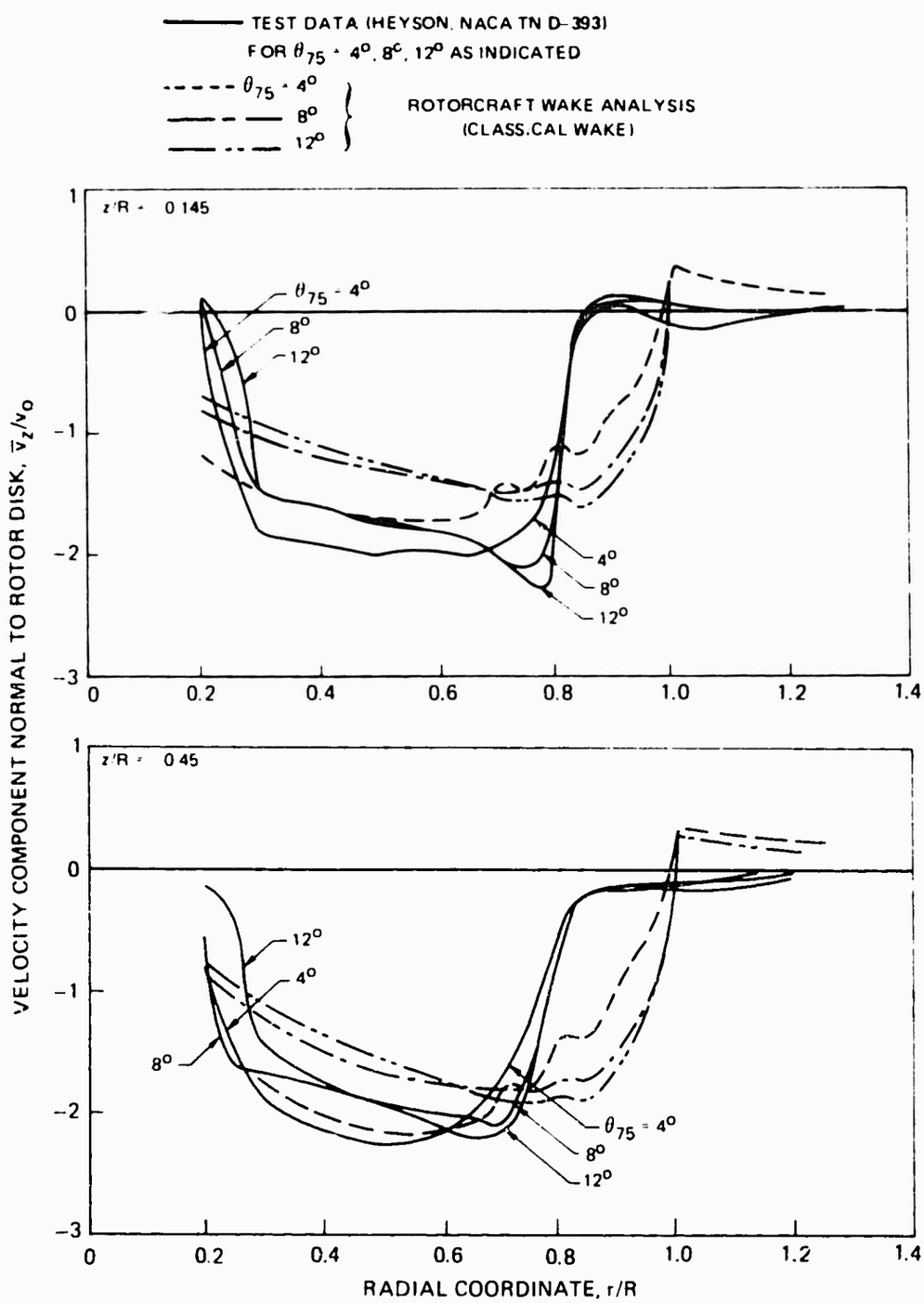

Figure 30. Comparisons of Time-Averaged Normal Component of Induced Velocity for Three Collective Pitch Values and Classical Wake--Heyson, NACA TN D-393, μ = 0, ΩR = 700 fps, z/R = -0.145 and -0.45.

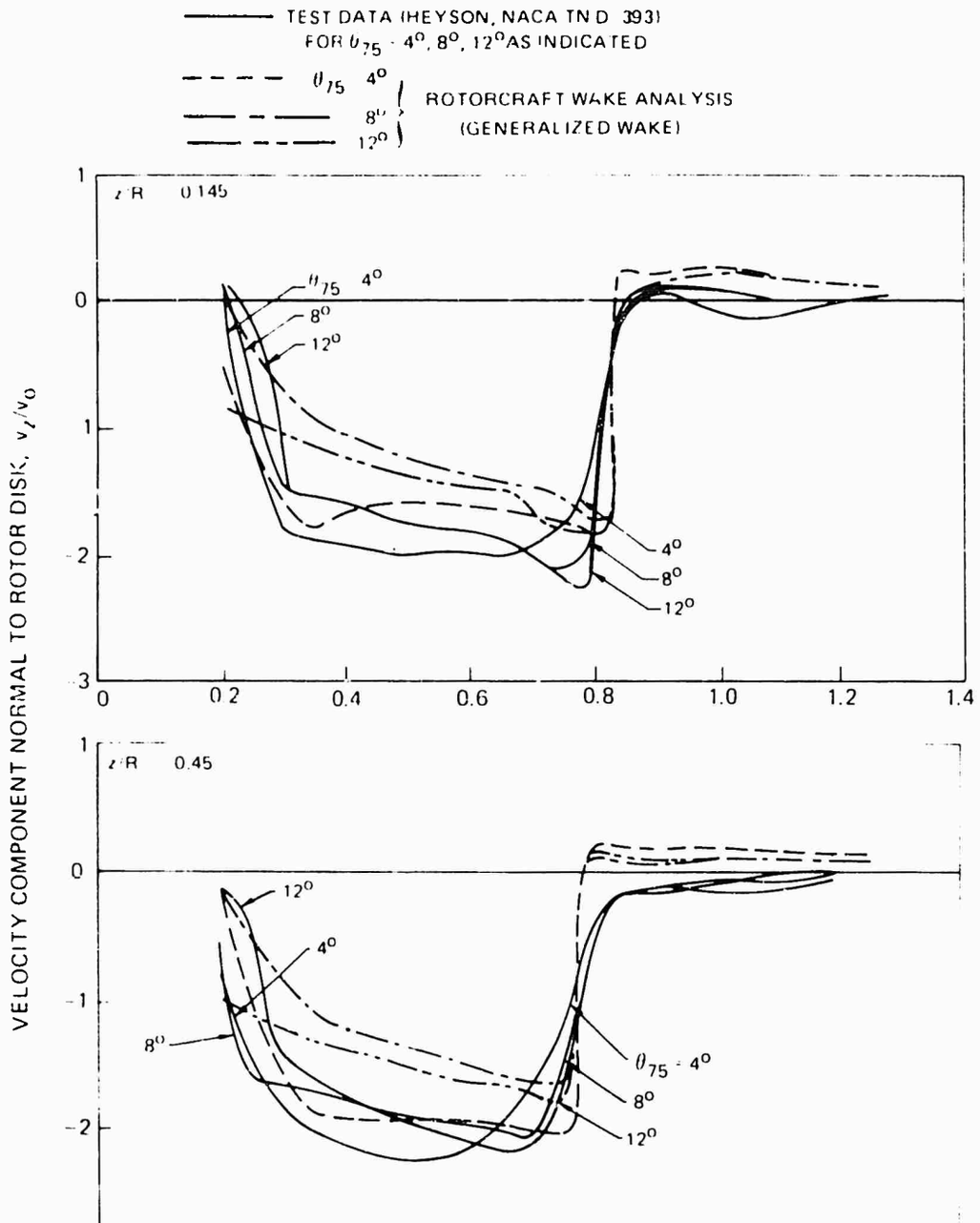

Figure 31. Comparison of Time-Averaged Normal Component of Induced Velocity for Three Collective Pitch Values and Generalized Wake -- Heyson, NACA TN D-393, $\mu = 0$, $\Omega R = 700$ fps, z/R = -0.145 and -0.45.

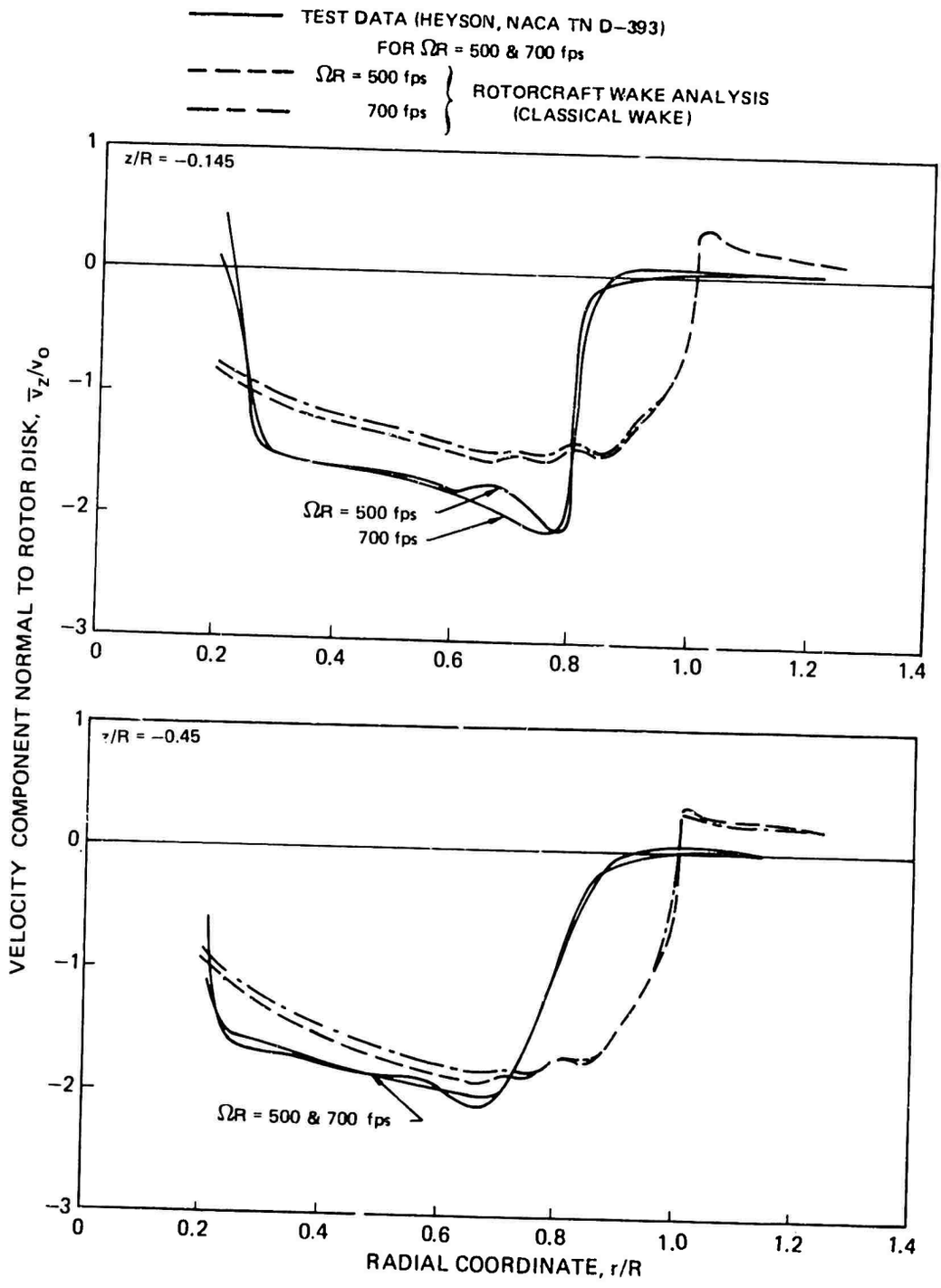

Figure 32. Comparison of Time-Averaged Normal Component of Induced Velocity for Two Tip Speeds and Classical Wake--Heyson, NACA TN D-393, $\mu = 0$, $\theta_{75} = 8^{\circ}$, $z/R = -0.145$ and -0.45.

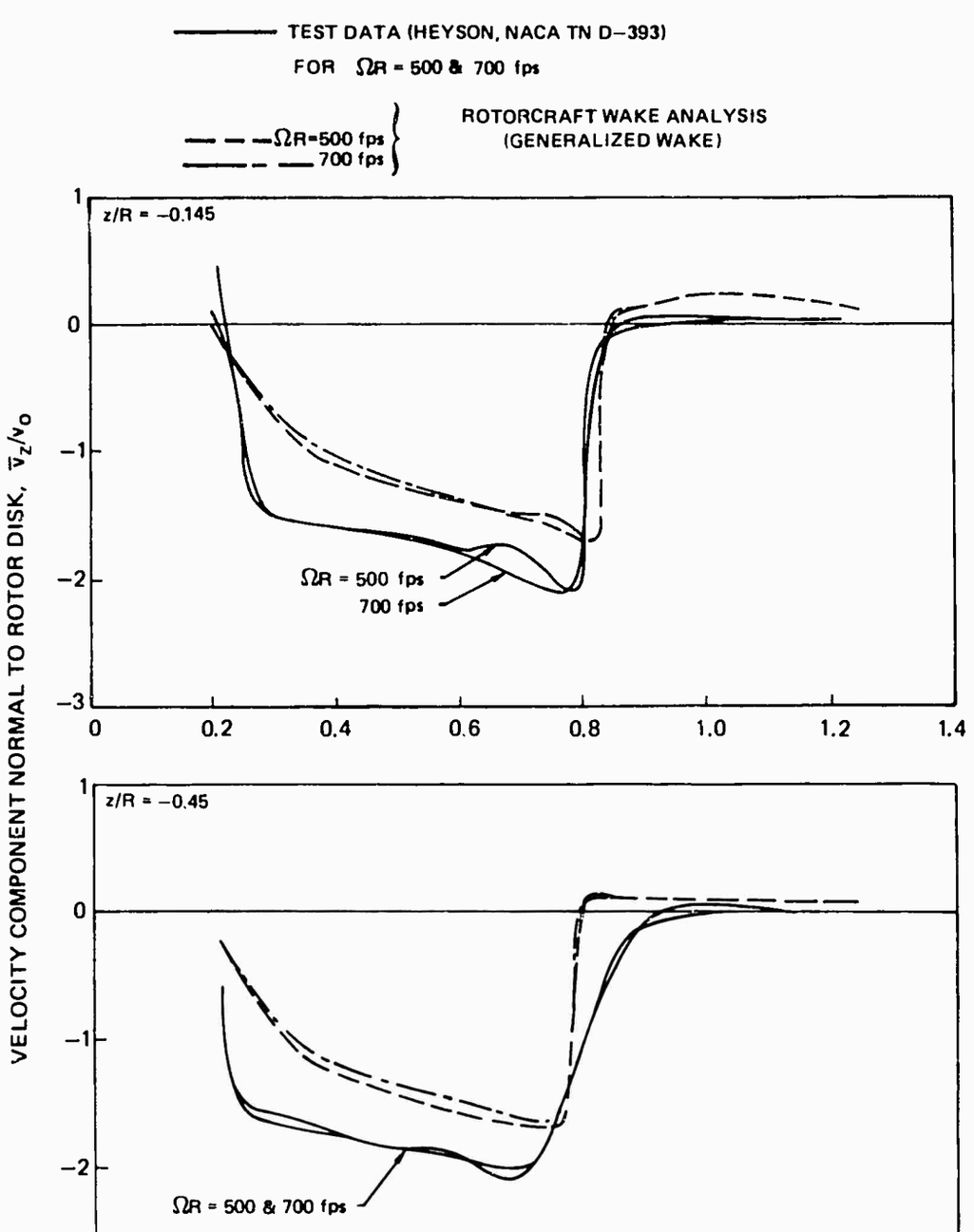

Figure 33. Comparison of Time-Averaged Normal Component of Induced Velocity for Two Tip Speeds and Generalized Wake--Heyson, NACA TN D-393, $\mu = 0$, $\theta_{75} = 8^\circ$, $z/R = -0.145$ and -0.45.

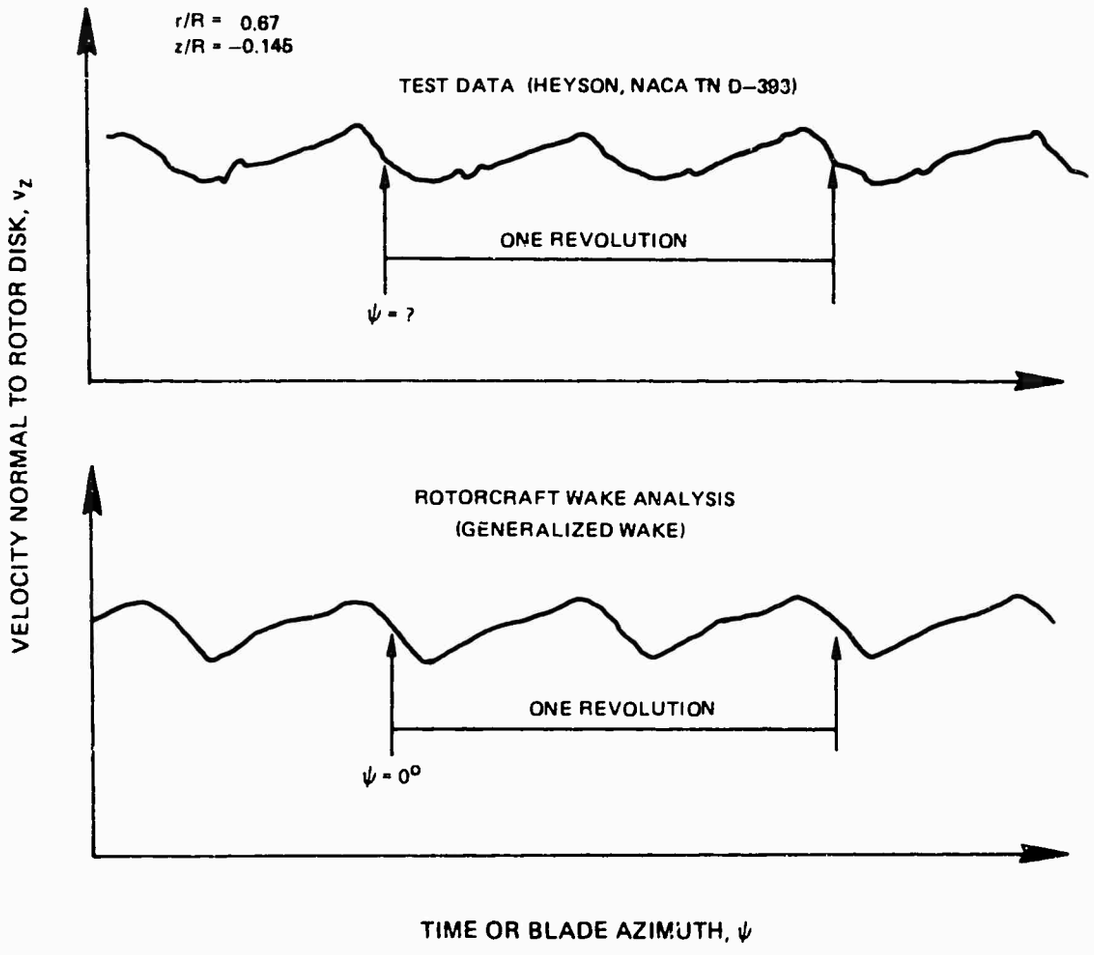

Figure 34. Comparison of Time Histories of Local Instantaneous Normal Component of Induced Velocity -- Heyson, NACA TN D-393, $\mu = 0$, $\theta_{75} = 12°$, $\Omega R = 700$ fps, $r/R = 0.67$ $z/R = -0.145$.

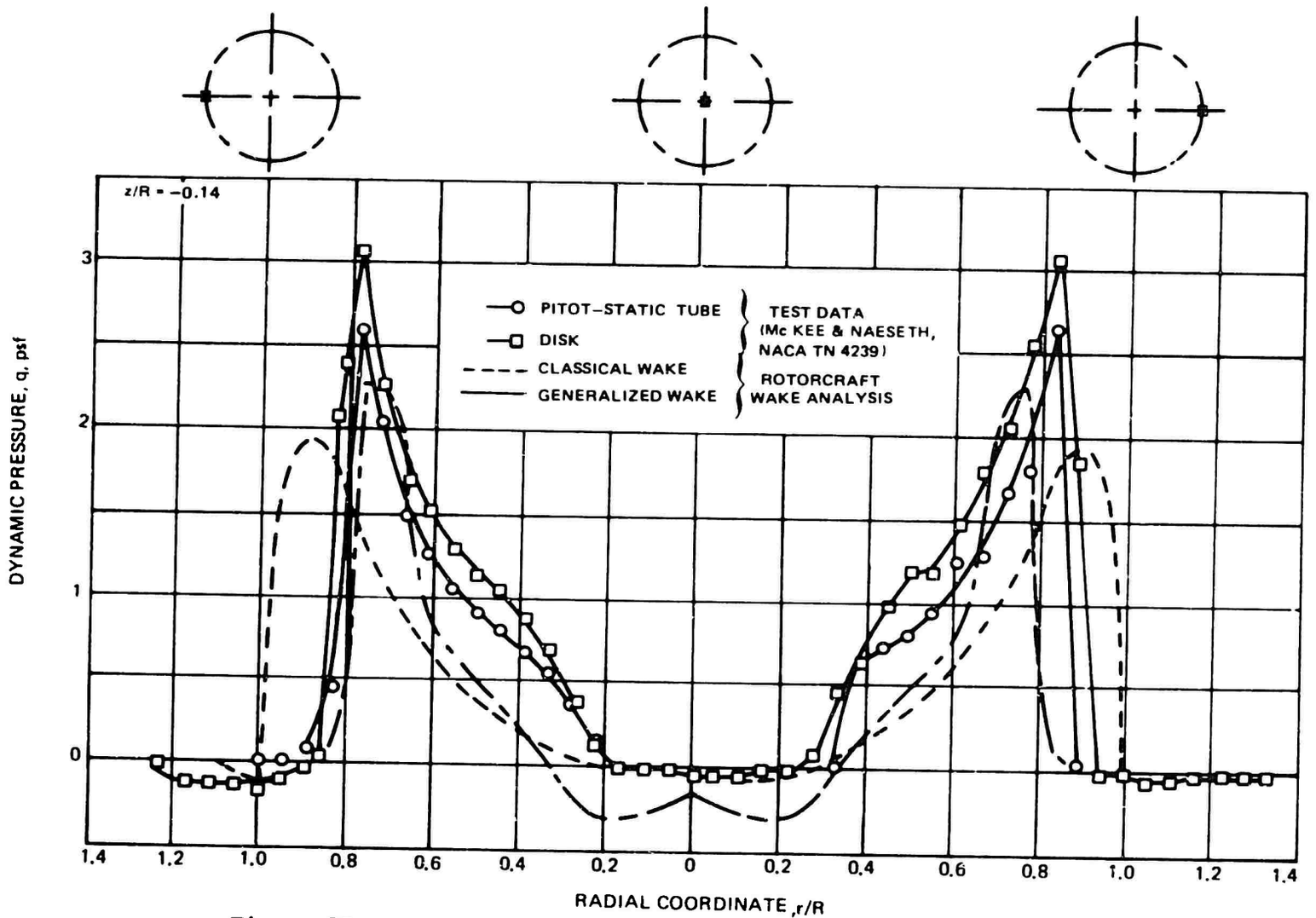

Figure 35. Comparison of Time-Averaged Dynamic Pressure in a Vertical Direction Below a Hovering Rotor--McKee and Naeseth, NACA TN 4239, $\mu = 0$, $z/R = -0.140$.

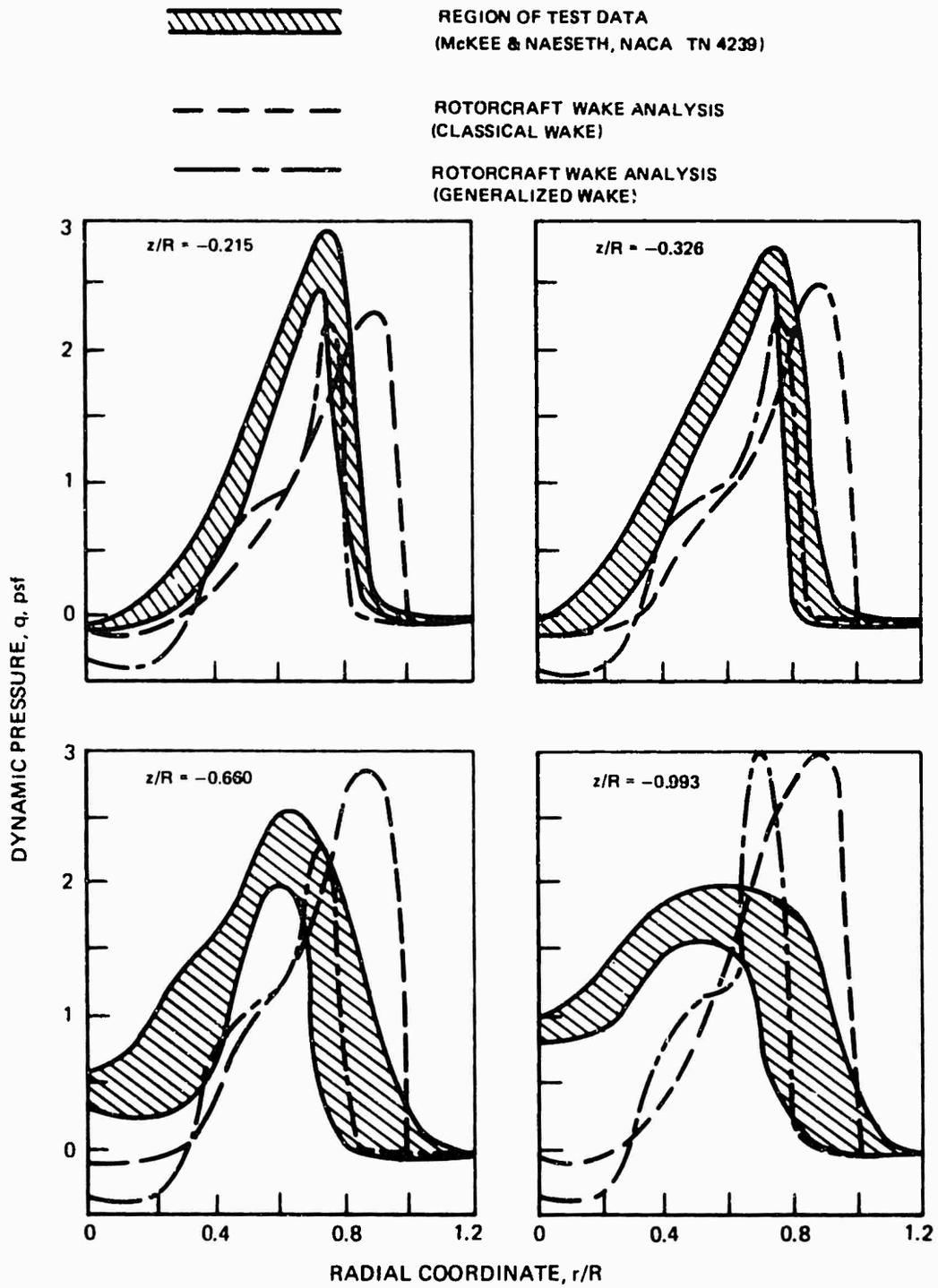

Figure 36. Comparison of Time-Averaged Dynamic Pressure in the Vertical Direction Below a Hovering Rotor--McKee and Naeseth, NACA TN 4239, z/R = -0.215, -0.326, -0.66, -0.993.

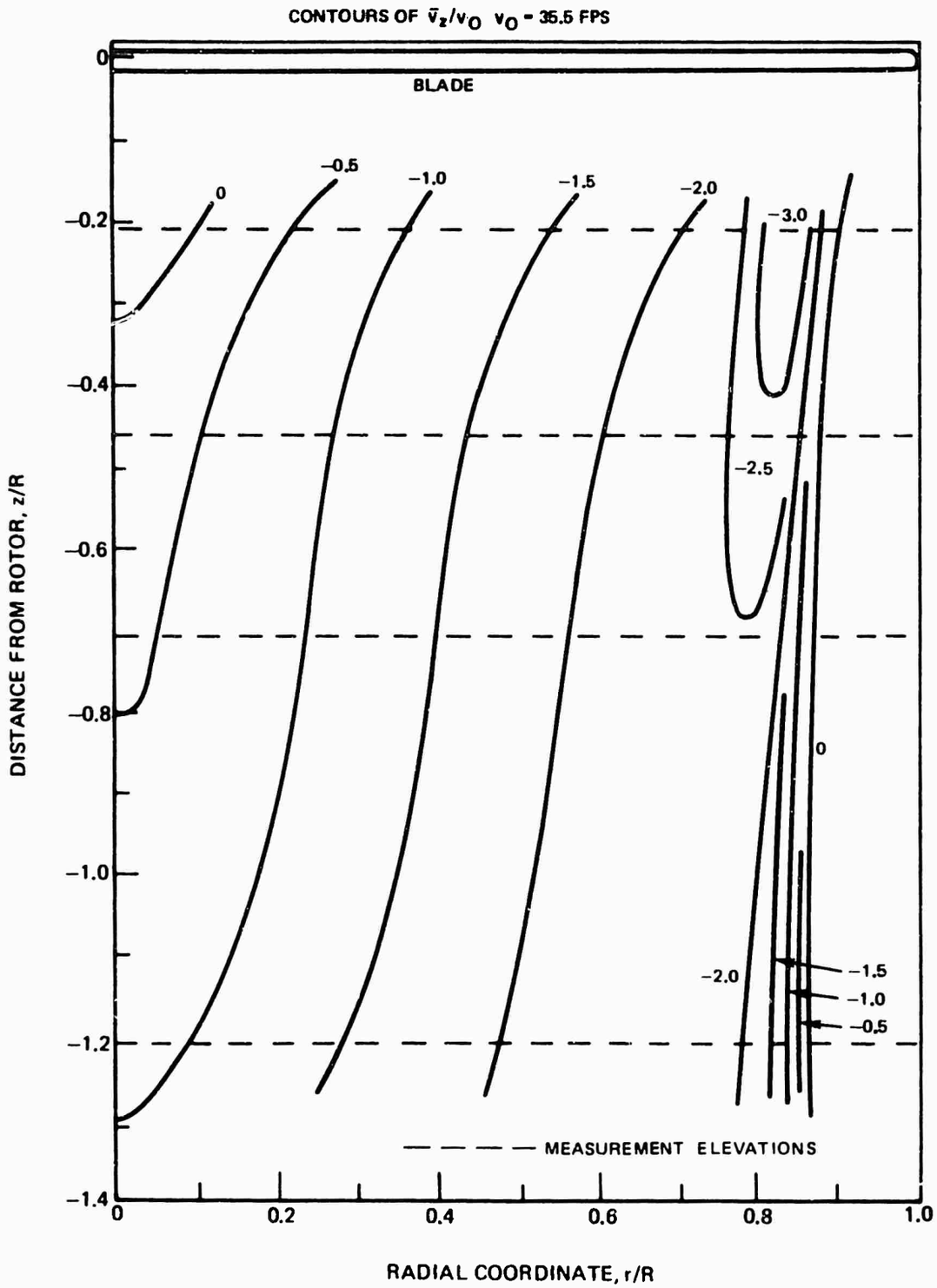

Figure 37. Experimental Time-Averaged Normal Induced Velocity Contours -- Fradenburgh Model Rotor, $\mu = 0$.

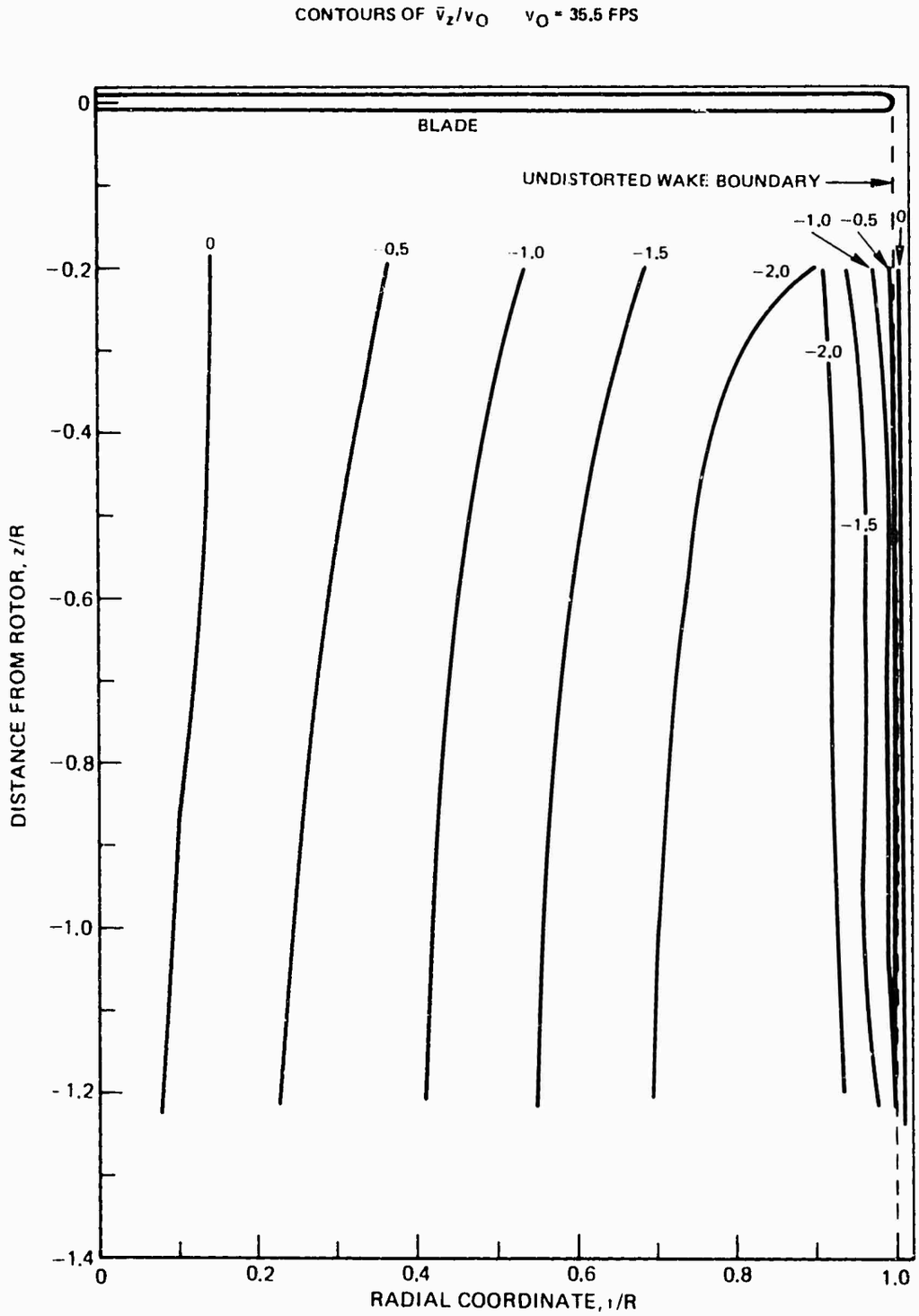

Figure 38. Analytical Time-Averaged Normal Induced Velocity Contours Based on Classical Wake Representation--Fradenburgh Model Rotor, $\mu = 0$.

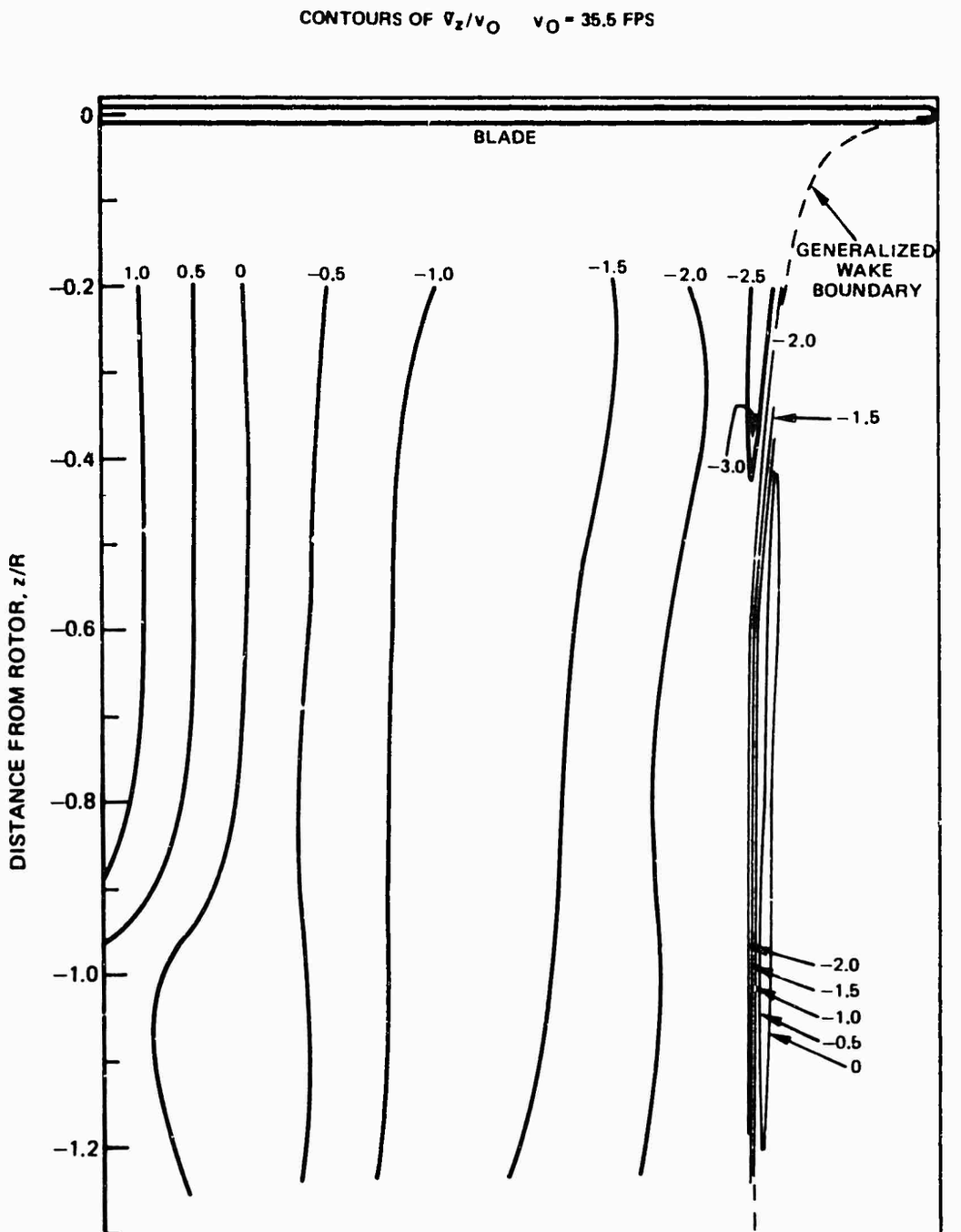

Figure 39. Analytical Time-Averaged Normal Induced Velocity Contours Based on Generalized Wake Geometry--Fradenburgh Model Rotor, $\mu = 0$.

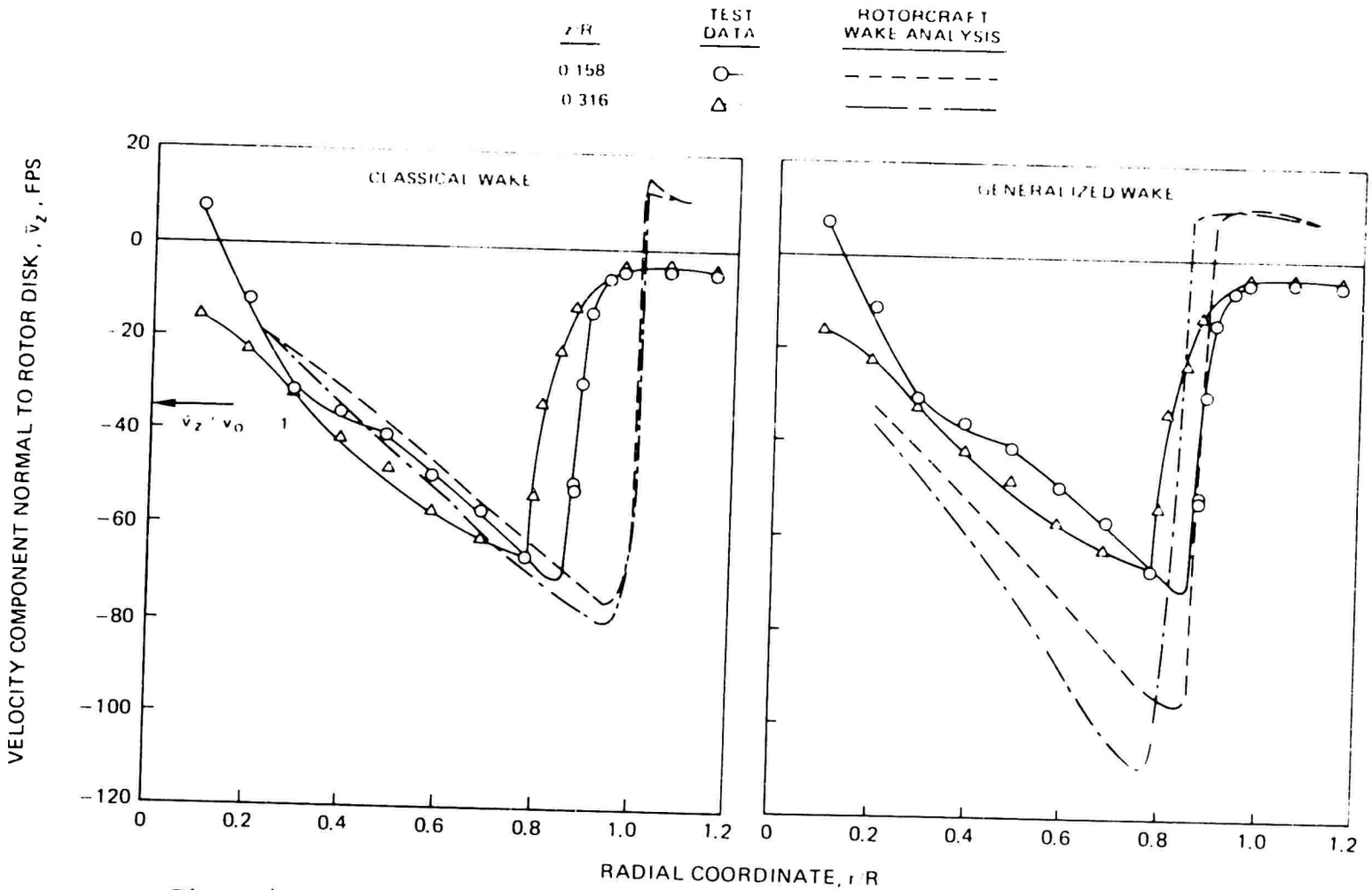

Figure 40. Comparison of Time-Averaged Normal Component of Induced Velocity for Two Distances Below a Hovering Rotor--Flemming, Condition 1, C_T = 0.0069, ΩR = 620 fps, v_o = 36.3 fps, z/R =-0.158 and -0.316.

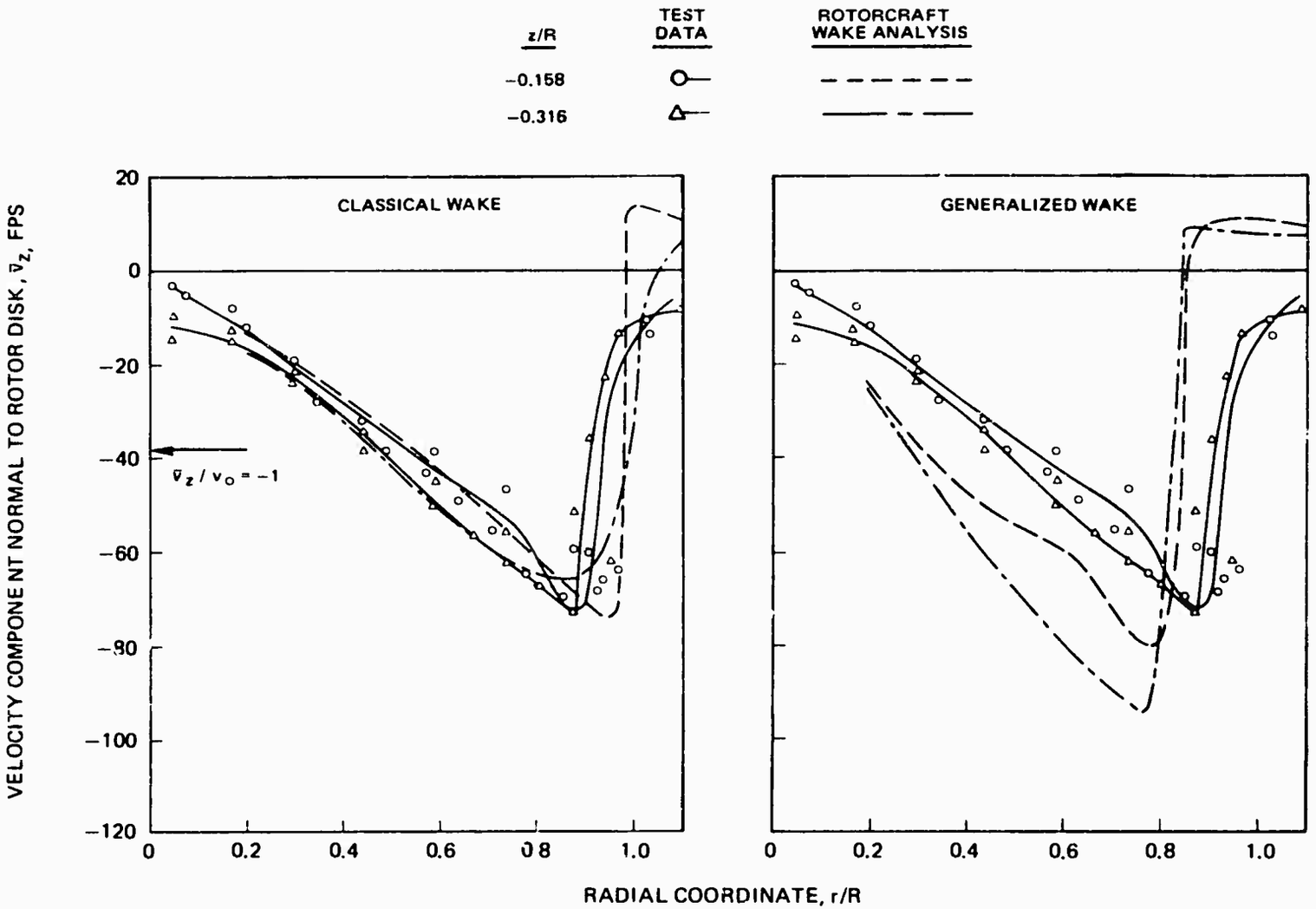

Figure 41. Comparison of Time-Averaged Normal Component of Induced Velocity for Two Distances Below a Hovering Rotor -- Flemming, Condition 2, C_T = 0.0079, ΩR = 620 fps, v_o = 39 fps, z/R = -0.158 and -0.316.

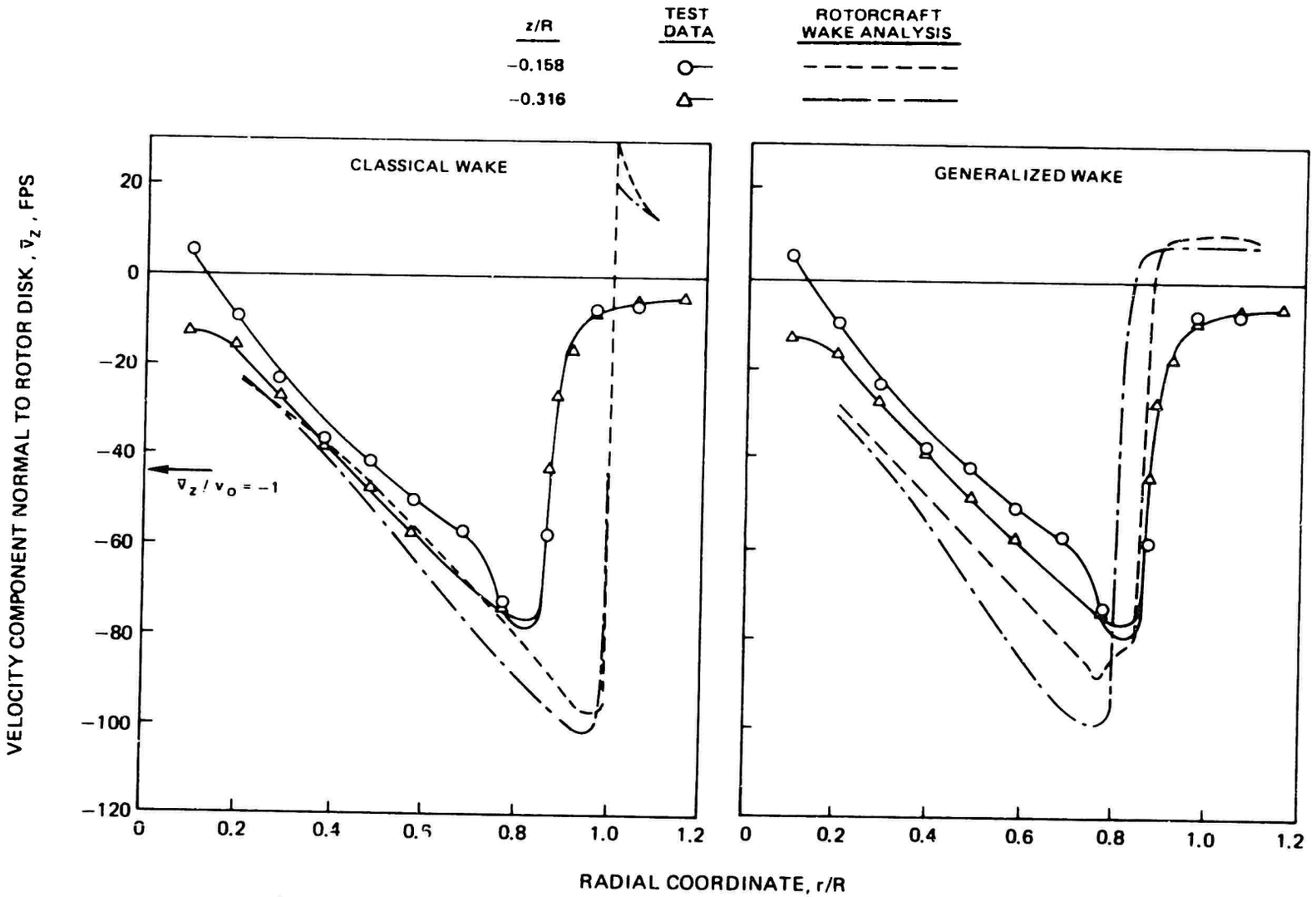

Figure 42. Comparison of Time-Averaged Normal Component of Induced Velocity for Two Distances Below a Hovering Rotor -- Flemming, Condition 3, C_T = 0.0103, ΩR = 620 fps, v_o = 44.5 fps, z/R = -0.158 and -0.316.

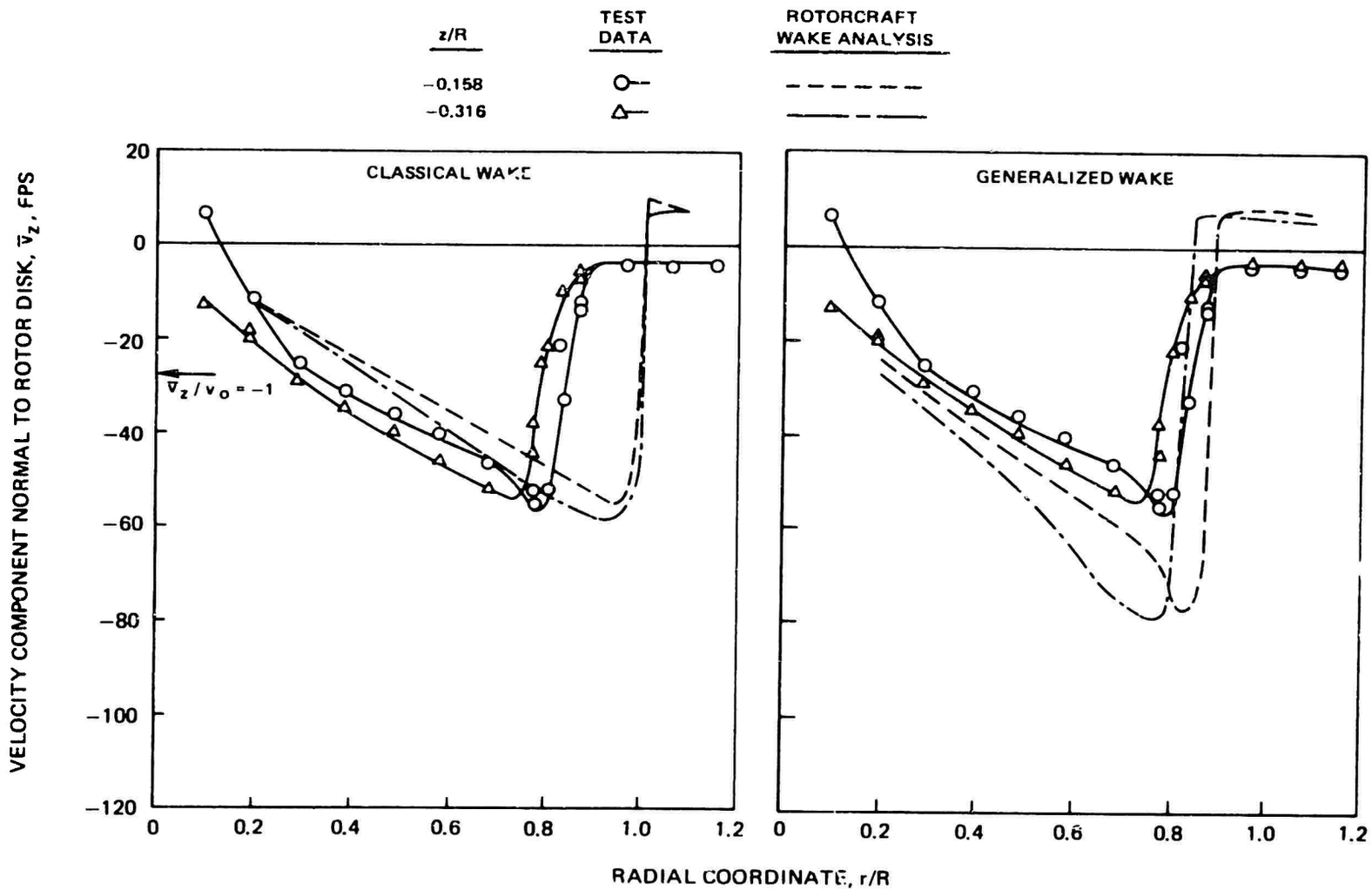

Figure 43. Comparison of Time-Averaged Normal Component of Induced Velocity for Two Distances Below a Hovering Rotor -- Flemming, Condition 4, C_T = 0.0067, ΩR = 465 fps, v_o = 27.0 fps, z/R = -0.158 and -0.316.

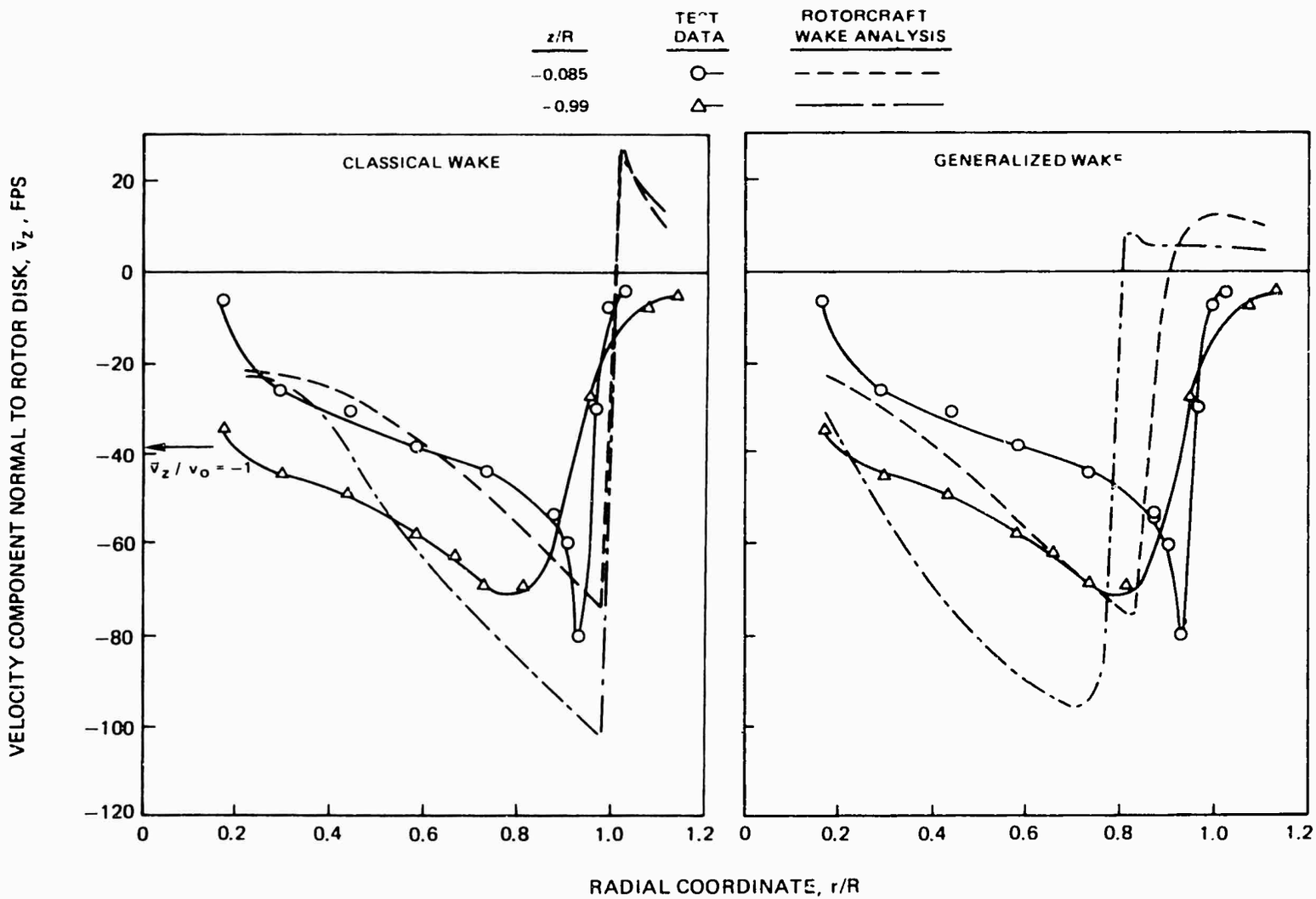

Figure 44. Comparison of Time-Averaged Normal Component of Induced Velocity for the Nearest and Furthest Axial Distances -- Flemming, Condition 2, C_T = 0.0079, ΩR = 620 fps, v_o = 39 fps, z/R = -0.085 and -0.99.

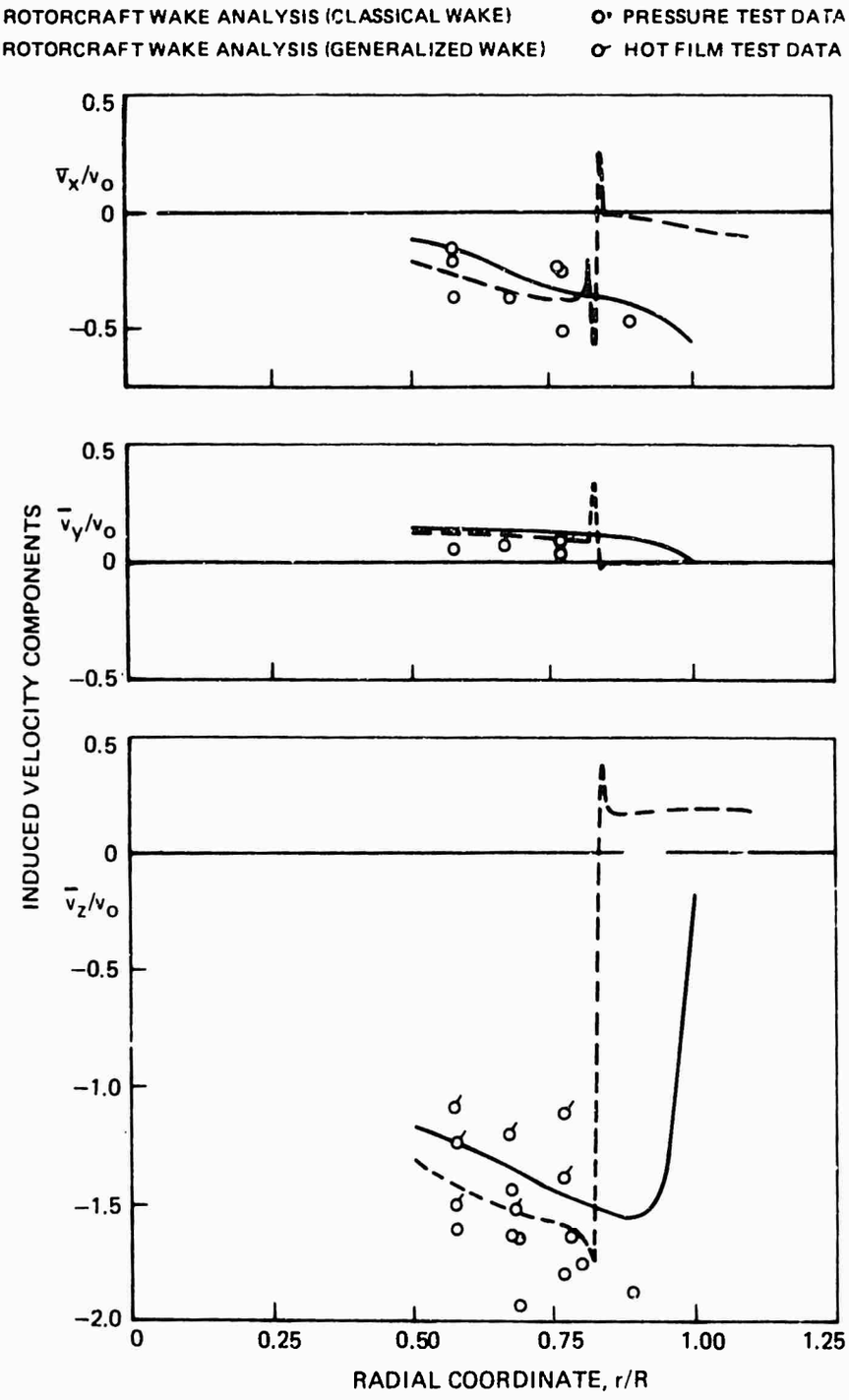

Figure 45. Comparison of Time-Averaged Induced Velocity Components at z/R = -0.22 -- Miller, Tang and Perlmutter, USAAVLABS TR 67-68 .

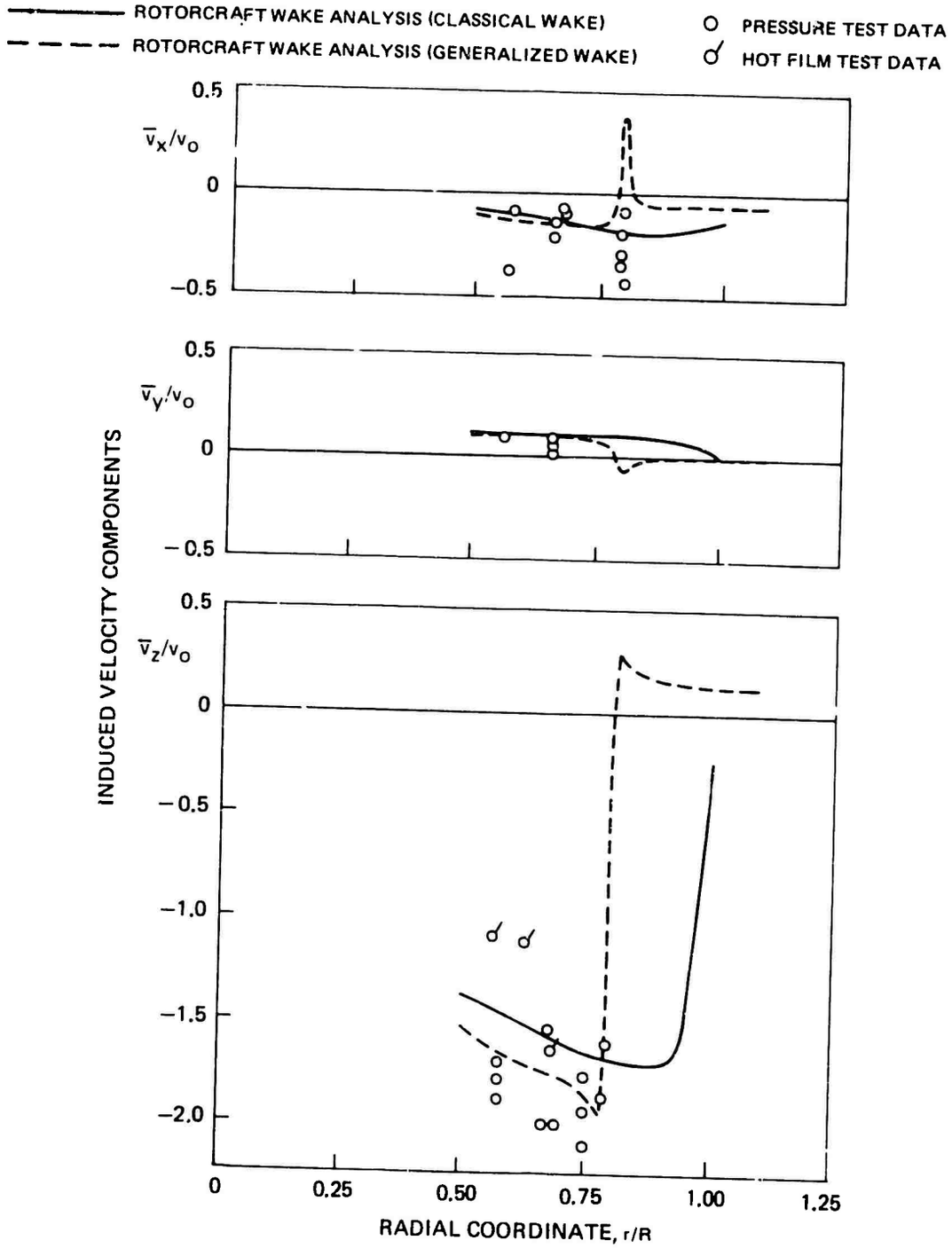

Figure 46. Comparison of Time-Averaged Induced Velocity Components at z/R = -0.49 -- Miller, Tang and Perlmutter, USAAVLABS TR 67-68.

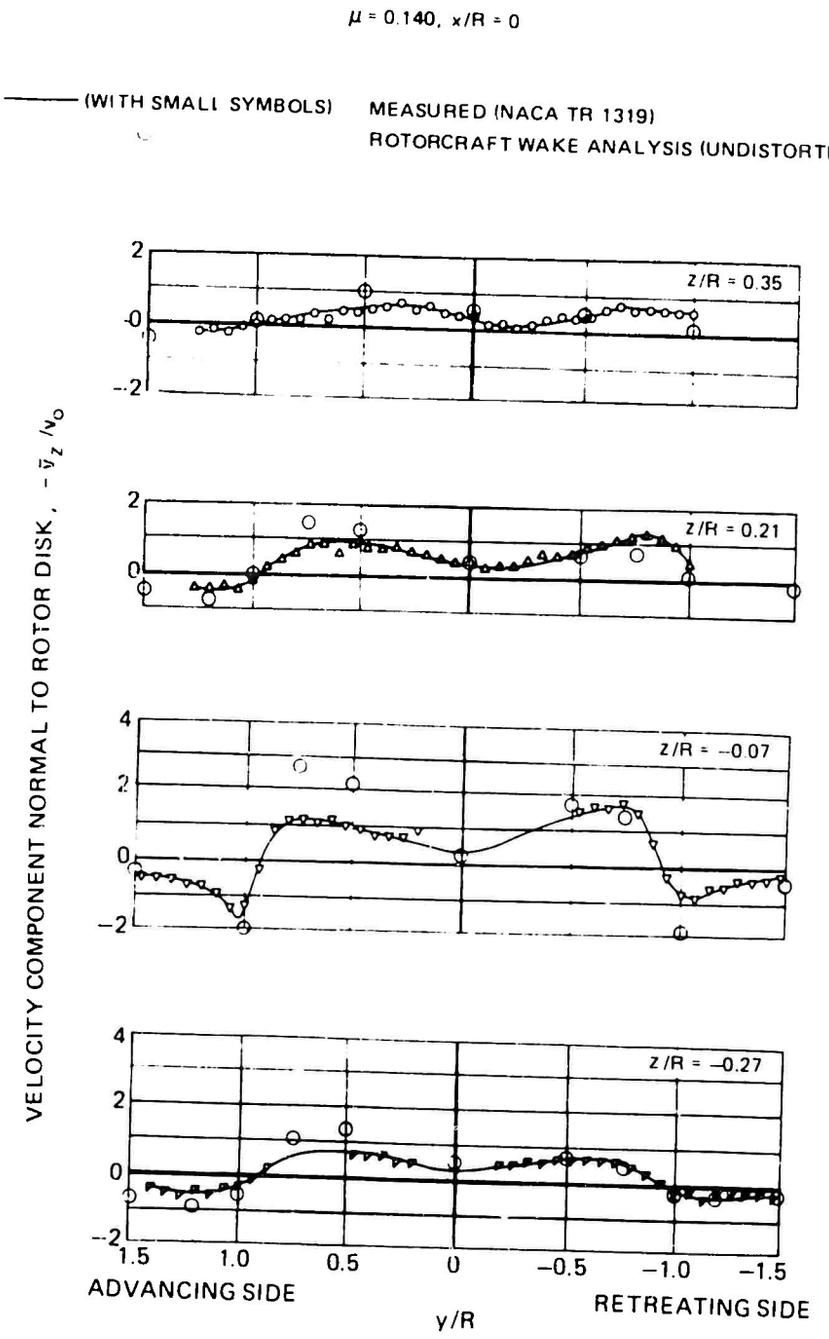

Figure 47. Comparison of Time-Averaged Normal Component of Induced Velocity in the Rotor Lateral Plane of Symmetry--Heyson and Katzoff, NACA TR 1319, Condition 2, $\mu = 0.140$, $x/R = 0$.

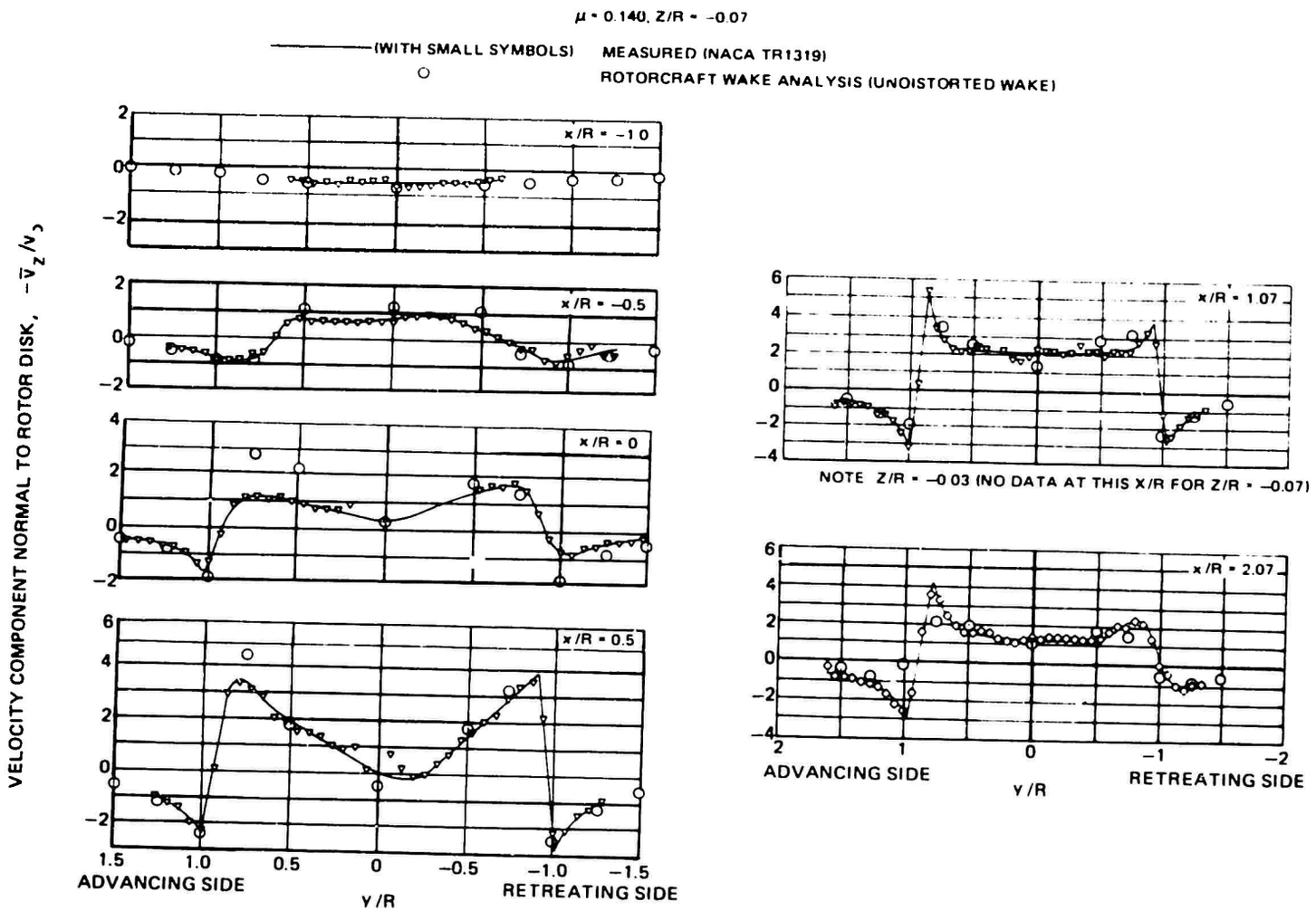

Figure 48. Comparison of Time-Averaged Normal Component of Induced Velocity in a Plane Parallel to and 0.07 R Beneath the Rotor--Heyson and Katzoff, NACA TR 1319, Condition 2, $\mu = 0.140$, $z/R = -0.07$.

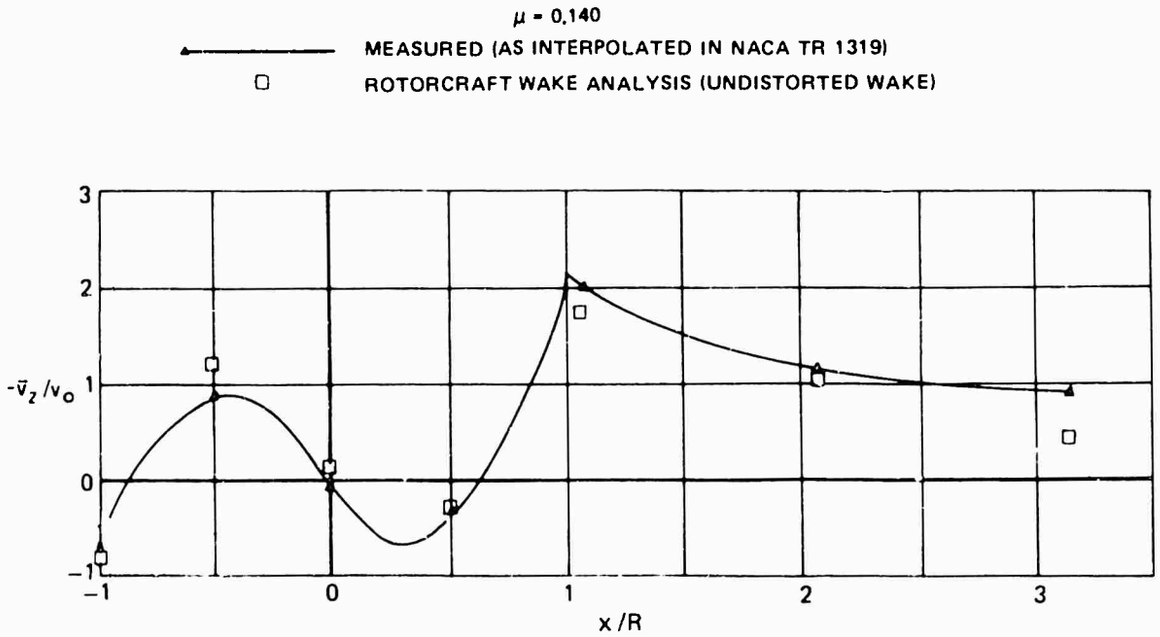

a) ALONG THE LONGITUDINAL CENTERLINE: y/R = 0, z/R = 0

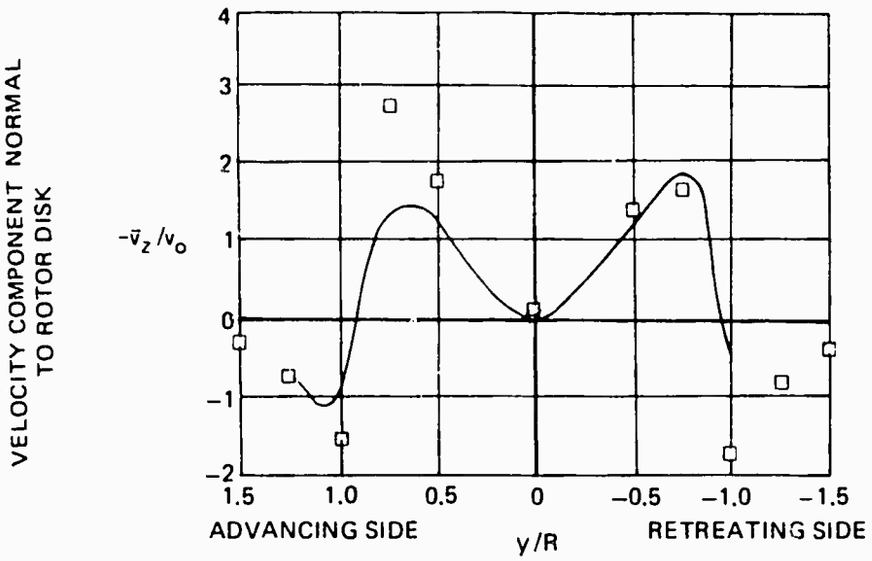

b) ALONG THE LATERAL CENTERLINE: x/R = 0, z/R = 0

Figure 49. Comparison of Time-Averaged Normal Component of Induced Velocity Along the Centerlines of the Rotor Disk -- Heyson and Katzoff, NACA TR 1319, Condition 2, $\mu = 0.140$, $z/R = 0$.

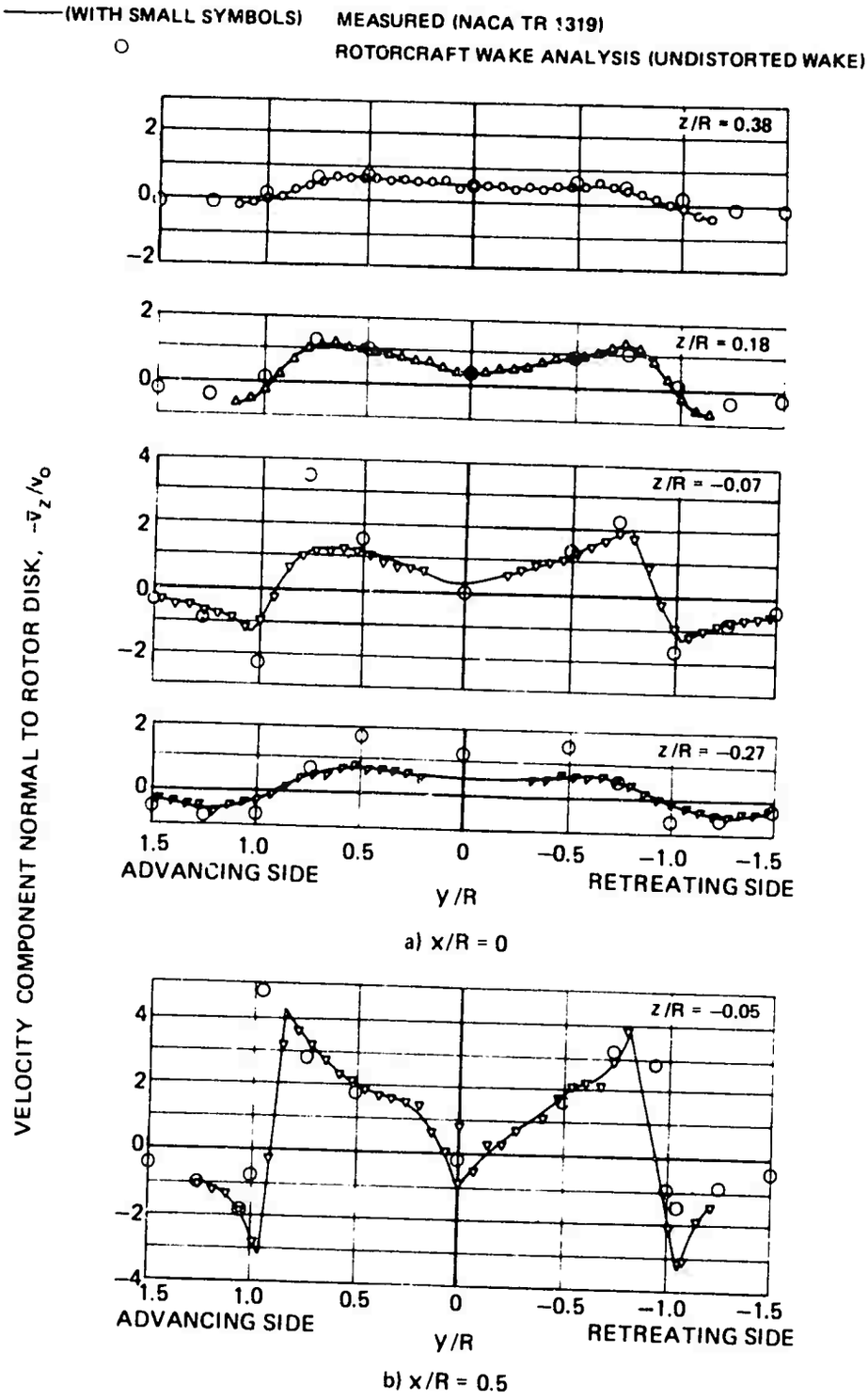

Figure 50. Comparison of Time-Averaged Normal Component of Induced Velocity for x/R = 0 and 0.5 -- Heyson and Katzoff, NACA TR 1319, Condition 1, $\mu = 0.095$.

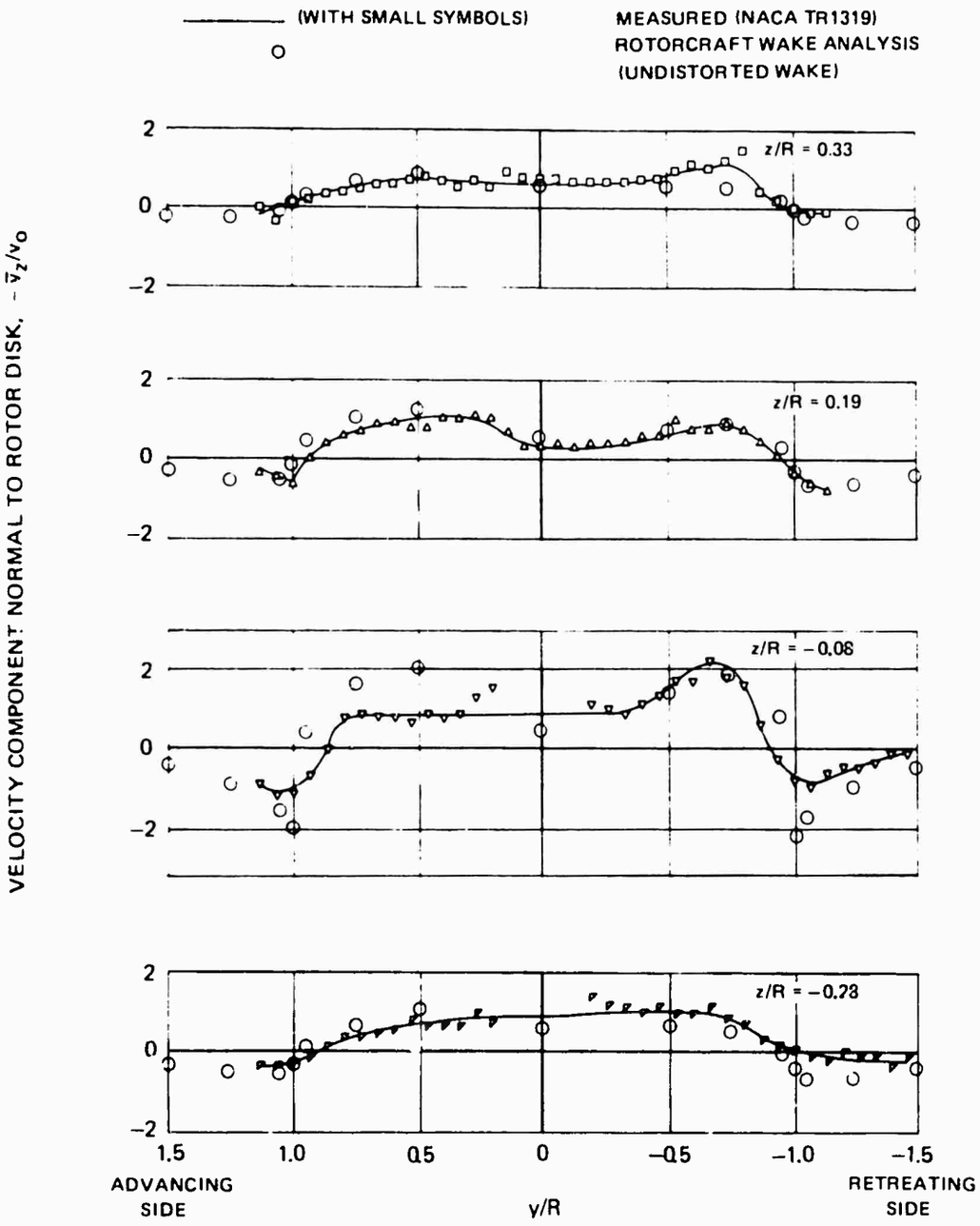

Figure 51. Comparison of Time-Averaged Normal Component of Induced Velocity at x/R = 0 -- Heyson and Katzoff, NACA TR 1319, Condition 3, $\mu = 0.232$.

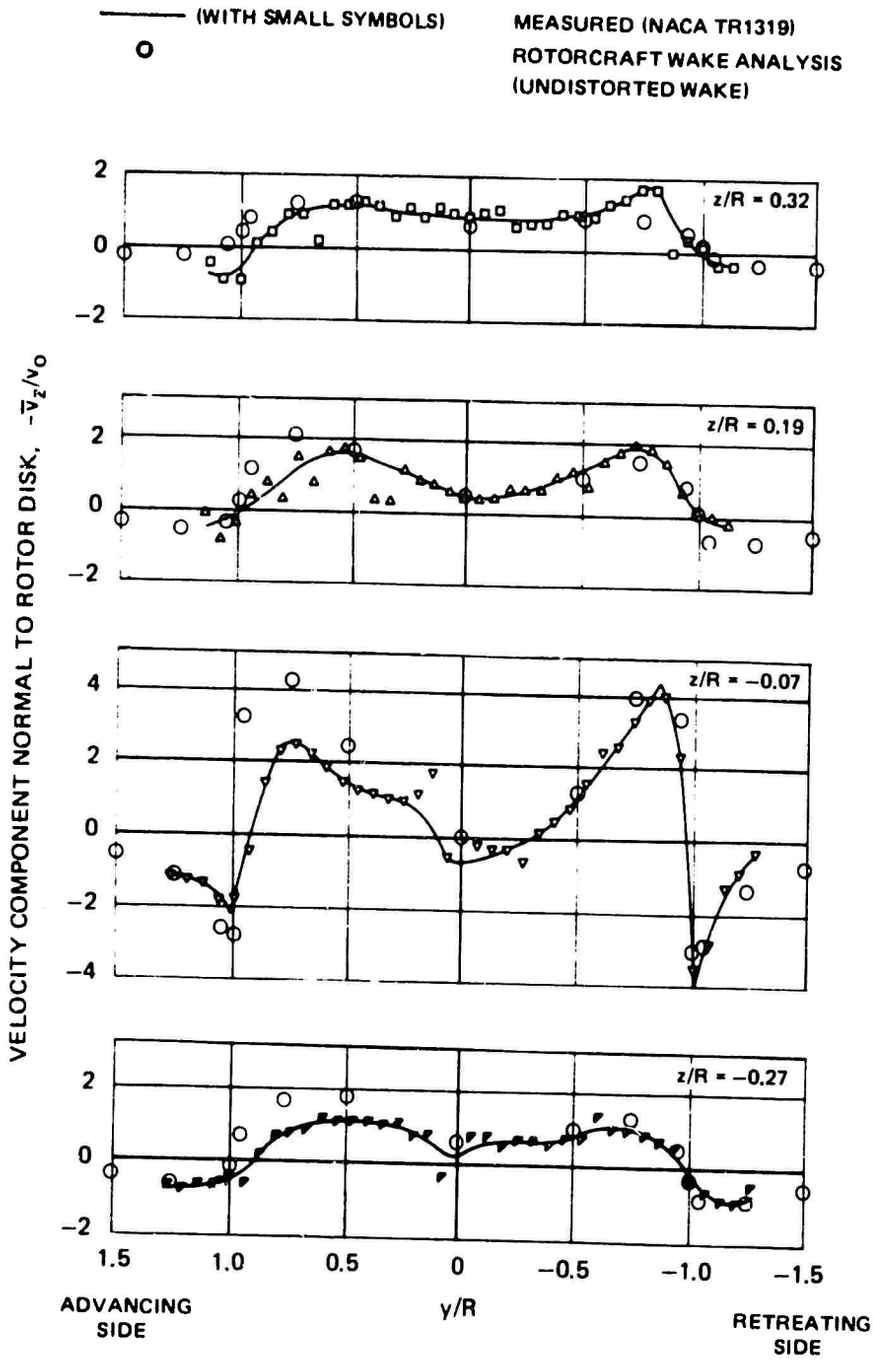

Figure 52. Comparison of Time-Averaged Normal Component of Induced Velocity at x/R = 0.5 -- Heyson and Katzoff, NACA TR 1319, Condition 3, $\mu = 0.232$.

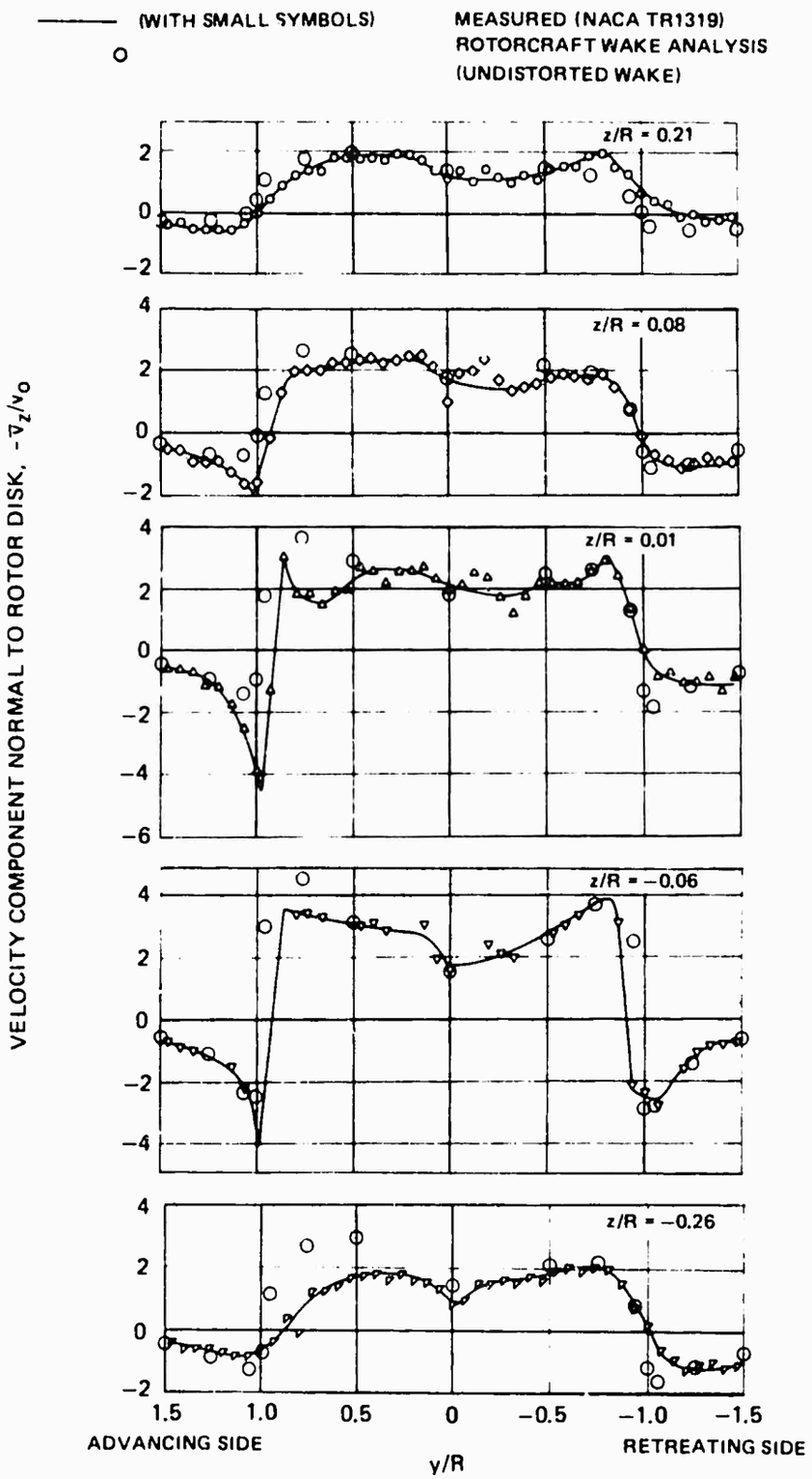

Figure 53. Comparison of Time-Averaged Normal Component of Induced Velocity at x/R = 1.07 -- Heyson and Katzoff, NACA TR 1319, Condition 3, μ = 0.232.

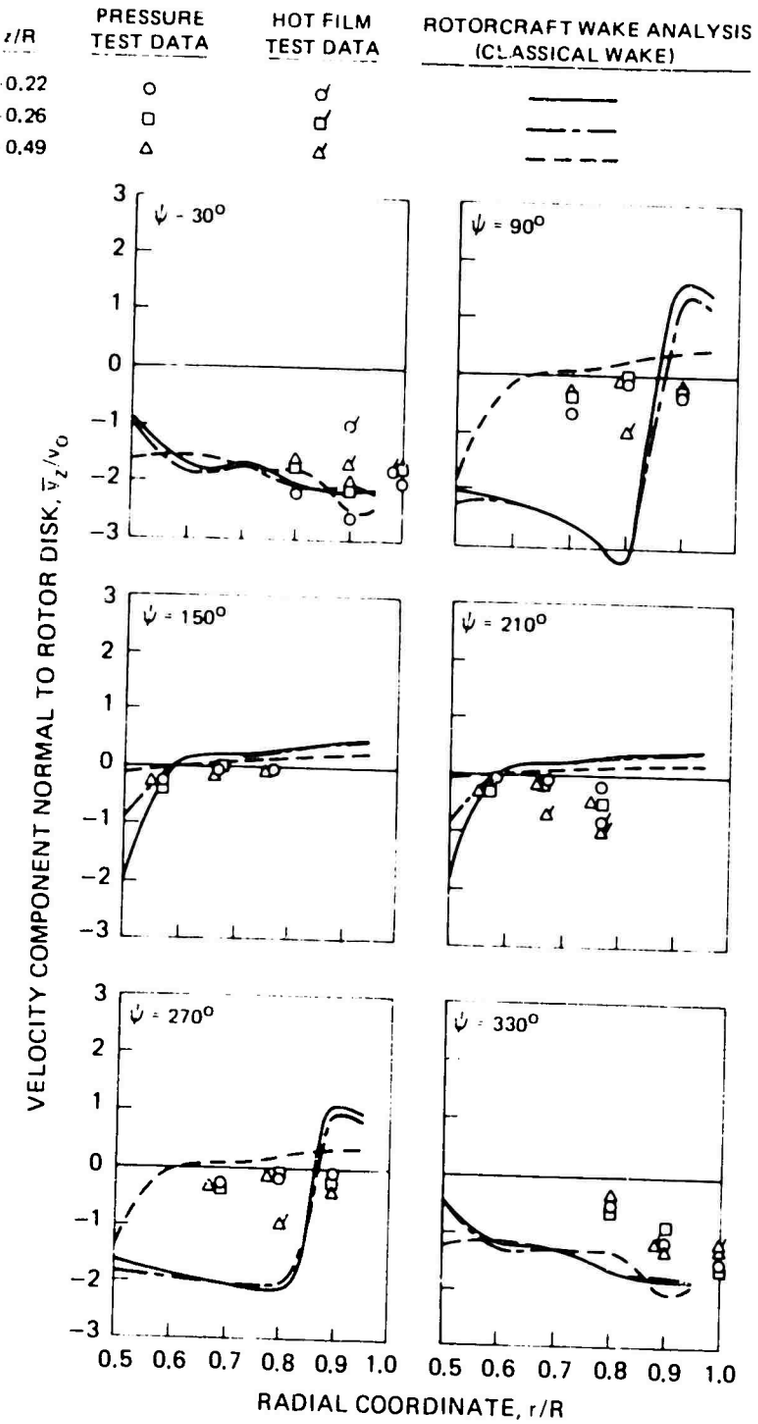

Figure 54. Comparison of Radial Distributions of Time-Averaged Normal Component of Induced Velocity at Several Axial and Aximuth Locations for $\mu = 0.049$--Miller, Tang, and Perlmutter, USAAVLABS TR 67-68.

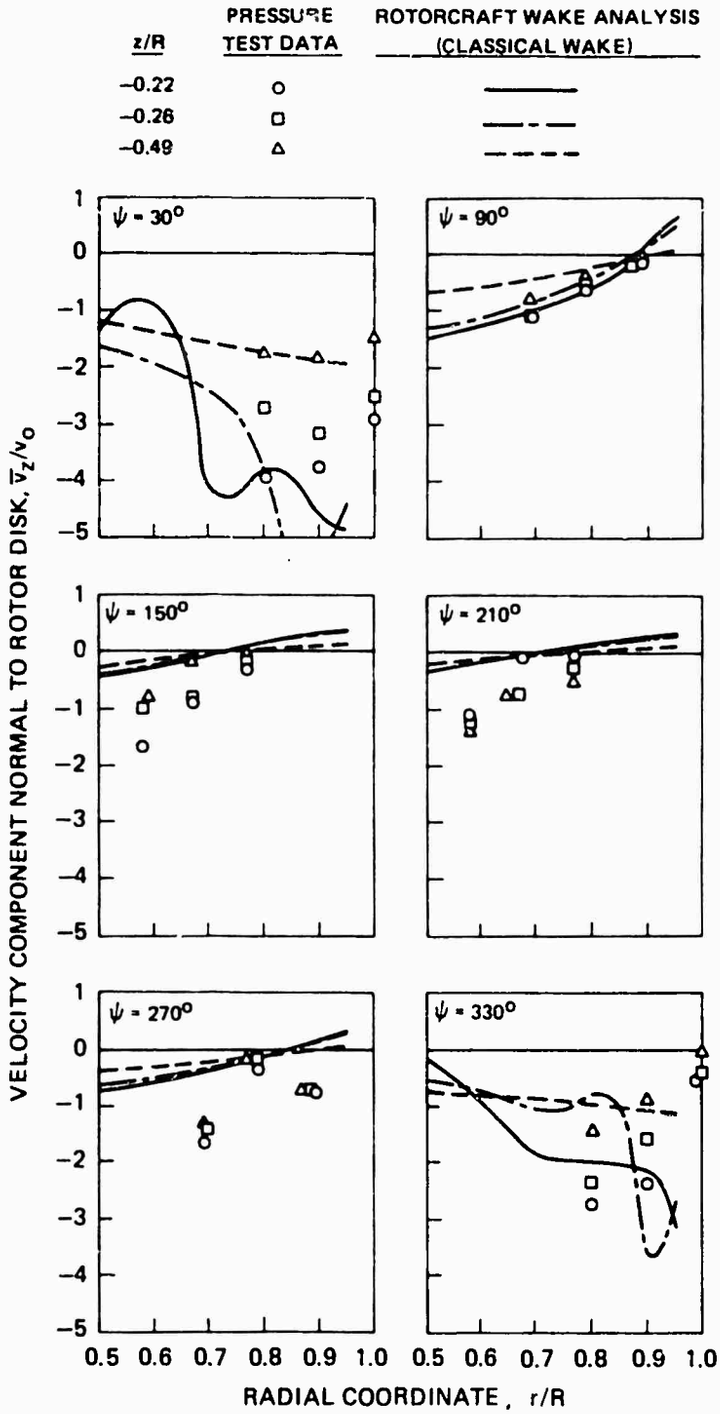

Figure 55. Comparison of Radial Distributions of Time-Averaged Normal Component of Induced Velocity at Several Axial and Azimuth Locations for $\mu = 0.113$--Miller Tang, and Perlmutter, USAAVLABS TR 67-68.

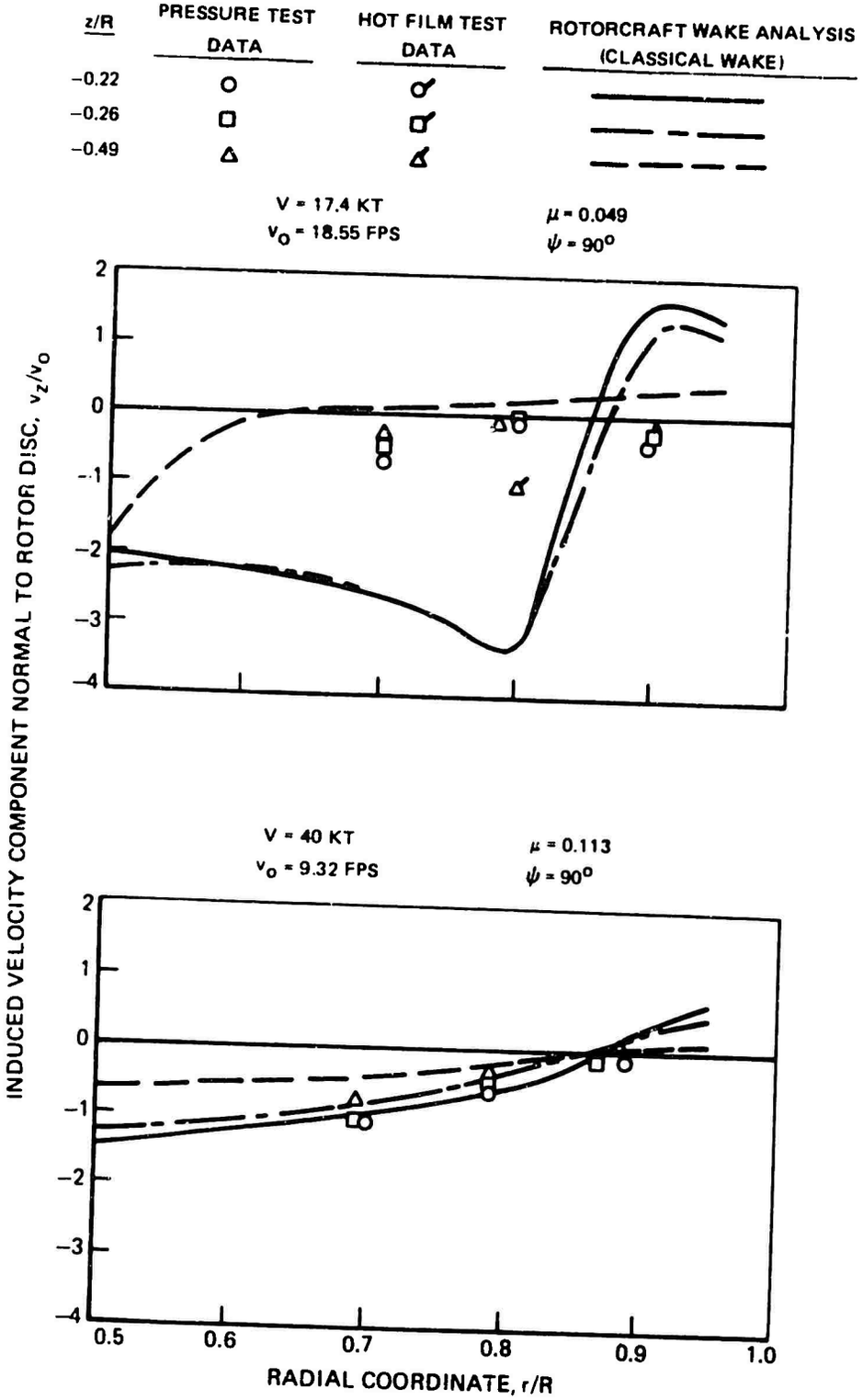

Figure 56. Comparison of Radial Distributions of Time-Averaged Normal Component of Induced Velocity for $\mu = 0.049$ and $\mu = 0.113$ and $\psi = 90$ deg -- Miller, Tang, and Perlmutter, USAAVLABS TR 67-68.

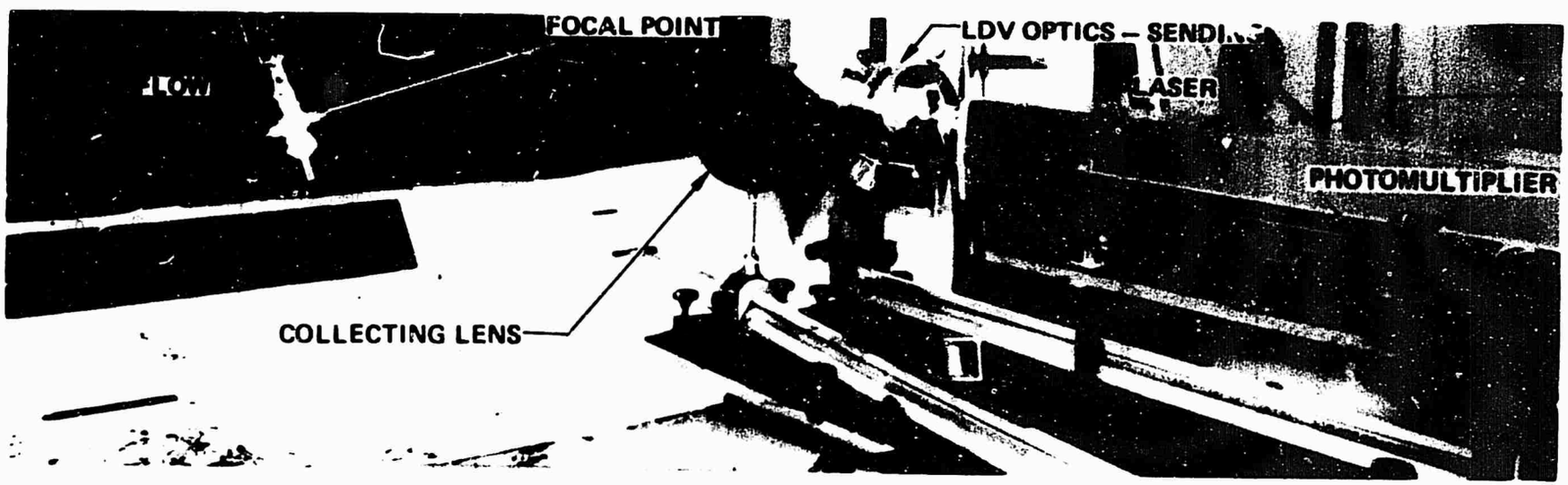

Figure 57. Laser Velocimeter as Used to Measure Local Flow Velocities in the Vicinity of a Model Rotor in a UTRC Wind Tunnel .

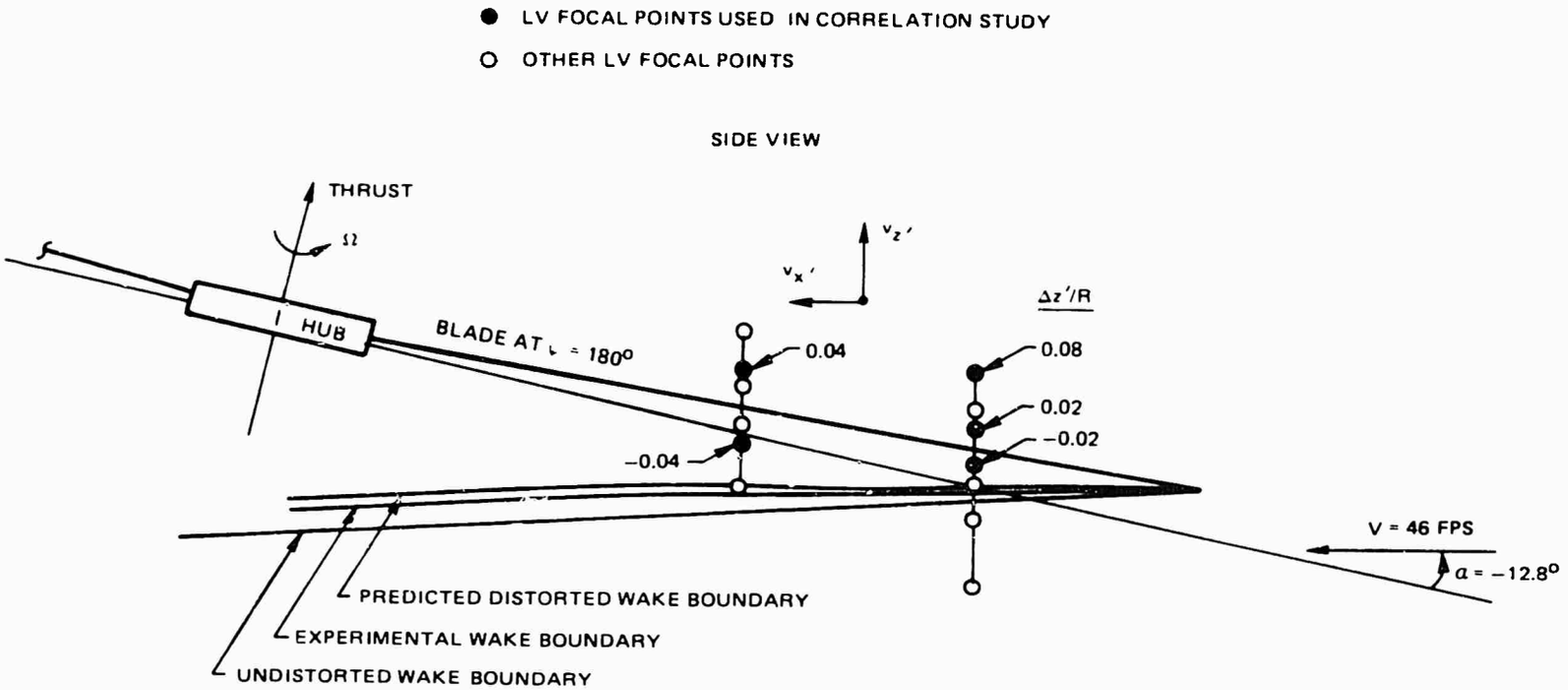

Figure 58. Schematic of Laser Velocimeter Focal Points Relative to Rotor and Wake Boundary--Landgrebe and Johnson, $\mu = 0.15$, Side View.

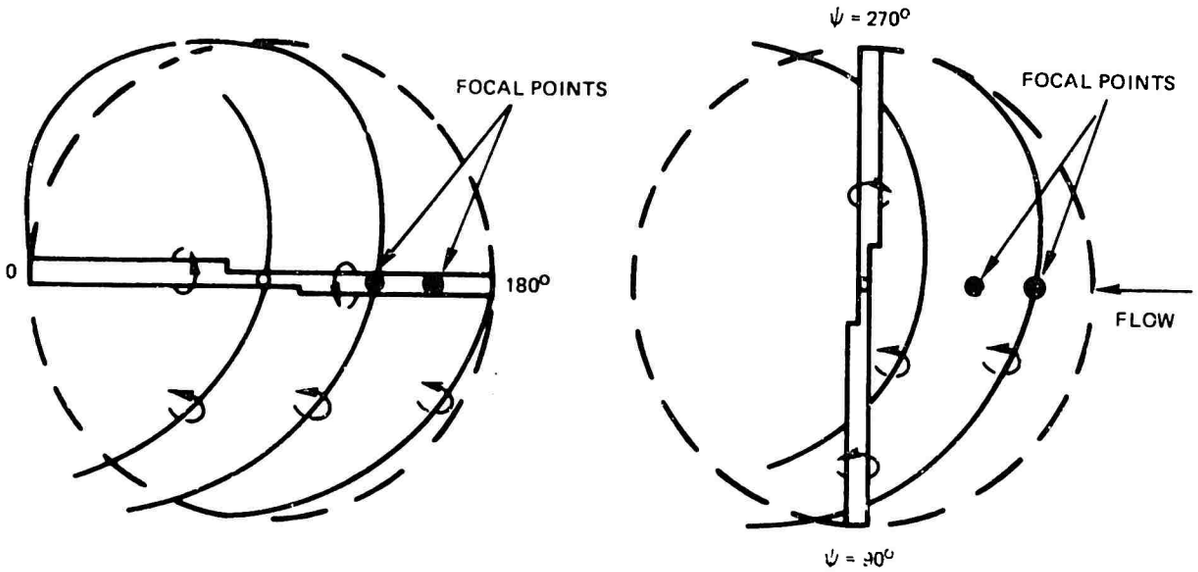

Figure 59. Schematic of Laser Velocimeter Focal Points Relative to Blades and Tip Vortices for Two Rotor Azimuth Positions--Landgrebe and Johnson $\mu = 0.15$, Top View.

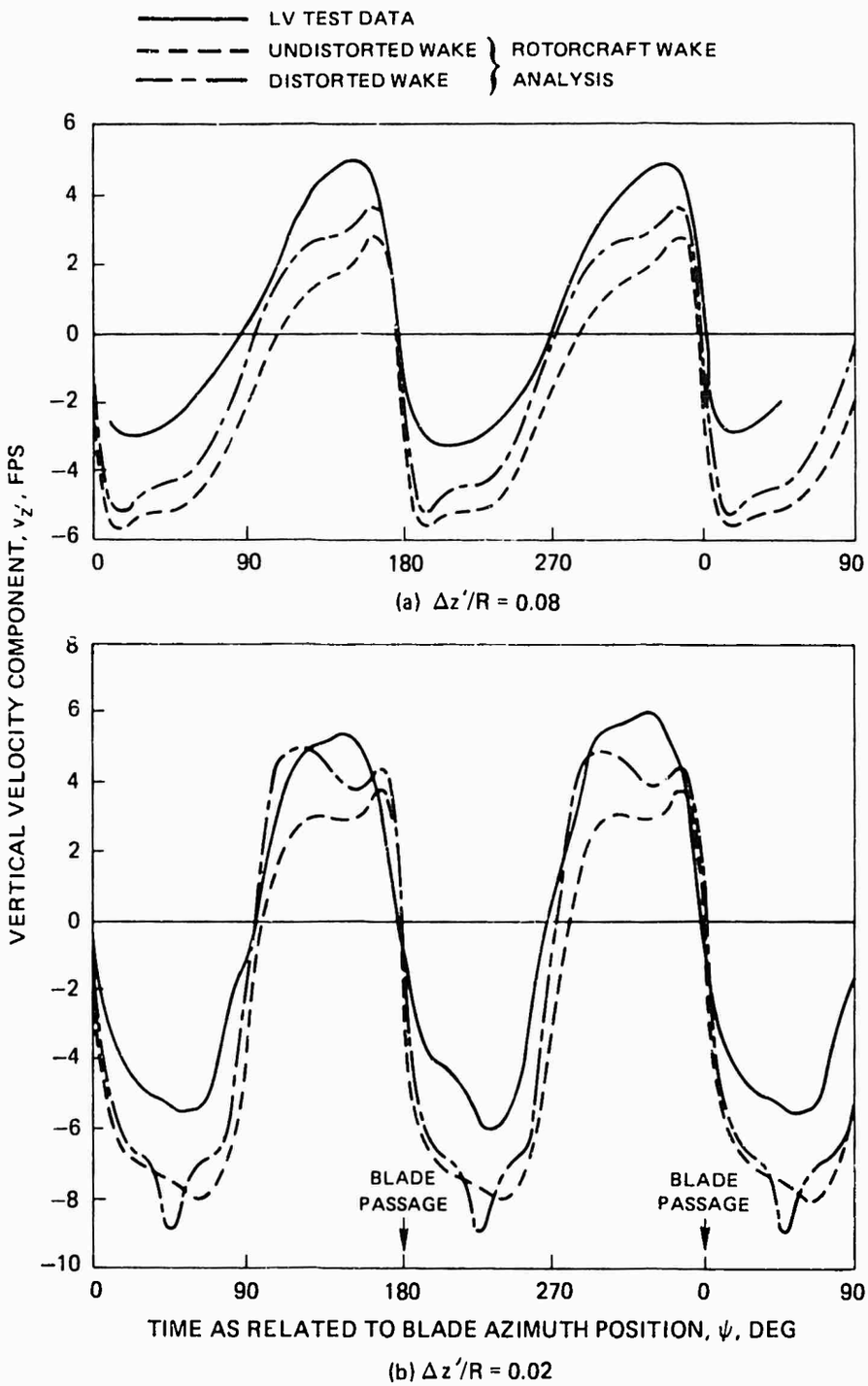

Figure 60. Comparison of Time Histories of the Vertical Component of Velocity for Three Focal Points at r/R = 0.75 -- Landgrebe and Johnson, $\mu = 0.15$.

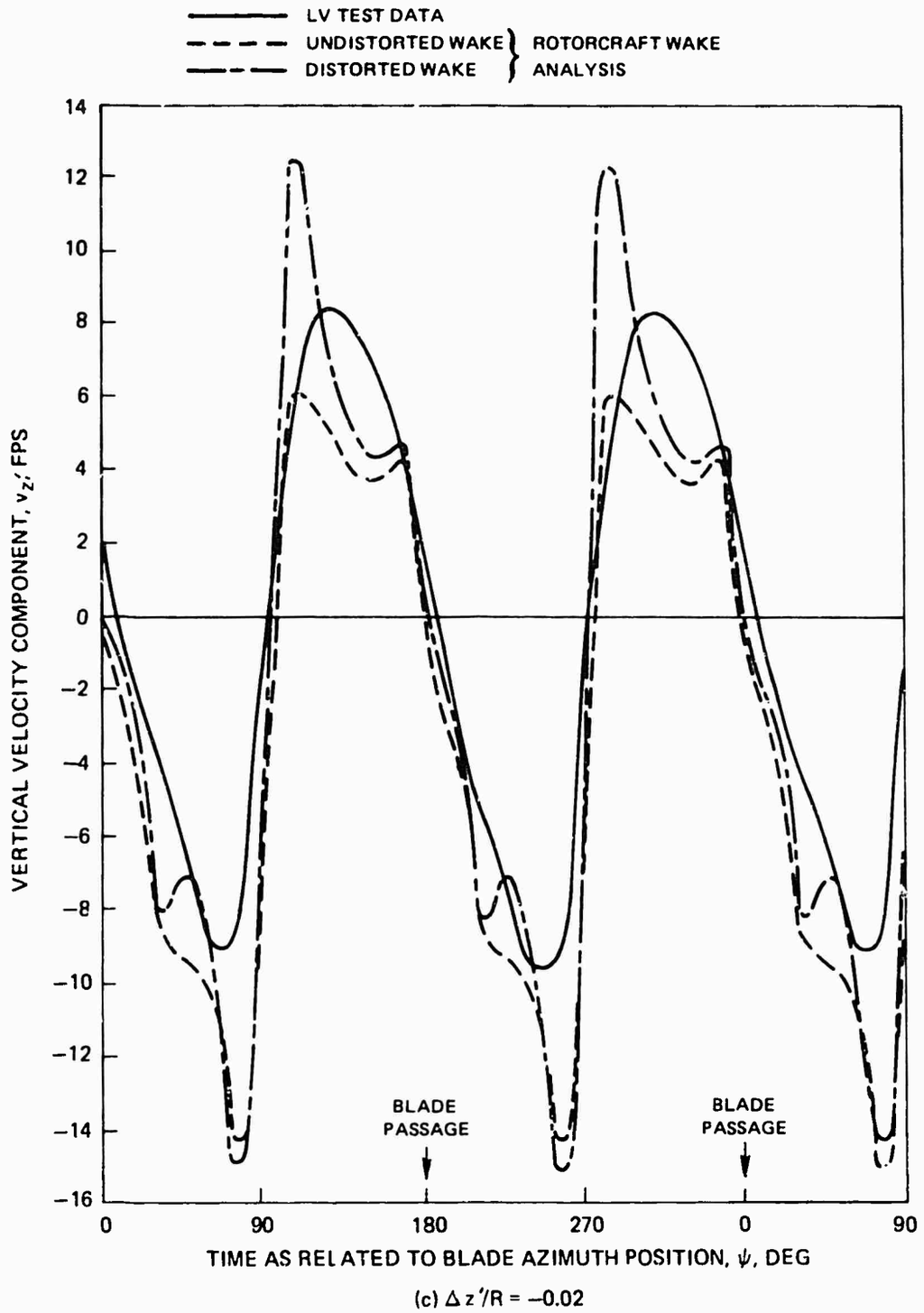

Figure 60. Concluded

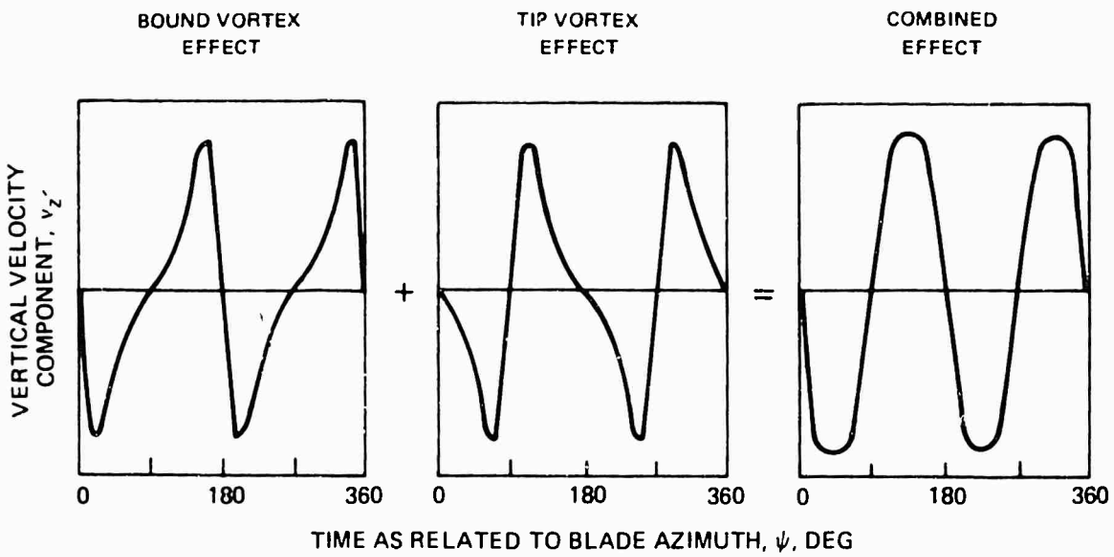

Figure 61. Illustration of Superposition of Bound and Tip Vortex Effects to Obtain Characteristic Shape of Time History of Vertical Velocity at r/R = 0.75 -- Landgrebe and Johnson, $\mu = 0.15$.

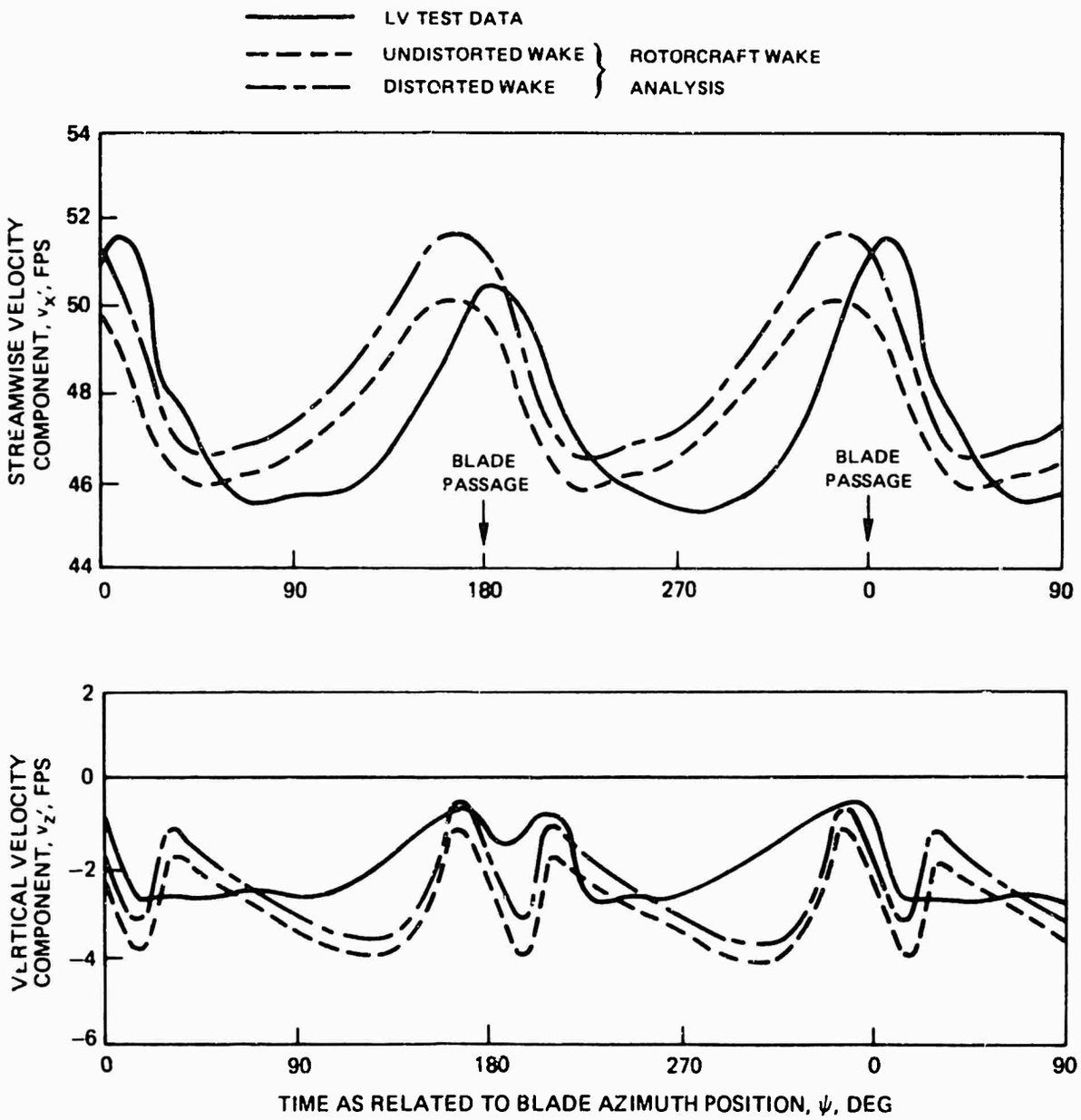

Figure 62. Comparison of the Time Histories of Vertical and Streamwise Velocity for a Focal Point at $r/R = 0.50$ $\Delta z'/R = 0.04$ -- Landgrebe and Johnson, $\mu = 0.15$.

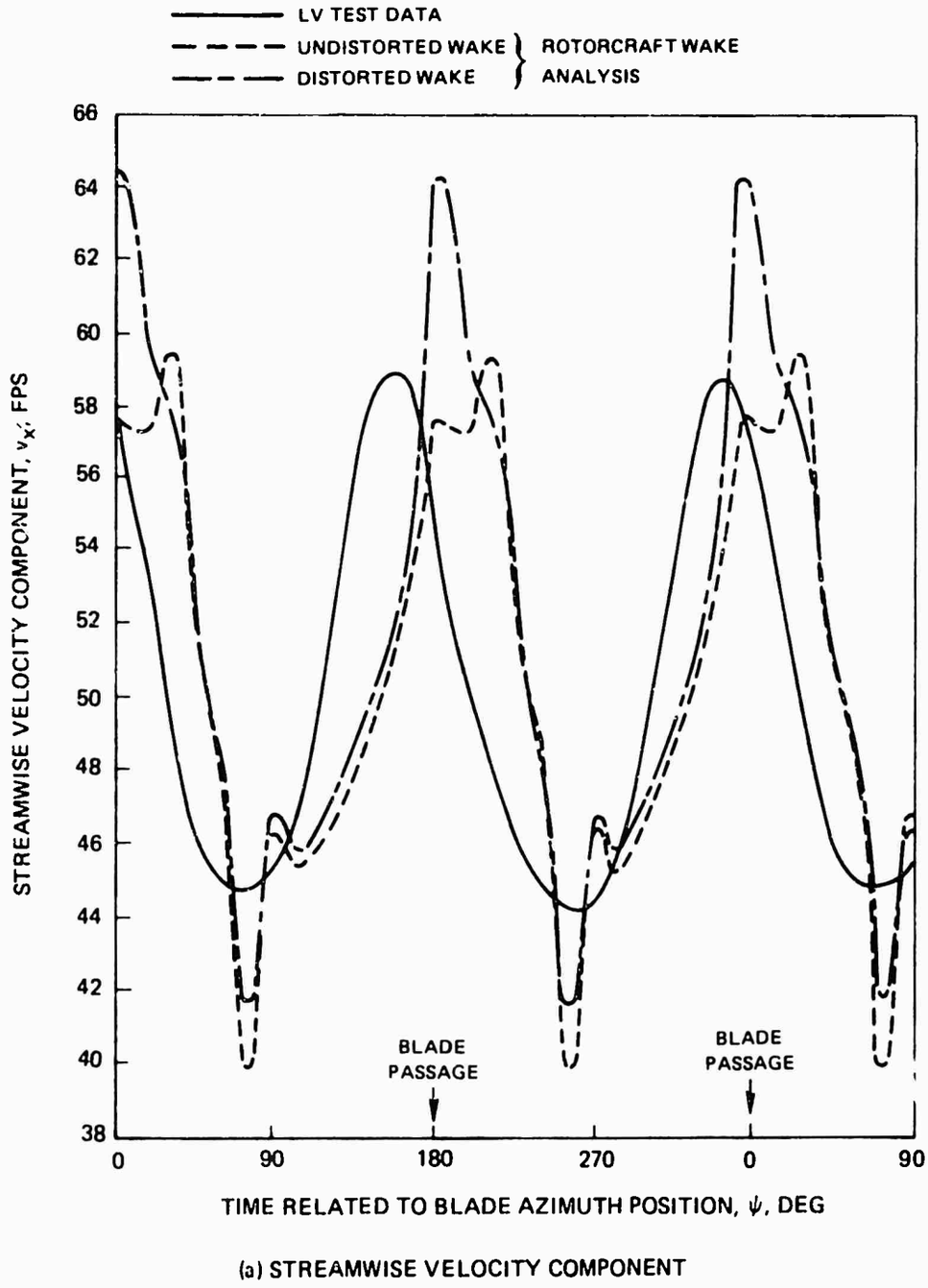

(a) STREAMWISE VELOCITY COMPONENT

Figure 63. Comparison of the Time Histories of Vertical and Streamwise Velocity for a Focal Point at r/R = 0.50 $\Delta z'/R$ = -0.04 -- Landgrebe and Johnson, μ = 0.15.

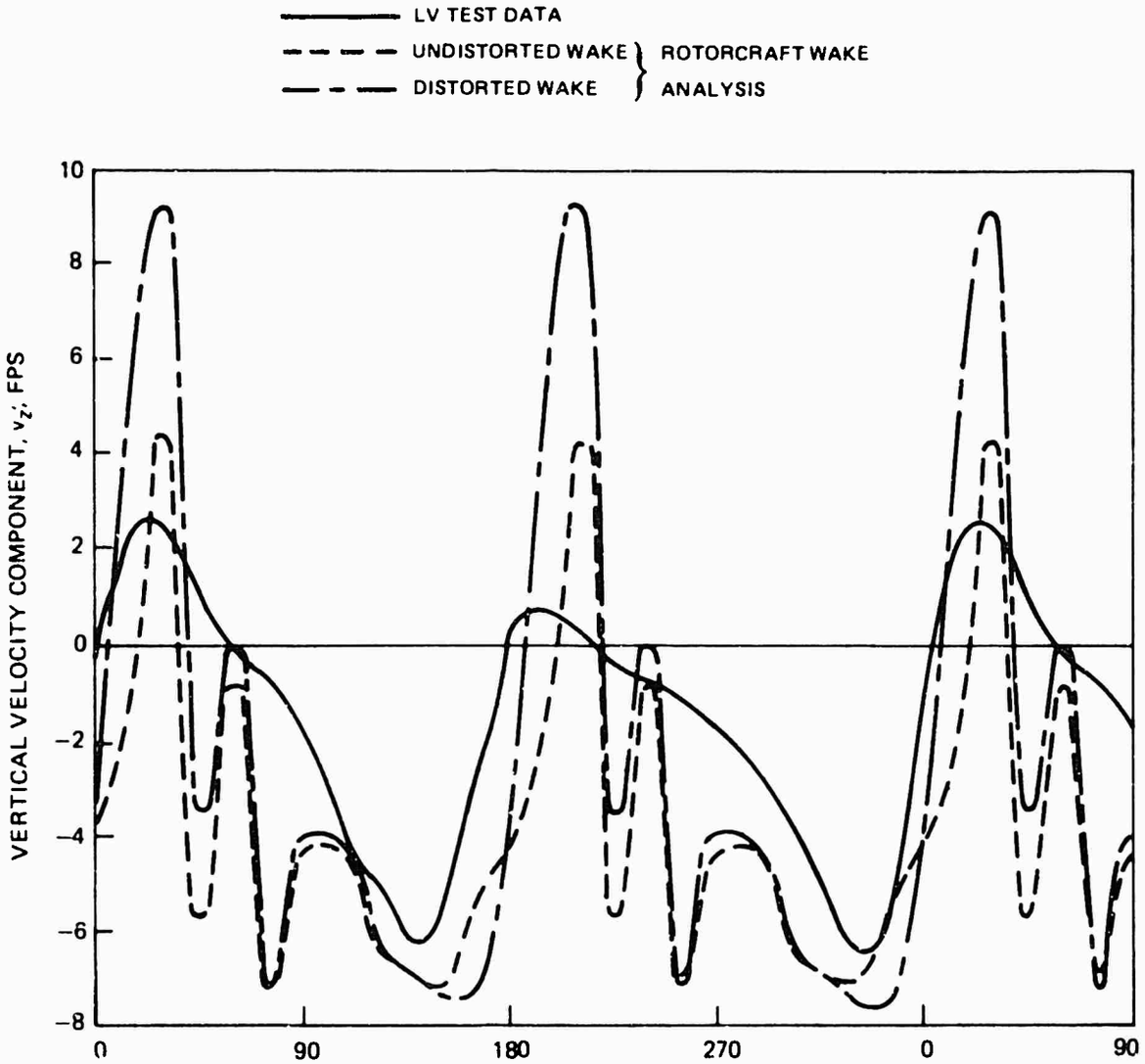

(b) VERTICAL VELOCITY COMPONENT

Figure 63. Concluded

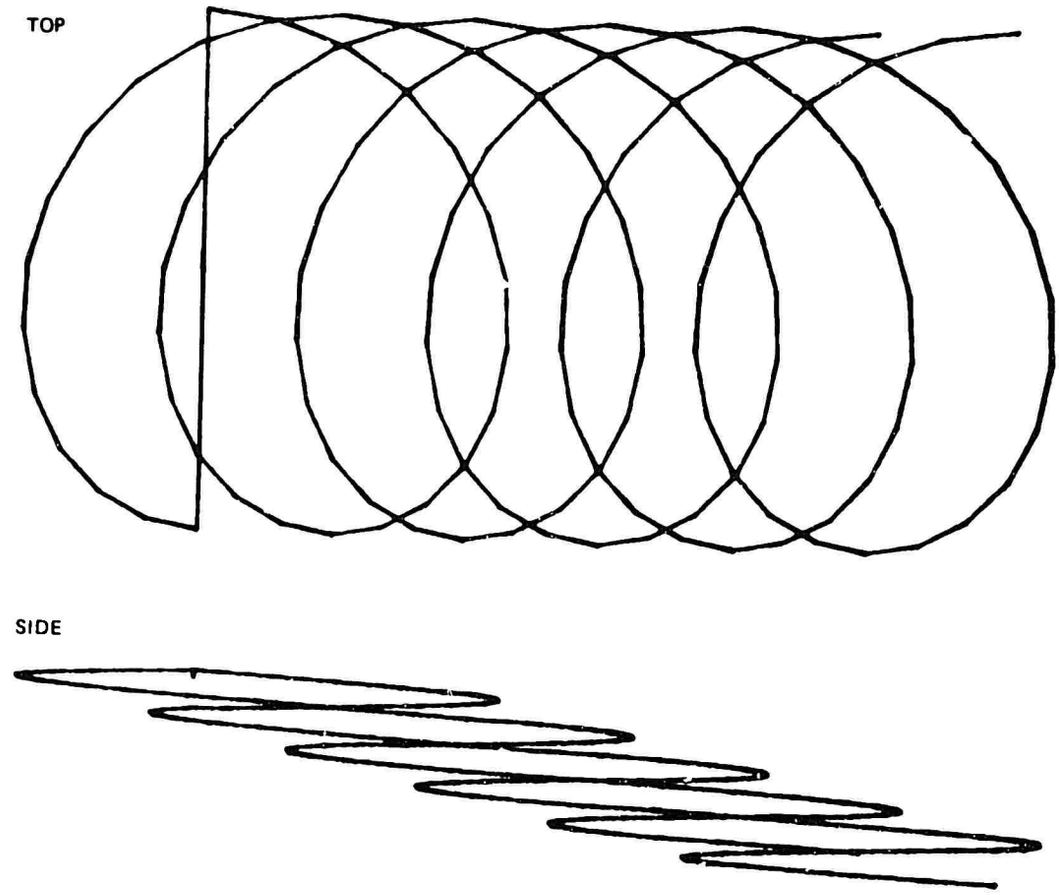

Figure 64. Three Views of Analytical Undistorted Tip Vortex Filament for Test Condition of Biggers and Orloff, $\mu = 0.18$.

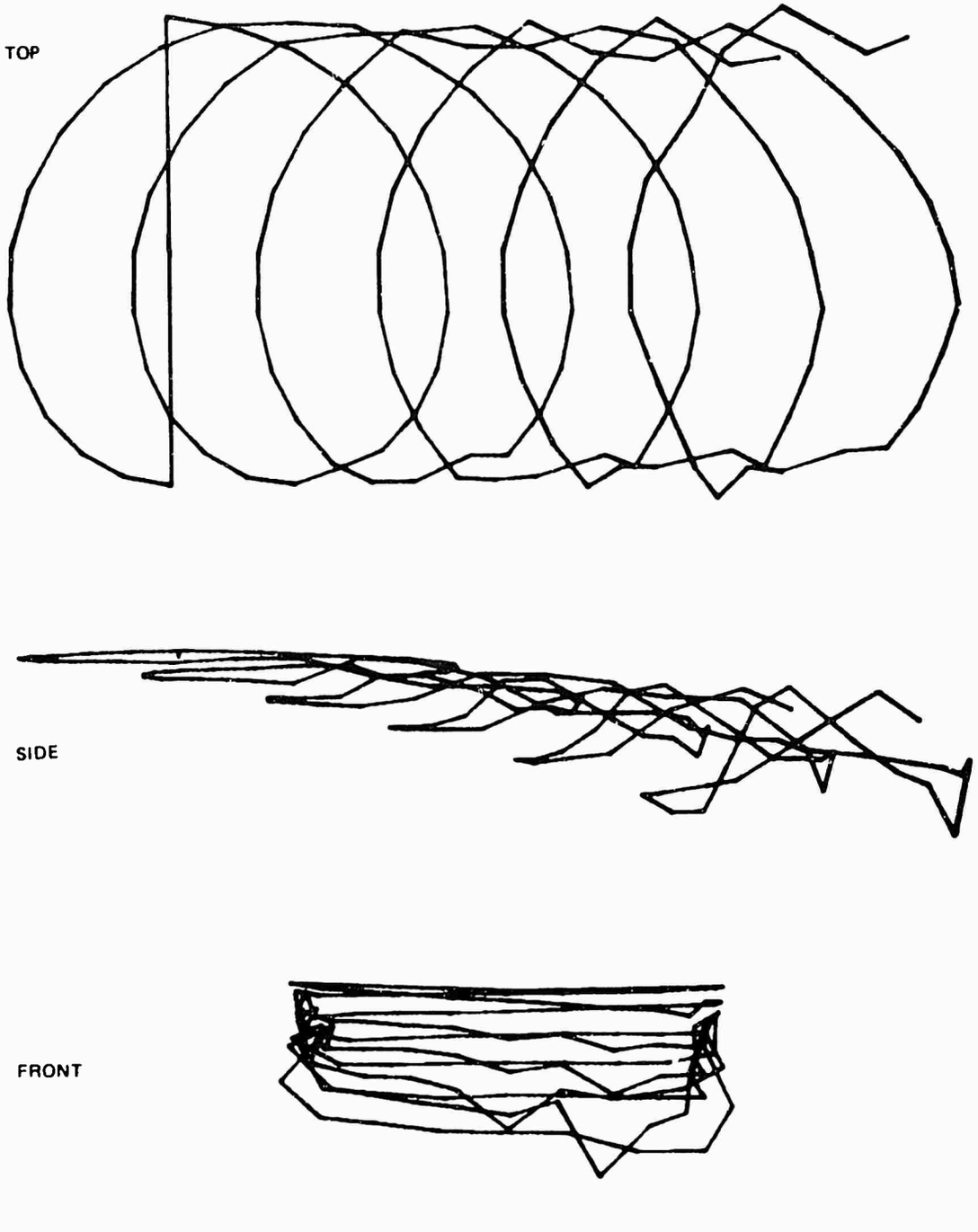

Figure 65. Three Views of Analytical Distorted Tip Vortex Filament for Test Conditions of Biggers and Orloff, $\mu = 0.18$.

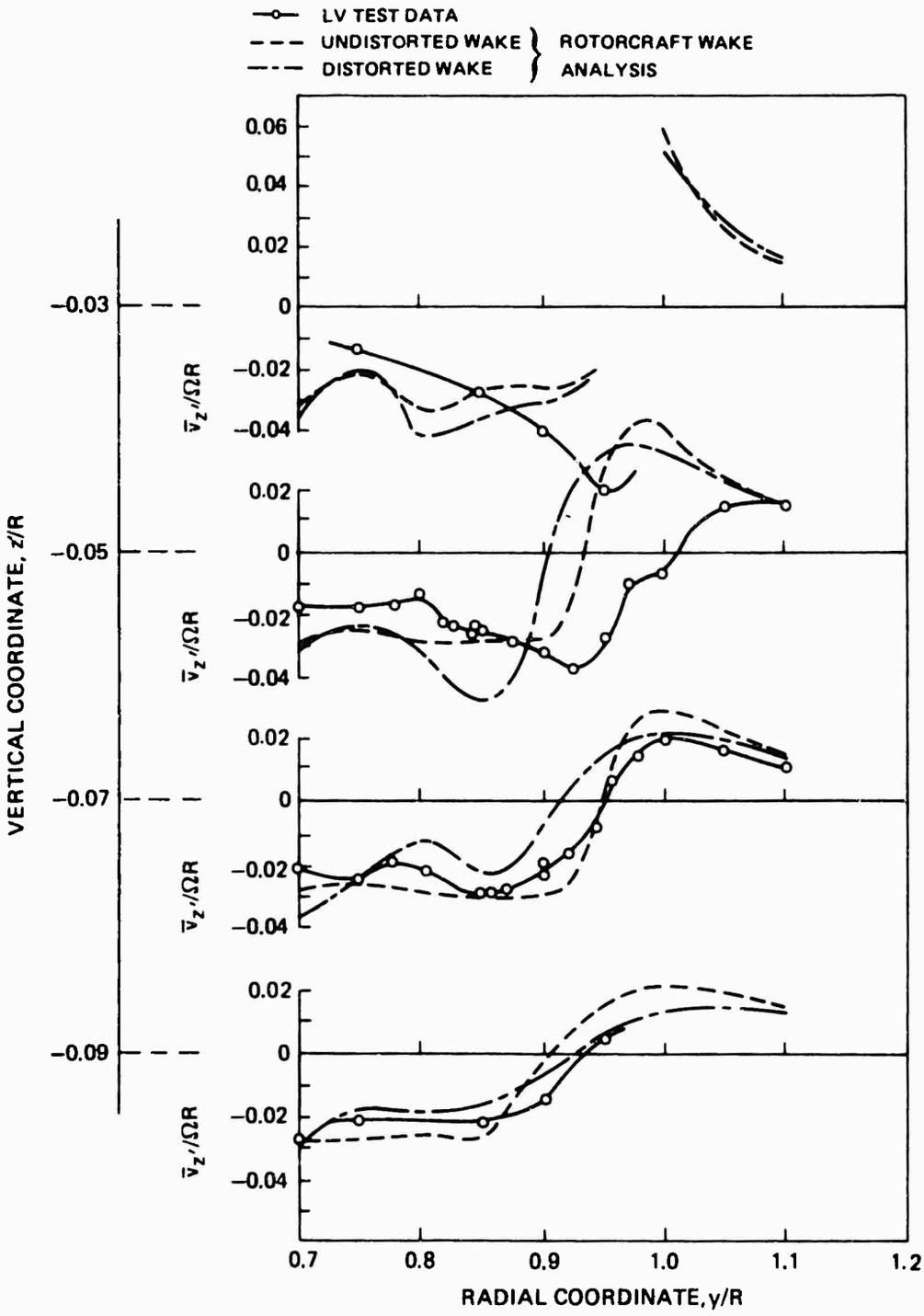

Figure 66. Comparisons of Radial Distributions of Time-Averaged Vertical Velocity on the Advancing Side for Several Vertical Positions--Biggers and Orloff, $\mu = 0.18$, $x/R = 0$.

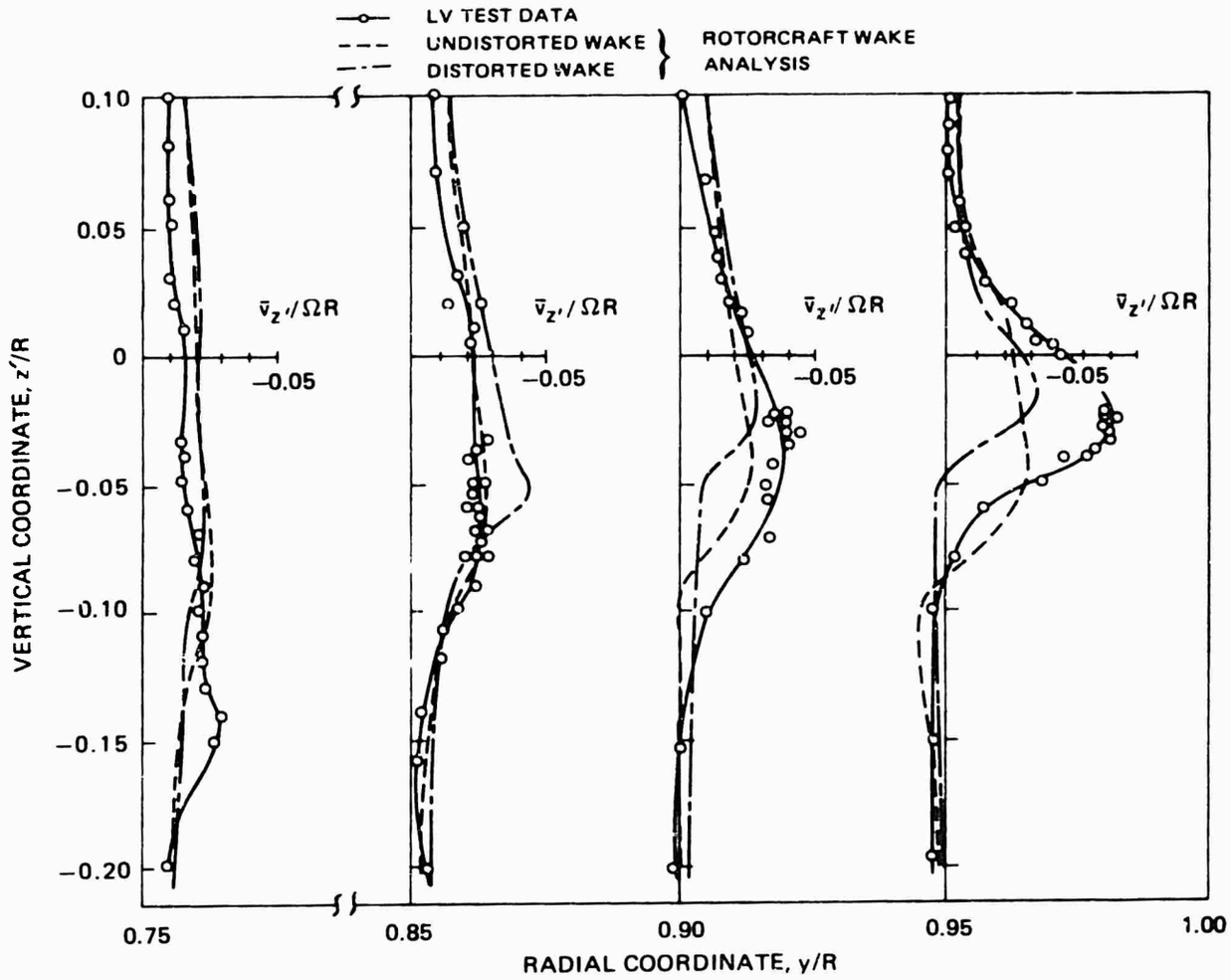

Figure 67. Comparisons of Vertical Distributions of Time-Averaged Vertical Velocity on the Advancing Side for Several Radial Positions-- Biggers and Orloff, $\mu = 0.18$, $x/R = 0$.

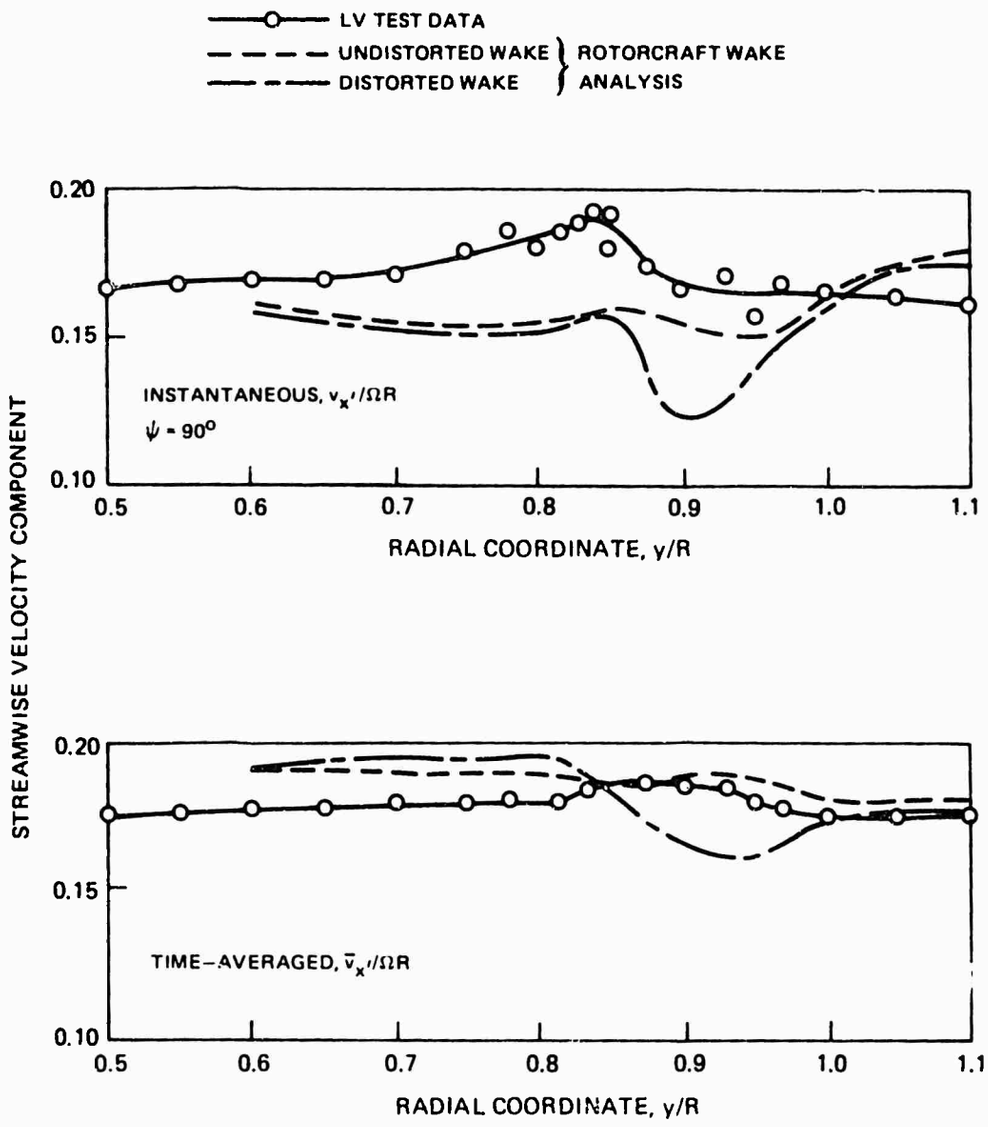

Figure 68. Comparisons of Radial Distributions of Time-Averaged and Instantaneous Streamwise Velocity on the Advancing Side at z/R = -0.05 -- Biggers and Orloff, μ = 0.18, x/R = 0.

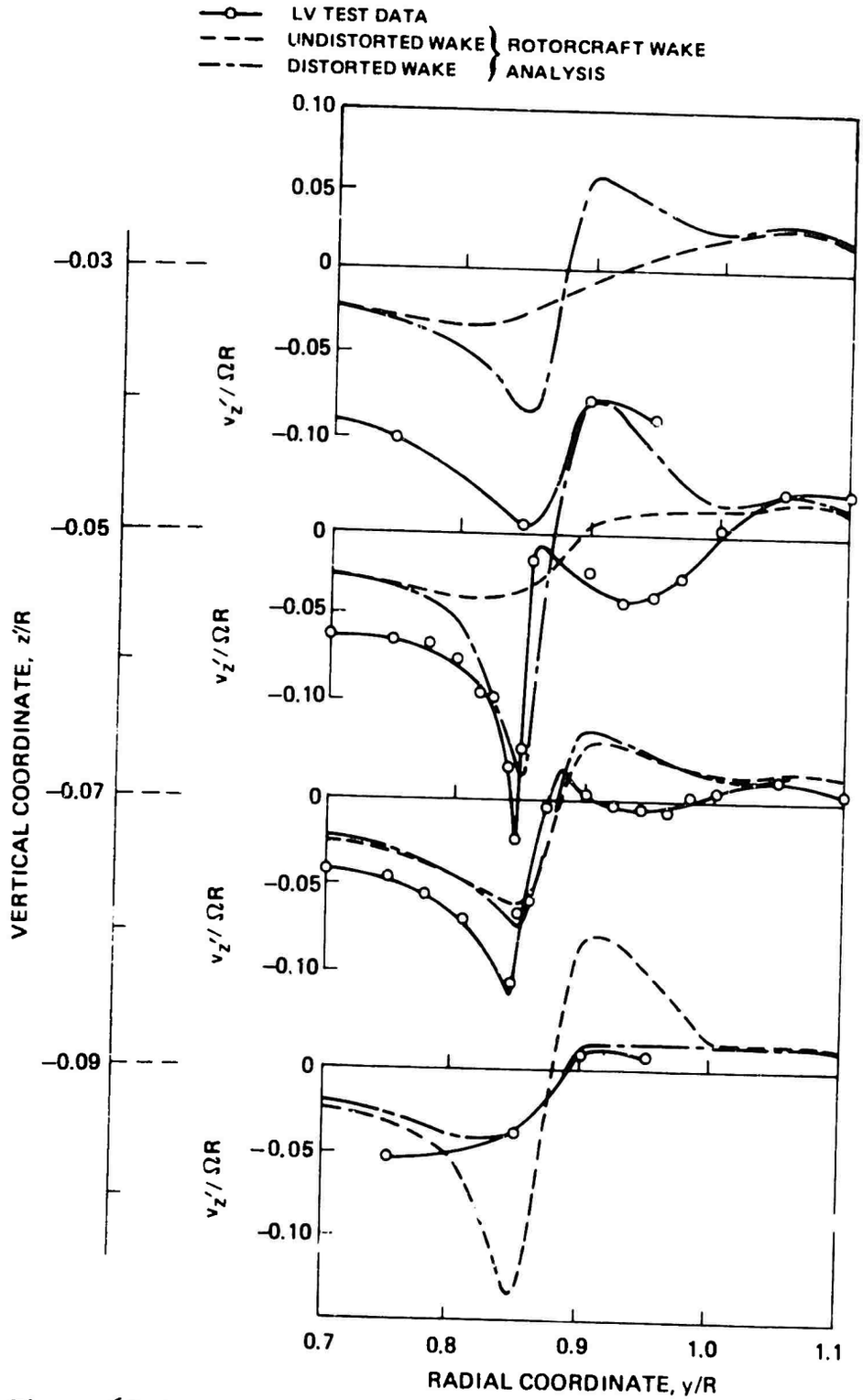

Figure 69. Comparisons of Radial Distributions of Instantaneous Vertical Velocity Under the Advancing Blade for Several Vertical Positions--Biggers and Orloff, $\mu = 0.18$, $x/R = 0$.

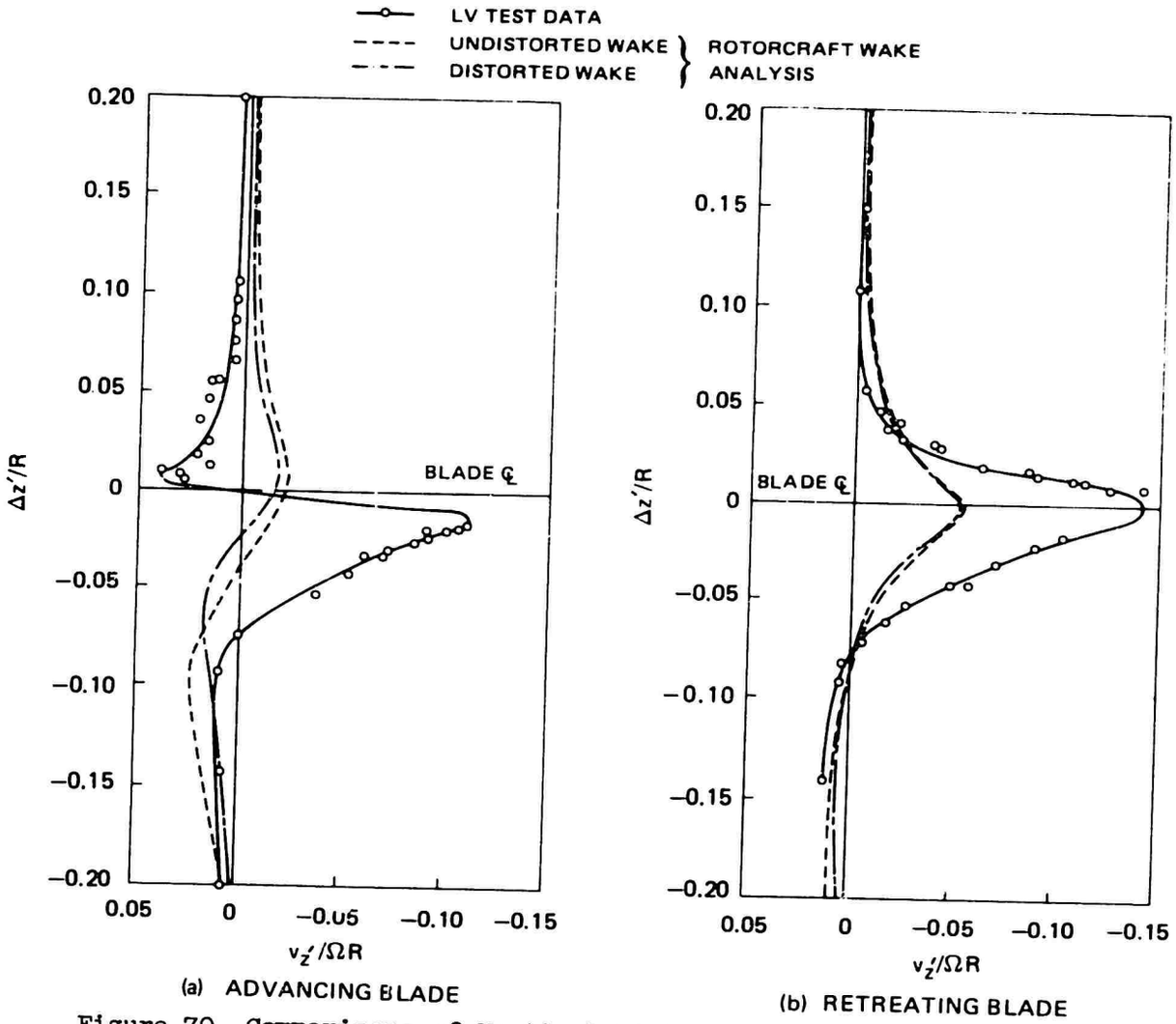

Figure 70. Comparisons of Vertical Distributions of Instantaneous Vertical Velocity Above and Below the 0.95R Station -- Biggers and Orloff, $\mu = 0.18$, $x/R = 0$, $r/R = 0.95$ $\psi = 90$ deg.

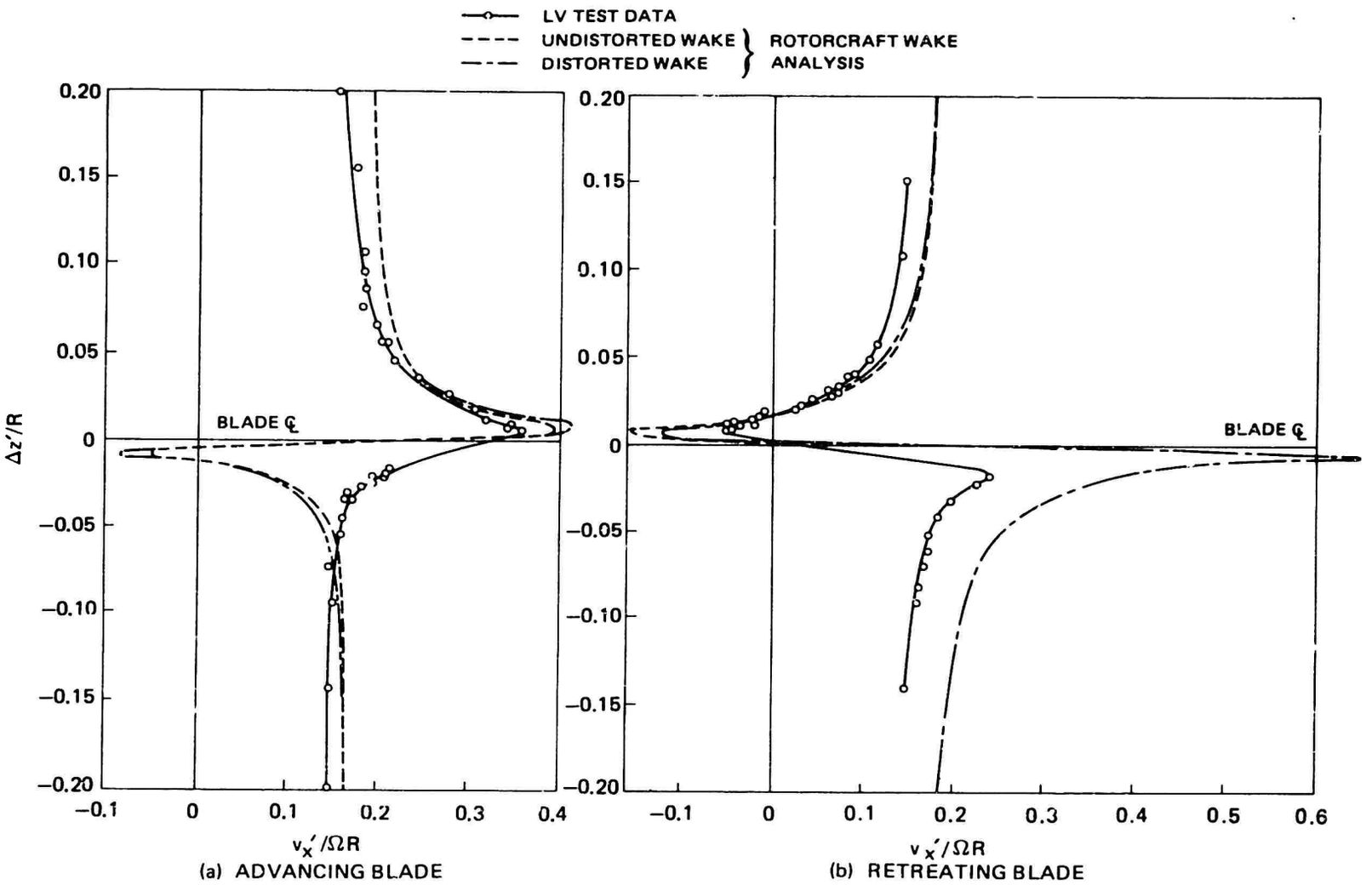

Figure 71. Comparisons of Vertical Distributions of Instantaneous Streamwise Velocity Above and Below the 0.95R Station--Biggers and Orloff, $\mu = 0.18$, $x/R = 0$, $r/R = 0.95$, $\psi = 90$ deg.

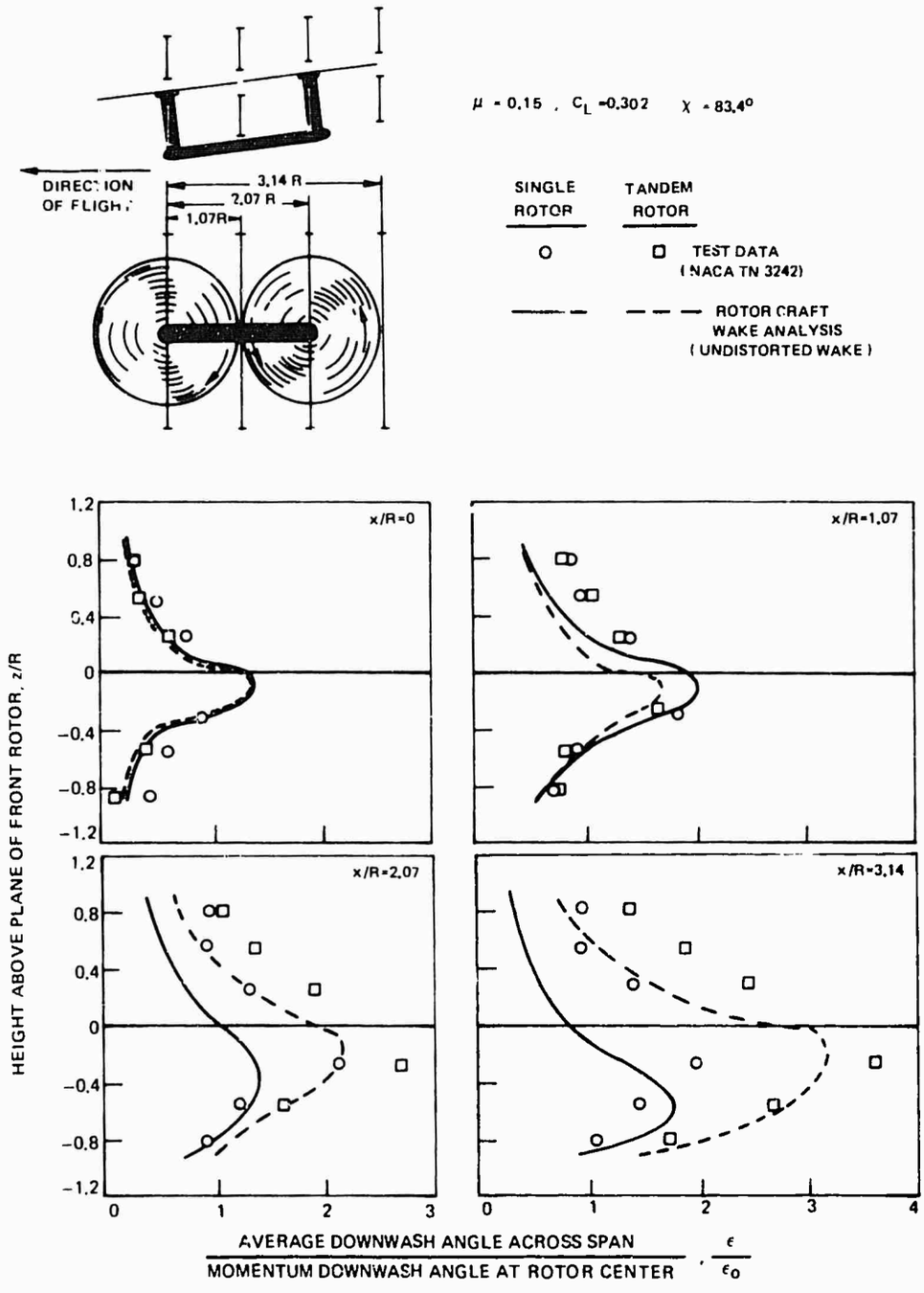

Figure 72. Comparison of Vertical Distributions of Spanwise- and Time-Averaged Downwash Angle at Several Streamwise Locations for a Single and Tandem Rotor--Heyson, NACA TN 3242, $\mu = 0.15$.

LITERATURE CITED

1. Landgrebe, A. J., and Cheney, M. C., ROTOR WAKES - KEY TO PERFORMANCE PREDICTION, AGARD-CP-111, AGARD Conference Proceedings No. 111 on Aerodynamics of Rotary Wings, Fluid Dynamics Panel Specialists Meeting, September 1972. (Also, paper presented at the Symposium on Status of Testing and Modeling Techniques for V/STOL Aircraft, Mideast Region of the American Helicopter Society, October 1972.)

2. Landgrebe, A. J., and Bellinger, E. D., AN INVESTIGATION OF THE QUANTITATIVE APPLICABILITY OF MODEL HELICOPTER ROTOR WAKE PATTERNS OBTAINED FROM A WATER TUNNEL, United Aircraft Research Laboratories; USAAMRDL Technical Report 71-69, Eustis Directorate, U.S. Army Air Mobility Research and Development Laboratory, Fort Eustis, Virginia, December 1971, AD739946.

3. Landgrebe, A. J., AN ANALYTICAL METHOD FOR PREDICTING ROTOR WAKE GEOMETRY; Journal of the American Helicopter Society, Vol. 14, No. 4, October 1969. (Also, AIAA Paper No. 69-196, AIAA/AHS VTOL Research, Design and Operations Meeting, Atlanta, Georgia, February 1969).

4. Bellinger, E. D., ANALYTICAL INVESTIGATION OF THE EFFECTS OF BLADE FLEXIBILITY, UNSTEADY AERODYNAMICS, AND VARIABLE INFLOW ON HELICOPTER ROTOR STALL CHARACTERISTICS, United Aircraft Research Laboratories, NASA CR-1769, NASA Langley Research Center, Langley, Virginia, September 1971.

5. Landgrebe, A. J., and Egolf, T. A., PREDICTION OF ROTOR WAKE INDUCED FLOW VELOCITIES ALONG THE ROCKET TRAJECTORIES OF AN ARMY AH-1G HELICOPTER, United Technologies Research Center; Picatinny Arsenal Technical Report 4797, U.S. Army Picatinny Arsenal, Dover, New Jersey, March 1975.

6. Clark, D. R., and Landgrebe, A. J., WAKE BOUNDARY LAYER EFFECTS IN HELICOPTER ROTOR AERODYNAMICS, AIAA Paper No. 71-581, AIAA 4th Fluid and Plasma Dynamics Conference, Palo Alto, California, June 21-23, 1971.

7. Arcidiacono, P. J., and Carlson, R. G., HELICOPTER ROTOR LOADS PREDICTION, Paper presented at the AGARD Specialists Meeting on Prediction and Verificantion of Loads on Helicopters, No. 7, Milan, Italy, April 11-12, 1973.

8. Landgrebe, A. J., AN ANALYTICAL AND EXPERIMENTAL INVESTIGATION OF HELICOPTER ROTOR HOVER PERFORMANCE AND WAKE GEOMETRY CHARACTERISTICS, United Aircraft Research Laboratories; USAAMRDL Technical Report 71-24, Eustis Directorate, U.S. Army Air Mobility Research and Development Laboratory, Fort Eustis, Virginia, June 1971, AD728835.

9. Landgrebe, A. J., THE WAKE GEOMETRY OF A HOVERING HELICOPTER ROTOR AND ITS INFLUENCE ON ROTOR PERFORMANCE, Journal of the American Helicopter Society, Vol. 17, No. 4, October 1972 (Also preprint No. 620, 28th Annual National Forum of the American Helicopter Society, May 1972.)

10. Jenney, D. S., Olson, J. R., and Landgrebe, A. J., A REASSESSMENT OF ROTOR HOVERING PERFORMANCE PREDICTION METHODS, United Aircraft Research Laboratories, Journal of the American Helicopter Society, Vol. 13, No. 2, April 1968, pp. 1-26.

11. Bellinger, E. D., EXPERIMENTAL INVESTIGATION OF EFFECTS OF BLADE SECTION CAMBER AND PLANFORM TAPER ON ROTOR HOVER PERFORMANCE, United Aircraft Research Laboratories; USAAMRDL Technical Report 72-4, Eustis Directorate, U.S. Army Air Mobility Research and Devlopment Laboratory, Fort Eustis, Virginia, March 1972, AD743232.

12. Bain, L. J., and Landgrebe, A. J., INVESTIGATION OF COMPOUND HELICOPTER AERODYNAMIC INTERFERENCE EFFECTS, United Aircraft Corporation, USAAVLABS Technical Report 67-44, U.S. Army Aviation Materiel Laboratories, Fort Eustis, Virginia, November 1967, AD665427.

13. Landgrebe, A. J., and Bellinger, E. D., EXPERIMENTAL INVESTIGATION OF MODEL VARIABLE-GEOMETRY AND OGEE TIP ROTORS, Prepared by United Aircraft Research Laboratories for the Langley Research Center, NASA, NASA CR-2275, February 1974. (Paper with Same Title: AHS Paper No. 703, 29th Annual National Forum of the American Helicopter Society, May 1973.)

14. Piziali, R. A., and DuWaldt, F. A., A Method for Computing Rotary Wing Airload Distributions in Forward Flight, Cornell Aeronautical Laboratory, Inc.; U.S. Army TRECOM Report TCREC TR62-44, U.S. Army Transportation Research Command, Fort Eustis, Virginia, November 1962.

15. Miller, R. H., UNSTEADY AIRLOADS ON HELICOPTER BLADES, Jl. Royal Aeronautical Society, Vol. 68, No. 640, April 1964.

16. Clark, D. R., CAN HELICOPTER ROTORS BE DESIGNED FOR LOW NOISE AND HIGH PERFORMANCE? Preprint 803, presented at the 30th Annual National Forum of the American Helicopter Society, May 1974.

17. Ladden, R. M., and Gilmore, D. C., ADVANCED V/STOL PROPELLER TECHNOLOGY, United Aircraft Research Laboratories, Hamilton Standard Division, Air Force Flight Dynamics Laboratory Report AFFDL-TR-71-88, Vo. II, Air Force Flight Dynamics Laboratory, V/STOL Division, Air Force Systems Command, Wright Patterson Air Force Base, Ohio, September 1971.

18. Boatwright, D. W., MEASUREMENTS OF VELOCITY COMPONENTS IN THE WAKE OF A FULL-SCALE HELICOPTER ROTOR IN HOVER, Mississippi State University; USAAMRDL Technical Report 72-33, Eustis Directorate, U.S. Army Air Mobility Research and Development Laboratory, Fort Eustis, Virginia, August 1972, AD754644.

19. Heyson, H. H., MEASUREMENTS OF THE TIME-AVERAGED AND INSTANTANEOUS INDUCED VELOCITIES IN THE WAKE OF A HELICOPTER ROTOR HOVERING AT HIGH TIP SPEEDS, NASA Technical Note D-393, July 1960.

20. McKee, J. W., and Naeseth, R. L., EXPERIMENTAL INVESTIGATION OF THE DRAG OF FLAT PLATES AND CYLINDERS IN THE SLIPSTREAM OF A HOVERING ROTOR, National Advisory Committee for Aeronautics Technical Note 4239, April 1958.

21. Fradenburgh, E. A., FLOW FIELD MEASUREMENTS FOR A HOVERING ROTOR NEAR THE GROUND, Paper presented at 5th Annual Western Forum of the American Helicopter Society, Los Angeles, California, September 25, 26, 1958.

22. Flemming, R. J., 1/20 SCALE MODEL ROTOR WAKE SURVEY, Sikorsky Aircraft Internal Documents, May 1969 and March 1972 (unpublished).

23. Miller, N., Tang, J. C., and Perlmutter, A. A., THEORETICAL AND EXPERIMENTAL INVESTIGATION OF THE INSTANTANEOUS INDUCED VELOCITY FIELD IN THE WAKE OF A LIFTING ROTOR, Dynasciences Corporation; USAAVLABS Technical Report 67-68, U.S. Army Aviation Materiel Laboratories, Fort Eustis, Virginia, January 1968, AD667384.

24. Heyson, H. H., and Katzoff, S., INDUCED VELOCITIES NEAR A LIFTING ROTOR WITH NONUNIFORM DISK LOADING, NACA Technical Report 1319, 1957.

25. Landgrebe, A. J., and Johnson, B. V., MEASUREMENT OF MODEL HELICOPTER ROTOR FLOW VELOCITIES WITH A LASER DOPPLER VELOCIMETER, Jl. American Helicopter Society, Vol. 19, No. 3, July 1974.

[illegible], [illegible] et al, [illegible], [illegible] THE "DIGITAL MEASUREMENT [illegible] [illegible] [illegible] BLADE [illegible], Jl. American Helicopter [illegible], [illegible], [illegible] 1, January 1975.

[illegible], [illegible], [illegible], "[illegible]" [illegible] "[illegible]-[illegible] MEASUREMENT [illegible] [illegible] IN AN [illegible]" [illegible] IN THE [illegible] FULL-SCALE FUTEL, [illegible] [illegible] [illegible] [illegible] Aeronautical Note [illegible], [illegible] 1974.

APPENDIX A

BIOT-SAVART LAW AS APPLIED TO A VORTEX ELEMENT

The velocities induced at an arbitrary point P by a straight vortex element of strength Γ and bounded by end points A and B can be computed using the classical Biot-Savart Law. The equations presented below are in Cartesian form. These equations apply only in the irrotational flow region outside of the vortex core.

$$v_{x_P} = \left(\frac{\Gamma}{4\pi}\right)\bar{k}\left[(y_P - y_A)(z_P - z_B) - (z_P - z_A)(y_P - y_B)\right] \tag{A-1}$$

$$v_{y_P} = \left(\frac{\Gamma}{4\pi}\right)\bar{k}\left[(z_P - z_A)(x_P - x_B) - (x_P - x_A)(z_P - z_B)\right] \tag{A-2}$$

$$v_{z_P} = \left(\frac{\Gamma}{4\pi}\right)\bar{k}\left[(x_P - x_A)(y_P - y_B) - (y_P - y_A)(x_P - x_B)\right] \tag{A-3}$$

where

$$\bar{k} = \frac{1}{R}\,\frac{(AP + BP)\,/\,(AP)(BP)}{(AP)(BP) + I + J + K} \tag{A-4}$$

$$I = (x_P - x_A)(x_P - x_B) \tag{A-5}$$

$$J = (y_P - y_A)(y_P - y_B) \tag{A-6}$$

$$K = (z_P - z_A)(z_P - z_B) \tag{A-7}$$

$$AP = \sqrt{(x_P - x_A)^2 + (y_P - y_A)^2 + (z_P - z_A)^2} \tag{A-8}$$

$$BP = \sqrt{(x_P - x_B)^2 + (y_P - y_B)^2 + (z_P - z_B)^2} \tag{A-9}$$

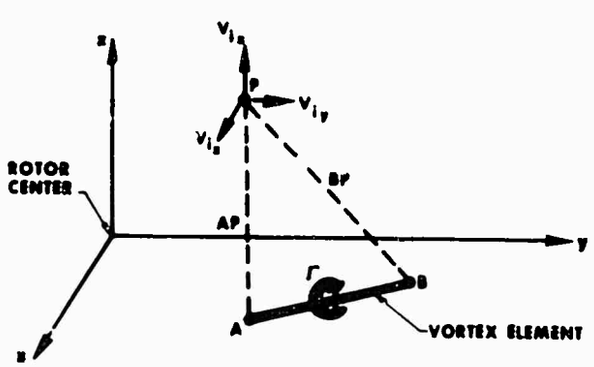

APPENDIX B

PRIMARY EQUATIONS FOR THE UTRC PRESCRIBED WAKE ROTOR INFLOW ANALYSIS*

In order to relate to the program input-output symbols and to describe some of the symbols generated within the program, program symbol notation is generally used in the following equations.

The blade circulation at any blade segment I, for any azimuthal position J, is, from the Kutta-Joukowski relation,

$$CIRC(I,J) = C(I) \cdot U(I,J) \cdot CL(I,J)/2 \qquad \text{(B-1)}$$

where CIRC(I,J) = local blade element circulation, ft^2/sec
C(I) = local blade element chord, ft
U(I,J) = local blade element resultant velocity, fps
CL(I,J) = local blade element lift coefficient

The local blade element resultant velocity U(I,J) can be expressed as

$$U(I,J)^2 = [UT(I,J) + UTI(I,J)]^2 + [W1(I,J) + W(I,J)]^2 \qquad \text{(B-2)}$$

where $$UT(I,J) = OMGR \cdot (RS(I) + MU \cdot SIN(PSI)) \qquad \text{(B-3)}$$

and OMGR = Rotor tip speed, fps
MU = Rotor advance ratio
RS(I) = Rotor blade segment radial position (nondimensionalized by R)
UTI(I,J) = Induced tangential velocity, fps
W(I,J) = Induced inflow velocity, fps

and with small angle assumptions,

---

* The fundamental background for the analytical formulation used in the computer program was obtained from the technical approach described by Piziali and DuWaldt in Reference 14. Although a new computer program has been developed, and many modifications and refinements have been incorporated, practicularly in regard to wake representation, many of the fundamental assumptions are retained from that reference.

W1(I,J) = Noninduced inflow velocity (flapping, pitching, aeroelastics, etc.), fps.

For helicopter rotors, UTI(I,J) may be neglected. Also since W(I,J) and W1(I,J) are small in the important blade tip region relative to the rotational velocity, it is assumed that

$$U(I,J) = UT(I,J) \tag{B-4}$$

so that a linear closed form solution can be obtained. Also in order to linearize the solution, the lift coefficient is expressed as

$$CL(I,J) = AT(I,J) \cdot ALPHAE(I,J) \tag{B-5}$$

where AT(I,J) = local blade element lift curve slope
ALPHAE(I,J) = local blade element angle of attack

In stall, the maximum lift coefficient is limited in the program to CLMAX(I,J) which is determined from input values of angle-of-attack values (ALMAX(I,J) beyond which stall is assumed. The angle of attack is, for small angle assumptions and consistent with the above assumptions,

$$ALPHAE(I,J) = [W1(I,J) + W(I,J)] / UT(I,J) \tag{B-6}$$

Substituting Equations (B-4) through (B-6) into Equation (B-1), the circulation equation becomes,

$$CIRC(I,J) = C(I) \cdot AT(I,J) \cdot [W1(I,J) + W(I,J)] / 2 \tag{B-7}$$

Since there are MSIZE unknowns,

where MSIZE = (ITOT + 1) · JTOT and ITOT and JTOT are the total number of blade segments and azimuth positions,

there are MSIZE equations of the form of Equation (B-7). This set of MSIZE equations can be written in matrix notation as:

$$CIRC(I,J) = [C(I) \cdot AT(I,J) \cdot \{W1(I,J) + W(I,J)\}] \tag{B-8}$$

The axial induced velocity in Equations (B-7) and (B-8) is expressed, using the Biot-Savart law, as a function of the trailing wake filaments and circulation strengths. The axial velocity induced by a given wake segment (subscript M) of filament K at a given blade segment (I,J) is expressed in terms of the Biot-Savart law as

$$W(K,M) = CIRCT(K,M)/4\pi R \cdot GC(K,M) \qquad (B\text{-}9)$$

where CIRCT(K,M) = circulation strength of the Mth segment of the Kth filament, ft^2/sec

GC(K,M) = geometric influence coefficient from the Biot-Savart law

The geometric coefficient, GC, is a function of the prescribed wake coordinates X(K,M), Y(K,M), Z(K,M). The lengthy expressions for GC may be obtained from the program listing. Since the circulation distribution is assumed to be periodic in time for the forward flight condition, each wake filament has a periodic circulation strength distribution along its length. The total axial induced velocity due to contributions of all trailing circulations for all of the filaments at the blade point (I,J) is the sum of Equation (B-9) evaluated for all segments in the wake. The resultant expression from Equation (B-9) becomes

$$W(I,J) = \frac{1}{4\pi R} \sum_{K}^{KLIM} \sum_{M}^{MLIM} CIRCT(K,M) \cdot GC(K,M) \qquad (B\text{-}10)$$

where KLIM is the total number of trailing filaments, and MLIM is the total number of segment end points for each filament.

However since the circulations are periodic in M this relationship can be expressed by combining elements with like circulations,

$$W(I,J) = \frac{1}{4\pi R} \sum_{K}^{KLIM} \sum_{MM}^{JTOT} CIRCT(K,MM) \cdot GCTROW(K,MM) \qquad (B\text{-}11)$$

where

$$GCTROW(K,MM) = \sum_{(M=MM)}^{MLIM} GC(K,M)$$

MM combines all elements of a vortex filament shed from a blade at the same blade azimuth position, and thus combines elements with like circulations. The total induced velocity due to all bound circulations of the rotor can be expressed as,

$$WB(I,J) = \frac{1}{4\pi R} \sum_{IB}^{B} \sum_{I}^{ITOT} \sum_{MM}^{JTOT} CIRC(I,MM) \cdot GCB(I,MM) \qquad (B\text{-}12)$$

where GCB(I,MM) = geometric coefficient due to bound circulation (using Biot-Savart law)

WB(I,J) = induced axial velocity due to bound circulation

IB = number of blades

ITOT = number of bound segments per blade

In order to express the total axial induced velocity due to all of the trailing circulations in terms of the bound circulation, the circulation strength of each trailing filament segment may be expressed as the difference between the bound circulation of the two blade segments adjacent to its point of origin at the blade at the time of generation. Thus,

$$CIRCT(K,MM) = CIRC(K,MM) - CIRC(K-1,MM) \qquad \text{(B-13)}$$

Substituting Equation (B-12) and Equation (B-13) in Equation (B-11) the total axial induced velocity becomes

$$W(I,J) + \frac{1}{4\pi R} \sum_{K}^{KLIM} \sum_{MM}^{JTOT} CIRCT(K,MM) \cdot GCTROW(K,MM) \qquad \text{(B-14)}$$

$$+ \frac{1}{4\pi R} \sum_{IB}^{B} \sum_{I}^{ITOT} \sum_{MM}^{JTOT} CIRC(I,M) \cdot GCB(I,MM)$$

Rearranging Equation (IB-14) to combine like circulations leads to

$$W(I,J) = \frac{1}{4\pi R} \sum_{IB}^{B} \sum_{II}^{ITOT} \sum_{MM}^{JTOT} CIRC(II,MM) \cdot GCDIM(II,MM) \qquad \text{(B-15)}$$

where GCDIM(II,MM) = GCTROW(II+1,MM) - GCTROW(II,MM) + GCT(II,MM)

Substitution of Equation (B-15) in Equation (B-8) results in a matrix equation in which the only unknowns are the bound circulation, CIRC(I,J)

$$[CIRC] = [CONST] + \{GCMAT\}\,[CIRC] \qquad \text{(B-16)}$$

where GCMAT = final matrix influence coefficients

CONST = matrix constants which are functions of the following known quantities: R, UT, AT, C, and blade twist.

Solving for CIRC:

$$[CIRC] = [CONST]\,\{1\text{-}GCMAT\}^{-1} \qquad \text{(B-17)}$$

A Gauss-Seidal numerical iteration technique for evaluating this circulation matrix is included in the computer program. Following the circulation solution, the induced velocity distribution is obtained from Equation (B-8).

The above equations are the fundamental equations in the analysis for unstalled, potential flow conditions. Modifications providing for blade stall and finite vortex core size are included in the computer program.

APPENDIX C

GENERALIZED WAKE EQUATIONS FOR HOVERING ROTOR

The generalized wake equations for a hovering rotor, based on the model rotor experimental data of Reference 8, are presented below. These equations have been taken directly from Reference 8, where they are described in greater detail. The flow visualization data in the near stable wake region of the rotor was used in the generalization, and thus the equations are not intended to accurately represent the unstable far wake. However, for performance calculations at the rotor, the wake instability generally occurs sufficiently distant from the rotor to allow the far wake to be approximated by the generalized wake equations.

The generalized wake equations (applicable in the stable wake region) are summarized below.

Tip Vortex Axial Coordinates:

$$\bar{z}_T = \begin{cases} k_1 \psi_w \quad \text{for} \quad 0 \le \psi_w \le \dfrac{2\pi}{b} & \text{(C-1)} \\ (\bar{z}_T)_{\psi_w = \frac{2\pi}{b}} + k_2 \left(\psi_w - \dfrac{2\pi}{b}\right) \quad \text{for} \quad \psi_w \ge \dfrac{2\pi}{b} & \text{(C-2)} \end{cases}$$

$$k_1 = -0.25 \left(C_T/\sigma + 0.001\, \theta_{1_{deg}}\right) \qquad \text{(C-3)}$$

$$k_2 = -\left(1.41 + 0.0141\, \theta_{1_{deg}}\right) \sqrt{C_T/2} \qquad \text{(C-4)}$$

$$\sim -\left(1 + 0.01\, \theta_{1_{deg}}\right) \sqrt{C_T}$$

Tip Vortex Radial Coordinates:

$$\bar{r} = A + (1 - A) e^{-\lambda \psi_w} \qquad \text{(C-5)}$$

$$A = 0.78 \quad \text{(near wake)} \qquad \text{(C-6)}$$

$$\lambda = 0.145 + 27\, C_T \qquad \text{(C-7)}$$

Vortex Sheet Axial Coordinates:

$$(\bar{z}_T)_{\bar{r}=1} = \begin{cases} K_{1_{\bar{r}=1}}\, \psi_w \quad \text{for} \quad 0 \le \psi_w \le \dfrac{2\pi}{b} & \text{(C-8)} \\ \left(K_{1_{\bar{r}=1}}\right) \dfrac{2\pi}{b} + \left(K_{2_{\bar{r}=1}}\right)\left(\psi_w - \dfrac{2\pi}{b}\right) \quad \text{for} \quad \psi_w \ge \dfrac{2\pi}{b} & \text{(C-9)} \end{cases}$$

$$K_{1_{\bar{r}=1}} = -2.2 \sqrt{C_T/2} \qquad \text{(C-10)}$$

$$K_{2_{\bar{r}=1}} = -2.7 \sqrt{C_T/2} \qquad \text{(C-11)}$$

$$\bar{z}_{\bar{r}=0} = \begin{cases} 0 \text{ for } 0 \le \psi_w \le \frac{\pi}{2} & \text{(C-12)} \\ \left(K_{2\bar{r}=0}\right)\left(\psi_w - \frac{\pi}{2}\right) \text{ for } \psi_w \ge \frac{\pi}{2} & \text{(C-13)} \end{cases}$$

$$K_{2\bar{r}=0} = \left[\frac{\theta_{1_{deg}}}{128}\left(0.45\,\theta_{1_{deg}} + 18\right)\right]\sqrt{C_T/2} \qquad \text{(C-14)}$$

Since the cross sections of the vortex sheet from each blade are essentially lines rather than discrete points, as is the case for the tip vortex cross sections, it was assumed that the vortex sheet cross sections are linear, and the axial position of a vortex sheet at a given azimuth can be defined by two points. For simplicity, the two points selected were the imaginary extensions of the cross section to $\bar{r} = 0$ at one end and to $\bar{r} = 1.0$ at the other end (Equations C-6 through C-14). These two points establish the intercept at the axis of rotation and the slope of the vortex sheet at a particular wake azimuth. The axial coordinates of a specific point on a vortex filament forming part of a vortex sheet representation are obtained in the computer program from this intercept, slope and the radial coordinate of the point defined below.

Vortex Sheet Radial Coordinates:

It was assumed that the radial position of a point on a vortex filament forming part of the vortex sheet representation (point $\bar{A}$) is linearly proportional to the radial coordinate of the intersection of the vortex sheet with the outer vortex sheet boundary (point $\bar{B}$). With the exception of the immediate vicinity of the blade ($\psi_w < 2\pi/b$), the vortex sheet boundary was assumed to be equivalent to the boundary formed by the locus centers of the tip vortex cross sections (equivalently, tip vortex streamline). For ψ_w less than the blade spacing, $2\pi/b$, the boundary was faired from the point of maximum circulation on the blade (point $\bar{D}$) to the tip vortex boundary. The constant of proportionality was assumed to be the ratio of the radial position of the origination of the vortex filament at the blade (point $\bar{C}$) to the radial position of the vortex sheet boundary at the blade (point $\bar{D}$). That is,

$$\bar{r}_{\bar{A}} = \left(\frac{\bar{r}_{\bar{C}}}{\bar{r}_{\bar{D}}}\right)\bar{r}_{\bar{B}} \qquad \text{(C-15)}$$

Detailed equations to calculate each of the items in Equation (C-15) are contained in the computer analysis. Equation (C-15) essentially assumes that the contraction of the inboard vortex filaments (as measured along the sheet cross section) is determined by the degree of contraction of the tip vortex at the axial location where the inboard sheet extension intersects the tip vortex trajectory. Figure C-1 is a cross section of the wake geometry described above.

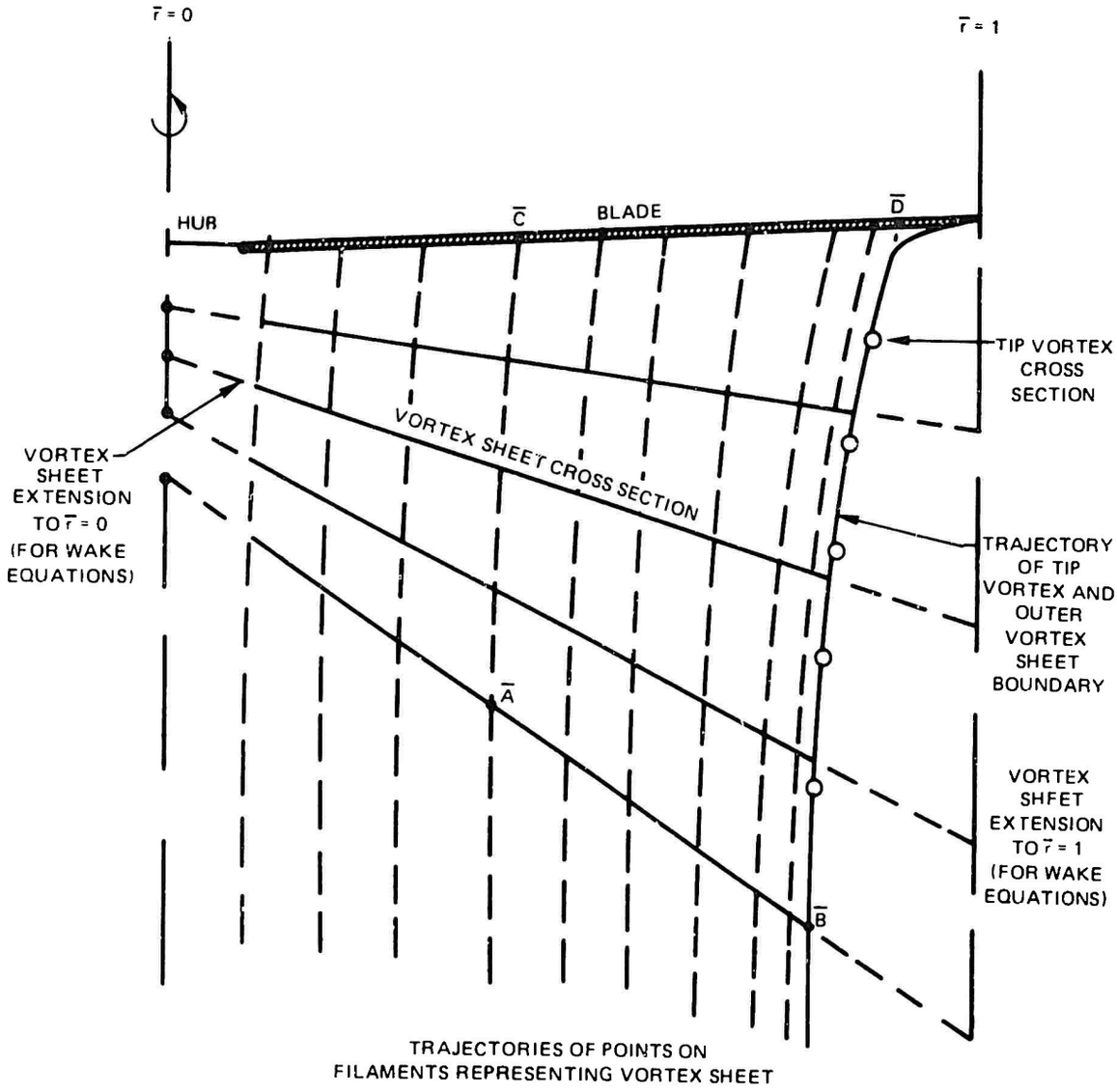

Figure C-1. Cross Section of the Generalized Wake Model.

APPENDIX D

PRIMARY EQUATIONS FOR THE UTRC PRESCRIBED WAKE HOVER PERFORMANCE ANALYSIS

In order to relate to the program input-output symbols and to describe some of the symbols generated within the program, program symbol notation is used in the following equations. The equations for the Prescribed Wake Hover Performance Analysis follow closely the equations for the Prescribed Wake Rotor Inflow Analysis (Appendix B), except that they are not time dependent.

The blade circulation at any blade segment I is, from the Kutta-Joukowski relation,

$$CIRC(I) = C(I)\cdot V(I)\cdot CL(I)/2 \tag{D-1}$$

where CIRC(I) = local circulation, ft^2/sec
C(I) = local blade chord, ft
V(I) = local resultant velocity, fps
CL(I) = local lift coefficient

The local resultant velocity V(I) can be expressed as

$$V(I)^2 = (VPSI(I) + VTI(I))^2 + W(I)^2 \tag{D-2}$$

where

$$VPSI(I) = OMGR\cdot RSC(I) \tag{D-3}$$

and OMGR = Rotor tip speed, fps
RSC(I) = Blade segment radial position
VT(I) = Induced tangential velocity, fps
W(I) = Induced axial velocity, fps (also symbolized as VZI in program).

For helicopter rotors (versus propellers), VT(I) may be neglected. Also, since W(I) is small in the important blade tip region relative to the rotational velocity, it is assumed that

$$V(I) = OMGR\cdot RSC(I) \tag{D-4}$$

so that a linear closed form solution can be obtained. Also, in order to linearize the solution, the lift coefficient is expressed as

$$CL(I) = AA(I) \cdot ALPHAE(I) \tag{D-5}$$

where AA(I) = local lift curve slope
ALPHAE(I) = local blade angle of attack

In stall, the maximum lift coefficient is limited in the program to CLMAX(I), which is determined from input values of ALPHAE (ALPMAX) beyond which stall is assumed. The angle of attack below stall is,

$$ALPHAE(I) = THETA(I) + PHII(I) \tag{D-6}$$

where THETA(I) = blade pitch angle
PHII(I) = blade inflow angle

The blade inflow angle, PHII(I) is

$$PHII = \tan^{-1} (W(I)/VPSI(I)) \tag{D-7}$$

If the tangential induced velocity is again neglected, to linearize the solution, it is assumed that PHII(I) is a small angle and thus,

$$PHII(I) = \tan PHII(I) \tag{D-8}$$

Substituting Equations (D-4) through (D-8) in Equation (D-1), the circulation equation becomes

$$CIRC(I) = C(I) \cdot AA(I) \cdot (VPSI(I) \cdot THETA(I) + W) \tag{D-9}$$

Since there are ITOTI blade segments, there are ITOTI equations of the form of Equation (D-9). This set of ITOTI equations can be written in matrix notation as:

$$[CIRC(I)] = [C(I) \cdot AA(I) \cdot (VPSI(I) \cdot THETA(I) + W(I))] \tag{D-10}$$

The axial induced velocity in Equations (D-9) and (D-10) is expressed, using the Biot-Savart law, as a function of the geometry of the trailing wake filaments and their circulation strengths. The axial velocity induced by a given wake segment (subscripts K, JJJ, N) on trailing filament K at a given blade segment (I,JJ) is expressed in terms of the Biot-Savart law as

$$W(K,N,JJJ) = (CIRCT(K)/4\pi R)\cdot GC\ (K,N,JJJ) \qquad (D\text{-}11)$$

where $CIRCT(K)$ = circulation strength of Kth filament, ft^2/sec

$GC(K,N,JJJ)$ = geometric influence coefficient from the Biot-Savart law

The nondimensional geometric coefficient, GC, is a function of the prescribed wake cylindrical coordinates (RW, ZW, and PHI) only. The lengthy expressions for GC may be obtained from the program listing. Since the blade circulation is assumed constant with time for the hovering condition, each wake filament has a constant strength along its length. The total velocity due to the Kth filament at the blade point (I,JJ) is the sum of Equation (D-11) evaluated for each segment in the Kth filament and can be expressed as

$$W(K) = (CIRCT(K)/4\pi R)\cdot GCK(I,J,K) \qquad (D\text{-}12)$$

where
$$GCK(I,J,K) = \sum_{N} \sum_{JJJ} GC(K,N,JJJ) \qquad (D\text{-}13)$$

for a single K. Equation (D-12) expresses the axial induced velocity due to filament K in terms of the trailing filament circulation. A summation of the induced velocity contributions from all the trailing wake filaments, through a summation of the results of Equation (D-12), would lead to an expression for the total axial induced velocity at a blade segment in terms of unknown trailing filament circulations.

It will now be shown that the axial induced velocity can be expressed as the product of a matrix of geometric coefficients representing the wake geometry and the bound circulations. Since all blades are assumed to be equally spaced azimuthally around the rotor disc, the effect of the bound circulation of all the blades cancels at each blade. Therefore, the bound circulation does not directly contribute to the induced velocity distribution at the blades. However, the circulation strength of each trailing filament CIRCT(K) may be expressed as the difference between the bound circulation of the two blade segments adjacent to its point of origin at the blade. Thus

$$CIRCT(K) = CIRC(I=K) - CIRC(I=K-1) \qquad (D\text{-}14)$$

Substituting Equation (D-14) in Equation (D-12) and summing the effects of all filaments from all blades, the total axial induced velocity at a point (I,J) is

$$W(I) = (1/4\pi R)\sum_{K}(CIRC(I=K) - CIRC(I=K-1))\cdot GCK(I,J,K) \qquad (D\text{-}15)$$

Rearranging Equation (D-15) to combine like circulations leads to

$$W(I) = 1/4\pi R \sum_{II} GCDIM(I,II) \cdot CIRC(II) \qquad \text{(D-16)}$$

where $GCDIM(I,II) = GCK\ (I,J,K = II+1) - GCK(I,J,K = II)$ (D-17)
(summed on blade J values for influence of wakes from all blades)
II = dummy subscript for I'

The azimuthal subscript, JJ, was eliminated from W due to the azimuthal independence of the induced velocity.

Substitution of Equation (D-16) in matrix Equation (D-10) results in a matrix equation in which the only unknowns are the bound circulations, CIRC(I):

$$[CIRC] = [CONST] - \{GCMAT\}\ [CIRC] \qquad \text{(D-18)}$$

where GCMAT = final matrix influence coefficients which are functions of the geometric coefficients and input constants.
CONST = matrix constants which are only functions of the following known quantities: R, UT, AT, C, and blade twist.

Solving for [CIRC]:

$$[CIRC] = [CONST]\ \{1 + GCMAT\}^{-1} \qquad \text{(D-19)}$$

A Gauss-Seidel numerical procedure for evaluating this circulation matrix is included in the computer program. Following the circulation solution the induced velocity distribution is obtained from Equation (D-16).

The above equations are the fundamental equations in the analysis for unstalled, potential flow conditions. Modifications providing for blade stall and finite vortex core size are included in the computer program.

LIST OF SYMBOLS

a_o	blade coning or precone angle, deg
a_{1_s}	longitudinal flapping angle for the first harmonic; coefficient of $-\cos\psi$ term in Fourier series expansion of blade flap angle with respect to plane normal to the rotor shaft axis, deg
A_w	wing area, ft^2
AR	blade aspect ratio, AR = R/c
A_{1_s}	cosine component of first harmonic cyclic pitch; coefficient of $-\cos\psi$ term in Fourier series expansion of the blade pitch angle with respect to the plane normal to the rotor shaft, deg
b	number of blades
B_{1_s}	sine component of first harmonic cyclic pitch; coefficient of $-\sin\psi$ term in Fourier series expansion of blade pitch angle with respect to the plane normal to the rotor shaft, deg
c	blade chord, in.
C_L	rotor lift coefficient, $L/\rho\pi R^2(\Omega R)^2$
C_{L_w}	wing lift coefficient, $L_w/\frac{1}{2}\rho V^2 A_w$
C_T	rotor thrust coefficient, $T/\rho\pi R^2(\Omega R)^2$
L	rotor lift, lb
L_w	wing lift, lb
q	dynamic pressure, $\frac{1}{2}\rho V^2$, psf
r	radial coordinate from z or z' axis, ft
R	rotor radius, ft

T	rotor thrust, lb
v_o	momentum theory value of rotor induced velocity, absolute value, fps Hover: $v_o = \Omega R\sqrt{\frac{C_T}{2}}$ Forward Flight: $v_o \quad \frac{\Omega R\, C_T}{2\sqrt{\mu^2+\lambda^2}}$
v_x, v_y, v_z	local instantaneous induced velocity component in the x, y, or z directions, positive in positive axis direction, fps
$v_{x'}$, $v_{y'}$, $v_{z'}$	local instantaneous induced velocity component in the x', y', or z' directions, positive in positive axis direction, fps
$\bar{v}_x$, $\bar{v}_y$, $\bar{v}_z$	local time-averaged induced velocity component in the x, y, or z directions, positive in positive axis direction, fps
$\bar{v}_{x'}$, $\bar{v}_{y'}$, $\bar{v}_{z'}$	local time-averaged induced velocity component in the x', y', or z' directions, positive in positive axis direction, fps
v_w	velocity component induced at rotor by wing, normal to rotor disk, positive up, fps
V	free-stream velocity, fps
x	longitudinal coordinate from rotor hub center in plane parallel to rotor disk, positive in downstream direction, ft
x'	longitudinal coordinate in wind axis system measured from rotor hub center, positive in downstream direction, ft
y	lateral coordinate from rotor hub center in plane parallel to rotor disk, positive toward advancing side of rotor, ft
y'	lateral coordinate from rotor hub center in wind axis system, positive toward advancing side of rotor, ft

z	coordinate from rotor hub center in direction normal to rotor disk, positive up, ft
$\bar{z}$	z/rotor radius, R
z'	vertical coordinate from rotor hub center normal to wind axis, positive up, ft
Δz	coordinate from center of, and normal to, the rotor tip-path plane, positive up, ft
$\Delta z'$	vertical coordinate from local point on a blade, positive up, ft
$\bar{z}_T$	same as $\bar{z}$ except measured from tip of blade
α	rotor tip-path-plane angle of attack. Angle between free-stream velocity and tip-path-plane
Γ	local blade circulation or circulation of a wake vortex element, ft^2/sec
ϵ	spanwise average of downwash angles, rad, $\epsilon \cong v_z/V\cos\alpha$
ϵ_o	theoretical downwash angle at center of rotor as defined in Reference 27, $\epsilon_o \cong v_o/V\cos\alpha$
θ_1	blade linear twist rate from center of rotation to tip, deg (normally negative)
θ_{75}	blade collective pitch angle measured at r = 0.75 R, deg
λ	rotor inflow ratio, $\lambda = (V\sin\alpha - v_o)/\Omega R$
μ	rotor advance ratio, $\mu = V\cos\alpha/\Omega R$ (or $V/\Omega R$ as indicated)
ρ	air density, $lb\text{-}sec^2/ft^4$
σ	rotor solidity ratio, $\sigma = bc/\pi R$

χ	wake skew angle: skew angle of undistorted wake based on momentum induced velocity, positive when wake is below tip-path-plane, deg, see Equation 1
ψ	blade azimuth angle measured from positive x (or x') axis (downstream direction) to blade, in direction of blade rotation, deg
ψ_w	wake azimuth angle measured from blade, deg (represents age of wake point)
Ω	rotational frequency of blade, rad/sec